

Hot Dry Rock Reservoir Modelling

Musa Dahiru Aliyu

A thesis submitted in partial fulfilment of the requirements of the University
of Greenwich for the Degree of Doctor of Philosophy

February 2018

Declaration

“I certify that the work contained in this thesis, or any part of it, has not been accepted in substance for any previous degree awarded to me, and is not concurrently being submitted for any degree other than that of Doctor of Philosophy being studied at the University of Greenwich. I also declare that this work is the result of my own investigations, except where otherwise identified by references and that the contents are not the outcome of any form of research misconduct.”

Musa Dahiru Aliyu
(Student)

Date

Professor Colin Hills
(First supervisor)

Date

Dr Cecilia Macleod
(Second supervisor)

Date

Acknowledgements

PhD research is a long journey full of different experiences. Therefore, it requires support and help from individuals and organisations, and hence it is essential for me to acknowledge their efforts. To start with, I am grateful to my supervisor Professor Colin Hills for his continued support, encouragement and supervision, which enabled the completion of this thesis.

The continuous support I received from my former supervisors Dr Ouahid Harireche, Dr Assad Famarzi and Professor Amir Alani, who initially employed me for this PhD, is particularly acknowledged. These three individuals have been very supportive during their time as my supervisors at the university: thank you, all.

My highest gratitude goes to my parents Dr Aliyu Dahiru and Mrs Maryam Aliyu Dahiru for their endless support, sacrifice and encouragement in all my life's endeavours. It is indeed the greatest honour to have you both as parents, and I will be forever grateful to you till the last breath of my life.

I am sincerely grateful to my beloved wife Hanifa and daughter Maryam for their support, understanding, and excessive perseverance while I was undertaking this PhD research.

This PhD would not have been possible without the Scholarship Funding support I received from both the University of Greenwich (UK) and the Petroleum Technology Development Fund (PTDF) (Nigeria). Special thanks to Alhaji Ahmed Galadima Aminu (Bappa Tijjani), the General Manager for Education and Training of the PTDF for the endless support and encouragement.

I appreciate the support of my eldest brother Aminu and my younger brother Sadiq, and that of my uncle Barkindo (Kawu Ballo), and all my siblings.

Many thanks to Dr Raj Bhatti, Professor Peter Kyberd, Dr Kong Fah Tee, Dr Mike McGibbon, Julie Boyer and Nikki Jack of the Department of Engineering Science of the University of Greenwich for their extraordinary support while I was conducting the research.

Abstract

Geothermal energy reserves are significantly underdeveloped resources, and field experiments have shown the energy produced from this resource is clean and sustainable. Deep geothermal resources represent one form of geothermal energy, and the most widely used, in terms of commercial viability, are the hot dry rock (HDR) geothermal reservoirs.

The field investigation of HDR systems is costly. The interaction between key rock properties during reservoir operation requires clear understanding to predict long-term performance. Therefore, there is a need for a numerical modelling tool to capture the coupled interactions between the thermal, hydraulic, mechanical and chemical processes operating during exploration-exploitation.

A multitude of computational models have been developed over the past two decades, based on different modelling approaches; however, there are still some limitations associated with their conceptual models concerning their ability to capture the structures present in deep subsurface media. To address some of these shortcomings, a fully coupled transient thermo-hydraulic (TH) model of an HDR geothermal reservoir is developed using the finite element method. The model is developed based on the open outlooks of HDR geothermal reservoir concepts established in the US, UK and France and is carried out following an intense review, with the identification of research limitations and shortcomings. Before that, the governing equations are derived based on the conservation laws of mass, energy and momentum from modifying the existing equations used.

Moreover, extensive verifications and validations are conducted to evaluate the efficiency and reliability of the developed model based on well-established analytical solutions and experimental field measurements available in the related literature, and the results obtained are in good agreement. Subsequently, additional extensions are examined based on the limitations of the previous techniques identified. The aforementioned additions include simulation of a field case study, modelling of heterogeneous HDR systems, and the effect of multiple pore media in probing the productivity of reservoirs during long-term performance. Thus, these three contributions represent a more realistic model of reservoir concepts that account for the faults, fractures and rock matrix concurrently. The different

sets of the results obtained from these models are analysed in-depth, and several breakthroughs are identified that advance the knowledge in the field of geotechnical engineering and particularly HDR geothermal systems.

This present work has shown the modelling of geothermal systems can be improved by using field data selectively with existing methods. The key outcome from this research is new insight into the way geothermal energy reserves can be exploited, and modelled. This work shows that a computational modelling approach can increase our understanding of complex subsurface interactions in geothermal reservoirs, and how they can be simulated effectively.

Table of contents

Declaration	i
Acknowledgements	ii
Abstract	iii
Table of contents	v
List of figures	xi
List of tables	xv
List of symbols	xvi
Acronyms	xviii
Subscripts	xviii
Chapter one – Introduction	1
1.1 Research background	1
1.2 Geothermal resources and applications	2
1.2.1 Categories of geothermal resources	3
1.2.2 Overview of installed capacity worldwide	4
1.3 Motivation	4
1.4 Aims of this research	7
1.4.1 Objectives of this research	10
1.4.2 Scope of this research	10
1.4.3 Research method	11
1.5 Thesis outline	12
Chapter two – Literature review	14
2.1 Introduction	14
2.2 Brief history of HDR geothermal energy	14
2.2.1 The birth of HDR geothermal energy	14
2.2.2 Preliminary works and developments of HDR geothermal energy	16

2.3 Geometric representation of reservoir models	17
2.3.1 Abstract geometric model	17
2.3.2 Reduced geometric model	19
2.3.3 Realistic geometric model	22
2.4 HDR simulation methods and codes	24
2.4.1 Overview of HDR simulation codes	25
2.4.2 Previous HDR simulation codes and limitations	25
2.4.3 Current HDR simulation codes	30
2.5 Coupled processes	31
2.5.1 Review of coupled processes applicable to HDR geothermal energy	32
2.6 Permeability and porosity models	34
2.7 Research gaps and limitations	35
2.7.1 The effect of reservoir connectivity on HDR energy mining	35
2.7.2 Numerical verifications and validations of modelling approaches for HDR systems	35
2.7.3 The effect of multiple pore media on HDR geothermal mining	36
2.8 Summary	36
Chapter three – Governing equations and FEM solutions	37
3.1 Introduction	37
3.1.1 Bases for the derivation of the governing equations	37
3.2 Theoretical background of naturally fractured porous media	38
3.3 Governing equations for modelling fluid flow in porous media	39
3.4 Governing equations for modelling heat transport in porous media	42
3.5 Finite element formulation	43
3.5.1 Initial and boundary conditions	43
3.5.2 The solution to the boundary value problem	44
3.5.3 The weighted residual method	46

3.5.4 The weak formulation of the solution	47
3.5.6 The Galerkin FEM discretisation	48
3.5.7 Element choice	50
3.5.8 Temporal discretisation and convergence criteria	51
3.6 Coupling strategy for the TH processes	52
3.7 Numerical implementation of the FE model	54
3.8 Summary	55
Chapter four – Code verification and validation studies	56
4.1 Introduction	56
4.2 Overview of verification and validation processes	56
4.3 Verification study on the FE model	58
4.3.1 Verification of one-dimensional numerical model against analytical solutions	59
4.3.2 Verification of two-dimensional numerical model against analytical solutions	63
4.4 Validation of the FE model	70
4.4.1 Validation of temperature profile at Soultz well	70
4.4.2 Validation of Fenton Hill HDR field experiment	74
4.5 Summary	77
Chapter five – Numerical modelling of field case study for the Soultz geothermal reservoir	78
5.1 Introduction	78
5.2 Overview of the Soultz geothermal reservoir	78
5.2.1 Physical and petrophysical settings of the reservoir	79
5.3 Numerical modelling of the lower reservoir	81
5.3.1 Geometrical and physical properties of the reservoir	82
5.3.2 Initial and boundary conditions	84
5.3.3 Meshing and solutions	85

5.4 Results and discussions.....	86
5.4.1 The effect of human-controlled parameters on production temperature....	87
5.5.2 Parameter influence on reservoir cooling.....	90
5.5 Findings and limitations.....	93
5.6 Summary.....	94
Chapter six – Numerical modelling of geothermal reservoir with interaction between the components	95
6.1 Introduction.....	95
6.2 Research contribution	96
6.3 Geothermal reservoir case study	97
6.3.1 Mesh and solution convergence	100
6.4 Results and discussions.....	103
6.4.1 Effect of cold-water front in the reservoir	103
6.4.2 Parametric studies.....	105
6.4.3 Energy extraction rates.....	112
6.5 Summary.....	115
Chapter seven – Numerical modelling of geothermal reservoir with multiple pore media: A case of triple porosity-permeability model	116
7.1 Introduction.....	116
7.2 Background	116
7.2.1 Motivation	117
7.3 Triple porosity-permeability model for the fractured porous reservoir	119
7.3.1 Theoretical assumptions for triple porosity-permeability media	120
7.3.2 The transient flow of mass in triple porosity-permeability media.....	120
7.3.3 The transient flow of heat in triple porosity-permeability media.....	121
7.4 Numerical case study one: Doublet geothermal reservoir	121
7.4.1 Material and petrophysical properties of the media.....	122

7.4.2 Initial and boundary conditions	123
7.4.3 Results	124
7.5 Numerical case study two: Triplet geothermal reservoir	129
7.5.1 Reservoir initial and boundary conditions	131
7.5.2 Results	132
7.6 Discussions	137
7.7 Summary	139
Chapter eight – Conclusions and recommendations for future work	141
8.1 Introduction	141
8.2 Conclusions	141
8.2.1 Review of existing models	141
8.2.2 FE formulation and solutions	141
8.2.3 FE model verification and validation	142
8.2.4 Numerical modelling of a field case study	142
8.2.5 Numerical modelling of geothermal reservoirs with feedback interaction	143
8.2.6 Numerical modelling of geothermal systems with multiple pore media	143
8.2.7 Concluding statement	144
8.3 Recommendations for future work	144
8.3.1 Development of mini-scale experiment to further validate the model	145
8.3.2 Implementation of mechanical and chemical processes	145
8.3.3 Implementation of fracture propagation models	145
8.3.4 Incorporation of non-Darcian flow	146
8.3.5 Development of multi-phase flow models	146
8.3.6 Development of realistic 3-D model of reservoirs	147
References	148
Appendices	170
Appendix one: Numerical implementation of the FE model	170

Appendix two: Analytical solution for heat transfer in porous medium.....	172
Appendix three: Analytical solutions for the heat transport in fractures.....	174
Appendix four: Fluid transport in triple porosity-permeability media.....	175
Appendix five: Heat transport in triple porosity-permeability media.....	176
Publications from the PhD research	177

List of figures

Figure 1.2: Installed capacity as of 2015 worldwide 12.6 GWe (Bertani, 2016).....	4
Figure 1.3: How electricity is produced using HDR (Boyd, 2013).....	5
Figure 2.1: The original concept for an HDR geothermal system (Adapted from: Brown et al., 2012).....	15
Figure 2.2: Abstract geometric model (Adapted from: (Elsworth, 1989a)	18
Figure 2.3: Reduced 1-D geometry (Modified from: (Willis-Richards and Wallroth, 1995)	19
Figure 2.4: Reduced 2-D geometry type one (Jupe et al. 1995b).....	20
Figure 2.5: Reduced 2-D geometric model type two (Hicks et al., 1996).....	21
Figure 2.6: 3-D reduced geometry model (Modified from: Pruess, 1988).....	21
Figure 2.7: Realistic geometry model for three different distributions of fracture lengths (Lanyon et al., 1993).....	22
Figure 2.8: Realistic geometric model using stochastic fracture network designed from data available for the Rosemanowes HDR site (Kolditz and Clauser, 1998)	23
Figure 2.9: Detail of temperature and fluid flow field in subsurface obtained from FRACTure software (Kohl et al. 2000).....	27
Figure 2.10: Temperature in reservoir after 720 days of operation (min=70°C, max=278°C) obtained from GEOCRACK reservoir simulator (Swenson et al., 1999)	29
Figure 3.1: 3-D representation of naturally fractured porous media	38
Figure 3.2: 2-D problem domain and boundary	45
Figure 3.3: General representation of 3-D isoparametric elements.....	51
Figure 3.4: Fully coupled TH processes representation	53
Figure 4.1: A typical representation of model verification and validation process (Modified from: Society for Computer Simulation, 1979).....	57
Figure 4.2: Geometry of the 1-D porous medium	60
Figure 4.3: Temperature distribution along the medium after five years.....	61
Figure 4.4: Dimensionless temperature at the right edge point of the fracture	63
Figure 4.5: 2-D fractured porous media	65
Figure 4.6: Analytical solution (left) and FE model solution (right)	66
Figure 4.7: Pressure profile along a diagonal from the bottom-left passing via the fracture to the top-right	66
Figure 4.8: Geometry of the fracture-matrix heat transport (adopted from Holtz, 2012) ..	68

Figure 4.9: Grid alignment and boundary conditions for the numerical model	68
Figure 4.10: Observation points positions (i.e., 6, 10, and 12) for temperature history curves	69
Figure 4.11: Temperature history curves at specific points on the rock matrix block for both the analytical and numerical models	69
Figure 4.12: The Soultz site showing the location of the upper and lower reservoirs, and the wellbores (Genter et al., 2010a).	71
Figure 4.13: Temperature profile at GPK2 wellbore (Measured vs Simulated)	73
Figure 4.14: Simplified reservoir geometry of Fenton Hill, HDR system, Phase I (Murphy et al., 1981)	75
Figure 4.15: Production temperature of measured vs simulated at well GT-2B	76
Figure 5.1: “The Soultz location and geology of the terrain; (1) Cenozoic sediments, (2) Cenozoic volcanism, (3) Jurassic, (4) Trias, (5) Hercynian basement, (6) Border faults, (7) Temperature distribution in °C at 1500m depth, and (8) Local thermal anomalies. Simplified cross-section through the Soultz site: (a) Cenozoic filling sediments (b) Mesozoic sediments (c) Granite basement” (Dezayes et al., 2004)	79
Figure 5.2: 2-D geological profile of the Soultz geothermal formation (Dezayes et al., 2004)	80
Figure 5.3: Temperature profile and geothermal gradient of GPK2 (Vidal et al., 2015)...	80
Figure 5.4: Schematic representation of the Soultz geothermal system.....	82
Figure 5.5: Lower reservoir geometry (km)	83
Figure 5.6: Lower reservoir mesh element sizes and distributions (m)	86
Figure 5.7: Production temperature at wellhead GPK2 with constant injection rate 10 l/s and 300 m lateral well spacing under the influence of various injection temperatures and pressures	89
Figure 5.8: Production temperature at wellhead GPK2 with constant injection rate 10 l/s and 600 m lateral well spacing under the influence of various injection temperatures and pressures	90
Figure 5.9: Reservoir cooling (°C) under the effect of 60°C fluid injection temperature with 25 MPa injection pressure	91
Figure 5.10: Reservoir cooling (°C) under the effect of 60°C fluid injection temperature with 10 MPa injection pressure	92

Figure 5.11: Reservoir cooling ($^{\circ}\text{C}$) under the effect of 30°C fluid injection temperature with 25 MPa injection pressure	92
Figure 5.12: Reservoir cooling ($^{\circ}\text{C}$) under the effect of 30°C fluid injection temperature with 10 MPa injection pressure	93
Figure 6.1: A typical geothermal reservoir with a single planar fracture.....	95
Figure 6.2: Geometry of the heterogeneous reservoir	98
Figure 6.3: Reservoir mesh of the model	102
Figure 6.4: Mesh convergence study.....	102
Figure 6.5: Error estimation	103
Figure 6.6: Cold-water front propagation within the reservoir ($^{\circ}\text{C}$) for different wellbore spacing at various simulation stages.....	104
Figure 6.7: Production temperature history under 40°C with 600 m well spacing	106
Figure 6.8: Fluid injection temperature 50°C with 600 m lateral well spacing	107
Figure 6.9: Production temperature history under 40°C with 700 m well spacing	107
Figure 6.10: Production temperature history under 20 l/s with 600 m well spacing	109
Figure 6.11: Production temperature history under 20 l/s with 700 m well spacing	110
Figure 6.12: Production temperature history under 20 l/s with 30°C injection temperature	111
Figure 6.13: Production energy as function of fluid injection rate under different lateral well spacing and fluid injection temperatures	113
Figure 6.14: Production energy as function of fluid injection temperature under different lateral well spacing and fluid injection rates	114
Figure 6.15: Production energy as function of lateral well spacing under different injection flow rates and fluid injection temperatures	114
Figure 7.1: Network of micro-cracks, fissures and fractures (Rosemanowes Cornwall, UK Adopted from: (Tenzer, 2001).....	118
Figure 7.2: Interconnected large fractures and faults (Soultz, France) (Modified from: (Clauser, 2006)	119
Figure 7.3: A typical representation of triple porosity-permeability (TPP) media	120
Figure 7.4: Doublet geometry of the triple porosity-permeability media	122
Figure 7.5: Temperature distribution ($^{\circ}\text{C}$) within the fault plane (yz (m)) after 5 years of simulation	125

Figure 7.6: Temperature distribution ($^{\circ}\text{C}$) within the fault plane (yz (m)) after 18 years of simulation	126
Figure 7.7: Temperature distribution ($^{\circ}\text{C}$) within the fault plane (yz (m)) after 30 years of simulation	126
Figure 7.8: Temperature changes along the injection fracture-fault interface at various simulation stages	128
Figure 7.9: Pressure distribution along the injection fracture-fault interface at various simulation stages	129
Figure 7.10: Geometry of the triplet reservoir with its various components.....	130
Figure 7.11: Mesh quality plot for the triplet reservoir	131
Figure 7.12: Conductive heat flux direction (W/m^2) after one-year of simulation	133
Figure 7.13: Convective heat flux direction (W/m^2) after one-year of simulation	133
Figure 7.14: Conductive heat flux direction (W/m^2) after 30 years of simulation.....	134
Figure 7.15: Convective heat flux direction (W/m^2) after 30 years of simulation.....	134
Figure 7.16: Temperature contour plot for the surfaces after one-year of simulation	135
Figure 7.17: Temperature contour plot for the surfaces after 30-years of simulation.....	136
Figure 7.18: Pressure profile at observation points A and B.....	137
Figure 1.A.1: Procedure for the numerical implementation of the FE model.....	171

List of tables

Table 1.1: Categories of geothermal resources (White and Williams, 1975).....	3
Table 2.1: Heat flow values for the depth test holes (U.S. Department of Energy, 2006). 17	
Table 2.2: Assumptions and limitations of abstract, reduced and realistic HDR models (Modified from: Willis-Richards and Wallroth, 1996)	24
Table 4.1: Material properties used in the test case one (Xia et al., 2017).....	60
Table 4.2: Initial and boundary conditions employed in test case one (Xia et al., 2017)...	60
Table 4.3: Material properties used in the test case two (Barth et al., 2010)	62
Table 4.4: Initial and boundary conditions employed in test case two (Barth et al., 2010)	62
Table 4.5: Model parameters adopted in model verification (Holtz, 2012)	65
Table 4.6: Model parameters used for the analytical verification (Holtz, 2012).....	67
Table 4.7: Geological properties and densities of the Soultz reservoir system	72
Table 4.8: The petro-physical properties of main lithological formations	72
Table 4.9: Percentage difference between measured and simulated temperature profiles at wellbore GPK2	73
Table 4.10: Rock properties for Fenton Hill, HDR system (Elsworth et al., 2016)	75
Table 5.1: Physical properties attributed to lower reservoir (less permeable granitic basement) (Guillou-Frottier et al., 2013; Magenet et al., 2014).....	84
Table 5.2: Range of values for the human-controlled parameters used in the reservoir model	87
Table 5.3: Human-controlled parameter combinations	88
Table 6.1: Geological properties of the system (Guillou-Frottier et al., 2013)	99
Table 6.2: The boundary conditions employed in the geothermal reservoir model.....	100
Table 7.1: Material properties employed for modelling the geothermal reservoir (Guillou-Frottier et al., 2013)	123

List of symbols

a	unknown field variable (1)
b	fracture aperture (m)
C_F	fluid compressibility (1/Pa)
C_m	matrix compressibility (1/Pa)
$C_{P,L}$	fluid heat capacity (J/kg/K)
$C_{P,S}$	solid heat capacity (J/kg/K)
C_p	effective heat capacity (J/kg/K)
f	load vector
g	acceleration due to gravity (m/s ²)
K	stiffness matrix
n	normal to boundary
N_p	shape function for fluid flow (1)
N_T	shape function for heat transport (1)
P	fluid pressure (MPa)
Q_E	heat source/sink term (W/m ³)
Q_{ext}	external source term (W/m ³)
$Q_{f,E}$	heat fracture source term (W/m ³)
Q_m	mass source/sink term (kg/m ³ s)
$Q_{m,E}$	heat external source term (W/m ³)
Q_{mf}	fracture source term (kg/m ³ s)
S	storativity (1)
t	time (s)
T	temperature (°C)
\bar{T}	normalised temperature (1)
v	Darcy's field velocity (m/s)
w	weighting function for domain (1)
\hat{w}	weighting function for boundary (1)
z	elevation (m)

$\nabla \cdot$	divergent operator
∇	gradient operator
δ	Dirac delta function
Ω	domain volume
χ_i	characteristic function
ϕ	porosity (1)
ρ	effective density (kg/m ³)
ρ_L	fluid density (kg/m ³)
ρ_S	solid density (kg/m ³)
κ	permeability (m ²)
μ	dynamic viscosity (Pa·s)
Γ	boundary
Ω	domain
Γ_P	Dirichlet boundary condition for fluid flow
Γ_T	Dirichlet boundary condition for heat transport
Γ_P^q	Neumann boundary condition for fluid flow
Γ_T^q	Neumann boundary condition for heat transport
φ	arbitrary function
λ	effective thermal conductivity (W/m/K)
λ_S	solid thermal conductivity (W/m/K)
λ_L	fluid thermal conductivity (W/m/K)
η	relaxation parameter

Acronyms

1-D	one-dimensional
2-D	two-dimensional
3-D	three-dimensional
BC	boundary condition
BDM	backward difference method
DP	dual-porosity
FD	finite difference
FDM	finite difference method
FE	finite element
FEM	finite element method
HDR	hot dry rock
TH	thermo-hydraulic
THM	thermo-hydro-mechanical
THC	thermo-hydro-chemical
THMC	thermo-hydro-mechanical-chemical
TPP	triple porosity-permeability
UK	United Kingdom
US	United States
WRM	weighted residual method

Subscripts

f	fracture
F	fault
M	matrix
inj	injection boundary condition
0	initial condition at $t = 0$

Chapter one – Introduction

1.1 Research background

Energy and the carbon emission crisis are the two main challenges for the twenty-first century that many countries are facing (Zhang et al., 2017). The events arising from these issues are due specifically to increasingly scarce fossil fuels and the burning of these fuels, which generates carbon dioxide (CO₂), a contributory factor in the warming of the atmosphere (Cheng et al., 2013). The resulting concern for undesired climate change and the increase of greenhouse gases in the atmosphere has led many industrialised countries to the establishment of an international regulatory framework for the reduction of CO₂ emissions (Karvounis and Wiemer, 2015). As a result, the key to the world's increasing prosperity and economic growth has been access to clean, affordable and reliable energy sources (Ghasemi et al., 2014). In addition, there is an increase in pressure to expedite the adoption and promote the sustainable development of renewable energy resources worldwide in order to protect the environment (Zheng et al., 2015). For instance, the EU Directive 2009-28-EN has been accepted by EU member states, introducing the application of renewable energy sources (RES) and aiming for the proportion of RES systems used to reach 20% by the year 2020 in Europe (Arola et al., 2014). As of 2010, RES have grown to supply an estimated 16.7% of total global energy consumption, and of that amount wind, solar and geothermal accounted for 8.2% approximately (Li, 2013). The results show that the wind, solar and geothermal are the most widely used RES across the globe (Li et al., 2015). Wind and solar accounted for almost 40% and 30% of the RES capacity, respectively, due precisely to their ease and lower cost of development. Unfortunately, the contribution of geothermal power is less 10%. However, geothermal energy sources have many advantages over solar and wind systems, among which are base loading, being weatherproof, high thermal efficiency, and excellent stability (Li et al., 2015).

Geothermal energy is an abundant renewable energy resource that is available underneath us. Depending on the temperature gradient and chemistry of the resources, geothermal energy can be used for both direct uses and electricity generation (Farghally et al., 2014). One of the sources of this energy is hot dry rock (HDR), and if this resource at a depth of 10 km can be exploited efficiently, it is estimated it could provide 200,000 times

the current world energy demand (Zhu et al., 2017). According to the International Energy Agency, by 2050 geothermal power could generate approximately 1,400 TWh/yr, supplying about 3.5% of global electricity production, which will reduce the rate of CO₂ emission to about 0.76 Gt/yr (International Energy Agency, 2013). Thus, to reach this target, more research is required in the field of geotechnical engineering, socioeconomics, and natural sciences in order to bring geothermal energy to a standard level where it can be accurately integrated into the nation's energy palette (Kolditz et al., 2013).

1.2 Geothermal resources and applications

The term geothermal originates from two Greek words, “geos”, which signifies earth, and “thermos”, meaning heat (Blázquez et al., 2016). Thus, the thermal energy generated and stored in the earth is called geothermal, and the earth's volume has temperatures greater than 1000°C, with only 0.1% at temperatures less than 100°C (Bayer et al., 2013). The internal structure of our planet and the physical processes occurring there are linked with the origin of this heat (Barbier, 2002) as well as to the decay of naturally occurring radioactive isotopes (Brunner et al., 2015). Across the globe, it is estimated that there is 1.45×10^{26} J of geothermal energy, which is approximately equal to 4.95×10^6 billion tons of standardised coal (Huang et al., 2015). Figure 1.1 shows the global map of heat flow in the earth (Hamza et al., 2008).

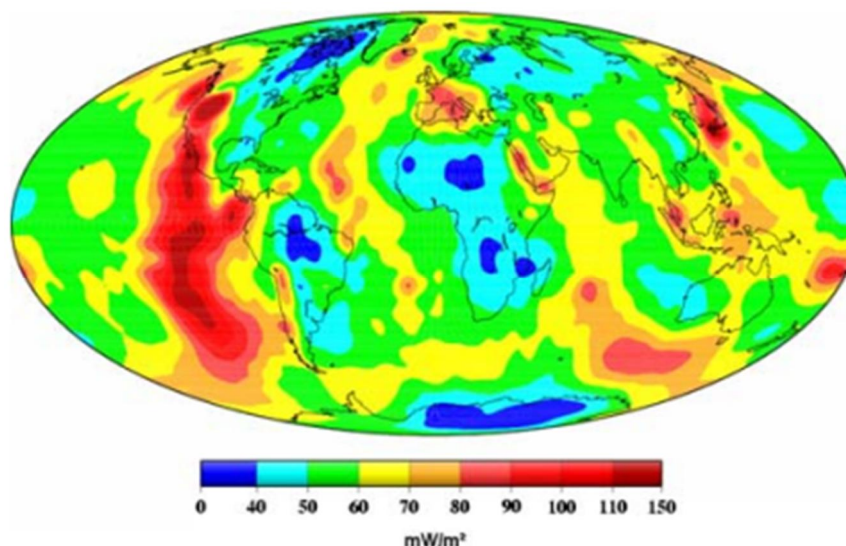


Figure 1.1: Global map derived from spherical harmonic expansion to degree 36 of conductive heat flow data (Hamza et al., 2008)

1.2.1 Categories of geothermal resources

Table 1.1 shows several categories of geothermal resources according to formation geology and temperature (White and Williams, 1975). The temperature ranges from the mean annual ambient of around 20°C to over 300°C. In almost all cases, for electric power generation, resources above 150°C are utilised; however, it has been reported that power had been generated using a 74°C geothermal resource at Chena Hot Spring Resort in Alaska (Lund, 2007). In addition, resources below 150°C are employed in direct-use schemes for cooling and heating. Geothermal (ground-source) heat pumps are also utilised for heating and cooling when the ambient temperature ranges from 5–30°C (World Energy Council, 2013).

Table 1.1: Categories of geothermal resources (White and Williams, 1975)

Resource category	Temperature range (°C)	Natural fluid supply
❖ Convective hydrothermal		
▪ Vapour-dominated	~ 240	Available, not always adequate
▪ Hot-water dominated		
• High-temperature	> 150	Available, not always adequate
• Intermediate-temperature	~ 90–150	Available, not always adequate
• Low-temperature	< 90	Available, not always adequate
❖ Conduction-dominated		
▪ Sedimentary basin	20–150	Adequate
▪ Geopressured	90–200	Generally, inadequate
▪ Radiogenic	30–150	Generally, inadequate
❖ Hot igneous rock		
▪ Assumed part still molten (Magma)	> 650	Inadequate
▪ Assumed not molten but very hot (HDR)	90–650	Generally, inadequate

1.2.2 Overview of installed capacity worldwide

Historically, the international geothermal meetings have provided a window at the World Geothermal Congress (WGC) to describe in detail the status of geothermal electric power generation worldwide by an in-country geothermist and summarised for the attendees by a Rapporteur (Huttrer, 1996). Every five years the meetings are convened to describe the geothermal activities carried out in their respective countries, new findings and plans for the future (Huttrer, 2001). These pieces of information are documented and published as Country Update (UC) papers. Figure 1.2 presents the total installed capacity from geothermal power plants worldwide as of 2015 based on the UC gathered from WGC in 2015 (Bertani, 2016). The current value of 12.6 GWe is a crucial result, and provides hope for achieving the short-term forecasting for 2020 of 20 GWe (Bertani, 2015).

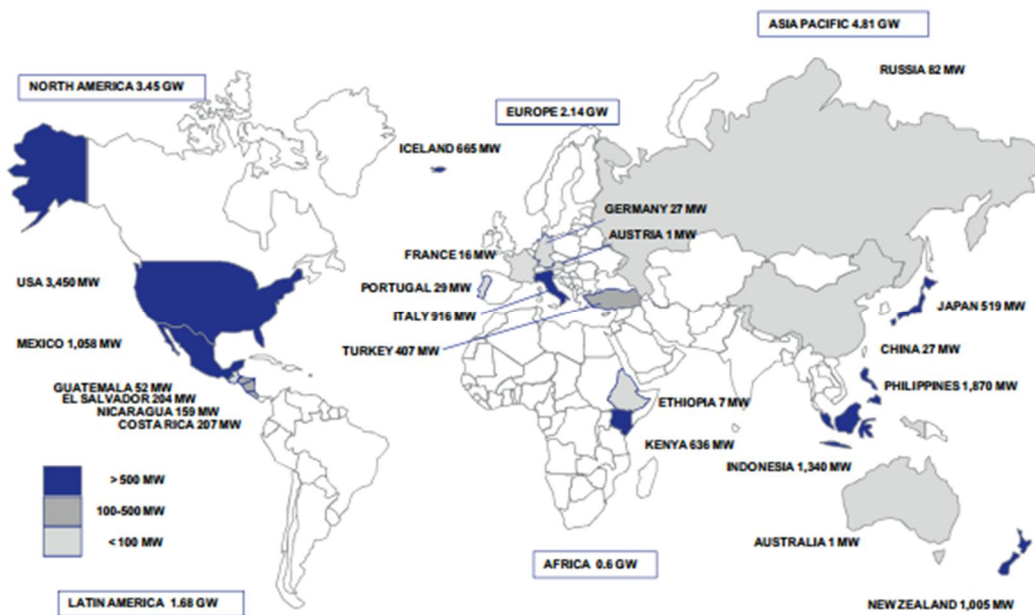


Figure 1.2: Installed capacity as of 2015 worldwide 12.6 GWe (Bertani, 2016)

1.3 Motivation

Geothermal energy is mined by way of force circulating fluid between injection and production wells through a naturally fractured rock mass (i.e. usually granitic or similar crystalline basement) to create a reservoir by hydraulic fracturing (Brown and Duchane,

1999; Willis-Richards and Wallroth, 1995) as shown in Figure 1.3 (Boyd, 2013). The in situ stress condition in the reservoir will perturb as a result of injection/extraction stimulation, which may lead to fracture initiation/propagation and activation of joints and faults (Ghassemi et al., 2007). Moreover, during reservoir stimulation, the interaction between the working fluids and the host rock may result in mineral dissolution/precipitation in the fractures, faults and wellbores. Consequently, engineering design is vital to understand the response of the fractures, faults and bedding planes to external stresses in HDR reservoirs (Taron and Elsworth, 2010).

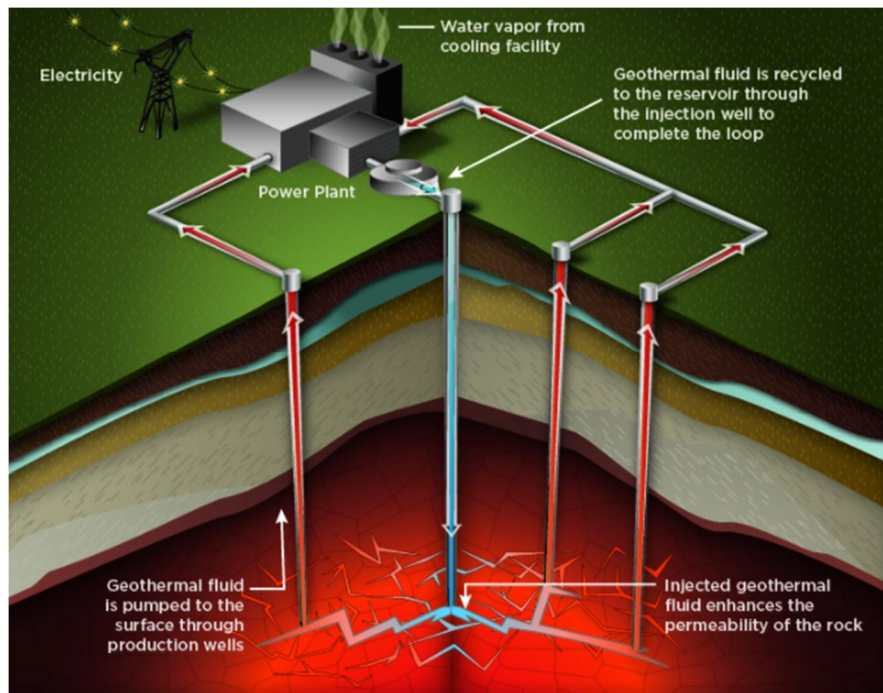


Figure 1.3: How electricity is produced using HDR (Boyd, 2013)

Figure 1.3 shows a typical way of which a geothermal system operates. As can be seen, the operation involves injection and extraction of fluid within a closed-loop. As the operation continues, different physical phenomena will be triggered in a feedback manner. Therefore, there is need to study the effect of such a system that behaves in a multi-physical context under a long-term performance. The reservoir represents a heat source of large dimensions over an extended period. Thermally induced convection and rock expansion effects do not depend directly on the value of temperature rise, but the integrated heat input into the system.

The assessment of the long-term performance of a geothermal system involves the understanding of combined effects of many different processes that may affect the transport of fluid and heat. The large perturbations initiate these coupled or combined processes to the rock mass due to the injection of fluid under high pressure. The coupled processes induced by these drastic changes in the system involves four different effects, namely thermal (T), hydrological (H), mechanical (M), and chemical (C). However, in this research, only two of those coupled effects will be considered due to the computational challenges involved in experimenting the full effects. The coupled effects that will be investigated in this research include the thermal (T) and hydraulic (H) processes.

The HDR field experiments are costly to perform for both reservoir circulation and stimulation. According to the global survey conducted by the World Bank on geothermal energy development, it has been found that a typical exploration campaign and initial test drilling program of three to five geothermal wells carries a cost ranging from \$20 to 30 million. Besides, the exploration and drilling stages of a geothermal project averagely take three to five years to guarantee the steam supply and to build a power plant.

To demonstrate an understanding of the available experimental results and to extend the understanding to other conditions, numerical experimentation and efficient physical/mathematical modelling are required to forecast or predict capability, lending support to design and operational planning (Cheng et al., 2001; Willis-Richards and Wallroth, 1995).

Furthermore, since field experiments are expensive to perform, the nature and properties of a geothermal reservoir can be estimated, and its behaviour understood through modelling, and the most powerful tool available to the reservoir engineer constitutes the use of different modelling approaches (Axelsson, 2003). One of the best instruments for predicting the behaviour of a geothermal reservoir is system models and hence ensuring sustainable output because they give an insight into what the system is before exploitation, the heat sources and much more (Dayan and Ambunya, 2015). An example of system model applicable to geothermal energy is the Temperature Control System Model (TCSM). The TCSM relies on the application of energy balance principles that assumes energy

accumulated by a system is equal to the energy into the system subtracted from the energy out of the system.

Accordingly, a conceptual model must be developed before a computer model of a geothermal field can be set up (O’Sullivan et al., 2001, 2000), because it is the first model of any system, with experimental and computational models essentially serving to prove their consistency with available data (Fairs et al., 2015). The purpose of geothermal modelling is two-fold:

- to obtain information on its nature and properties as well as its petrophysical conditions, and
- to estimate its production potential and predict its response to future production (Axelsson, 2013).

Nevertheless, the modelling technique is quite demanding, although there have been efforts to find some numerical and analytical solution. In some aspects, physical models can be complicated, depending on factors including the fracture system, operational conditions such as the fluid pressures encountered during high-pressure injection and lack of sufficient field data on the features of the rock mass (Cheng et al., 2001; Willis-Richards and Wallroth, 1995). Thus, numerical modelling is extremely powerful when based on comprehensive and detailed data, and is increasingly used to simulate geothermal reservoirs in different parts of the world (Axelsson, 2013).

1.4 Aims of this research

This PhD thesis focuses on the development of a numerical model of a HDR geothermal reservoir system, the processes that control these long-term system performances, and the potential effects of different geological formations on reservoir exploitation. The thesis also uses the currently available outlook of concepts developed at the Fenton Hill (US), Rosemanowes (UK), and Soultz (France) HDR projects for modelling such systems. The fundamental research questions addressed in this thesis are:

- **What is the pattern of fluid and heat transport in a heterogeneous fractured geothermal reservoir?**

To date, the majority of the transport models reported on deep geothermal reservoirs have been dedicated to fracture systems as a major pathway, rather than faults or vugs and matrix systems. This question will be addressed through a real-life case study of a geothermal field: (1) heat and fluid flow in Soultz formation, (2) transport via combined matrix-fracture systems, (3) the contribution of multiple pore media in subsurface transport. The research examined the effect of complex formation on energy mining of deep geothermal reservoirs. The field case studies selected are used as a reference for the implementation of the numerical model of the Soultz geothermal reservoir before exploitation, hydrothermal alteration, and tectonic activity. The geothermal system configuration in the present-day Soultz geological formation is directly studied from well log and borehole data available in the literature. Furthermore, thermal exploitation in naturally fractured-faulted media is explored in the context of larger-scale active faults, which provide additional pathways during extraction.

In addition, four key underlying research questions lead the investigation throughout the thesis:

- **How can the understanding of transport in deep geothermal reservoirs improve?**

At the stage of governing equations, to answer the question above, there is a need to modify the existing or to develop a more comprehensive mathematical model describing the coupled thermo-hydraulic (TH) processes of deep heterogeneous porous media in general, and of the geothermal reservoirs in particular. The models should explicitly capture the fluid and heat flow processes, and fracture and fault transport phenomena should be treated efficiently, beside commonly considered equations on dual-porosity. Transport changes that occur with the interfaces of the different media should be explicitly considered according to the mass conservation equations of each of the media, instead of only depending on the dual-porosity models as often used in other TH models of porous media.

- **How can the nonlinearity and ill-conditioning challenges caused by the coupled processes be solved?**

By developing a finite element (FE) model based on the modified or developed governing equations for real-life cases; the implementation of process couplings is a major goal of this research. As a result, unique solution methods and strategies are required to obtain efficient and stable numerical simulations, which are often the most challenging problem for modelling coupled transient TH processes with the FE techniques, due to high nonlinearity of the coupled equations caused by the coupling and numerical ill-conditioning. These numerical issues are a result of the coupling terms such as density and viscosity dependencies occurring in the fluid due to thermal gradients. Thus, this thesis prepares the basis for the implementation of these coupling effects.

- **What are the procedures used to authenticate the numerical results?**

To validate and verify the developed numerical code against available experimental data and existing analytical solutions, and then apply the code to simulate the full-scale 3-D numerical model for evaluating the forecasting capability of the solver for modelling long-term coupled transient TH behaviours in deep heterogeneous geothermal reservoirs. Thus, modelling such complex formations with multiphysics effects requires a graphical user interface that allows for visualisation of the numerical results for accurate and efficient analysis.

- **How can the long-term performance of heterogeneous geothermal systems be enhanced?**

One of the goals of this PhD thesis is to examine the influence of process interaction in a multiphysics context. A sufficient understanding of a deep heterogeneous geothermal system and its main processes is required, especially if long-term processes are involved. The analysis of sensitivities is crucial for the assessment of the long-term energy exploitation of dual and triple porosity-permeability systems. Stakeholders or governments need to assess the operation criteria as they have to ensure the long-term safety performance of the energy mining under different operational conditions before investment. The significance of various parameters to system performance and the surrounding media are key to an

understanding of deep subsurface media and its coupled processes. Consequently, the classification of coupling processes according to their importance is a significant result of the application of coupled numerical codes to be developed. In order to accomplish sensitivity analysis, it is useful to consider executable process coupling.

1.4.1 Objectives of this research

This thesis is concerned with numerical modelling of deep HDR geothermal energy under different geological formations and conditions. Therefore, the objectives set out here are based on the research questions raised in section 1.4, which include:

- to develop a 3-D FE model of a deep HDR geothermal reservoir with multiple pore media;
- to model the coupled thermo-hydraulic processes of a HDR geothermal reservoir;
- to carry out a verification and validation study on the developed FE model;
- to model the effect of heat and fluid transport in complex geological formations;
- to develop a triple porosity-permeability model of geothermal reservoirs.

1.4.2 Scope of this research

This thesis addresses several key questions in relation to understanding and modelling heat and fluid transport in deep HDR geothermal reservoirs. Despite the fact that they are set out separately, it is important to recognise that these questions are closely intertwined and that research addressing any one problem will affect the others. As a consequence, an overall 3-D model of a deep geothermal system is developed within a broader context of a complex geological formation. These questions are addressed within five interrelated chapters developed around the principal idea of developing a unified numerical model and structural framework for the geothermal systems. The chapters are written in a form fit for publication and are displayed as independent studies. Furthermore, published or accepted versions have been amended only slightly regarding style and formatting for inclusion into a consistent overall thesis design.

1.4.3 Research method

To address the fundamental research question and the underlying questions, an appropriate solver is needed because the research is dealing with the mathematical description and numerical modelling of subsurface media. It is about a medium that controls the movement of fluids, the transfer of heat, the deformation of media, and the transport of chemicals, as well as about the physical laws that describe the relationship between stress and strain, the flux of fluids, heat and chemicals. Understanding the mechanisms that control the occurrence of these processes and their interplay is the ultimate goal of this research. Accurate numerical methods are required to make this goal possible: approximating efficiently and accurately mathematical descriptions is of ultimate importance. In addition, extensive coverage of finite element methods (FEM) used in fluid flows and Lagrangian-Eulerian approaches best suited to dealing with advection-dominant transport will be applied. The major processes that this research is concerned with are fluid flow and heat transport. Thus, even though only two major processes are considered in this research, the computational models conceived are gigantic.

To solve the processes mentioned earlier, a multiphysics solver is required to couple the processes; this is because there are numerous application-dependent variations, depending on the type of media, the phase of fluid, and the factors causing these processes. For example, solving heat transports requires a dependent variable such as temperature and also application-dependent variations such as porous media, conduction or diffusion. Due to the complexity mentioned, functions were developed in MATLAB and linked with a multiphysics solver. The multiphysics solver is a powerful FEM tool that provides a platform for coupling physics and also allows for user-defined variables such as interpolation functions, analytic functions and many more. It also has a mathematical model that operates on partial differential equations (PDE) and ordinary differential equations (ODE), which makes it unique in solving FEM problems.

1.5 Thesis outline

Chapter one: presents the need for the research with the motivations behind it and introduces the key concepts in the understanding of geothermal resources. The aim of the thesis, the key and underlying research questions, and the research scope are also dealt with herein. The chapter ends with the research method chosen and the thesis outline.

Chapter two: provides a summary of the literature on geothermal reservoirs starting with a brief overview of the history of geothermal reservoirs and followed by the modelling approaches used. It also discusses the simulation codes developed previously, and the coupled processes considered. Particular problems such as coupled processes and the role of critical geomechanical properties such as porosity and permeability models are reviewed. Additionally, the limitations of the research available to date and the particular difficulties related to the modelling of geothermal reservoirs are presented.

Chapter three: this chapter introduces the governing equations and develops a finite element model for coupled thermo-hydraulic processes of a deep geothermal reservoir, based on the conservation laws of mass, energy, and momentum utilised in modelling such systems. Furthermore, a solution scheme for the developed FE model is briefly discussed.

Chapter four: this chapter presents verification and validation study to establish the practicability and accuracy of the FE model developed in Chapter 3. Several cases are presented, starting with the more straightforward and progressing to more complex practical problems applicable to HDR systems. The chapter aims to establish the validity and reliability of the FE model in solving practical engineering problems.

Chapter five: in this chapter, a field case study of the Soultz geothermal system is developed. The system behaviour as result of long-term performance over 60 years was modelled and predicted. In addition, sensitivity analyses were also performed using the factorial design for determining the suitable operational condition for optimal productivity. The outcomes of this chapter had been published in the Energy volume 129 pages 101–113, Elsevier, 2017.

Chapter six: this chapter presents a new 3-D numerical model of a deep and heterogeneous geothermal reservoir with a discrete fracture using the Soultz HDR scheme. The chapter addresses the limitations of previous research, which ignored the influence of fractures, reservoir representation, open boundaries influence and the inclusion of different operational schemes. Moreover, mesh convergence studies were performed and efficiently addressed. A solution convergence criterion for error estimation in the results was also investigated to confirm the reliability of the model. In the end, the chapter estimates the consequence of individual parameters and their corresponding influences on the productivity of a geothermal reservoir. This chapter had been published in *Renewable Energy*, volume 112, pages 151–165, Elsevier, 2017.

Chapter seven: in this chapter, a novel modelling-based approach of a triple porosity-permeability technique for a deep geothermal reservoir with multiple pore media is presented. Two numerical models of geothermal reservoirs (i.e., doublet and triplet) were developed using a computationally efficient finite element method for coupled transient fluid and heat transport in a fully saturated porous media. The fluid and heat interaction among the fractures, faults, matrix and wellbore components were explicitly incorporated into the numerical model, enabling the conversion of the spatial discretisation from 3-D to 1-D and making the model highly efficient. This chapter has been submitted to the *Applied Energy*, a journal in Elsevier Publishers for publication.

Chapter eight: this chapter presents the concluding remarks made on the thesis, which include contributions, findings and limitations. Additionally, it also recommends work that is needed to be addressed in future research.

Chapter two – Literature review

2.1 Introduction

The problem of modelling deep geothermal reservoirs has been the subject of extensive literature over the last four decades. Intensive research on this topic is still ongoing, due specifically to the compound nature of the problem which takes place in a multi-physical context and involves the coupling of many phenomena. In general, the most important aspects that characterise the analysis of a geothermal reservoir consist of a suitable modelling technique with appropriate numerical procedures applied to the coupled processes taken into consideration.

This chapter outlines the literature on HDR geothermal reservoir modelling, starting with a brief overview of the history of geothermal reservoirs, followed by the modelling approaches used. The chapter discusses the simulation codes developed previously and currently, and the coupled processes that are taken into consideration. Particular problems, such as the role of critical geomechanical properties, including porosity and permeability models, are also dealt with. Limitations of the research that is available to date and the particular difficulties related to the modelling of geothermal reservoirs are also discussed.

2.2 Brief history of HDR geothermal energy

This section focuses on the history and evolution of HDR geothermal energy. It emphasises how the idea of extracting heat from hot crystalline rock arose and became a known technique with a promising future in the field of renewable energy. Also mentioned and discussed in this section are the preliminary works and developments in the field of HDR reservoir technology.

2.2.1 The birth of HDR geothermal energy

HDR geothermal energy began as a serendipitous event. The idea was first conceived in the Los Alamos Laboratory in the US in the early 1970s during a scientific discussion about

developing a rock-melting device (Bowen, 1989; Brown and Duchane, 1999). The drilling device notion sparked the interest of one of the active and creative members of the team, Bob Potter. Potter had long been interested in a drilling technique that could recover geothermal energy from hot crystalline rock found in the deepest part of the earth's crust (Brown et al., 2012). The second event that reinforced Potter's dream was the article published in the *Journal of Geophysical Research* in 1969 portraying the concept of hydraulic fracturing techniques as practised in the petroleum industries (Brown et al., 2012; U.S. Department of Energy, 2006).

As the result of these two events, Potter deduced that the hydraulic fracturing method could also be applied to hot crystalline rock in the heat recovery of geothermal energy. He believed that the hydraulic pressurisation of the hot basement rock could create a colossal "hydraulic fracture" that would allow access to the heat contained in a fixed region of the rock material, by circulating a pressurised water via a closed-loop to recover the heat (U.S. Department of Energy, 2006).

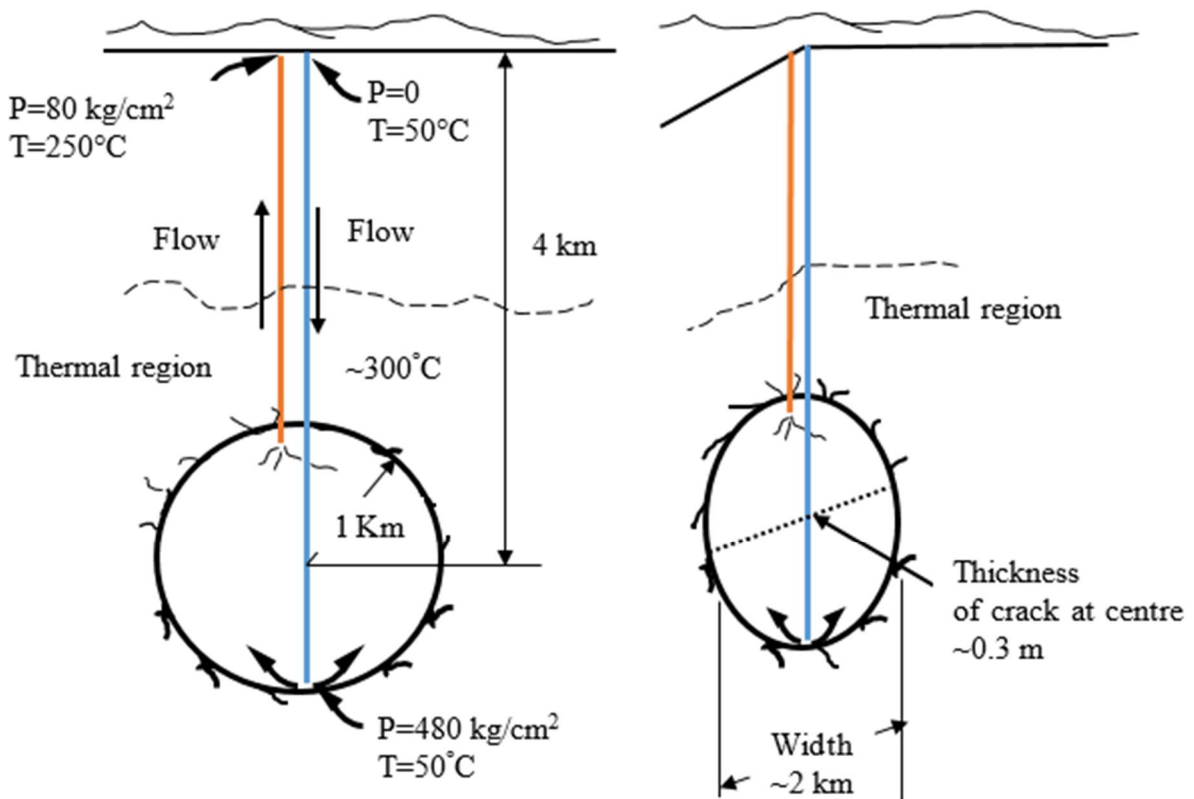


Figure 2.1: The original concept for an HDR geothermal system (Adapted from: Brown et al., 2012)

A conceptual model was developed based on Potter's deduction, in which the model consists of an inlet and outlet that communicates via a single vertical crack at a certain depth within the innermost area of the hot crystalline rock as shown in Figure 2.1 (Brown et al., 2012). In the conceptualised model, the crack was assumed to open as a result of the hydraulic fracturing operation.

2.2.2 Preliminary works and developments of HDR geothermal energy

The geothermal research group at the Los Alamos Laboratory started their investigations informally, due to inadequate funding at the initial stage of the project (Brown et al., 2012). In these investigations they gathered and studied the relevant literature linked to rock mechanics, hydraulic fracturing, geology, and geophysics (U.S. Department of Energy, 2006). In addition, the group went over the hills west of the Los Alamos Laboratory in the Jemez Mountains to observe the geological formations and to determine a suitable location with an appropriate geothermal gradient (Duchane and Brown, 2002, 1994). They finally decided to conduct the experiments in a region near the Valles Caldera due to volcanic activity taking place at the scene (Cremer et al., 1980).

Additionally, the drilling of a series of shallow holes was conducted to measure the geothermal gradient, and heat flows within the vicinity were recorded (Bowen, 1989). The holes demonstrated high values of heat flow measurements as expected due to the ring fault present, as shown in Table 2.1 (U.S. Department of Energy, 2006). A 775m-deep borehole, GT-1, was drilled in Barley Canyon in 1972, 5 km west of the Caldera (Bowen, 1989). The bottom-hole temperature exhibited during the exploration was 100.4°C with an outstanding mean gradient of over 100°C/km (Cremer et al., 1980). However, due to monsoon season difficulties, in particular mud and snow, which led to inaccessibility of the site, a permanent test facility was established at Fenton Hill, New Mexico (Brown et al., 2012). As a result, the first HDR geothermal system was set up in 1974 at the Fenton Hill site by drilling a borehole in a granitic rock to a depth of 2.9 km, which corresponds to a bottom-hole temperature of 197°C (Dash et al., 1983; Smith et al., 1985).

Subsequently, a reservoir was created, and flow testing was conducted between 1978 and 1980 (Brown and Duchane, 1999). The testing results showed that it was possible to

extract heat from HDR reservoirs at reasonable rates. As a result of this outcome, the Fenton Hill project set the stage for a worldwide interest in HDR technology (Aguilar et al., 1989). Both phases one and two of the Fenton Hill project were successful leading to fully operational plants (Brown, 2009). The lessons learned from the scheme expanded to Europe: in Britain (Rosemanowes), Germany (Bad Urach), France (Soultz) and other parts of the globe (MIT, 2006).

Table 2.1: Heat flow values for the depth test holes (U.S. Department of Energy, 2006)

Parameter	Hole 1	Hole 2	Hole 3
Completion date	10/04/1972	13/04/1972	16/04/1973
Distance from ring fault (Km)	3.22	3.86	4.83
Depth (m)	179.83	198.12	228.60
Heat flow (cal/cm ² -sec)	5.13 x 10 ⁻⁶	5.50 x 10 ⁻⁶	5.88 x 10 ⁻⁶

2.3 Geometric representation of reservoir models

In this section, the review will categorise HDR models by their approach to the representation of reservoir geometry. Reservoir geometry remains an important part of HDR systems in naturally fractured porous media and requires adequate representation for the modelling purpose. The geometric representation provides the means to characterise the system well enough to determine the actual geometry. In addition, the necessity of incorporating many coupled processes into the system demands the use of simple geometric models because input data are limited. In this thesis, the HDR models were classified by their geometric representation into abstract, reduced, and realistic.

2.3.1 Abstract geometric model

In this class of model, the geometry of the rock mass is simplified into a block parameter to determine a length scale for conductive heat transport within the reservoir and the total fracture surface area available (Willis-Richards and Wallroth, 1995). Axelsson (1989) developed this model type using a system of capacitors and resistors to represent various

geothermal fields in Iceland to predict future pressure changes in the systems. However, the model does not account for critical parameters in geothermal operations such as temperature, enthalpy, and energy prediction. Thus, the model was of limited use in HDR geothermal reservoir modelling.

Elsworth (1989) introduced pure abstract geometry for a geothermal reservoir using a simplified mathematical model based on spherical element approximations as shown in Figure 2.2. The model was employed to investigate the production histories from the 300-day circulation run segment at Fenton Hill HDR geothermal reservoir. The results achieved in the examination showed some correspondence with the data recovered from the 300-day circulation test (Elsworth, 1989a). Elsworth (1990) also validated his model with the 1000-day circulation test conducted at the Rosemanowes reservoir, which was part of the Camborne geothermal project development in the UK. The results were in good agreement with the observed thermal drawdown of the reservoir (Elsworth, 1990). Other related works on this model are available in the literature (Batchelor, 1986; Elsworth, 1989b, 1986).

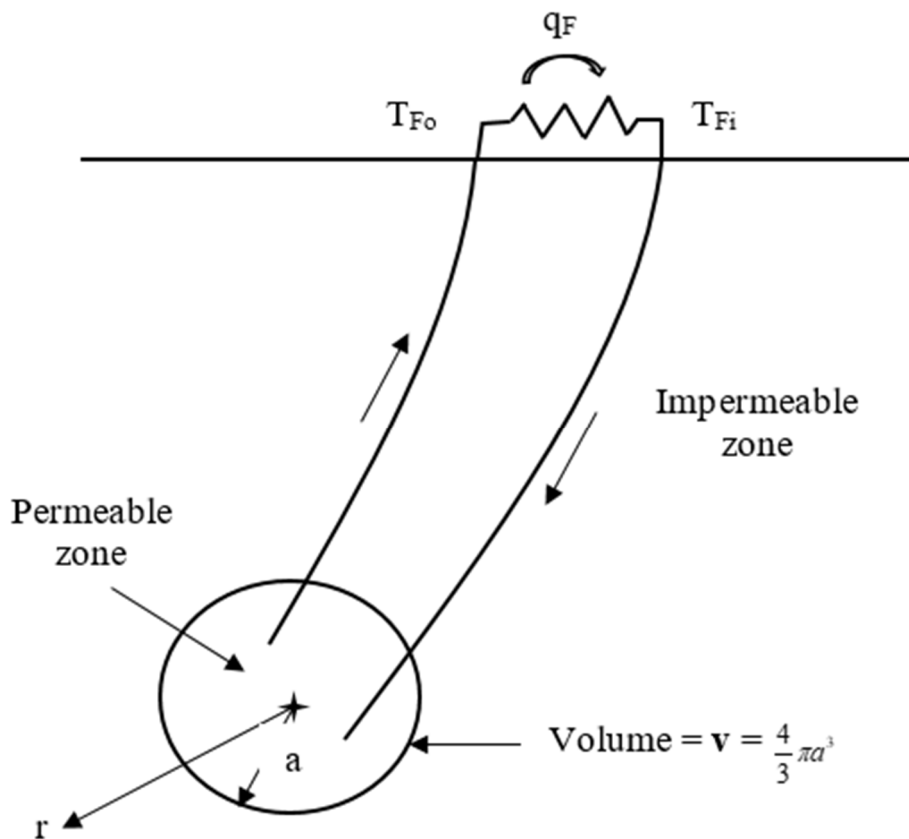


Figure 2.2: Abstract geometric model (Adapted from: (Elsworth, 1989a))

2.3.2 Reduced geometric model

In this system, the geometry of the HDR reservoir is explicitly simplified to varying degrees, and it is formed as a spectrum with one-dimensional flow paths. It can usually be modelled with a semi-analytic solution, though efforts or attempts were made to represent distributed fractures, which are not realistic in practice due to computational limitations (Willis-Richards and Wallroth, 1995). The model is grouped according to dimensional representation that includes one-dimension (1-D), two-dimension (2-D), and three-dimension (3-D).

Robinson & Kruger (1988) first employed 1-D reduced geometry to estimate the thermal drawdown of the HDR reservoir at Fenton Hill, US, and the results obtained agreed well with the field experiments at certain stages. Kruger et al. (1992) also applied this model to evaluate the potential for energy mining and the reservoir life of the hot granitic rock massifs in Cornwall, UK. As a result, the model was adopted by many other sites (e.g., Kruger, (1995); Kruger et al., (1996), 1988; Kruger and Quijano, (1995)). Figure 2.3 presents the 1-D reduced geometry model. The drawback of this model is that it is likely to predict unrealistically large shear displacements due to the elongated planar crack assumptions.

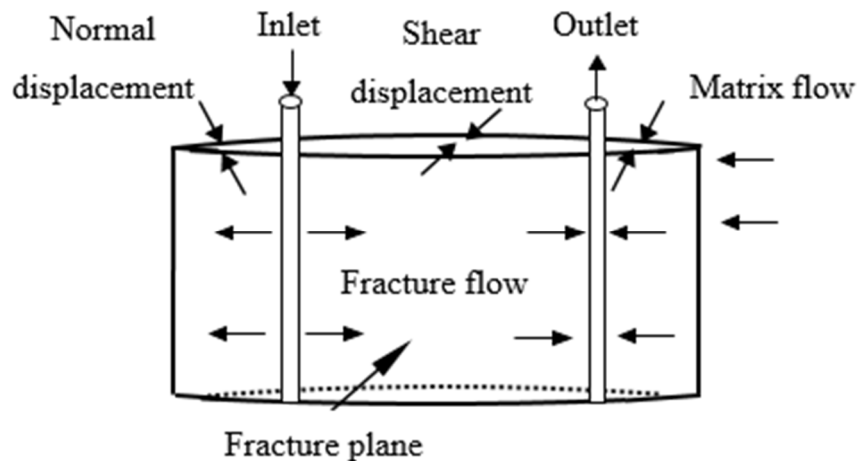


Figure 2.3: Reduced 1-D geometry (Modified from: (Willis-Richards and Wallroth, 1995))

Jupe et al. (1995a) grouped the 2-D reduced geometry model into two. The first group consists of an elliptical reservoir shape and the second group used a rectangular plate model to describe the system geometry. The most common application of the first type is the model proposed by Jupe et al. (1995b) in modelling the Soultz geothermal reservoir located in France. In the model, the geometry of the reservoir consists of an elliptical fracture shape that communicates through the injection and the production wellbores. The concept represents a straightforward approach to modelling the HDR reservoir system as shown in Figure 2.4 (Jupe et al., 1995b).

The second type of the reduced 2-D geometric model discussed here is the one reported by Hicks et al. (1996). The geometry of the reservoir is represented as a system of rectangular rock elements that form a grid. The grid cells are separated either by intact and impermeable “glued” elements or hydraulically conductive fracture elements as shown in Figure 2.5 (Hicks et al., 1996). The model was initially developed by Kohl et al. (1995) and it deals with the effects of stress perturbation under fluid flow.

The limitation of the 2-D reduced geometry model in achieving a genuine representation of a HDR reservoir is the failure to capture the vertical components of fracture fluid transport.

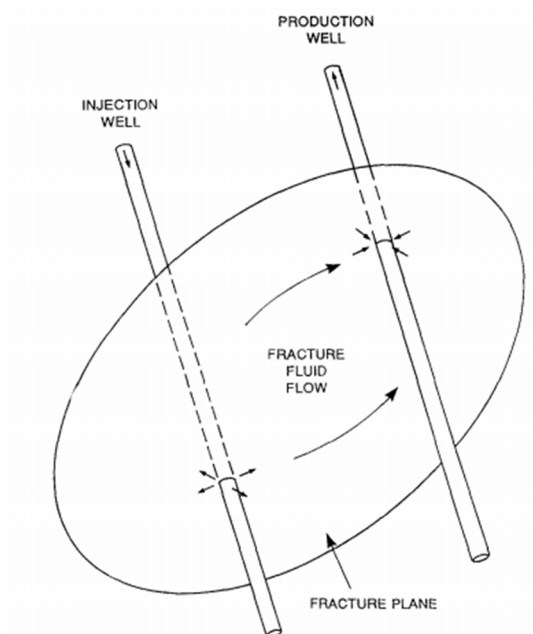


Figure 2.4: Reduced 2-D geometry type one (Jupe et al. 1995b)

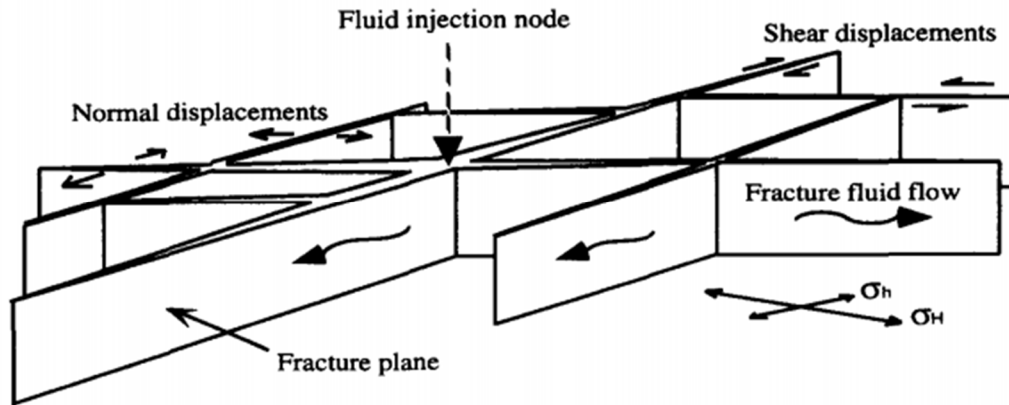


Figure 2.5: Reduced 2-D geometric model type two (Hicks et al., 1996)

The 3-D reduced geometry model is similar to the 2-D cases because both models can be represented as grid-based. However, in this case, a third plane is introduced, and the concept of equivalent porous media can easily be used to achieve the solution (Willis-Richards and Wallroth, 1995). Pruess (1988) developed an idealised double-porosity model of a fractured porous medium as presented in Figure 2.6 to study the flow effect in fractured media. The model also examined reservoir dynamics, well test design and analysis, and the modelling of particular field parameters. Zyvoloski et al. (1999) have provided more details on this type of model and are the source of the most primary literature.

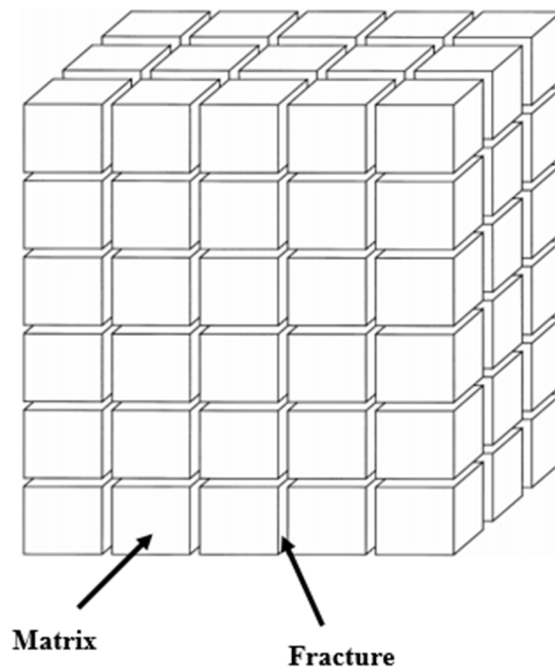


Figure 2.6: 3-D reduced geometry model (Modified from: Pruess, 1988)

2.3.3 Realistic geometric model

Realistic geometric models are capable of handling more than multiple arbitrary oriented fracture elements to start with, without undue computational problems (Willis-Richards and Wallroth, 1995). In this model, the reservoir is represented as discrete network models, and Lanyon et al. (1993) first applied such models to investigate the HDR systems of Rosemanowes phase 2B in the UK. Such investigation aimed to understand the basic thermal extraction process of geothermal reservoirs. Three different distributions were used, with mean fracture lengths of 24 m, 16 m and 11 m, respectively, to perform flow simulations on 200 m side cubes of fractured rock block as shown in Figure 2.7 (Lanyon et al., 1993).

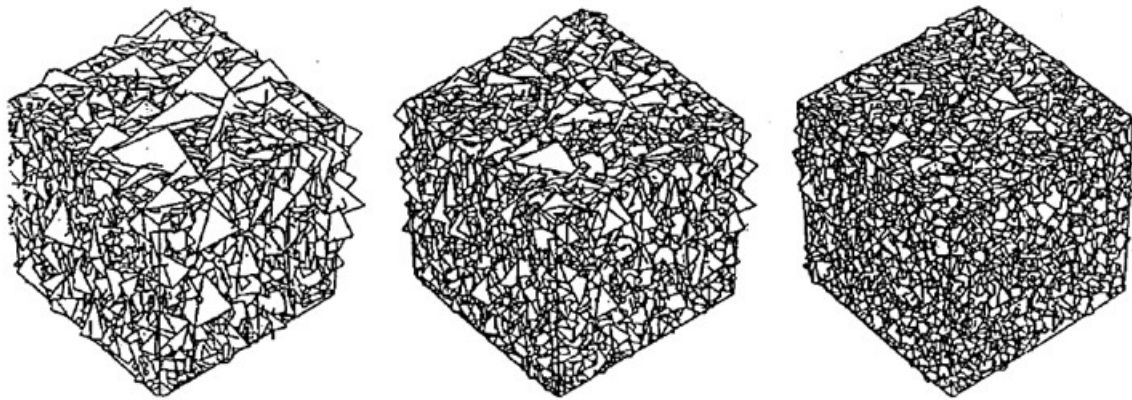


Figure 2.7: Realistic geometry model for three different distributions of fracture lengths (Lanyon et al., 1993)

Kolditz & Clauser (1998) also developed a realistic 3-D geometric model using the stochastic fracture network model as presented in Figure 2.8. As seen, the fractured medium was simulated in a true 3-D representation that considered the effect of transient coupled flow and heat transport. By using this approach, it was easier to predict the thermal performance of HDR systems under long-term simulation.

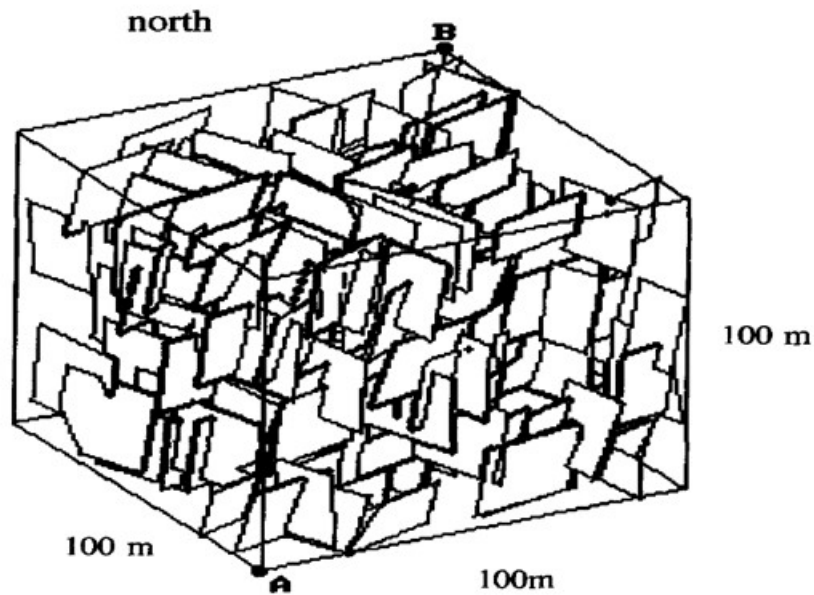


Figure 2.8: Realistic geometric model using stochastic fracture network designed from data available for the Rosemanowes HDR site (Kolditz and Clauser, 1998)

In summary, this review classifies the HDR geometric representation into abstract, reduced, and realistic. Based on the review, a summary of the assumptions and limitations of the three models are presented in Table 2.2 as modified from Willis-Richards and Wallroth (1996).

Table 2.2: Assumptions and limitations of abstract, reduced and realistic HDR models
(Modified from: Willis-Richards and Wallroth, 1996)

Features	Abstract	Reduced	Realistic
Modelling	Analytical solution, only	Both numerical and analytical solutions are solved	Numerical solutions, only
Coupling	Approximate TH	Simplified THM	Simplified THM
Fracture geometry	Parameterised into single values	Represented as a porous medium	Allows for individual size and orientation to be discretised with many fractures
Rock physics	May capture essential features approximately	Typically poor	Computationally limited, but reasonably captured

2.4 HDR simulation methods and codes

The long-term HDR reservoir simulations are crucial for the understanding of reservoir behaviour because field experiments are expensive to perform. Despite the fact that geothermal modelling tools have existed for over 5 decades, they were not able to cope with modern demands, both in resolving scientific and resource-specific questions and in terms of computational practicability (Burnell et al., 2015). Thus, it is never too late to establish a computational model of the geothermal reservoirs, as long as the model can be rigorously tested for consistency with available field data.

This section presents simulation methods and codes applied to the modelling of HDR geothermal reservoirs. Simulation methods are paramount in the reservoir exploration, stimulation, circulation and heat extraction stages. The present section also discusses the various codes applicable to HDR systems and their impact on modelling the reservoir lifespan.

2.4.1 Overview of HDR simulation codes

The history of geothermal reservoir simulation goes back to the early 1970s with the pioneer works of Cheng and Lau (1973) and Mercer and Pinder (1973). Nevertheless, the application of computer simulation started to gain acceptance from the geothermal industry during the code comparison study of 1980 organised by the US Department of Energy (O'Sullivan et al., 2009). In the study, several geothermal simulators were tested on a set of six problems to determine the capability of the codes to capture fundamental reservoir behaviour (O'Sullivan et al., 2001). The results showed that all the codes tested produced very similar outcomes for the six selected geothermal reservoir problems (O'sullivan, 1985). This confirms that the main features of the method applied by all the groups participating in the study appear to be very similar.

Furthermore, the knowledge gained from the study has led to improvement in the capacity of the geothermal reservoir simulation codes to develop site-specific models and carry out generic reservoir modelling studies (O'Sullivan et al., 2001). Many developments were made in terms of the range of physical phenomena, thus it was possible to include in a geothermal reservoir simulator, and there were improvements in the numerical methods employed in the reservoir models. Geothermal modellers have easily adopted these advances (O'Sullivan et al., 2001). However, despite the advancements, the fundamental studies of the required fluid, heat, chemical and physical processes that control the behaviour of geothermal systems have been the major thrust of modelling research.

2.4.2 Previous HDR simulation codes and limitations

This subsection reviewed the applicability of two HDR simulators relevant to the finite element method: FRACTure and Geocrack2D. The simulators studied for this thesis are in no way exhaustive; there exist a few other renowned simulators that may also be applied to modelling HDR reservoirs. Thus, each of the codes chosen is discussed based on the method applied and the coupled processes addressed.

The simulators selected were able to pass some of the criteria laid by the geothermal community in the US. The U.S. Department of Energy (1999) conducted a review of

numerical simulators used for HDR reservoir modelling to determine the lack of certain capabilities that were hindering the development. As a result, a proposal of the desirable features of an HDR reservoir simulator was made that include:

- representation of fractures explicitly;
- ensuring the fracture conductivity and fracture aperture correspond;
- flow channelling in fractures;
- to implement the fracture opening as a function of effective stress;
- to also incorporate the mineral deposition and dissolution as a function of time;
- to implement the thermoelastic effects; and
- implementing shear deformations and associated jacking of the fractures.

Although not all the listed characteristics are required for a given simulation effort, a complete simulation code would have all of these features (U.S. Department of Energy, 1999).

2.4.2.1 FRACTure HDR reservoir simulator

FRACTure is a 3-D finite element (FE) code developed to study the coupled interactive mechanisms in the subsurface with the specific aim of predicting the long-term behaviour of an HDR reservoir (Kohl and Hopkirk, 1995). The code development started in 1988, during a conference programme organised by the geothermal community in Switzerland to study the coupled processes within operating HDR systems (Kohl et al., 1995). The development of multi-purpose finite element code FRACTure was the central idea of the project (Kohl and Rybach, 1996). In another version of the literature, the code development started in 1988 during a time when the geoscience community was researching for a simulator that could handle the effect of thermal shrinkage on an HDR reservoir as reported in a workshop organised in France by Elsworth (Kohl and Hopkirk, 1995).

The acronym FRACTure stands for (Flow, Rock, And, Coupled, Temperature effects) while at the same time representing the fracture as the dominant hydraulic structure in HDR systems (Kohl and Hopkirk, 1995). The code structure was implemented based on the finite element code initially developed for teaching linear and dynamic finite element

analysis (DLEARN) by Hughes (1987). The programming language used was FOTRAN77 (Kohl and Hopkirk, 1995).

The code can simulate basic coupled interactions between hydraulic (H), thermal (T) and mechanical (M), as well as individual hydraulic (i.e. laminar, and turbulent), and different transport (thermal) and elastic (mechanical) processes (Kohl et al., 1997). The steady state and transient simulations of the coupled hydraulic and thermal processes in the subsurface are also supported in the software (Kohl and Rybach, 1996). Among other features of the code is the capability to model a reservoir in three dimensions to some extent. In addition, nonlinear stress-dependent joint aperture laws or linear elastic effects of pore pressure perturbations and temperature mechanisms on the stress field developing in the bulk rock are also considered (Kohl et al., 2000). Figure 2.9 presents a typical simulation results obtained from FRACTure software.

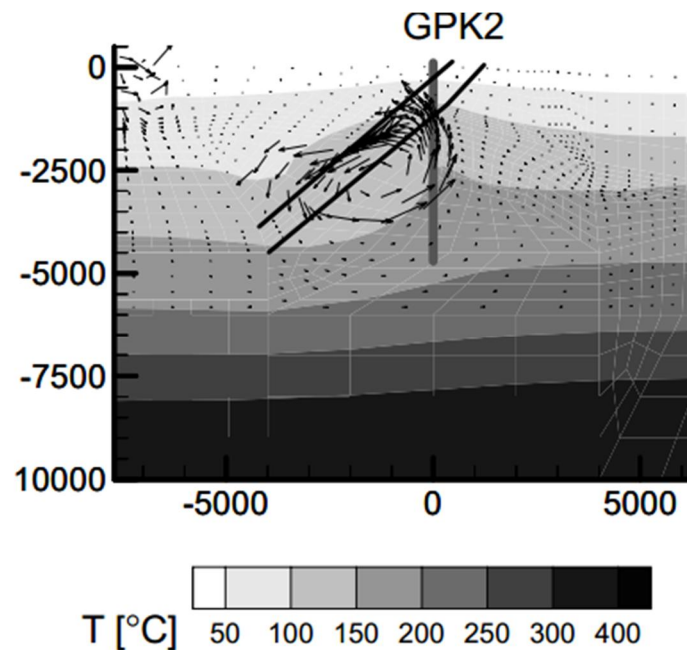


Figure 2.9: Detail of temperature and fluid flow field in subsurface obtained from FRACTure software (Kohl et al. 2000)

The desired coupling is usually achieved through a primary driver that is linked with the three core modules of the thermal, hydraulic and elastostatic fields (Baria et al., 1999). The code also has an option that permits the definition of stepwise linear time-flow

functions, which helps in modelling the experimental injection steps precisely (Kohl and Rybach, 1996).

In conclusion, the code applies to various analyses of reservoir operations that include geothermal, radioactive and oil industry due to the approach and concepts implemented in its development (Sanyal et al., 2000). The preceding paragraphs of this subsection have already mentioned the major strengths of the FRACTure simulation code. Nevertheless, the code also has some limitations as it cannot model the coupling between fracture shear displacement and aperture. Likewise, phenomena such as two-phase flow and chemical processes were not addressed.

2.4.2.2 GEOCRACK HDR reservoir simulator

GEOCRACK is a finite element code initially developed at Kansas State University (Brown, 1997) for HDR research at Los Alamos Laboratory (DuTeaux et al., 1996; Swenson and Hardeman, 1997). The mathematical formulations contain coupled state of earth stress, hydraulic, and heat transfer processes with the mechanisms of discrete fracture behaviour (DuTeaux et al., 1996). The GEOCRACK2D model consists of rock blocks with discrete fluid paths and nonlinear contact between the blocks. The code assumes that conduction in the rock blocks occurs as a result of heat transfer and transport of liquid (Swenson et al., 1999).

Furthermore, the code permits the user to specify and monitor solution problems by providing an interactive graphics environment in a simple and reliable way (Swenson et al., 1995). A menu and a graphic display allow the user to interact with the analysis to specify/modify the geometry, mesh, material properties and boundary conditions and to examine results (Swenson et al., 1995).

The GEOCRACK reservoir simulator is based on a numerical solution scheme that requires the user to have an in-depth knowledge of the problem descriptions in the form of a finite element mesh, which is necessary as the primary data for the simulation (Hardeman and Swenson, 1998). According to the first quarter progress report issued on August 15, 1997, the effort has been devoted to developing a 3-D version of the code with a goal of

allowing the user to work at the geometry level of a problem, while meshing details and solutions are handled automatically (Swenson, 1997). The phrase “geometry level” means that the user defines the boundary of a reservoir and the geometric features of the model such as fractures and wellbores (Swenson, 1998a). Despite many challenges, a 3-D geometric representation was accomplished to some extent with the inclusion of fractures and wells as reported by Swenson (1998b). Figure 2.10 presents a typical simulation results obtained from GEOCRACK reservoir simulator.

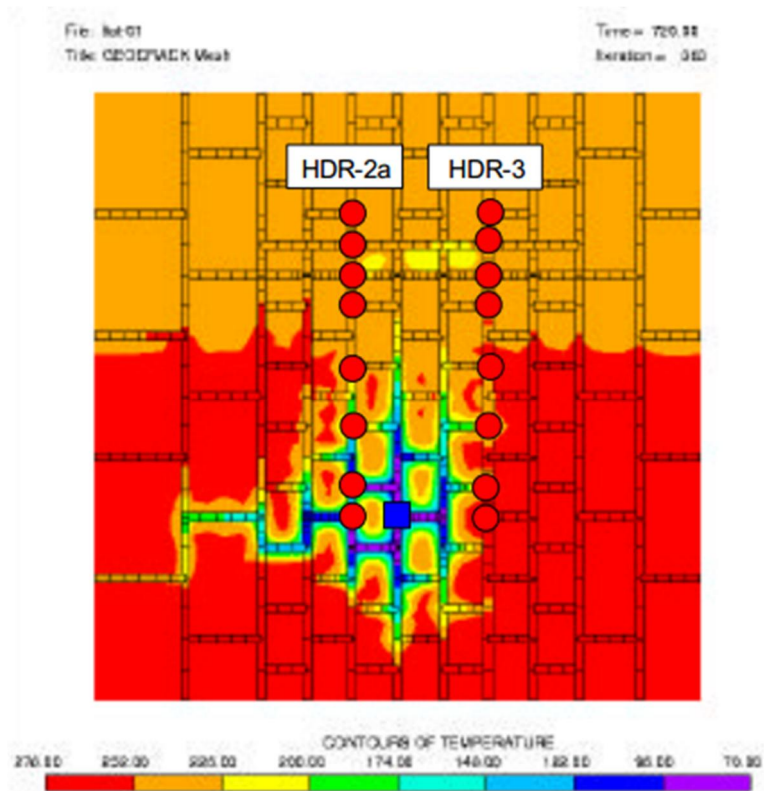


Figure 2.10: Temperature in reservoir after 720 days of operation (min=70°C, max=278°C) obtained from GEOCRACK reservoir simulator (Swenson et al., 1999)

In summary, owing to the variety of physical processes that can be coupled and simulated, the code has gained popularity as a numerical tool for the analysis of reservoir performance, which provides important guidelines for the design of HDR geothermal systems. Moreover, validations of field data were also performed on Hijiori and Fenton Hill HDR projects by many researchers using the application; for instance, the research results of the following authors: Duchane (1995); Okabe et al. (2000); Schroeder et al. (1999, 1998); Swenson et al. (2000). The drawbacks of the code include the non-existence of a porous medium model and the lack of capability to couple fracture aperture and shear displacement.

2.4.3 Current HDR simulation codes

There have been substantial advances in numerical simulators for HDR geothermal reservoirs over the past few decades, with the steady increase in computational strength and the development of numerical codes that have reduced several simplifying hypotheses. The advances include the application of more realistic equations of state for the fluid system, for example, in the TOUGH2 and TOUGHREACT codes and the FALCON code (Wong et al., 2016; Xia et al., 2016a; Xing et al., 2015). There has been extensive progress in the ability to represent heterogeneity and geometric complexity in simulation codes; examples include GOCAD, FEFLOW and OpenGeoSys (Blöcher et al., 2010; Fischer et al., 2015). Computational schemes that are faster and more precise have also been elaborated in reservoir modelling.

Other numerical modelling codes are still under development, particularly those by the current reservoir modelling working group, initiated with the help of the International Partnership for Geothermal Technology (IPGT). The IPGT is an international organisation with five member countries (Australia, Iceland, New Zealand, Switzerland, and the U.S.) that aims to improve understanding of geothermal potentials and usage across the globe (Wall, 2010). The organisation proposed to develop a standard geothermal simulation code that would couple the various interactions arising during exploitation by the year 2020 (IPGT, 2012). Several workshops were held in the member nations with a vision to develop a fully coupled thermo-hydro-mechanical-chemical (THMC) reservoir simulation program (IPGT, 2012). Subsequently, all the processes required for implementation in the proposed code have been identified. These processes comprise the complex nonlinear interactions associated with a multiphase hydraulic flow, thermal transport, regional and local scale geomechanical deformation (and fracturing) and geochemical interactions between the working fluid and host reservoir rock at highly variable time scales (Podgorney et al., 2011).

The Geothermal Technology Office (GTO) under the US Department of Energy has also inaugurated a code comparison study programme to enhance the state of the art of HDR geothermal simulation codes (White et al., 2015). The programme focused on analysing existing codes, identifying differences and demonstrating the modelling capabilities of a global collection of various numerical simulators for evaluating geothermal technologies.

Six benchmark problems were suggested, and the programme commenced in 2014 (Bahrami et al., 2015). According to White and Phillips (2015), 12 groups took part in the challenge, and each group had a unique numerical simulator and analytical methods, providing a thorough mechanistic approach, modelling process and solution scheme. Ghassemi et al. (2015) commented on some of the outcomes of the programme, affirming that none of the 12 members was able to take part in all six problems due to code limitations.

2.5 Coupled processes

In various engineering problems and geoscientific applications, coupled process modelling has been considered since the introduction of the computation method for problems of soil consolidation, dam construction, and oil/gas field exploration (Kolditz et al., 2012a). Thermal, hydraulic, mechanical and chemical (THMC) were the processes considered in the study of coupled behaviour (Tsang, 1991). Multiphysics coupling between the THMC processes in geological media, are essential for a broad range of engineering practices, including geothermal energy extraction, as well as oil/gas extraction, geologic carbon sequestration, and geologic nuclear storage of nuclear waste (Rutqvist and Tsang, 2012). The term “coupled” implies that these individual processes interact with each other and may amplify the effect of a certain process, or diminish it through a feedback mechanism (McDermott et al., 2012; Tsang, 1999).

Tsang (1985) classified the coupled processes into two: one-way coupling and two-way coupling. In the one-way coupled processes, the effect(s) of one or more processes on the others is/are continuous over time. On the other hand, in the two-way coupled processes the impact of the interaction is reciprocal and makes it more complex to analyse than the one-way coupled processes (Tsang, 1986). Minkoff et al. (2003) further classified the coupled simulators into three: full coupling, loose coupling and one-way coupling. The coupled processes that are of interest to this review are those related to geothermal energy exploitation, and they are presented in the following subsection.

2.5.1 Review of coupled processes applicable to HDR geothermal energy

Simulation of coupled heat transfer and fluid flow in fractured reservoirs are of significant benefits to HDR design, particularly when there exist coupled interactions among fluid and heat flow, and a mechanical response of the matrix and fracture (Tao and Ghassemi, 2010).

Shibuya et al. (1985) developed a two-dimensional model of a geothermal reservoir with multiple cracks to study the effect of thermoelastic coupling of crack propagation by applying the inversion formula and collocation method in solving the integral equation derived from boundary conditions. Zimmerman (2000) derived the equation of linearised poroelasticity and thermoelasticity and the coupling parameters between them. Ghassemi and Zhang (2006) developed a transient displacement discontinuity (DD) boundary element method to study the response of fracture in porothermoelastic rock when subjected to stress, pore pressure and temperature perturbation. They also investigated the full range of crack opening due to the applied loads (Ghassemi and Zhang, 2006). A similar analysis was carried out by Norbeck and Horne (2015), by using a rate-and-state earthquake model. Nonetheless, before that Ghassemi et al. (2001), Ghassemi and Zhang (2004a), and Ghassemi and Zhang (2004b) used the indirect boundary element methods by applying the fictitious stress (FS) to solve the thermoelastic and poroelastic effects of wellbores and cracks in geothermal reservoirs.

Ghassemi and Tarasovs (2006) further developed a coupled 3D model of the DD method to study the influence of thermal stresses on fracture opening and slippage with particular reference to the Coso geothermal field. A similar method was applied to study the stress and pore pressure changes around a cooled fracture in low-permeability rock and their contribution to rock failure and seismicity (Ghassemi, 2007). Zhou and Ghassemi (2008) further extended the DD method with the finite element method link to study the poroelastic response of a reservoir to fluid injection into an irregularly shaped fracture using a 3-D model. In addition, the effect of non-uniform cooling in response to fracture aperture changes and a pressure effect were also investigated (Ghassemi et al., 2008). Lee and Ghassemi (2010) developed a fully coupled thermo-poro-mechanical finite element model with damage mechanics and stress-dependent permeability to investigate the effect of stress-induced micro-seismicity and fracture propagations in a geothermal reservoir. Tao and

Ghassemi (2010) developed inversion techniques to study the role of thermo-poroelastic effects on wellbore stability and wellbore breakout. Lee and Ghassemi (2011) developed a finite element model to investigate the effect of altered elastic modulus and permeability with reflection to rock damage evolution.

Zhou and Ghassemi (2011) analysed the temporal variations of fracture opening and slip upon immediate application of a fluid pressure by developing a 3-D time-domain poroelastic DD method. The model was also used to investigate the fracture aperture variation to the pressure in the fracture and the effect of injecting cold water into an arbitrarily shaped fracture in geothermal reservoirs by considering the impact of the coupled poro-thermoelastic processes (Zhou and Ghassemi, 2011). Safari and Ghassemi (2011) extended the algorithm by using a coupled finite element/boundary element method to model injection/extraction problems in pre-existing fractures for variable injection/extraction rates. Farmahini-farahani and Ghassemi (2015) and Verde and Ghassemi (2013) considered the nonlinear joint response and mechanical response of the fractures and multiple interactions using the same model. Huang and Ghassemi (2012a, 2012b) and Min et al. (2011) used an FEM along with an element partition algorithm (EPA) to study the 3-D mixed-mode fracture growth from an embedded circular crack.

Wang and Ghassemi (2012) developed a 3-D poroelastic model for a naturally fractured geothermal reservoir using a stochastic fracture network to assess the permeability enhancement and mechanical rock mass response to stress variation caused by injection/extraction. Ghassemi et al. (2013) investigated rock failure around the vicinity of a fracture that has an irregularly shape using a 3-D poroelastic model and the stress distribution around the fracture. Similar studies were conducted using the FEHM code in evaluating the thermoelastic and poroelastic stress changes in a self-propping shear failure of pre-existing fractures (Dempsey et al., 2014, 2013).

Safari and Ghassemi (2015) analysed the role of coupled thermo-hydro-mechanical processes using the DD method for fracture opening and matrix heat diffusion. The finite element method was used for the fluid and heat conduction and convection inside the fractures by taking into account the nonlinear characteristics of fracture deformation in the normal and shear deformation (Safari and Ghassemi, 2015).

2.6 Permeability and porosity models

Naturally fractured media have been the object of multiple studies for more than 40 years. To explain their behaviour in different fields such as groundwater, geothermal and petroleum reservoirs, various models have been created with inherent difficulties to capture the realistic models of fractured media because of the partial ignorance about the dimensions, spatial distribution and interconnections of the fractured network (Suirez-Arriaga, 2002).

Zimmerman et al. (1993) developed a dual-porosity (DP) model for a single-phase fluid transport in a naturally fractured porous media using a lumped parameter method for the rock matrix block. Lim and Aziz (1995) derived a matrix-fracture transfer shape factor for dual-porosity modelling of naturally fractured reservoirs by linking analytical solutions for pressure diffusion with flow geometries. Choi et al. (1997) applied the Forchheimer equation to simulate a dual-porosity/dual-permeability model of a reservoir and related the results to those obtained from the Darcian-flow. Bower and Zyvoloski (1997) extended the stress solution of the FEHM code to the dual-porosity ability to investigate the hydraulic conductivity/permeability of the fracture system. Furthermore, amendments were made to the coupled hydrologic, thermal and mechanical behaviour of the fracture systems.

Ranjbar and Hassanzadeh (2011) developed a semi-analytical, dual-porosity model and employed a fine-grid, single-porosity numerical simulator for verifications. Nie et al. (2012) developed a semi-analytical model to examine a dual-porosity and dual-permeability flow model of horizontal production wellbore in a fractured reservoir. Austria and Sullivan (2015) performed a sensitivity analysis to determine when to utilise a dual-porosity model over single-porosity models in simulating geothermal systems. In summary, extensive research has been done on this model and is available in the following literature: Chen et al. (2016); Cheng et al. (2016a, 2016b); Magnenet et al. (2014); Poulsen et al. (2015); Xia et al. (2017); and Zeng et al. (2016).

2.7 Research gaps and limitations

Sections 2.2 to 2.6 have reviewed the research carried out concerning HDR geothermal reservoir modelling. Based on the review, some of the outstanding research issues and limitations are presented and outlined in the following subsections.

2.7.1 The effect of reservoir connectivity on HDR energy mining

The models reviewed overlooked the influence of the surrounding medium, the fractures and the reservoir in the estimation of the effect of core reservoir parameters on geothermal energy extraction. Most importantly, cases where the fractures were not connected to the injection wellbore or the producer were not captured in the existing models because the existing models were limited to the direct connection between the two media (i.e. fractures and wellbores). Nevertheless, various field experiments have proven that assumption to be invalid. For example, the field experiment conducted in Soultz confirmed that sometimes the wellbores were disconnected from the fractures. Thus, a realistic numerical model is required to capture the effect of such events in order to predict the long-term performance of HDR systems efficiently.

2.7.2 Numerical verifications and validations of modelling approaches for HDR systems

The review carried out has shown that numerous modelling approaches exist for simulating HDR geothermal systems; however, none of the literature provided an account of verification and validation studies of these methods. The commonly used models in modelling such systems are the equivalent porous media and the dual-porosity models. It is necessary to validate and verify the models with a standard analytical solution and an experimental measurement in order to justify their applicability. Thus, a verification and validations study is required to identify which of the approaches accurately predict the system performance.

2.7.3 The effect of multiple pore media on HDR geothermal mining

The literature discussed in this chapter has emphasised the significance of permeability and porosity models on HDR systems representation. The review also showed that investigation into complex geological formations and their effect on HDR long-term performance remains outstanding. Although HDR geothermal models have been successfully advanced, their application to multiple pore media remains challenging, primarily because of their natural heterogeneity. Multiple pore media is controlled by a) primary (matrix), b) secondary (fractures), c) tertiary (faults) or d) micro-fracture, in which each of the media is linked with porosity and permeability as a major flow pathway.

In order to better represent the heterogeneity of naturally fractured-faulted HDR geothermal reservoirs, the concept of the triple porosity-permeability (TPP) model is required. Thus, a 3-D numerical model of a deep geothermal reservoir (based on the Soultz graben formation) is needed to conceptualise a porous media with multiple interactions involving faults, fractures, and rock matrices.

2.8 Summary

In this chapter, the literature review conducted has shown the significance of modelling in HDR geothermal energy. The importance of studying the coupled processes of the system has also been demonstrated. The review presented in this chapter has served as a foundation for this research work, and the outcomes are outlined in the remaining chapters.

Chapter three – Governing equations and FEM solutions

3.1 Introduction

This chapter presents the derivation of the governing equations and FEM formulations for TH coupled processes of naturally fractured porous media. The nomenclature list provides the physical meanings of the major parameters or variables used in the derivations; however, where necessary some of the variables' meanings were given in the text following their appearance in relevant equations.

3.1.1 Bases for the derivation of the governing equations

Several sets of equations have been developed for modelling coupled transient TH processes of deep geological porous media, such as GeoSys, OpenGeoSys, TOUCH2, TOUGHREACT, FALCON, and GEOCRACK2D (Kolditz et al., 2012b; Xia et al., 2016b). In addition, commercial codes have been adopted that include FLAD3D, ABAQUS and ANSYS (Kolditz et al., 2015). Some of these models, such as TOUGH2 and TOUGHREACT assumed that the mass fluxes due to diffusion and dispersion are so small that they are negligible. Other approaches, for example, FALCON and GEOCRACK2D consider the fluid-solid interface as a material surface concerning the fluid mass so that no mass of the fluid can cross it. In some models, such as OpenGeoSys and GeoSys, the fluid is considered to first flow into fractures, and then flows into another matrix block or remains in the fractures. The last case is the most widely used in modelling HDR geothermal systems; nevertheless, it does not describe the influence of other media present in deep subsurface structures efficiently. These approaches make it difficult to predict the long-term performance of an HDR geothermal system accurately. Likewise, the influence of full interaction between subsurface structures cannot be modelled according to its physical definition due to the limitation of the existing empirical methods.

Fluid and heat transport phenomena of an HDR geothermal system play a vital role in predicting the long-term performance of energy mining of deep geothermal resources. Therefore, it is necessary to develop or derive a more general form of governing equations that can capture and simulate more accurately the coupled transient TH effect of naturally

fractured geological formations for enhanced energy recovery. The derived equations provided in this thesis were based on the existing laws used in modelling geological formations.

3.2 Theoretical background of naturally fractured porous media

A naturally fractured porous medium is a system intersected by a network of interconnected fractures, faults, vugs or solution channels (Nelson, 2001), as shown in Figure 3.1. The porosity and permeability of such a system are allowed to change rapidly and discontinuously over the whole domain when modelled. The permeability is greater in the fractures, faults and vugs while it is smaller in the matrix block. In the case of the porosity, it is much larger in the matrix and less in the other systems. In this research, the effect of micro-fractures, vugs and the gas phase are assumed to be negligible as they do not contribute much in a macroscopic scale model.

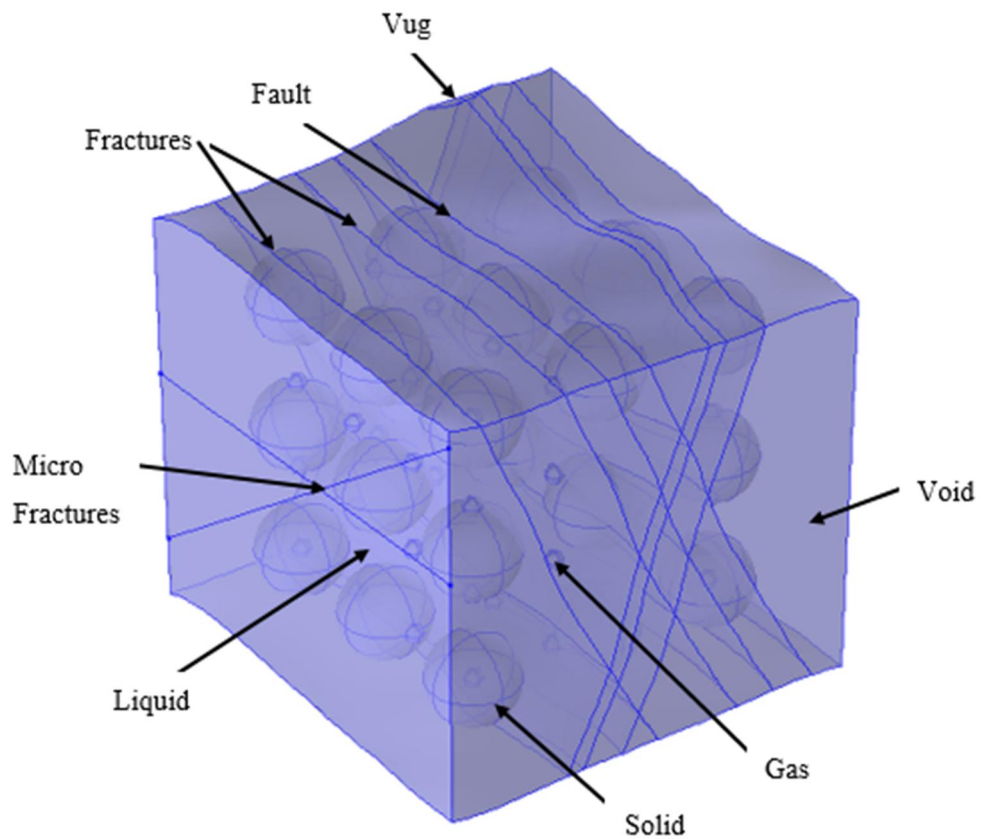


Figure 3.1: 3-D representation of naturally fractured porous media

Furthermore, in this system, the fluid in the void space is assumed to be made up of two parts, one part in the matrix block and the other part in the fractures. Thus, each part is treated as a continuum that occupies the entire domain. Both of the two overlapping continua are allowed to coexist and interact with the other.

3.3 Governing equations for modelling fluid flow in porous media

The governing equations used for modelling fluid in a fully saturated fractured porous media are the conservation of mass, the equation of state, and Darcy's law (Kolditz et al., 2016).

For the matrix block, the conservation of mass for the fluid flow in a porous matrix block is the difference between the mass inlet and outlet equal to the sum of mass accumulated within the matrix block. The fluid flow in the porous matrix block (Bear, 1993) is described by

$$\frac{\partial}{\partial t}(\phi\rho_L) + \nabla \cdot (\rho_L v) = Q_m \quad (3.1)$$

where ϕ is the porosity, ρ_L is the fluid density, v is the Darcy's velocity term and Q_m is the mass source term.

The conservation of momentum is stated in the form of Darcy's law, which indicates a linear relationship between the velocity field and the pressure gradient of the fluid (Nield and Bejan, 2006), expressed as

$$v = -\frac{\kappa}{\mu}(\nabla P - \rho_L g \nabla z) \quad (3.2)$$

where κ is the permeability, μ is the fluid viscosity, P is fluid pressure, g is the acceleration due to gravity and z is the depth of formation. Substituting equations (3.2) into (3.1) yields

$$\frac{\partial}{\partial t}(\phi\rho_L) + \nabla \cdot \left(\rho_L \frac{\kappa}{\mu} (-\nabla P + \rho_L g \nabla z) \right) = Q_m \quad (3.3)$$

The equation of states defines the fluid and matrix compressibilities as

$$C_F = \left(\frac{1}{\rho_L} \right) \left(\frac{\partial \rho_L}{\partial P} \right) \quad (3.4)$$

$$C_m = \left(\frac{1}{\phi} \right) \left(\frac{\partial \phi}{\partial P} \right) \quad (3.5)$$

where C_F is the fluid compressibility and C_m is the matrix compressibility.

Expanding the first term in equation (3.3) and applying the product and chain rule of differentiation yields

$$\frac{\partial}{\partial t} (\phi \rho_L) = \phi \frac{\partial \rho_L}{\partial P} \frac{\partial P}{\partial t} + \rho_L \frac{\partial \phi}{\partial P} \frac{\partial P}{\partial t} \quad (3.6)$$

Substituting equations (3.4) and (3.5) into (3.6) gives

$$\frac{\partial}{\partial t} (\phi \rho_L) = \phi \rho_L (C_F + C_m) \frac{\partial P}{\partial t} \quad (3.7)$$

$$\frac{\partial}{\partial t} (\phi \rho_L) = \rho_L S \frac{\partial P}{\partial t} \quad (3.8)$$

where the linearised storage S is given as

$$S = \phi (C_F + C_m) \quad (3.9)$$

Replacing equation (3.9) into (3.3) yields

$$\rho_L S \frac{\partial P}{\partial t} + \nabla \cdot \left(\rho_L \frac{\kappa}{\mu} (-\nabla P + \rho_L g \nabla z) \right) = Q_m \quad (3.10)$$

Here, the source and sink terms of the fluid in the matrix block are considered to be located at isolated points $x^{(i)}$. For point sinks, term Q_m in equation (3.1) is given as

$$Q_m = -\sum_i \rho_L Q_m^{(i)} \delta(x - x^{(i)}) \quad (3.11)$$

where $Q_m^{(i)}$ denotes the volume of the produced fluid per unit time at $x^{(i)}$. Similarly, for point sources, term Q_m is

$$Q_m = \sum_i \rho_L^{(i)} Q_m^{(i)} \delta(x - x^{(i)}) \quad (3.12)$$

where $Q_m^{(i)}$ and $\rho_L^{(i)}$ denote the volume of the injected fluid per unit time at $x^{(i)}$, respectively.

The fluid flow in the fractures is described by

$$\frac{\partial}{\partial t}(\phi_f \rho_L) + \nabla \cdot (\rho_L v_f) = Q_{mf} + Q_{ext} \quad (3.13)$$

$$v_f = \frac{\kappa_f}{\mu} (-\nabla P_f + \rho_L g \nabla z) \quad (3.14)$$

where ϕ_f is the porosity, v_f is the Darcy's velocity term, Q_{mf} denotes the flow from the matrix block to the fractures, Q_{ext} indicates the external sources and sinks, where κ_f is the permeability, and P_f is fluid pressure. The permeability in the fractures is assumed to obey the laminar flow law for parallel plates (Kolditz et al., 2015), expressed as

$$\kappa_f = \frac{b^2}{12} \text{ or } \frac{b^3}{12w} \quad (3.15)$$

where b is the fracture aperture, and w is the fracture spacing. Substituting equation (3.14), (3.15) and (3.8) concerning fractures into equation (3.13) yields

$$\rho_L S_f \frac{\partial P_f}{\partial t} + \nabla \cdot \left(\rho_L \frac{b^2}{12\mu} (-\nabla P_f + \rho_L g \nabla z) \right) = Q_{mf} + Q_{ext} \quad (3.16)$$

The matrix-fracture transfer term can be defined as a boundary condition imposed explicitly on the matrix block (Faust and Mercer, 1979a), expressed as

$$Q_{mf} = -\sum_i \chi_i(x) \frac{1}{|\Omega_i|} \int_{\Omega_i} \frac{\partial(\phi \rho_L)}{\partial t} dx \quad (3.17)$$

where $|\Omega_i|$ denotes the volumes of Ω_i and χ_i is its characteristic function given as

$$\chi_i(x) = \begin{cases} 1 & \text{if } x \in \Omega_i, \\ 0 & \text{otherwise.} \end{cases} \quad (3.18)$$

The boundary condition on the surface of each matrix block is now established with the definition of Q_{mf} in a general format. In the case of the external sources or sinks Q_{ext} , it may comprise injection or production sources or other sources from the surrounding boundaries (Bower and Zyvoloski, 1997b), which is expressed as

$$Q_{ext} = - \int_{\text{Cellboundary}} \nabla \cdot \frac{\kappa \rho_L}{\mu} \nabla P \cdot \vec{n} dx \quad (3.19)$$

3.4 Governing equations for modelling heat transport in porous media

In this work, the heat transport is assumed to obey a local thermal balance between the solid and the fluid phases. That is, the solid temperature is approximately equal to the fluid temperature at any given depth in the system. The conservation of energy in a naturally fractured porous medium for the matrix block (Bower and Zyvoloski, 1997b) is given as

$$\frac{\partial}{\partial t} V_E + \nabla \cdot q_E = Q_E \quad (3.20)$$

where the energy per unit volume V_E is given as

$$V_E = \phi \rho_S C_{P,S} T + (1 - \phi) \rho_L C_{P,L} T = \rho C_P T \quad (3.21)$$

where ρ_s is the solid density, $C_{P,S}$ is the solid heat capacity of the solid, T is temperature, $C_{P,L}$ is the fluid heat capacity, and q_E is the energy flux, Q_E is the energy source term and ρ is the effective density.

The energy flux in the system q_E is expressed as

$$q_E = \rho_L \nu C_{P,L} T + q \quad (3.22)$$

in which

$$q = -\lambda \nabla T \quad (3.23)$$

and

$$\lambda = \phi \lambda_S + (1 - \phi) \lambda_L \quad (3.24)$$

where λ is the effective thermal conductivity, λ_S is the solid thermal conductivity, λ_L is the fluid thermal conductivity and q is the heat flux. Substituting equations (3.21) and (3.22) and their derivatives into equation (3.20) yields the general expression for solving heat transport in the porous matrix as

$$\rho C_P \frac{\partial T}{\partial t} + \nabla \cdot (\rho_L \nu C_{P,L} T) - \nabla \cdot (\lambda \nabla T) = Q_E \quad (3.25)$$

Similarly, equation (3.25) can be employed for the conservation of energy within the fracture, expresses as

$$\frac{\partial}{\partial t} V_{f,E} + \nabla \cdot q_{f,E} = Q_{f,E} + Q_{m,E} \quad (3.26)$$

$$(\rho C_P)_f \frac{\partial T}{\partial t} + \nabla \cdot (\rho_L v_f C_{P,L} T) - \nabla \cdot (\lambda \nabla T) = Q_{f,E} + Q_{m,E} \quad (3.27)$$

where

$$Q_{m,E} = - \int_{\text{Cellboundary}} \nabla \cdot \left(\frac{\kappa \rho_L v_f C_{P,L} T}{\mu} \nabla P_{m,f} + \lambda \nabla T_{m,f} \right) \cdot \bar{\mathbf{n}} dx \quad (3.28)$$

3.5 Finite element formulation

This section presents the application of the FEM in modelling coupled TH processes for deep HDR geothermal reservoirs based on the literature (Lewis et al., 2005; O.C.Zienkiewicz et al., 2000; Zienkiewicz et al., 2005; Zienkiewicz and Taylor, 2000). The application is built upon the partial differential equations described in sections 3.3 and 3.4. The FEM has been in existence since the late 1950s, and it is now a sophisticated tool for solving a broad range of engineering problems. The robustness of the technique has made many other numerical analysis methods and experimental testing methods redundant (Fagan, 1992).

3.5.1 Initial and boundary conditions

The first step that is required to formulate an FE solution is to define the initial and boundary conditions (BC) of the system. In this study, the initial conditions were fully specified for the pressure and temperature fields at time $t=0$, given as

$$P = P_0, T = T_0 \text{ in } \Omega \text{ and on } \Gamma \quad (3.29)$$

where Ω is the domain of interest and Γ is the boundary. In the case of the boundary condition, it is either imposed as value or flux. The imposed value is called the Dirichlet BC or is sometimes referred to as the First Kind BC, which is represented here for both the pressure and temperature as

$$P = \hat{P} \text{ on } \Gamma_p \text{ and } T = \hat{T} \text{ on } \Gamma_T \quad (3.30)$$

The flux BC or the Neumann BC for the fluid flow can be prescribed as a mass flux normal to the boundary or at the injection or extraction wellbore boundaries, namely

$$q_p = \rho_L \frac{\kappa}{\mu} (-\nabla P + \rho_L g \nabla z)^T \cdot \mathbf{n} \quad \text{on } \Gamma_p^q \quad (3.31)$$

Equation (3.31) can sometimes be employed as a no-flow boundary by setting it to zero.

The flux or Neumann BC for the heat transfer can be imposed as an injection wellbore boundary (in the case of non-isothermal condition) or a heat flux normal to a boundary as

$$q_T = (-\lambda \nabla T + \rho_L C_{p,L} v T)^T \cdot \mathbf{n} \quad \text{on } \Gamma_T^q \quad (3.32)$$

Equation (3.32) can also be employed as heat flux value at the heat outflow BC in the production wellbore boundary using the expression for the convective heat transfer as

$$q_T = \rho_L \mathbf{v} \cdot \mathbf{n} \cdot$$

3.5.2 The solution to the boundary value problem

The boundary value problem presented in sections 3.3 and 3.4 can be simplified as a 2-D system as shown in Figure 3.2. For example, equations (3.10) and (3.31) can be written as

$$X(u) = B(u) + J = 0 \quad \text{in } \Omega \quad (3.33)$$

$$Y(u) = D(u) + K = 0 \quad \text{on } \Gamma \quad (3.34)$$

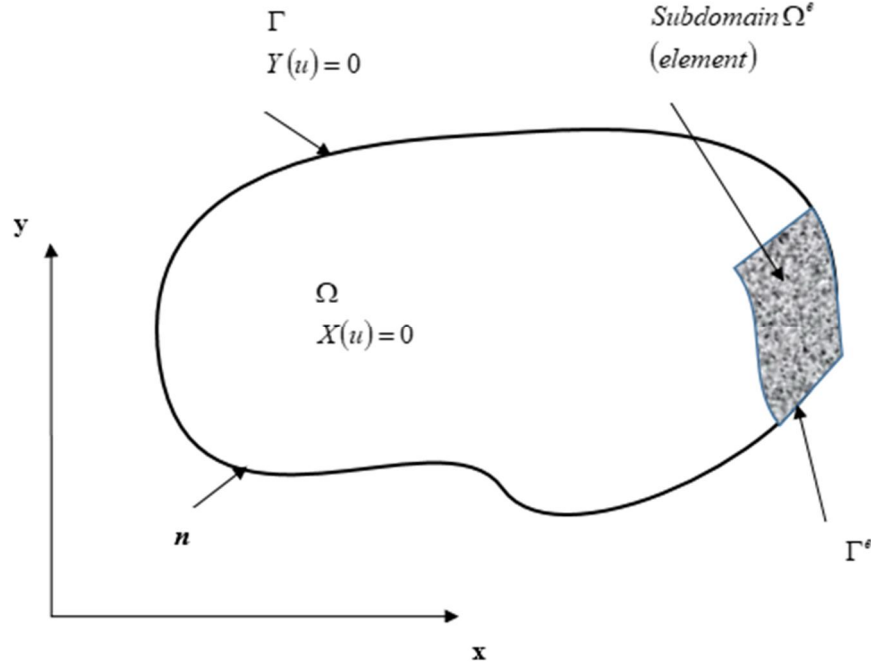


Figure 3.2: 2-D problem domain and boundary

where X and Y are the derivatives of differential operators, and B and D are appropriate differential operators. The parameters J and K are known functions independent of the field variable u , and are the correct solution of the boundary value problem. The set of differential equation (3.10) has to be zero at each point of the domain Ω ; it can follow that

$$\int_{\Omega} \varphi^T X(u) d\Omega \equiv \int_{\Omega} [\varphi_1 X_1(u) + \varphi_2 X_2(u) + \dots] d\Omega \equiv 0 \quad (3.35)$$

where

$$\varphi = \{\varphi_1, \varphi_2, \dots\}^T \quad (3.36)$$

is the set of arbitrary functions that is equal in number to the number of unknown equations involved; it can be asserted that if equation (3.35) is satisfied for all φ then the differential equation (3.10) must be satisfied at all points of the domain. In the case of the boundary condition, if they are to be simultaneously satisfied with the domain, then it is necessary that

$$\int_{\Gamma} \hat{\varphi}^T Y(u) d\Gamma \equiv \int_{\Gamma} [\hat{\varphi}_1 Y_1(u) + \hat{\varphi}_2 Y_2(u) + \dots] d\Gamma \equiv 0 \quad (3.37)$$

for any set of arbitrary function $\hat{\varphi}$. By considering the integral statement

$$\int_{\Omega} \varphi^T X(u) d\Omega + \int_{\Gamma} \hat{\varphi}^T Y(u) d\Gamma = 0 \quad (3.38)$$

equation (3.38) is satisfied for all φ and $\hat{\varphi}$, and is equivalent to the satisfaction of the differential equation (3.10) or (3.35) and its boundary conditions (i.e. equation (3.31) or (3.37)). If equations (3.35) and (3.37) are satisfied, then equation (3.38) is true. An approximate solution is required in the class of functions \hat{u} , explicitly

$$u \approx \hat{u} = \sum_i^j N_i a_i = Na \quad (3.39)$$

where N is the shape function matrix, and a is nodal field vector.

3.5.3 The weighted residual method

The solution to equation (3.39) is obtained by introducing a set of trial or shape functions N_i concerning the coordinates, and a_i are the unknown values defined at points (nodes) in the domain Ω and the boundary Γ . If equation (3.39) is substituted into (3.33) and (3.34), an error or residual remains in the solution, that is

$$R = R_\Omega + R_\Gamma = X(\hat{u}) + Y(\hat{u}) \quad (3.40)$$

Thus, to minimise the error or residual over the whole domain and the boundary, a zero value is required for a suitable number of integrals of the error over Ω and Γ , weighted by weighting functions w and \hat{w} , which is called the weighted residual method (WRM), namely

$$\int_\Omega w^T X(\hat{u}) d\Omega + \int_\Gamma \hat{w}^T Y(\hat{u}) d\Gamma = 0 \quad (3.41)$$

Statement (3.41) is an approximation to the integral expression defined in equation (3.38) and results in a set of equations for the unknowns a_i , which can be written as

$$Ka = f \quad (3.42)$$

where

$$K_{ij} = \sum_{e=1}^m K_{ij}^e \quad f_i = \sum_{e=1}^m f_i^e \quad (3.43)$$

where m is the total number of element adopted.

3.5.4 The weak formulation of the solution

By applying the WRM, that is, equation (3.41), to mass conservation equations (3.10) and its Neumann boundary condition equation (3.31) yields

$$\begin{aligned} & \int_{\Omega} w^T \left\{ \nabla^T \left[\frac{\kappa}{\mu} (-\nabla P + \rho_L g \nabla z) \right] \right\} d\Omega + \int_{\Omega} w^T S \frac{\partial P}{\partial t} d\Omega + \int_{\Gamma} w^T Q_m d\Gamma \\ & + \int_{\Gamma_p^q} \hat{w}^T \left[\frac{\kappa}{\mu} (-\nabla P + \rho_L g \nabla z)^T \cdot \mathbf{n} - \frac{q_p}{\rho_L} \right] \cdot d\Gamma = 0 \end{aligned} \quad (3.44)$$

The choice of weighting functions is limited such that

$$w = 0 \quad \text{on} \quad \Gamma_p \quad (3.45)$$

$$\hat{w} = -w \quad \text{on} \quad \Gamma_p^q \quad (3.46)$$

Applying the Green's theorem to the terms of the divergence operator of equation (3.44) and incorporating equations (3.45) and (3.46) into it, gives

$$\int_{\Omega} \left[-(w \nabla)^T \left(-\frac{\kappa}{\mu} \nabla P + \frac{\kappa}{\mu} \rho_L g \nabla z \right) \right] d\Omega + \int_{\Omega} w^T S \frac{\partial P}{\partial t} d\Omega + \int_{\Gamma} w^T Q_m d\Gamma + \int_{\Gamma_p^q} w^T \frac{q_p}{\rho_L} d\Gamma = 0 \quad (3.47)$$

Similarly, the procedures applied arriving at equation (3.47) for the fluid flow are employed in the energy equations (3.25) and (3.32), which yields

$$\begin{aligned} & \int_{\Omega} w^T c_p \rho \frac{\partial T}{\partial t} d\Omega + \int_{\Omega} w^T \rho_L v c_{p,L} \cdot \nabla T d\Omega + \int_{\Omega} (\nabla w)^T \cdot (-\lambda \nabla T) d\Omega \\ & + \int_{\Gamma} w^T Q_E d\Gamma + \int_{\Gamma_f^q} w^T q^T d\Gamma = 0 \end{aligned} \quad (3.48)$$

Equations (3.47) and (3.48) are the weak formulation (weak form) of the governing equations presented in sections 3.3 and 3.4.

3.5.6 The Galerkin FEM discretisation

The FE approximation is now applied to equations (3.47) and (3.48). The pressures and temperatures are expressed regarding their values P and T at a finite number of points in space as shown in equation (3.39). The procedure involves discretisation of the continuum into elements and the expression of P and T within an element regarding their values at a finite number of points within the domain or on the boundary of that element. Therefore, to ensure continuity of pressures and temperatures between the elements, it is necessary to place a sufficient number of nodes on the element boundary to satisfy the shape functions being used for the elements. The state variables are expressed regarding the nodal values and shape functions as

$$P = \mathbf{N}_p \hat{\mathbf{P}} \quad (3.49)$$

$$T = \mathbf{N}_T \hat{\mathbf{T}} \quad (3.50)$$

where $\hat{\mathbf{P}}$ and $\hat{\mathbf{T}}$ are the scalars of the nodal values of the pressures and temperature, \mathbf{N}_p and \mathbf{N}_T are shape functions. For a coarse tetrahedral element of 3-D problem, they can be represented as

$$\mathbf{N}_p = [\mathbf{N}_{p1} \ \mathbf{N}_{p2} \ \mathbf{N}_{p3} \ \mathbf{N}_{p4}], \ \mathbf{N}_{pi} = \text{diagonal} \{ \mathbf{N}_{pi} \ \mathbf{N}_{pi} \ \mathbf{N}_{pi} \ \mathbf{N}_{pi} \}, \ i=1,4 \quad (3.51)$$

$$\mathbf{N}_T = [\mathbf{N}_{T1} \ \mathbf{N}_{T2} \ \mathbf{N}_{T3} \ \mathbf{N}_{T4}], \ \mathbf{N}_{Ti} = \text{diagonal} \{ \mathbf{N}_{Ti} \ \mathbf{N}_{Ti} \ \mathbf{N}_{Ti} \ \mathbf{N}_{Ti} \}, \ i=1,4 \quad (3.52)$$

By introducing approximations (3.49) and (3.50) into equations (3.47) and (3.48); then applying the Galerkin FEM, and swapping the weighting functions w and \hat{w} with the equivalent shape functions \mathbf{N}_p and \mathbf{N}_T , gives

$$\int_{\Omega} \left[(\nabla \mathbf{N}_p)^T \frac{\mathbf{K}}{\mu} \nabla \mathbf{N}_p \hat{\mathbf{P}} - (\nabla \mathbf{N}_p)^T \frac{\mathbf{K}}{\mu} \rho_L g \nabla z \right] d\Omega + \int_{\Omega} \mathbf{N}_p^T S \mathbf{N}_p \frac{\partial \hat{\mathbf{P}}}{\partial t} d\Omega \quad (3.53)$$

$$+ \int_{\Gamma} \mathbf{N}_p^T Q_m d\Gamma + \int_{\Gamma_p^q} \mathbf{N}_p^T \frac{q_p}{\rho_L} d\Gamma = 0$$

$$\int_{\Omega} \mathbf{N}_T^T c_{\rho} \rho \mathbf{N}_T \frac{\partial \hat{\mathbf{T}}}{\partial t} d\Omega + \int_{\Omega} \left[(\mathbf{N}_T^T c_{\rho, L} q_m \cdot \nabla \mathbf{N}_T) \hat{\mathbf{T}} \right] d\Omega \quad (3.54)$$

$$+ \int_{\Omega} \nabla \mathbf{N}_T^T (-\lambda \nabla \mathbf{N}_T) \hat{\mathbf{T}} d\Omega + \int_{\Gamma} \mathbf{N}_T^T Q_E d\Gamma + \int_{\Gamma_f^q} \mathbf{N}_T^T q^T d\Gamma = 0$$

Further discretising equations (3.53) and (3.54) gives

$$\mathbf{K}_p = \int_{\Omega} \mathbf{N}_p^T S \mathbf{N}_p d\Omega \quad (3.55)$$

$$\mathbf{M}_p = \int_{\Omega} (\nabla \mathbf{N}_p)^T \frac{\mathbf{K}}{\mu} \nabla \mathbf{N}_p d\Omega \quad (3.56)$$

$$\mathbf{f}^p = \int_{\Omega} (\nabla \mathbf{N}_p)^T \frac{\mathbf{K}}{\mu} \rho_L g d\Omega + \int_{\Gamma} \mathbf{N}_p^T Q_m d\Gamma - \int_{\Gamma} \mathbf{N}_p^T \frac{q_p}{\rho_L} d\Gamma \quad (3.57)$$

$$\mathbf{K}_T = \int_{\Omega} \mathbf{N}_T^T c_{\rho} \rho \mathbf{N}_T d\Omega \quad (3.58)$$

$$\mathbf{M}_T = \int_{\Omega} \left\{ \mathbf{N}_T^T (\rho_L v c_{\rho,L} \cdot \nabla \mathbf{N}_T) + \nabla \mathbf{N}_T^T (-\lambda \nabla \mathbf{N}_T) \right\} d\Omega \quad (3.59)$$

$$\mathbf{f}^T = \int_{\Gamma} \mathbf{N}_T^T Q_E d\Gamma - \int_{\Gamma_f} \mathbf{N}_T^T q_T d\Gamma \quad (3.60)$$

where \mathbf{K}_p is the storativity matrix; \mathbf{M}_p is the permeability matrix; \mathbf{f}^p is the load matrix for the fluid flow process; \mathbf{K}_T is the capacity matrix; \mathbf{M}_T is the conductivity matrix, and \mathbf{f}^T is the load matrix for the heat transport.

Similarly, applying the FEM solution procedure obtained in equations (3.55) and (3.60) to the fracture equations in (3.16) and (3.27) yields the following discretisation

$$\mathbf{K}_{p,f} = \int_{\Gamma} \mathbf{N}_p^T S \mathbf{N}_p d\Gamma \quad (3.61)$$

$$\mathbf{M}_{p,f} = \int_{\Gamma} (\nabla \mathbf{N}_p)^T \frac{b}{12\mu} \nabla \mathbf{N}_p d\Gamma \quad (3.62)$$

$$\mathbf{f}^{p,f} = \int_{\Gamma} (\nabla \mathbf{N}_p)^T \frac{b}{12\mu} \rho_L g d\Gamma + \int_{\Gamma} \mathbf{N}_p^T Q_{mf} d\Gamma + \int_{\Gamma} \mathbf{N}_p^T Q_{ext} d\Gamma - \int_{\Gamma} \mathbf{N}_p^T \frac{q_p}{\rho_L} d\Gamma \quad (3.63)$$

$$\mathbf{K}_{T,f} = \int_{\Gamma} \mathbf{N}_T^T c_{\rho} \rho \mathbf{N}_T d\Gamma \quad (3.64)$$

$$\mathbf{M}_{T,f} = \int_{\Gamma} \left\{ \mathbf{N}_T^T (\rho_L v_f c_{\rho,L} \cdot \nabla \mathbf{N}_T) + \nabla \mathbf{N}_T^T (-\lambda \nabla \mathbf{N}_T) \right\} d\Gamma \quad (3.65)$$

$$\mathbf{f}^{\text{T},f} = \int_{\Gamma} \mathbf{N}_T^T Q_{f,E} d\Gamma + \int_{\Gamma} \mathbf{N}_T^T Q_{m,E} d\Gamma - \int_{\Gamma_f^g} \mathbf{N}_T^T q_T d\Gamma \quad (3.66)$$

The FE formulations of the solution for the discretisation in space can be written in a matrix form, for the fluid flow process

$$\mathbf{M}_p \hat{\mathbf{P}}^M + \mathbf{K}_p \hat{\mathbf{P}}^M = \mathbf{f}^p \quad (3.67)$$

$$\mathbf{M}_{p,f} \hat{\mathbf{P}}^f + \mathbf{K}_{p,f} \hat{\mathbf{P}}^f = \mathbf{f}^{p,f} \quad (3.68)$$

and for the heat transport process

$$\mathbf{M}_T \hat{\mathbf{T}}^M + \mathbf{K}_T \hat{\mathbf{T}}^M = \mathbf{f}^T \quad (3.69)$$

$$\mathbf{M}_{T,f} \hat{\mathbf{T}}^f + \mathbf{K}_{T,f} \hat{\mathbf{T}}^f = \mathbf{f}^{\text{T},f} \quad (3.70)$$

Here, it is assumed that there is continuity in the temperature and pressure of the matrix block and the fractures ($T^M = T^f, P^M = P^f$).

3.5.7 Element choice

In this research, isoparametric elements were employed due to their robustness in handling nonrectangular and curved-sided elements. This family of elements allows for the interpolation of an element within the coordinates using the same shape functions as for the variables. The mapping concepts permit the application of elements of a more arbitrary shape, such as nonrectangular and curved-sided types, than simple forms. Furthermore, the elements' coordinates define the geometry via a standard linear relationship, while the shape functions define the field variables (i.e. vectors or scalars), which in turn are expressed regarding the element coordinates. Figure 3.3 presents the 3-D representation of isoparametric elements. In equations (3.49) and (3.50) different shape functions have been employed to represent the pressure and temperature. That is essential when the permeability matrix and often the compressibility matrix are set to zero in the case when the solution is approaching an undrained limit state.

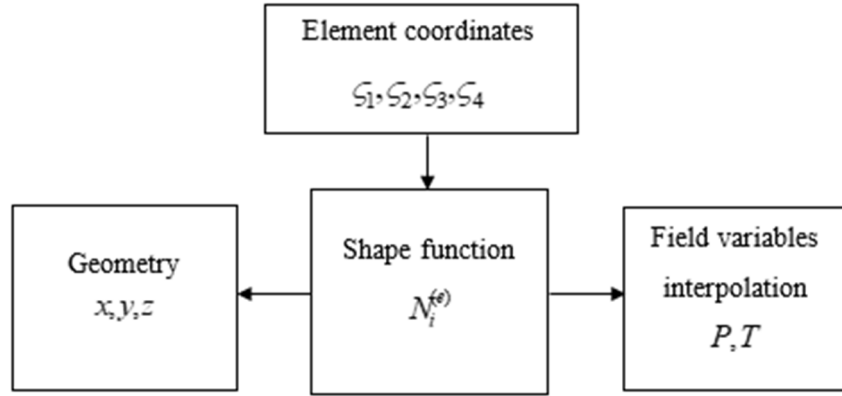


Figure 3.3: General representation of 3-D isoparametric elements

3.5.8 Temporal discretisation and convergence criteria

In this thesis, the method used for the time discretisation is the finite difference (FD) scheme. Variation of field variables P and T and the load vector f within each time step are assumed to follow a linear relationship.

$$\mathbf{P} = \mathbf{N}_1 \mathbf{P}^{t_k} + \mathbf{N}_2 \mathbf{P}^{t_k + \Delta t} \quad (3.71)$$

$$\mathbf{T} = \mathbf{N}_1 \mathbf{T}^{t_k} + \mathbf{N}_2 \mathbf{T}^{t_k + \Delta t} \quad (3.72)$$

$$\mathbf{f} = \mathbf{N}_1 \mathbf{f}^{t_k} + \mathbf{N}_2 \mathbf{f}^{t_k + \Delta t} \quad (3.73)$$

where $N_1 = 1 - \eta$, $N_2 = \eta$, and $\eta = (t - t_k) / \Delta t$, where η is the relaxation parameter. Thus, to generate an FD scheme the parameter ranges from 0 to 1. The value of η determines which of the FD schemes is employed. For example, the values of $\eta = 1$, $\eta = 0.5$, and $\eta = 0$ corresponds to the backward difference method, central difference method, and forward difference method. In this research, the backward difference method is used in modelling the TH processes.

$$\frac{\partial \mathbf{P}}{\partial t} = \frac{\partial \mathbf{N}_1}{\partial t} \mathbf{P}^{t_k} + \frac{\partial \mathbf{N}_2}{\partial t} \mathbf{P}^{t_k + \Delta t} = \frac{1}{\Delta t} [\mathbf{P}^{t_k + \Delta t} - \mathbf{P}^{t_k}] \quad (3.74)$$

$$\frac{\partial \mathbf{T}}{\partial t} = \frac{\partial \mathbf{N}_1}{\partial t} \mathbf{T}^{t_k} + \frac{\partial \mathbf{N}_2}{\partial t} \mathbf{T}^{t_k + \Delta t} = \frac{1}{\Delta t} [\mathbf{T}^{t_k + \Delta t} - \mathbf{T}^{t_k}] \quad (3.75)$$

$$\frac{\partial \mathbf{f}}{\partial t} = \frac{\partial \mathbf{N}_1}{\partial t} \mathbf{f}^{t_k} + \frac{\partial \mathbf{N}_2}{\partial t} \mathbf{f}^{t_k + \Delta t} = \frac{1}{\Delta t} [\mathbf{f}^{t_k + \Delta t} - \mathbf{f}^{t_k}] \quad (3.76)$$

Substituting equations (3.71 to 3.76) into (3.67 to 3.70) yields the matrix solutions for the temporal discretisation as

$$\mathbf{M}_P \left[\frac{\mathbf{1}}{\Delta t} + \boldsymbol{\eta} \mathbf{K}_P \right] \mathbf{P}^{t_k + \Delta t} = \left[\mathbf{M}_P \frac{\mathbf{1}}{\Delta t} - (\mathbf{1} - \boldsymbol{\eta}) \mathbf{K}_P \right] \mathbf{P}^{t_k} + [(\mathbf{1} - \boldsymbol{\eta}) \mathbf{f}^{t_k} + \boldsymbol{\eta} \mathbf{f}^{t_k + \Delta t}] \quad (3.77)$$

$$\mathbf{M}_T \left[\frac{\mathbf{1}}{\Delta t} + \boldsymbol{\eta} \mathbf{K}_T \right] \mathbf{T}^{t_k + \Delta t} = \left[\mathbf{M}_T \frac{\mathbf{1}}{\Delta t} - (\mathbf{1} - \boldsymbol{\eta}) \mathbf{K}_T \right] \mathbf{T}^{t_k} + [(\mathbf{1} - \boldsymbol{\eta}) \mathbf{f}^{t_k} + \boldsymbol{\eta} \mathbf{f}^{t_k + \Delta t}] \quad (3.78)$$

$$\mathbf{M}_{P,f} \left[\frac{\mathbf{1}}{\Delta t} + \boldsymbol{\eta} \mathbf{K}_{P,f} \right] \mathbf{P}^{t_k + \Delta t} = \left[\mathbf{M}_{P,f} \frac{\mathbf{1}}{\Delta t} - (\mathbf{1} - \boldsymbol{\eta}) \mathbf{K}_{P,f} \right] \mathbf{P}^{t_k} + [(\mathbf{1} - \boldsymbol{\eta}) \mathbf{f}^{t_k} + \boldsymbol{\eta} \mathbf{f}^{t_k + \Delta t}] \quad (3.79)$$

$$\mathbf{M}_{T,f} \left[\frac{\mathbf{1}}{\Delta t} + \boldsymbol{\eta} \mathbf{K}_{T,f} \right] \mathbf{T}^{t_k + \Delta t} = \left[\mathbf{M}_{T,f} \frac{\mathbf{1}}{\Delta t} - (\mathbf{1} - \boldsymbol{\eta}) \mathbf{K}_{T,f} \right] \mathbf{T}^{t_k} + [(\mathbf{1} - \boldsymbol{\eta}) \mathbf{f}^{t_k} + \boldsymbol{\eta} \mathbf{f}^{t_k + \Delta t}] \quad (3.80)$$

The convergence termination criterion applied for the nonlinear iterations in this research is the weighted Euclidean norm, which stops the iteration solutions when the relative tolerance exceeds the relative error computed, which is given as

$$Error = \sqrt{\frac{1}{N_F}} \sqrt{\sum_{j=1}^{N_F} \frac{1}{N_j} \sum_{i=1}^{N_j} \left(\frac{|E_{i,j}|}{W_{i,j}} \right)^2} \quad (3.81)$$

where N_F is the number of fields and N_j is the number of degrees of freedom in the field j . The double subscript denotes the degree of freedom index i and j component. $E_{i,j}$ is the estimated error in the scalar, $W_{i,j} = \max(|U_{i,j}|, S_j)$, $U_{i,j}$ is the current approximation to the solution scalar and S_j is a scale factor for which the program determines the scaling process. A solution procedure is presented in Appendix 1.

3.6 Coupling strategy for the TH processes

This section outlined the computational solution of the coupled TH processes. The chosen case consists of two processes: a thermo-hydraulic coupled problem with an FE formulation presented in section 3.5. Coupling between the fluid motion and heat transport is carried out through ρ_L , μ , $C_{P,L}$, and λ_L parameters that appear in almost all of the following equations (3.10), (3.16), (3.25) and (3.27), in which parameters are coupled by the temperature field (T), since all the parameters are temperature-dependent as will be discussed later. Similarly,

the coupling between heat transport and fluid flow is achieved through Darcy's velocity term (contribution of convective heat transfer), which appears in equations (3.25), (3.27) and (3.32) for both the matrix block and the fracture. The parameters are calculated and updated simultaneously during the numerical simulations. Figure 3.4 presents the diagrammatical representation of the coupling implementation.

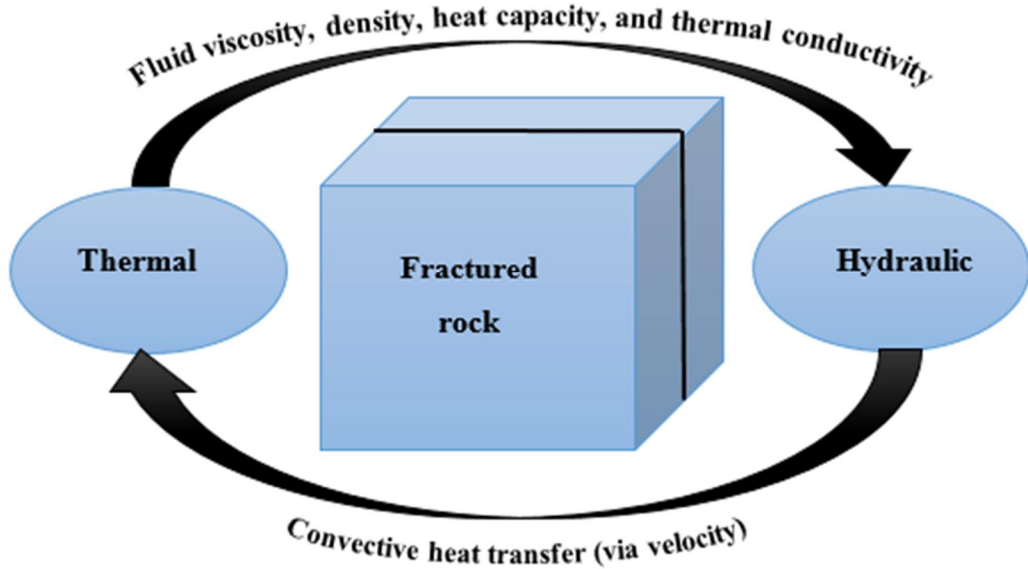


Figure 3.4: Fully coupled TH processes representation

The temperature-dependent fluid parameters provide the coupling processes through fitting the polynomial trend proposed by Holzbecher, 1998. For the fluid density (kg/m^3), it is given as

$$\rho_L(T) = 996.9 \left(1 - 3.17 \times 10^{-4} (T - 298.15) - 2.56 \times 10^{-6} (T - 298.15)^2 \right) \quad (3.82)$$

The temperature field (T) in equation (3.82) ranges from 20°C to 250°C . The expression adopted for the relationship between dynamic viscosity ($\text{Pa}\cdot\text{s}$) and temperature is given as

$$\mu(T) = 2.414 \times 10^{-5} \times 10^{\frac{247.8}{(T+133)}} \quad (3.83)$$

In equation (3.83) the temperature field (T) ranges from 4°C to 250°C . For the thermal conductivity in 10^3 W/m/K , the following fitting polynomial is employed

$$\lambda_L(T) = -922.47 + 2839.5 \left(\frac{T}{T_0} \right) - 1800.7 \left(\frac{T}{T_0} \right)^2 + 525.77 \left(\frac{T}{T_0} \right)^3 - 73.44 \left(\frac{T}{T_0} \right)^4 \quad (3.84)$$

in which T_0 is 273.15 K, and the temperature field (T) ranges from 0°C to 350°C. The specific heat capacity of fluid at temperatures from 100°C to 320°C can be approximated by

$$C_{P,L}(T) = 3.3774 - 1.12665 \times 10^{-2} T + 1.34687 \times 10^{-5} T^2 \quad (3.85)$$

The unit of equation (3.85) is [cal/g/K]; to obtain the SI units [J/kg/K] it is multiplied by 4187.6. Specific heat capacity at a constant pressure below the temperature of 100°C seems to be constant with a value of 4200 J/kg/K approximately.

3.7 Numerical implementation of the FE model

Since the developed FE model is nonlinear both in space and time, then it is difficult to obtain an analytical solution to the problem. Therefore, the complete set of the coupled equations derived are implemented in MATLAB via a LiveLink simulation into COMSOL Multiphysics. The Multiphysics solver allows the use of PDE-based modelling environment to complete the FEM analysis. The PDE-based modelling provides user control of the solver (i.e., not a black box) to select the appropriate shape functions and other essential FE solution tools.

Moreover, before implementing the FE solution, a Gmsh package was used for mesh generation due to its robustness in handling difficult meshes such as complex geological formations. Also, a code was developed in MATLAB to generate the element connectivity from the mesh created in Gmsh for the FEM analysis. A solution flowchart is provided in Appendix 1 for the entire modelling process implementation.

3.8 Summary

In this chapter, the governing equations for modelling TH processes in naturally fractured HDR reservoirs were derived using the conservation laws for mass, energy and momentum. Based on the derived equations, an FE formulation was developed to accurately model the coupled transient behaviour of energy mining in deep geothermal reservoirs. Although the code was intended for modelling HDR systems, it can also be employed in simulating TH behaviour of other subsurface media resources.

The present chapter serves as a major tool for obtaining the outcomes provided in the remaining chapters of this thesis. Thus, since the FE model developed is new, there is a need for standard verification and validation tests before solving practical engineering problems, such as HDR systems.

Chapter four – Code verification and validation studies

4.1 Introduction

The FE model developed in Chapter 3 is required to be verified and validated against well-established analytical solutions and experimental measurement before proceeding with the investigation. The goal of the verification and validation studies is to establish the validity and reliability of the model in solving practical engineering problems.

4.2 Overview of verification and validation processes

Verification and validation (V&V) studies are the processes used to assess the reliability and accuracy of a computational model that makes engineering predictions (Thacker et al., 2004). They are needed to reduce the time, cost and risk related to full-scale testing of materials, products and systems (Sargent, 1999). Thus, the primary processes for quantifying and establishing reliability in numerical models are the verification and validation test (Oberkampf et al., 2004). The terms “verification” and “validation” are of keen interest in this thesis; therefore, it is essential to ensure a basic understanding of their meanings (Cowles et al., 2012):

- Verification is the method used for determining that a numerical model accurately represents the critical mathematical model and its solution (Jeremić et al., 2008), or it is the process of identifying and removing errors in a computational model by comparing its solutions to an established analytical or accurate benchmark solution (Thacker et al., 2006).
- Validation is the process of setting up the degree to which a numerical model is a real representation of the actual world from the perspective of the proposed uses of the model (Oberkampf and Trucano, 2002). Alternatively, it is concerned with quantifying the accuracy of the numerical model by comparing computational results to experimental measurement (Thacker et al., 2006).

The technical committee on Model Credibility of the Society for Computer Simulation has developed a framework for evaluating the credibility of a computational model as shown in Figure 4.1 (Society for Computer Simulation, 1979). The inner triangle in Figure 4.1 represents the processes that relate the components to each other, and the dash-line circle refers to the procedures that evaluate the credibility of the processes.

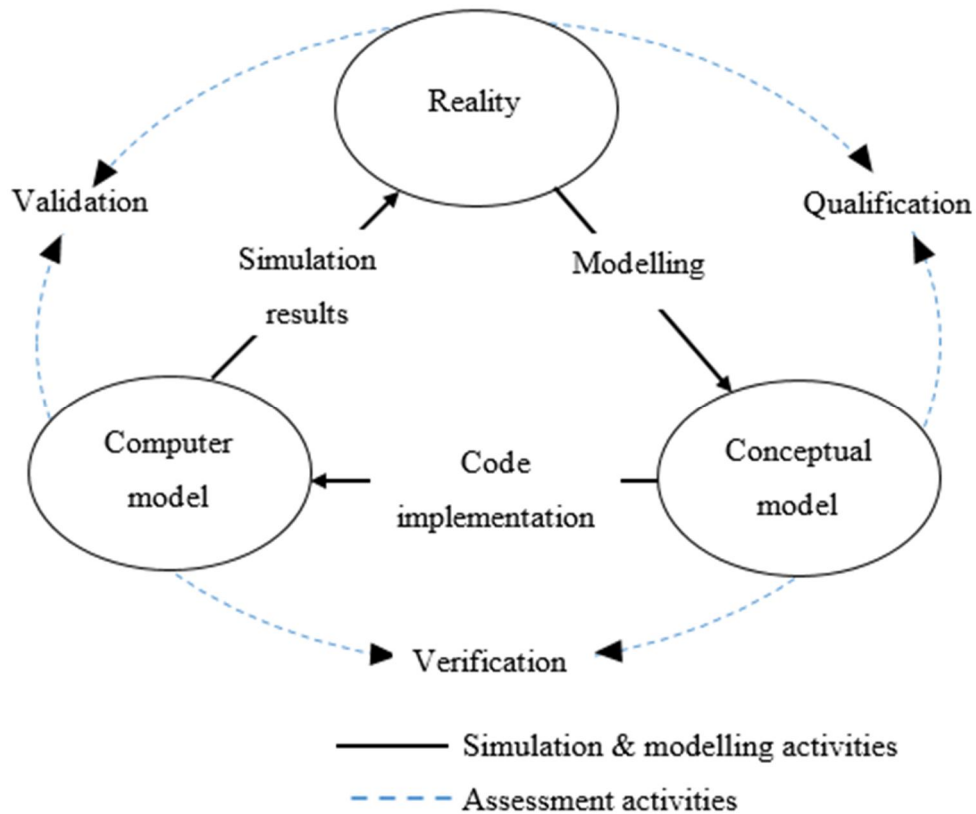


Figure 4.1: A typical representation of model verification and validation process
(Modified from: Society for Computer Simulation, 1979)

The interrelationships of each of the basic components presented in Figure 4.1 are dealt with in the following set of definitions (Society for Computer Simulation, 1979):

Reality represents the physical system being studied.

Conceptual model comprises equations, natural laws or governing relationships required to describe the *Reality*.

Computer model represents the implementation of the *Conceptual model* in the form of a numerical solution that includes a discretisation process, running the solution algorithms, and testing the solution convergence criteria.

Modelling comprises the selection of important features and related mathematical approximations required to represent the *Reality* in the *Conceptual model*.

Code implementation represents the activities performed to implement the *Conceptual model* adequately by providing all the necessary information required to run the *Computer model*.

Simulation results are the evaluation of a tested and certified *Computer model* to gain insight into the *Reality*.

Qualification represents the assessment of the correctness of the *Modelling* process.

Verification authentication that a *Computer model* represents a *Conceptual model* within specified limits of accuracy.

Validation quantification of the accuracy of the model via comparisons of experimental measurements with *Simulation results* from the *Computer model*.

4.3 Verification study on the FE model

In this section, different analytical solutions were employed to verify the FE model developed in Chapter 3 by the fundamental principles laid out in section 4.2. The approach used in this thesis for the verification study is a simple technique, in which simple 1-D problems were solved, before 2-D problems. This method helps in understanding the outcomes of a simple model before engaging in a more complex problem.

4.3.1 Verification of one-dimensional numerical model against analytical solutions

This subsection presents two 1-D problems to verify the capability of the FE model developed for the investigation of coupled transient heat and fluid transport processes in naturally fractured HDR geothermal systems. The first case presented here is the transport process in a porous medium without a fracture, and in the second case, heat transfer in a fully saturated fracture system is studied. In both cases a 1-D model of an existing analytical solution is utilised for the verification study. The reason for the selection of these two cases is to relate the models with a naturally fractured medium that couples both effects of porous matrix and fractures, respectively.

4.3.1.1 Heat transport in porous medium

In this example, a transient-coupled TH process of a 1-D transport in a porous medium is considered to verify the numerical code and demonstrate the accuracy and reliability of the proposed numerical approach with an existing analytical solution as shown in Appendix 2.

For the numerical simulation, 100 m length 1-D geometry is selected, with mesh that consists of line elements. The material properties used in the investigation are shown in Table 4.1 (Xia et al., 2017). Similarly, Table 4.2 and Figure 4.2 present the initial and boundary conditions employed in the verification study.

A comparison of numerical and analytical results concerning the temperature distribution along the domain of the medium after five years is shown in Figure 4.3. The comparison shows excellent agreement between numerical and analytical solutions with a slight mismatch observed in the region close to the fluid injection boundary. In the numerical solution, this boundary represents the injection point, and for the finite element grid, the mesh was refined to get an accurate solution because of the Dirichlet BC applied. As the result of that, as the distance from the injection boundary increases, the agreement between numerical and analytical solutions becomes excellent.

Table 4.1: Material properties used in the test case one (Xia et al., 2017)

Parameter	Value	Units
Fluid density	1000	kg/m ³
Solid density	2500	kg/m ³
Fluid heat capacity	4186	J/kg/K
Solid heat capacity	920	J/kg/K
Fluid thermal conductivity	0.6	W/m/K
Solid thermal conductivity	1.5	W/m/K
Fluid viscosity	1.2e-4	Pa·s
Porosity	0.2	1
Permeability	1e-15	m ²

Table 4.2: Initial and boundary conditions employed in test case one (Xia et al., 2017)

Physic	Condition	Reference	Condition
Hydraulic	Initial	Entire domain	10 MPa
	Boundary	Left side (inlet)	10.5 MPa
	Boundary	Right side (outlet)	10 MPa
Thermal	Initial	Entire domain	200°C
	Boundary	Left side (inlet)	150°C
	Boundary	Right side (outlet)	200°C

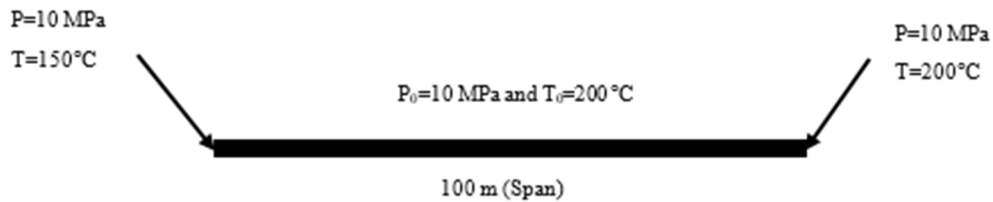


Figure 4.2: Geometry of the 1-D porous medium

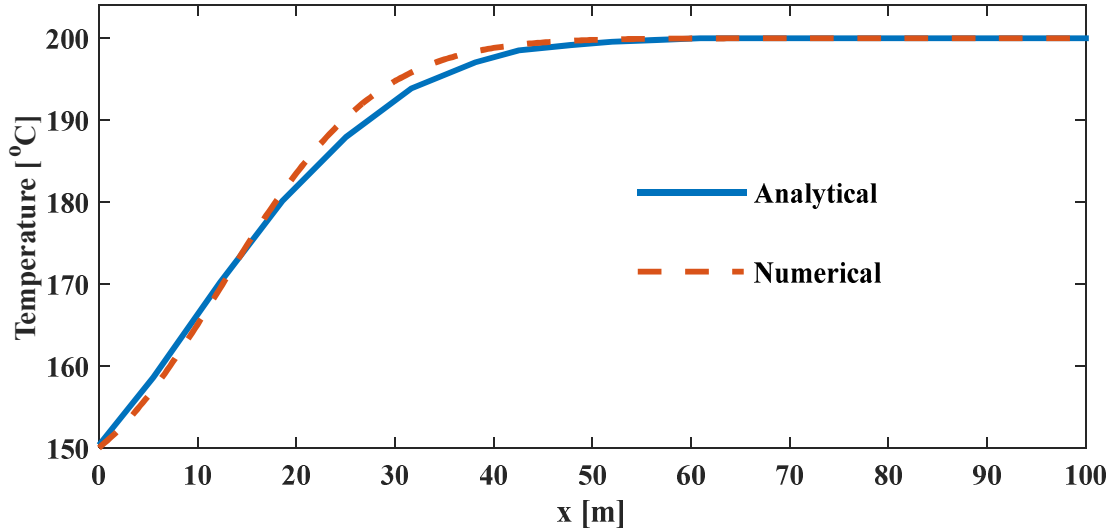


Figure 4.3: Temperature distribution along the medium after five years

4.3.1.2 Heat transfer in a fracture

In this study, heat transport by diffusion and advection within a 1-D fracture is presented. The fracture is assumed to be homogeneous and isotropic and that no heat transfer occurs between the surrounding medium and the fracture. The fluid transport across any fixed plane may be quantitatively represented as the product of the temperature gradient and a diffusion coefficient, due precisely to microscopic velocity variations in the flow medium. Thus, the average velocity is taken to be constant throughout the length of the flow field because of the assumption that the flow in the medium is unidirectional. (Ogata and Banks, 1961) developed an analytical solution capable of modelling 1-D transport processes driven by advection and diffusion, which is presented in Appendix 3.

The numerical model is precisely set up for comparison against Ogata and Banks' analytical solution. An inlet mass source of $3e-7 \text{ m}^3/\text{s}$ is used in the simulation; this ensures a sufficient flow via the assumed rigid fracture that manifest a thermal breakthrough curve at the production point occurred. Other parameter values and the initial and boundary conditions employed in the simulation are listed in Tables 4.3 and 4.4. The time discretisation is also graduated, with a tiny time step of 1.54 days, which is very tiny in comparison to the maximum simulation time. The lower bound time limit is 2314 days, and an upper bound limit of 5787 days is used in the investigation.

Table 4.3: Material properties used in the test case two (Barth et al., 2010)

Parameter	Value	Units
Fluid density	1000	kg/m ³
Fracture density	2850	kg/m ³
Fluid heat capacity	4000	J/kg/K
Fracture heat capacity	600	J/kg/K
Fluid thermal conductivity	0.6	W/m/K
Fracture thermal conductivity	5.0	W/m/K
Fluid viscosity	1e-3	Pa·s
Porosity	1	1
Permeability	1e-11	m ²

A comparison of the temperature breakthrough curve at the right edge point of the fracture predicted by the numerical solution and Ogata and Banks' solution is shown in Figure 4.4. After 5787 days, the difference in the prediction is less than 2% of the temperature breakthrough curve. The discrepancy can be attributed to the approximation of heat conduction and convection within the medium used by Ogata and Banks' model as a one-way coupled process, whereas the numerical model considers the effect of thermal convection in the fracture in addition to the conduction. The agreement is excellent even when the time is between 4200 and 4700 days; some differences become evident despite it being an artefact of the time integration of the FEM model. Thus, the result shows that the discretisation in space and time is sufficient for a thermo-hydraulic solution of a 1-D fracture flow for both the models with good agreement.

Table 4.4: Initial and boundary conditions employed in test case two (Barth et al., 2010)

Physic	Condition	Reference	Condition
Hydraulic	Initial	Entire domain	100 kPa
	Boundary	Left side (inlet)	3e-7 m/s
	Boundary	Right side (outlet)	100 kPa
Thermal	Initial	Entire domain	0°C
	Boundary	Left side (inlet)	1°C

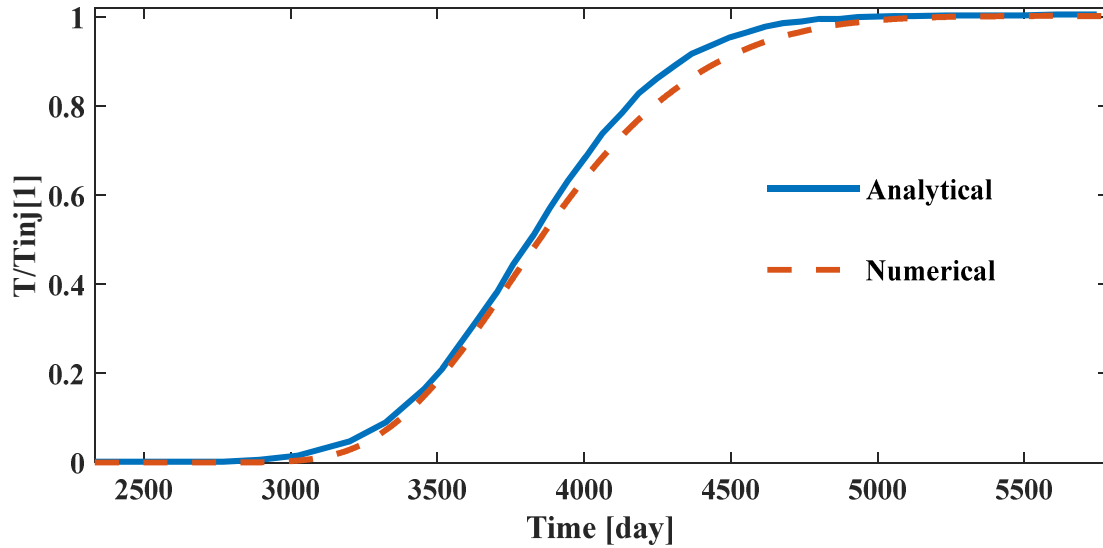


Figure 4.4: Dimensionless temperature at the right edge point of the fracture

4.3.1.3 Summary of findings on 1-D verification studies

In subsections 4.3.1.1 and 4.3.1.2, two verification studies are presented between numerical and existing analytical solutions with excellent agreement. To this end, it is worth noting that the comparison is satisfactory within the limitations of the numerical accuracy by which errors are brought in by finite time step size, FE discretisation and new artefacts of finite precision computation. The verification examination conducted instils confidence in the predictions presented in the subsequent subsection of this thesis, which represents 2-D prototype behaviour of naturally fractured porous media.

4.3.2 Verification of two-dimensional numerical model against analytical solutions

In subsection 4.3.1, a 1-D problem associated with a porous medium was successfully verified using the FE model developed with well-established analytical solutions, and the results obtained instilled more confidence in the numerical simulator. As a result, this subsection will further verify the current model into a 2-D domain, to build more confidence in the FE model tool developed for solving practical engineering problems relevant to the subsurface application.

In this study, two cases of 2-D problems applicable to fractured porous media are verified. The first case deals with a stationary 2-D fractured porous medium with a single discrete fracture. The second test example deals with coupled transient fluid and heat transport processes in an open fracture within a rock matrix block.

4.3.2.1 Fracture response to fluid injection on a 2-D fractured porous medium

In this verification test, a 2-D fractured porous medium is analysed to verify the solution capabilities described in Chapter 3. The test conducted is the disturbance triggered by the presence of fracture in porous media with a uniform flow. The analytical solution chosen for this study is the potential flow solution derived by Strack (1982), to examine the influence of fluid injection on fractures using the potential flow. The Strack's analytical solution was applied to compare the developed FE model results. Figure 4.5 shows the 2-D model of the problem with a 1-D fracture; where the fluid is injected and extracted on the left P_{in} and right P_{out} sides of the model, respectively (Holtz, 2012). On the other hand, the top and bottom represent no-flow boundaries $\nabla P \cdot n = 0$. The fracture is 2 m in length with an orientation angle of 45° , and the flow is assumed to be laminar along its surface. Table 4.5 presents other parameters employed in the numerical model of the porous media (Holtz, 2012).

The results obtained in this study are grouped into two. The first set of results is the pressure distribution within the domain of the problem and its flow pattern. Figure 4.6 presents the pressure distribution for the analytical solutions (left) and FE model numerical simulation results (right). As seen, the results of the FE model match very well with the analytical solution regarding fracture disturbance. The second set of results verified in this study is the pressure profile along a diagonal from the bottom-left passing through the fracture to the top-right of the domain. Figure 4.7 presents the results of both the analytical solution and the current FE model. As can be seen, the results for both solutions agree very well with each other. Thus, the capability of the newly developed FE model is verified using a related problem applicable to porous medium modelling.

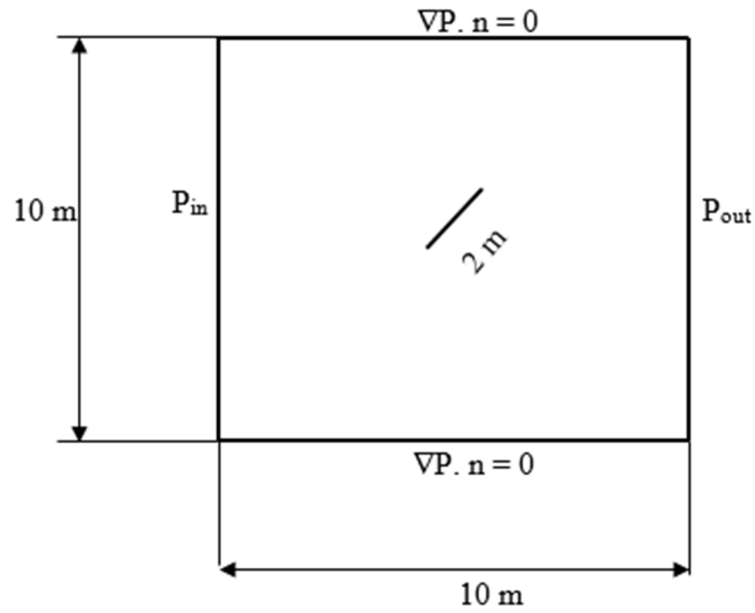


Figure 4.5: 2-D fractured porous media

Table 4.5: Model parameters adopted in model verification (Holtz, 2012)

Parameters	Symbol	Value	Unit
Porosity	ϕ	1	%
Hydraulic conductivity	K	1 e-5	m/s
Fracture hydraulic conductivity	K_f	1 e-3	m/s
Specific storage	S	1 e-4	m/s
Injection pressure	P_{in}	4.965 e+5	Pa
Extraction pressure	P_{out}	-4.965 e+5	Pa
Density	ρ	1,000	kg/m ³
Viscosity	μ	0.001	Pa.s

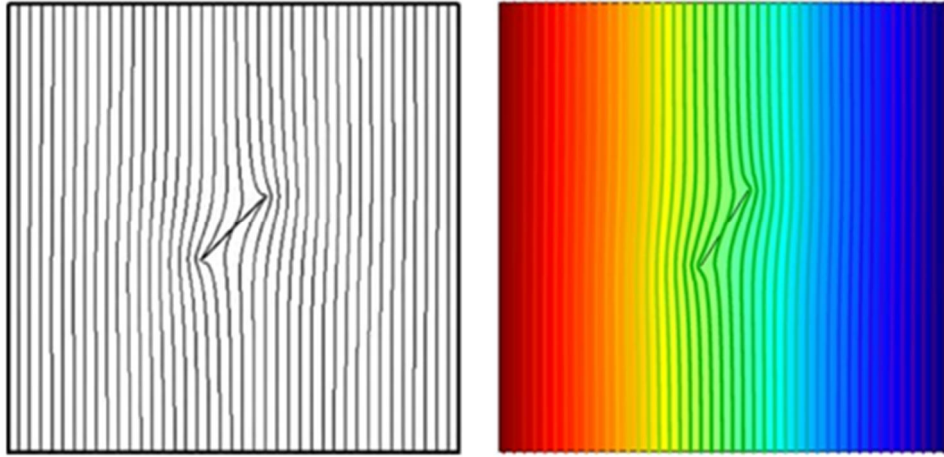


Figure 4.6: Analytical solution (left) and FE model solution (right)

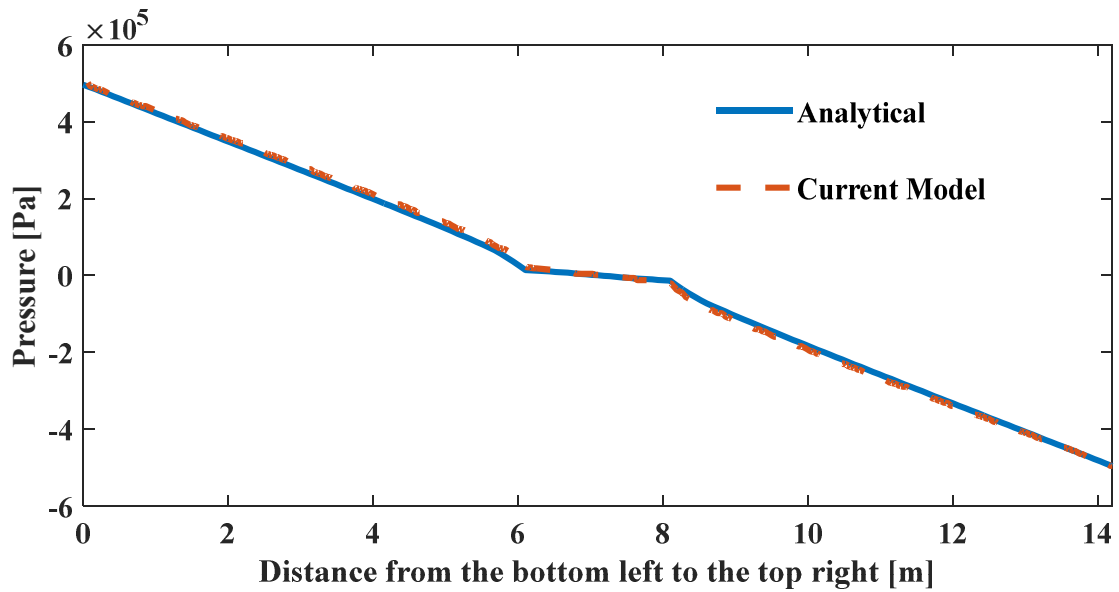


Figure 4.7: Pressure profile along a diagonal from the bottom-left passing via the fracture to the top-right

4.3.2.2 Coupled fluid and heat transport in fractured porous media

In this test case, the verification of the numerical model against the analytical model is based on heat diffusion and advection through a rock matrix orthogonal to a single fracture as shown in Figure 4.8. Coupling of the advective and diffusive heat transports in the fracture, as well as the rock matrix block, are also presented in the analytical solution. The rock matrix block elements are interconnected with the fracture elements orthogonally, which implies that the nodes in the matrix are not influenced by their right or left boundaries. The analytical solution referred to as Lauwerier's Solution is employed in this investigation, and its solution

is compared with numerical results concerning the temperature breakthrough curves at specific positions within the rock matrix block. The analytical solution is derived based on the assumption that heat is transferred only by advection in the fracture, whereas in the rock matrix block the heat transfer takes place by diffusion along the z-axis only (Holtz, 2012).

Table 4.6: Model parameters used for the analytical verification (Holtz, 2012)

Parameter	Value	Symbol
Spatial discretisation		
Fracture length (m)	50	L
Fracture width (m)	2e -3	b
Matrix width (m)	63.25	W
Increment size x-axis	2	dx
Increment size z-axis	0.1265	dz
Material properties		
Matrix porosity (%)	1.0	ϕ
Matrix permeability (m ²)	1e -15	κ
Thermal conductivity (W/m/K)	3.0	λ_s
Solid heat capacity (J/kg/K)	1000	$C_{\rho,S}$
Fluid heat capacity (J/kg/K)	4000	$C_{\rho,L}$
Solid density (kg/m ³)	2600	ρ_s
Fluid density (kg/m ³)	1000	ρ_L
Initial conditions		
Pressure (Pa)	1e +5	P_{in}
Temperature (°C)	0	T_{in}
Boundary conditions		
Injection temperature (°C)	1.0	T_{inj}
Inlet velocity (m/s)	1e -3	v
Production pressure (Pa)	1e +5	P_{pro}

Table 4.6 shows the model and material parameters employed in the study (Holtz, 2012). Figure 4.9 presents the schematic description of the model and the boundary conditions employed, but due to symmetry, only the domain above the x-axis is considered in the numerical investigations. Figure 4.10 presents the locations of specific points chosen to observe the temperature breakthrough curves to assess the numerical simulation in comparison with the analytical solutions.

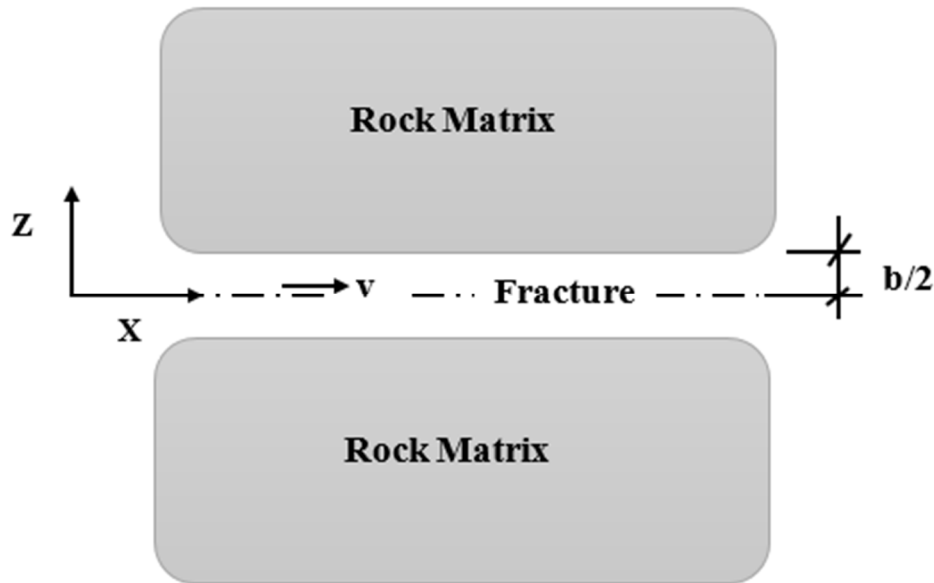


Figure 4.8: Geometry of the fracture-matrix heat transport (adopted from Holtz, 2012)

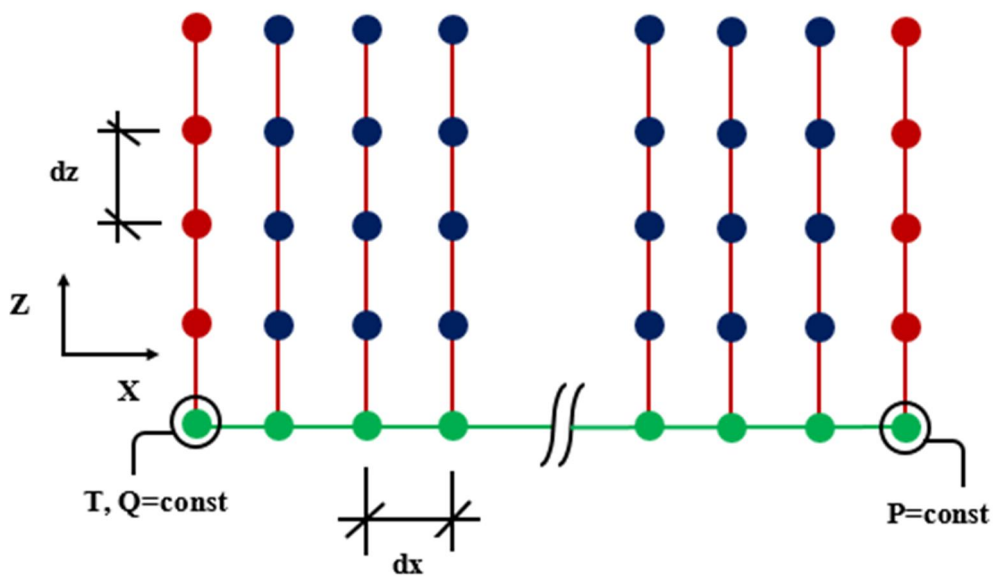


Figure 4.9: Grid alignment and boundary conditions for the numerical model

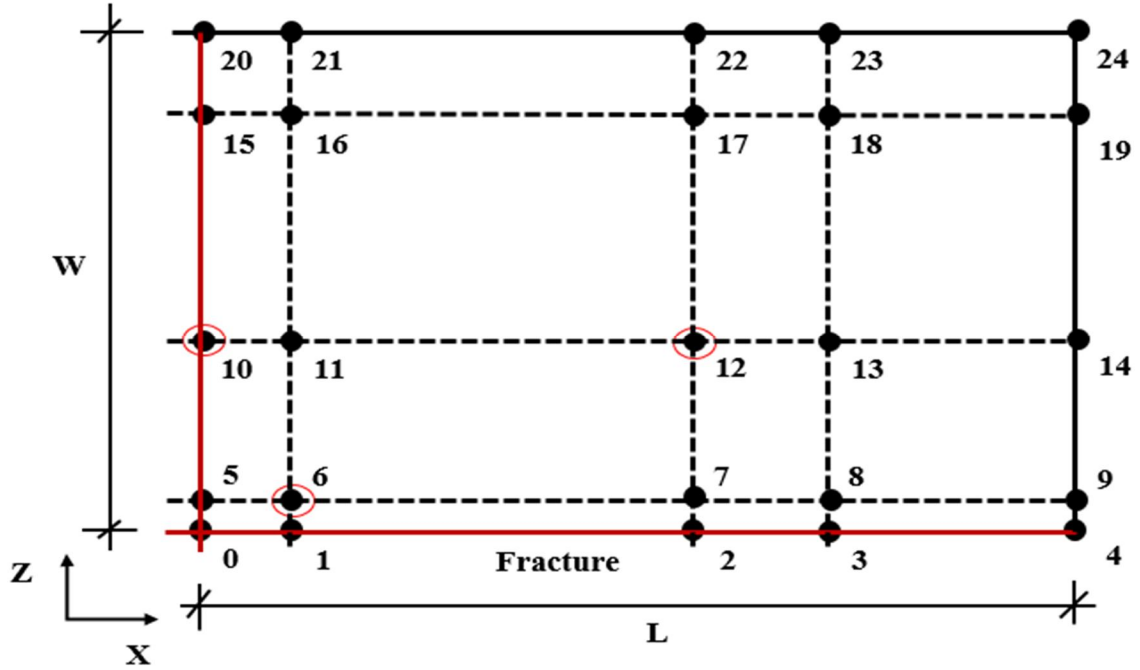


Figure 4.10: Observation points positions (i.e., 6, 10, and 12) for temperature history curves

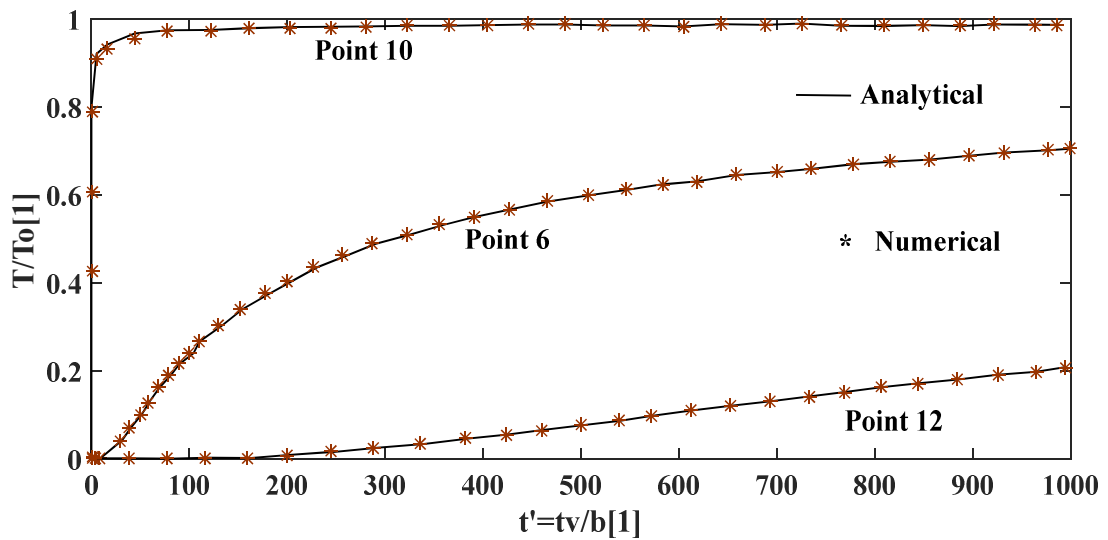


Figure 4.11: Temperature history curves at specific points on the rock matrix block for both the analytical and numerical models

Figure 4.11 presents the numerical simulation results, compared to the analytical solution at the different points on the rock matrix block. The temperature breakthrough curves and the time are both considered as dimensionless parameters. At the observed points, it can be seen that there are slight differences concerning the numerical results and the

analytical solutions, but after some time, both solutions fit very well. The reason for the slight deviation between the analytical solution and the numerical results is because, at the early simulation period, the breakthrough temperature of the numerical model points far from the fractures are not affected by the fluxes at the fracture's edge due to different modelling assumptions of fracture flow. The analytical model assumed the fracture to be an equivalent porous medium whereas the numerical model used the cubic law of parallel plates. However, after a more extended period of simulation (600, 800 and 1000), both results fit very well.

Another possible reason for the primary difference may be due to the inclusion of a viscosity parameter in the numerical simulations, which is not present in the analytical solution. In summary, it is concluded that both the numerical simulation and analytical solution are in good agreement.

4.4 Validation of the FE model

This section aims to validate the FE model developed using existing field experiments of real geothermal application to determine the accuracy and reliability of the numerical simulator. The techniques mentioned in section 4.2 were employed in this investigation for proper adherence to the standards. Here, two field cases are studied, and the first case concerns the field experiments conducted at the Soultz geothermal system in France. In the second case, a 75-day circulation test performed at the Fenton Hill HDR geothermal reservoir site in the US was chosen for the validations.

4.4.1 Validation of temperature profile at Soultz well

In this study, a validation study is conducted on the Soultz geothermal system. The reason for choosing the system for the validation exercise is due precisely to the critical lessons learned from the field and its contributions to the development of several geothermal fields worldwide. The current operational reservoir in the Soultz is located in the lower granite of the deep graben formation (Sanjuan et al., 2010). Figure 4.12 presents the reservoirs and the wellbores details of the geothermal system. As can be seen, the lower reservoir is located within 4 km to 5.2 km of the system (Genter et al., 2010a). As the current operation is carried

out in the vicinity of the lower reservoir, therefore, it is vital to validate the temperature profile of the reservoir with the FE model developed, in order to justify the reliability and accuracy of the numerical simulator.

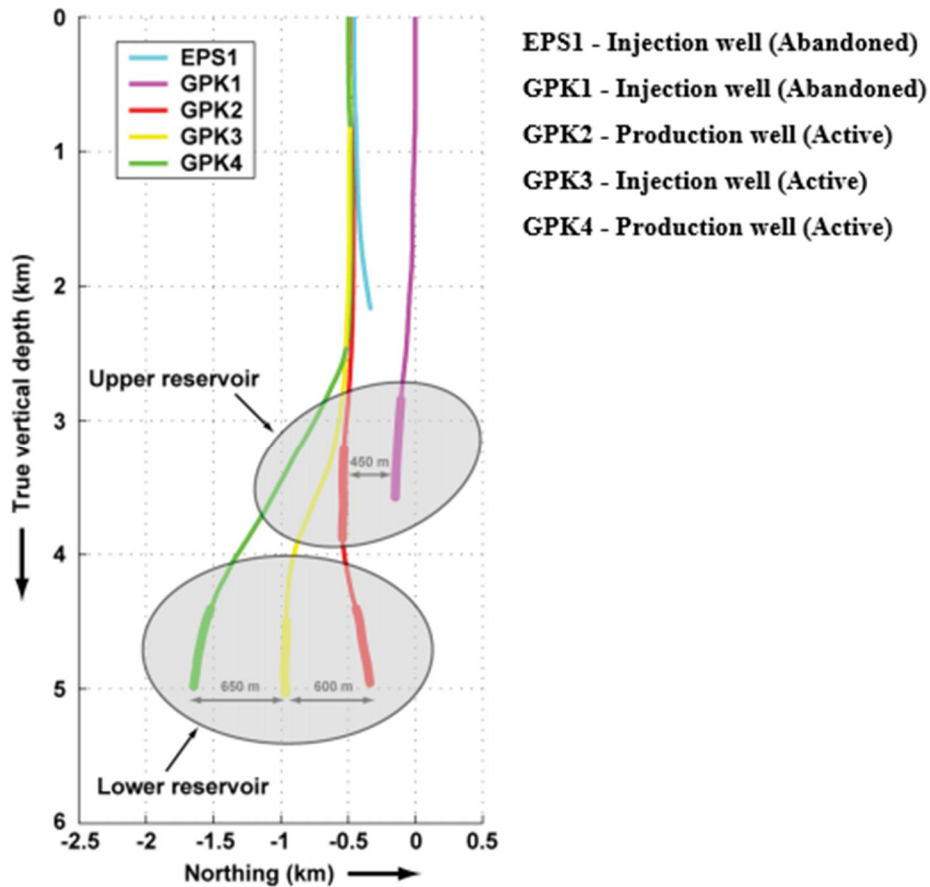


Figure 4.12: The Soutz site showing the location of the upper and lower reservoirs, and the wellbores (Genter et al., 2010a).

A steady-state simulation is conducted on the Soutz lower geothermal reservoir to validate the proposed model in predicting the temperature profile variation with depth. The measured temperature profile at Soutz wellbores is reported in the works of literature (Genter et al., 1997; Spichak et al., 2015). The simulated temperature profile predicted for the lower reservoir is between the depths of 3.5 km to 5.4 km instead of its actual locations of 4 km to 5.2 km; this is because the exact dimension may not produce a smooth transition of the temperature profile for the upper and lower reservoirs.

Table 4.7 shows the various geological formations present at the reservoir with their specific depths and densities. Also, Table 4.8 presents the petrophysical properties of the reservoir's components. Thus, the data provided in Tables 4.7 and 4.8 was employed in the validation studies of the FE model against the experimental measurement of the Soultz borehole. In this study, boundary conditions were applied from the ground surface of the reservoir (i.e., not at the injection wellbore). For the hydraulic case, the boundary condition was assumed to be hydrostatic (i.e., $P = \rho g z$), and in the case of the thermal boundary condition, a value of 12°C was assumed for the surface temperature.

Table 4.7: Geological properties and densities of the Soultz reservoir system (Guillou-Frottier et al., 2013; Magenet et al., 2014)

Formation	Depth (km)	Density (kg/m³)
Tertiary	0 - 0.75	2350
Jurassic	0 - 0.75	2550
Keuper	0.75 - 0.85	2700
Muschelkalk	0.85 - 1.0	2700
Buntsandstein	1.0 - 1.4	2500
Basement	1.4 - 5.5	2600

Table 4.8: The petro-physical properties of main lithological formations (Guillou-Frottier et al., 2013; Magenet et al., 2014)

Depth (km)	Permeability (m²)	Porosity (%)	Thermal Conductivity (W/m/K)
0 - 0.8	10 ⁻¹⁷	15	1.4
0.8 - 1.0	10 ⁻¹⁶	15	2.1
1.0 - 1.4	5×10 ⁻¹⁵ - 10 ⁻¹⁴	15	2.5
1.4 - 3.7	3×10 ⁻¹⁵	9	3.0
3.7 - 5.0	10 ⁻¹⁸	1	3.0
Faults	10 ⁻¹⁷ - 3×10 ⁻¹⁴	15	2.5

The simulation results are compared to the measured data obtained at well GPK2 for the Soultz geothermal system. Figure 4.13 shows the experimental measurement and

simulated temperature profiles. As seen, the simulation profile shows a typical trend pattern with increasing magnitude with depth as the measured profile; nevertheless, slight disparities are observed at some points. However, the current FE model overall agrees reasonably with the experimental measurements.

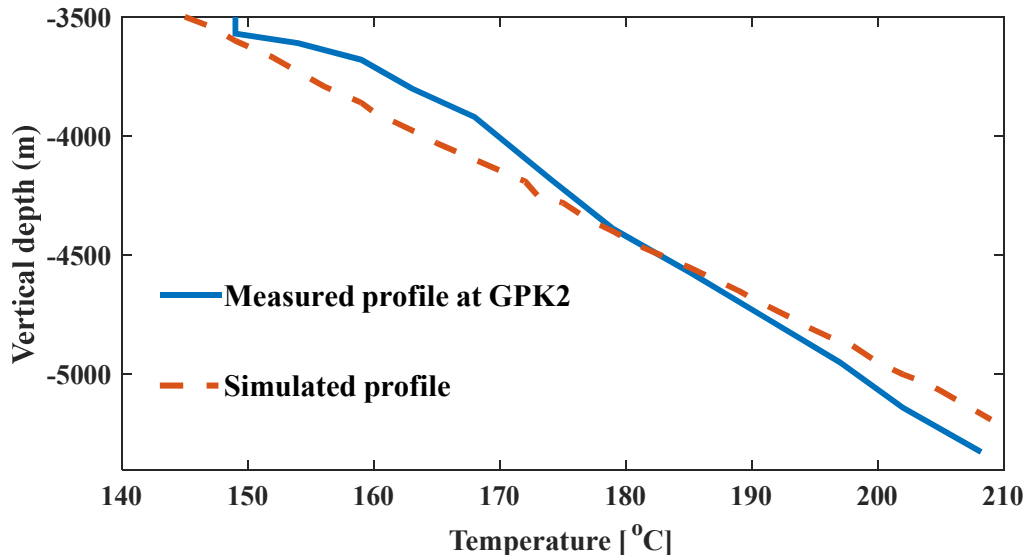


Figure 4.13: Temperature profile at GPK2 wellbore (Measured vs Simulated)

Table 4.9: Percentage difference between measured and simulated temperature profiles at wellbore GPK2

Vertical depth (m)	Measured temperature (°C)	Simulated temperature (°C)	Percentage difference (%)
-3570	149	147	1.35
-3730	159	154	3.19
-4030	168	165	1.80
-4400	179	179	0.00
-4760	191	193	1.04
-5140	202	207	2.44

Table 4.9 shows the percentage difference between the simulated and measured temperature profiles at wellbore GPK2. As can be seen, from the depths observed, the maximum deviation is 3.19%, and the minimum difference is 0%. These differences in the

temperature profiles could be attributed to the following reasons: (1) Both heat and fluid flow are modelled at a steady state; therefore, energy loss due to the acceleration of fluid is not accounted for. (2) Non-uniform fluid properties and geological formations having different thermal properties may influence the deviations between the results. (3) Other possible effects such as chemical and mechanical interactions presented during the measurements are not captured in the simulations. It is also worth noting that only measured values of the porosity, density, and permeability from the sample cores obtained are employed as inputs to this model. Thus, the uncertainties involved in getting the actual material measurements concerning the real-life dimensions of the overall porous media are also an apparent reason for the mismatch.

4.4.2 Validation of Fenton Hill HDR field experiment

This validation study has considered the first experimental HDR geothermal reservoir in the US, at Fenton Hill, Phase I. The reservoir was first evaluated with 75 days of closed-loop operation to test its performance, which was carried out from January 28 to April 13, 1978 (Murphy et al., 1981). The HDR system model has injection and production wellbores located at a depth of 2750 m and 2630 m, respectively, below the ground level. Both wellbores are connected to a single planar fracture as shown in Figure 4.14 (Murphy et al., 1981). The fracture has a diameter of 120 m with an injection wellbore located 25 m from its bottom, and the production wellbore, at the other end, is connected to the planar fracture 15 m from its top (Bahrami et al., 2015).

Table 4.10 shows some of the properties of the HDR system (Elsworth et al., 2016). The fluid properties are assumed to vary throughout the operations. Besides, during the 75-day experimental testing of the reservoir, the injection pressure ranged from 8.8 to 5.9 MPa, whereas the production pressure was maintained at approximately 1.1 MPa to avoid flushing (Murphy, 1979). The area's geothermal gradient is 100°C/km until about a depth of 2300 m when it decreases to 55°C. As a result, the rock temperature measured 185°C at a depth of 2750 m (Elsworth et al., 2016). In the case of the injection temperature, it was assumed to be constant at 25°C at the surface (Murphy, 1979). However, at a depth of 2750 m it is elevated, due to heat exchange with the well driven into the hot rock (Elsworth et al., 2016).

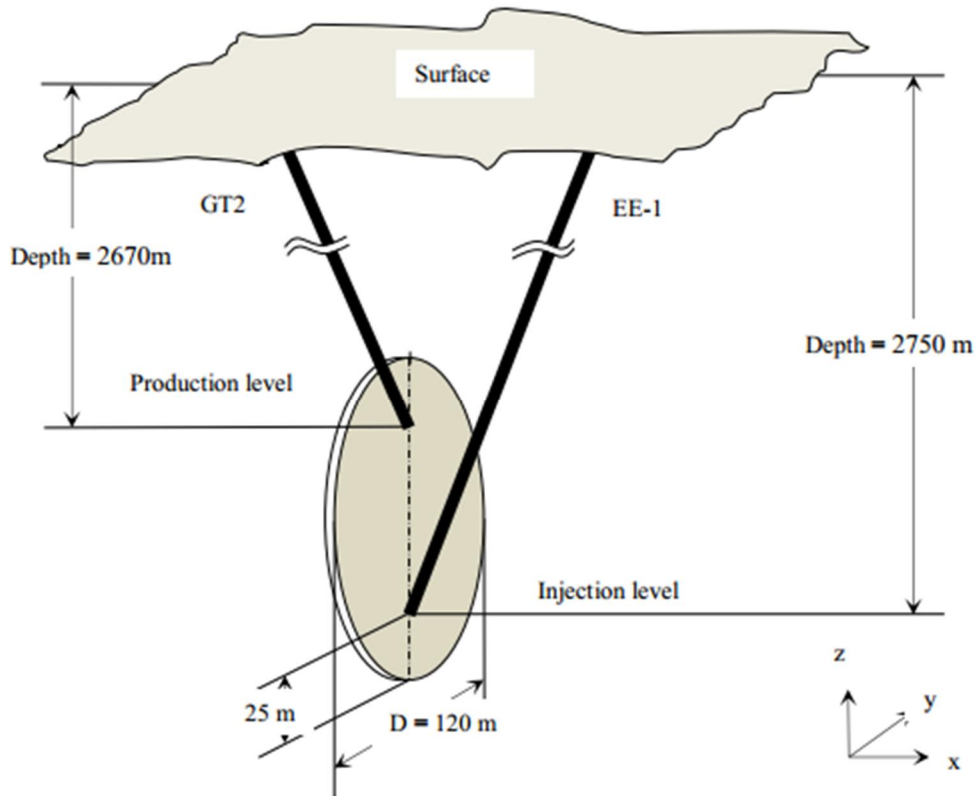


Figure 4.14: Simplified reservoir geometry of Fenton Hill, HDR system, Phase I (Murphy et al., 1981)

Table 4.10: Rock properties for Fenton Hill, HDR system (Elsworth et al., 2016)

Parameters	Symbol	Value	Unit
Thermal conductivity	λ	2.9	W/m/K
Heat capacity	$C_{P,S}$	990	J/kg/K
Diffusivity	D	1e-6	m ² /s
Injection rate	Inj_rate	7.5	kg/s
Geothermal gradient	α	55	°C
Fracture radius	r_f	60	m
Density	ρ_s	2700	kg/m ³
Elastic modulus	E	25	GPa

The availability of the primary reservoir data of the Fenton Hill experiment makes it possible to compare the current FE model prediction capability and results from a 75-day

circulation test conducted at the field. Figure 4.15 presents the temperature variation at the production wellbore with time for the experimental measurement and numerical simulation results. As can be seen, the correspondence is positive given the sensitivity of the physical parameters employed in the comparison and the time limit of the test duration. The FE model over-predicted the production temperature of the experimental results in the first 14 days and under-predicted the outcome from 16 days until the last simulation time (i.e. 75 days). The reason for the over-prediction can be attributed to the assumption of constant fracture aperture, which is not likely to be the case in field operation because as the fluid is injected under high pressure, the fracture aperture propagates and opens up. Nonetheless, the FE solution for the breakthrough temperature has a very similar trend, with the experimental measurement with slight disparities due to the experimental conditions.

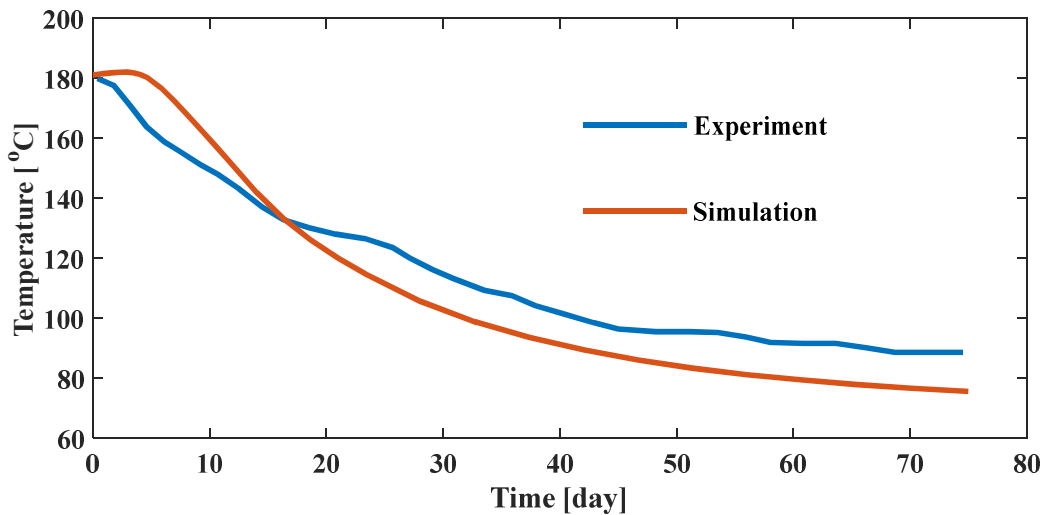


Figure 4.15: Production temperature of measured vs simulated at well GT-2B

A reasonably good agreement between the FE model and the measured temperature drawdown suggests that the heat transfer area was accurately simulated, despite the fact that the induced thermal stresses and aperture changes concerning the effective stress were not captured in the current model. However, it is important to note that the current FE model is limited to two physics (i.e. thermo-hydraulic) only and therefore other effects of mechanical and chemical features are ignored in the modelling. Thus, this reason may also affect the outcome of the numerical simulation results.

Furthermore, the geometrical representation of the HDR system perceived from the experiment cannot be considered unique because the actual fracture system need not be circular or elliptical and, in fact, multiple fractures may be possible in the system (Tester, 1979). Also, downhole measurements are challenging to perform, and they are highly localised, restricted to either the wellbore itself or a small radius of examination around the wellbore. Exact physical reservoir representations are challenging to achieve, and this could lead to the idealisation of the problem as a single circular fracture as in this case (Murphy, 1979).

4.5 Summary

This chapter presents a simple but meaningful verification and validation studies to establish the practicability and accuracy of the FE model developed in Chapter 3. Several cases were presented, first the more straightforward, and then the more complex practical problems applicable to HDR systems. The results obtained from the studies were encouraging and had built the expected confidence required to resolve real-life deep geothermal problems. Therefore, the chapter serves as a solid foundation for the remaining chapters of this thesis.

Chapter five – Numerical modelling of field case study for the Soultz geothermal reservoir

5.1 Introduction

This chapter aims to investigate the impact of thermo-hydraulic coupled processes on the Soultz geothermal system. The geothermal site has provided in-depth knowledge for several projects around the globe because of the achievement of energy production within a short period using novel techniques. A numerical model of the lower reservoir of the Soultz site is developed based on the available field data. Issues associated with meshing arising from different dimensional properties existing in the formation because of the reservoir's heterogeneity are addressed. A long-term simulation of 60 years is implemented in the model to determine the prediction performance of the numerical model and the system production behaviour during long-term operation. After testing the prediction capability of the solver, sensitivity analyses were performed using factorial design to evaluate which of the parameters affect the reservoir performance during exploitation.

5.2 Overview of the Soultz geothermal reservoir

Several experimental studies were conducted in European countries, including the United Kingdom, Germany and France, to develop a geothermal power plant after the successful implementation of the Fenton Hill geothermal project in the United States. Nevertheless, the high cost of large-scale experiments has led to the European countries reaching an agreement to pool both workforce and financial resources into a single project to develop a commercial plant within Europe (Charl  ty et al., 2007). The three most famous projects in the Europe then were the Rosemanowes (UK), Soultz (France), and Bad Urach (Germany). After rigorous assessments and coordinations by the European Commission for the selection of the most suitable site from the three, a decision was reached to locate the project at Soultz (Genter et al., 2009). The site was precisely chosen due to the high thermal gradient released at an existing oil field within the vicinity.

The European Commission with the help of other relevant energy institutions within Europe (France, Germany and the United Kingdom) initially funded the project (Charl  ty et

al., 2007; Genter et al., 2009; Held et al., 2014). The Soultz project was developed in three major stages: the preliminary stage (1984–1987), the drilling and exploration stage (1987–2007), and the power plant construction stage (2007–2008) (Genter et al., 2010b).

5.2.1 Physical and petrophysical settings of the reservoir

The Soultz geothermal site is located in north-eastern France, within the vicinity of the Upper Rhine Graben with an extensional tectonic regime (Dezayes et al., 2004). Figure 5.1 presents the site terrain and its geological characteristics. Figure 5.2 shows the vertical profile of the geological formation from the surface to about 5.4 km deep approximately (Ch. Dezayes et al., 2005). In addition, Figure 5.2 presents the wellbores drilled and their respective penetration depths.

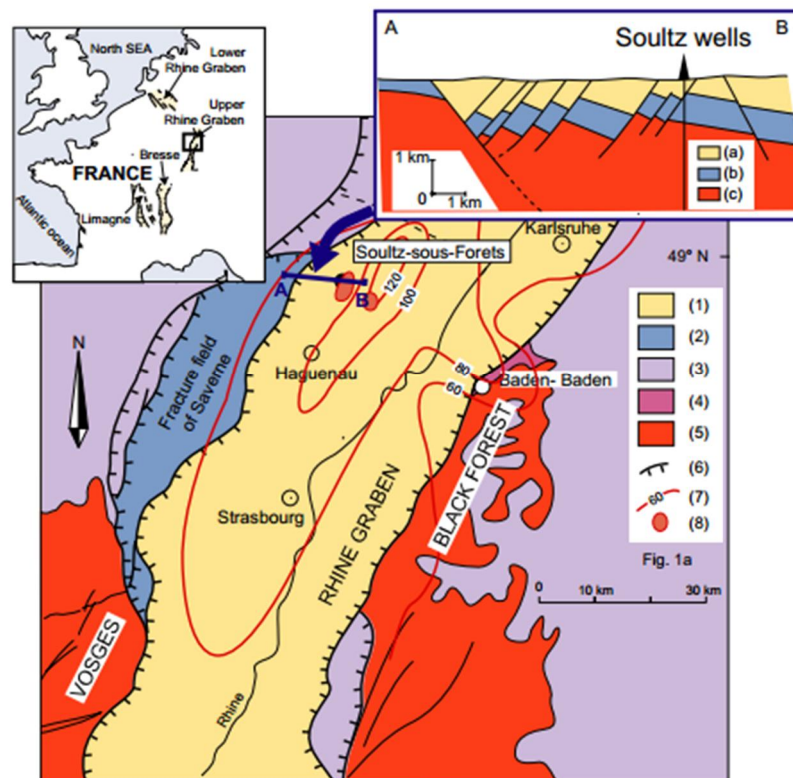


Figure 5.1: “The Soultz location and geology of the terrain; (1) Cenozoic sediments, (2) Cenozoic volcanism, (3) Jurassic, (4) Trias, (5) Hercynian basement, (6) Border faults, (7) Temperature distribution in °C at 1500m depth, and (8) Local thermal anomalies.

Simplified cross-section through the Soultz site: (a) Cenozoic filling sediments (b) Mesozoic sediments (c) Granite basement” (Dezayes et al., 2004)

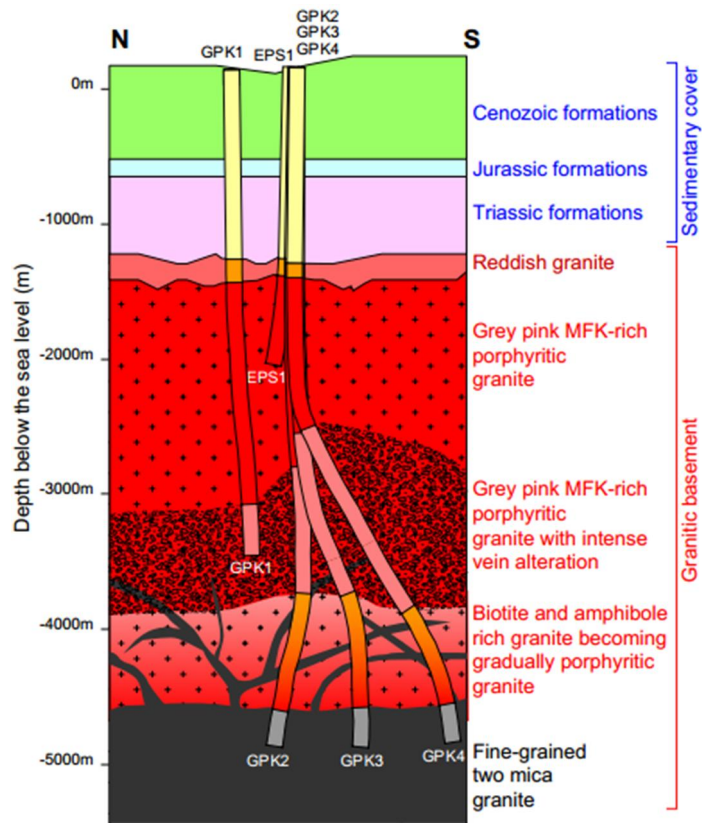


Figure 5.2: 2-D geological profile of the Soultz geothermal formation (Dezayes et al., 2004)

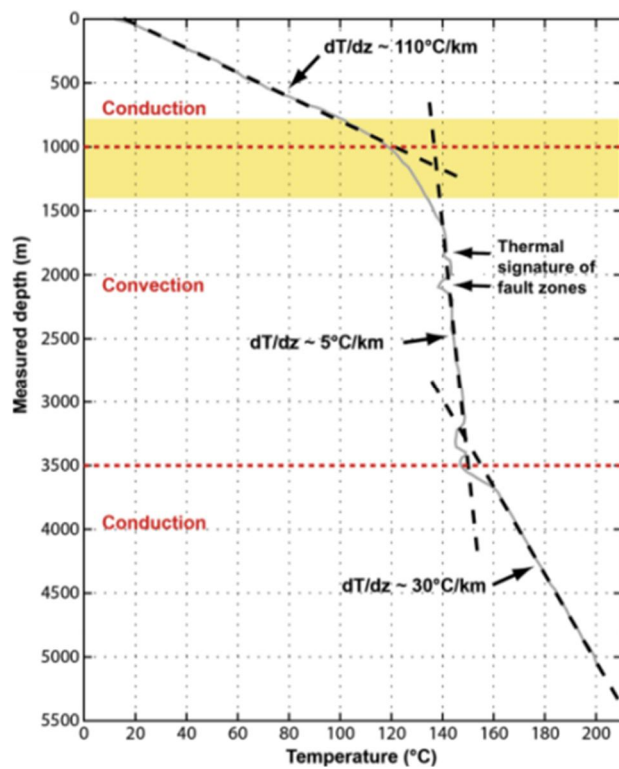


Figure 5.3: Temperature profile and geothermal gradient of GPK2 (Vidal et al., 2015)

Figure 5.3 presents the thermal regime of the Soultz formation, which is characterised by a series of geothermal gradient anomalies that changes from convection to conduction states, respectively. The uppermost part of the formation attributed a thermal gradient of approximately $100^{\circ}\text{C}/\text{km}$, which occurs as a result of the hydrothermal convective cells circulating inside a nearly vertical fracture network and large-scale faults cross-cutting the sedimentary cover (Vidal et al., 2015). In the intermediary section, the geothermal gradient was $5^{\circ}\text{C}/\text{km}$ due to the dominance of the advective heat transport within the section, while the lower part of the formation had a thermal gradient of $30^{\circ}\text{C}/\text{km}$ (Genter et al., 2010c).

5.3 Numerical modelling of the lower reservoir

This section aims to develop a numerical model of the lower reservoir, which happens to be at the second stage of the project as mentioned in section 5.2. Figure 5.4 shows the schematic representation of the Soultz geothermal system (Genter et al., 2010a). As seen, the wellbores were drilled from the same platform on the surface, with a lateral distance of 6 m between each wellbore. The lateral distance between the wellbore keeps increasing with depth because of the projection drilling. As a result, the distance between the two production wellbores and the injection wellbore reaches up to approximately 600 m at the lower reservoir (C Dezayes et al., 2005). Furthermore, the wellbores were fully cased from the surface down to the level of the lower reservoir (4.5 km); from that level onwards, the wellbores remain in an uncased (i.e. open hole) section of about 500 m length, which is same as the assumed reservoir size. The measured diameter of the wellbores was 215.9 mm approximately for each of the three (Genter et al., 2010d). Concerning fractures, they were of three categories within the lower reservoir, which ranges from active to non-active (Dezayes et al., 2010; Sausse et al., 2010), but in this study, only one active fracture is considered.

Figure 5.4 presents a typical representation of the geothermal system, showing the different structures existing in the media. However, Figure 5.4 does not represent the real-life representation of this system; it just provides a simple demonstration of how to perceive the physical meaning of the system. It is also explicit from the sketch that only a single fracture system is represented as a plane surface, and this representation may likely affect

the outcome of the results obtained from simulation by either overpredicting or underpredicting.

5.3.1 Geometrical and physical properties of the reservoir

A conceptual model of the lower reservoir has been developed to simplify the computations, as shown in Figure 5.5. It is essential to understand the changes of the features associated with reservoir parameters such as temperature and pressure as a result of extraction processes, not only within the fracture but also between the rock matrix and the fracture, concurrently.

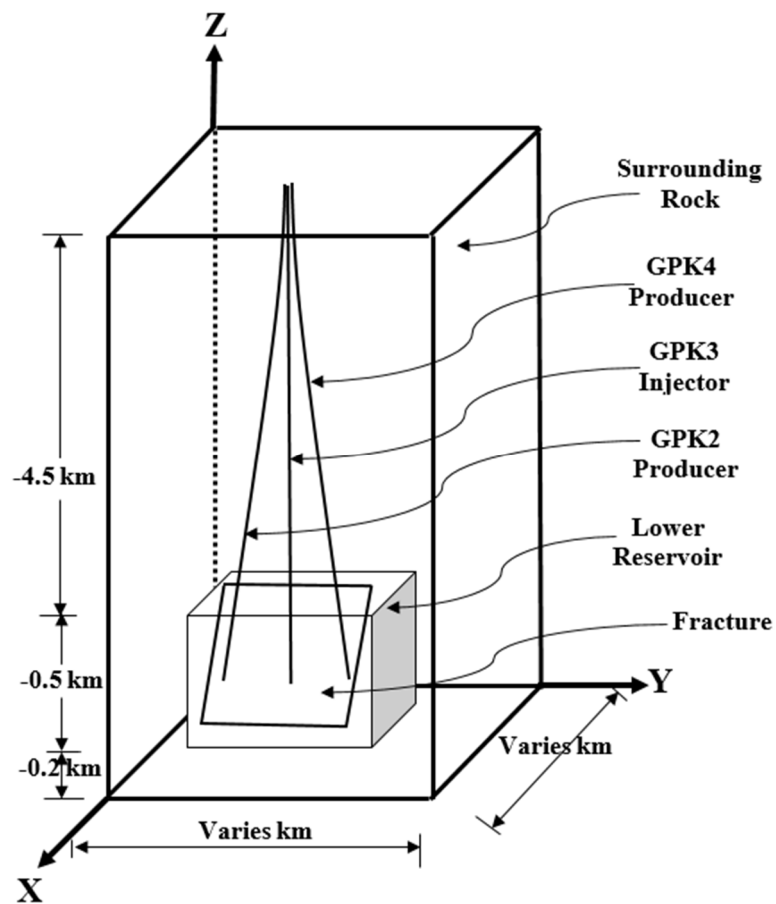


Figure 5.4: Schematic representation of the Soutlz geothermal system

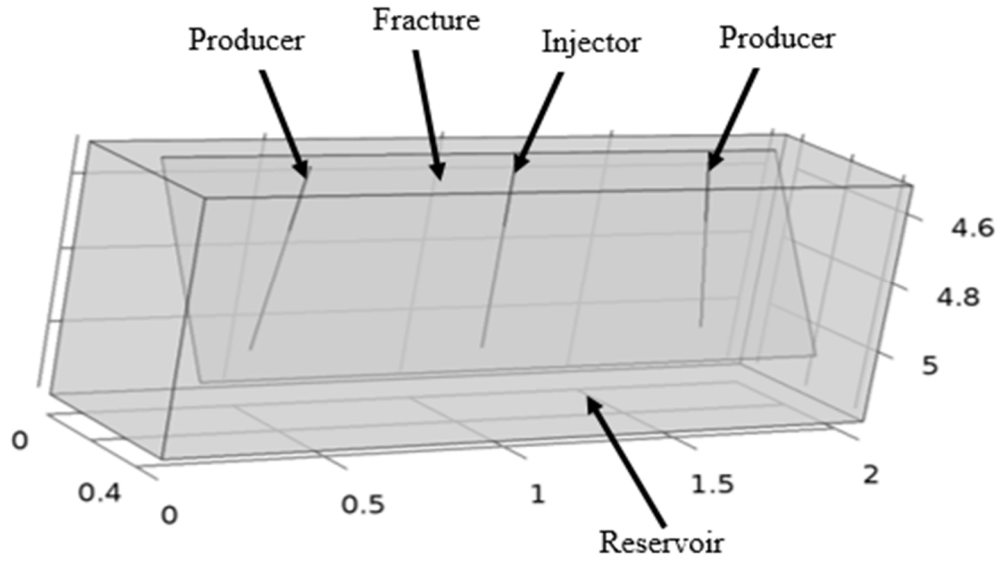


Figure 5.5: Lower reservoir geometry (km)

In this study, the fracture is located at a depth of 4770 m, with coordinates 150–1800 m in x-direction, 250 m in y-direction, 4500–5100 m in z-direction, and an inclination angle of 60° . The injection wellbore GPK3, in the lower reservoir, is at coordinates 1000 m in x-axis, 250 m in y-axis, 4500–5100 m in z-axis. The coordinates of the first and second production wellbores GPK2 and GPK4 were 1500 m in x-direction, 250 m in y-direction, 4500–5100 m in z-direction, and 500 m in x-axis, 250 m in y-axis, 4500–5100 m in z-axis, with inclination angles of 10° and -10° , respectively.

For the petrophysical rock properties such as thermal conductivity, density, porosity, permeability and heat capacity were taken from literature and previous hypotheses (Guillou-Frottier et al., 2013; Magnenet et al., 2014), and are provided in Table 5.1.

Table 5.1: Physical properties attributed to lower reservoir (less permeable granitic basement) (Guillou-Frottier et al., 2013; Magnenet et al., 2014)

Parameter	Value	Symbol
Matrix		
Porosity (%)	1.0	ϕ
Permeability (m ²)	1e-20	κ
Thermal conductivity (W/m/K)	3.0	λ_s
Heat capacity (J/kg/K)	850	$C_{\rho,s}$
Density (kg/m ³)	2600	ρ_s
Fracture		
Porosity (%)	0.1	ϕ_f
Permeability (m ²)	1e-16	κ_f
Thermal conductivity (W/m/K)	2.5	λ_f
Heat capacity (J/kg/K)	750	$C_{\rho,f}$
Density (kg/m ³)	2000	ρ_f

5.3.2 Initial and boundary conditions

Section 5.2 provided the geothermal gradient of the system; however, to achieve the required bottom-hole temperature of 200°C at the lower reservoir, a gradient of 38°C/km was adopted for the investigations. The initial temperature is given as

$$T_0(z) = 12^\circ\text{C} - 38^\circ\text{C}/\text{km} \times (-z) \quad (5.1)$$

where $T_0(z)$ is the initial temperature of the reservoir, 12°C is the assumed value of the surface temperature, 38°C/km is the geothermal gradient, and z is depth in kilometres. The initial pressure is assumed to be hydrostatic throughout the reservoir.

For the boundary conditions, an injection temperature of 30°C is employed for the thermal case, while for the hydraulic case, an injection pressure of 10 MPa is used. The

production pressures were assumed to be under pressure with -10 MPa for both wellbores. As for the remaining boundaries, they remain insulated throughout the simulations.

5.3.3 Meshing and solutions

A well-defined meshing technique is required to obtain a reliable FE solution. In particular, in deep reservoir modelling, several structures are considered with highly varying scales. For example, in the interaction between reservoir wellbores and rock matrix, the former is in millimetres, whereas the latter is in thousand metres or kilometres. Thus, meshing structures of this kind necessitate a special approach. In this study, isoparametric elements are chosen for meshing the various reservoir components. A four-node tetrahedral element is adopted for the discretisation of the matrix, a three-node triangular element for the fractures, and a two-node line element for the wellbores. Extremely fine, extra-fine and finer grids are employed to scatter computation vicinity. The major complexity of this meshing approach lies in maintaining the internal geometric uniformity between wellbore, fracture and matrix elements.

In Figure 5.6, finer meshes of moderate element size scatter the matrix domain and its boundaries far away from the fracture and the wellbores, whereas extra-fine grids were created within the fracture and the neighbouring matrix attached to it. For the wellbores, extremely fine grids are employed by regulating the element growth rate between the wellbores, fracture, and the rock matrix, as shown in Figure 5.6. Figure 5.6 also presents the element size distribution of the reservoir model. As can be seen in the figure, the minimum element size is 0.14 m, and the maximum size is 84.6 m. The distribution depends on a structural dimension; for example, the wellbore has the slender dimension and the elements within its region were smaller in size in comparison to the fracture and matrix elements. The mesh generated results in 966,213 tetrahedrons, 41,904 triangulars, 3272 edges and 58 vertex elements. The mesh division approach improves the calculation precision and also eliminates the deviation rate induced by unsuitable selected boundary conditions.

The simulation was run for 60 years, and because of the long simulation time and the stability provided by the constant temperature and pressure conditions, a backward difference formula (BDF) was employed in the numerical simulator. The scheme holds the

advantage of limiting time steps. In the present study, it took only 47 time steps to simulate the 60-year experimentation. The physical memory used for the simulation is 3750 MB, and the virtual memory is 3980 MB.

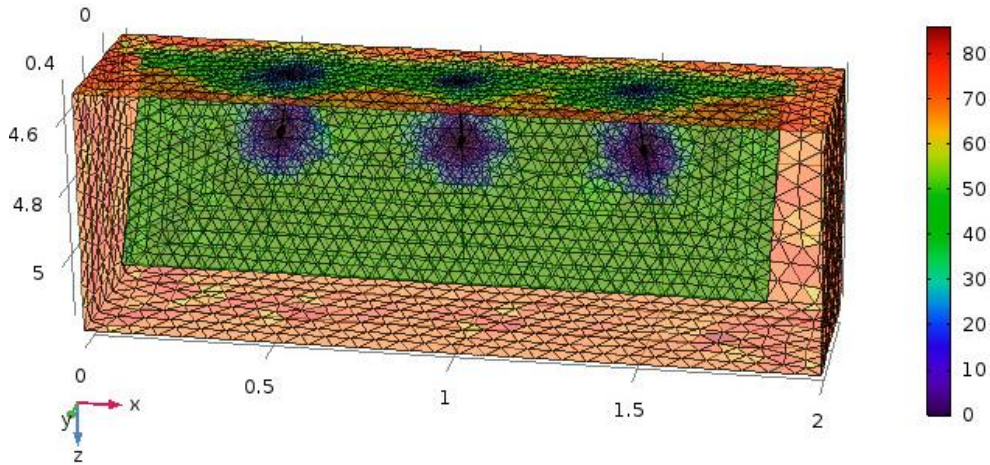


Figure 5.6: Lower reservoir mesh element sizes and distributions (m)

5.4 Results and discussions

This study seeks to identify some response parameters that govern the behaviour of geothermal reservoirs subjected to different operational conditions, as well as to assess their long-term performance. The proposed methodology consists of using a 3-D model of the Soultz lower geothermal reservoir to demonstrate the result of interactions between several independent parameters in geothermal energy exploitations by employing a complete factorial experimental design. Collins et al., (2014), provide a detailed explanation of factorial experimental design as it is beyond the scope of this research work.

For the human-controlled parameters, the injection pressure selection depends on the value of measured minimum principal stress to create hydraulic fractures. In this study, the choice of maximum and minimum injection pressure (10 MPa–25 MPa) is based on the Soultz and Fenton Hill projects, respectively. Similarly, for injection temperature, the values gathered for most reservoirs lie between 30°C and 60°C. Also, different value ranges are prescribed for the injection flow rate (10 l/s–70 l/s), and lateral well spacing (300 m–600 m).

Table 5.2 presents the human-controlled parameters chosen for the studies, for each of the parameters the values ranges from minimum to maximum. As a result, two values were assigned to each individual parameter and all the possible combinations of other parameters in the same group were evaluated. The number of runs required for each group is 2^n ; this identifies the number of parameters (n), how many levels each parameter has (2), and how many experimental conditions there are in the design (2^n). Each independent parameter is a factor in the design because there are four parameters and each parameter has two levels of factorial design in each group. Thus, these studies will have $2^n = 16$ different experimental conditions for each of the human-controlled parameters, as presented in Table 5.3.

Table 5.2: Range of values for the human-controlled parameters used in the reservoir model

Parameter	Minimum Value (-)	Maximum Value (+)
Injection rate (l/s)	10	70
Lateral well spacing (m)	300	600
Injection temperature (°C)	30	60
Injection pressure (MPa)	10	25

It is worth mentioning that the temperature in the production wellbores GPK2 and GPK4 were found to be identical in all cases. Thus, for purposes of clarity, only the simulation results obtained in production wellbore GPK2 are presented here.

5.4.1 The effect of human-controlled parameters on production temperature

A complete factorial experimental design is used in implementing the possible combinations required, and for this case, it results in 16 different operational scenarios as shown in Table 5.3. The studies involve understanding the effect of various interactions of these parameters on reservoir productivity.

Figure 5.7 shows the production temperature history at wellhead GPK2, during the long-term simulation of 60 years for the Soultz lower reservoir, under the influence of

multiple parameter interactions for the human-controlled parameters. Four interaction scenarios are considered by varying the injection temperatures and pressures while keeping the injection rate (10 l/s) and lateral well spacing (300 m) at a constant rate. As can be seen, lower injection temperature, when interacting with lower injection pressure, yields maximum production temperatures at the wellhead. The reason for this is that the propagation of cold water is much slower under moderate pressure than under a higher one, as in the case of a 30°C injection temperature with 10 MPa injection pressure. On the other hand, a higher injection pressure with a higher injection temperature results in faster reservoir cooling and yields rapid decline in the production temperature, as seen in the scenario involving a 25 MPa injection pressure with a 60°C injection temperature.

Table 5.3: Human-controlled parameter combinations

Run number	Lateral well spacing (m)	Injection rate (l/s)	Injection temperature (°C)	Injection pressure (MPa)
1	300	10	30	10
2	300	10	30	25
3	300	10	60	10
4	300	10	60	25
5	300	70	30	10
6	300	70	30	25
7	300	70	60	10
8	600	70	60	25
9	600	10	30	10
10	600	10	30	25
11	600	10	60	10
12	600	10	60	25
13	600	70	30	10
14	600	70	30	25
15	600	70	60	10
16	600	70	60	25

Similarly, further simulation investigations are carried out by changing only the injection rate from 10 l/s to 70 l/s under similar lateral well spacing of 300 m, by varying the injection temperatures and pressures as in the previous scenarios. The outcome yields exact results as in Figure 5.7, which means that the injection rate has no significance to the simulation results; this is likely due to the impact of the injection pressure applied to the reservoir.

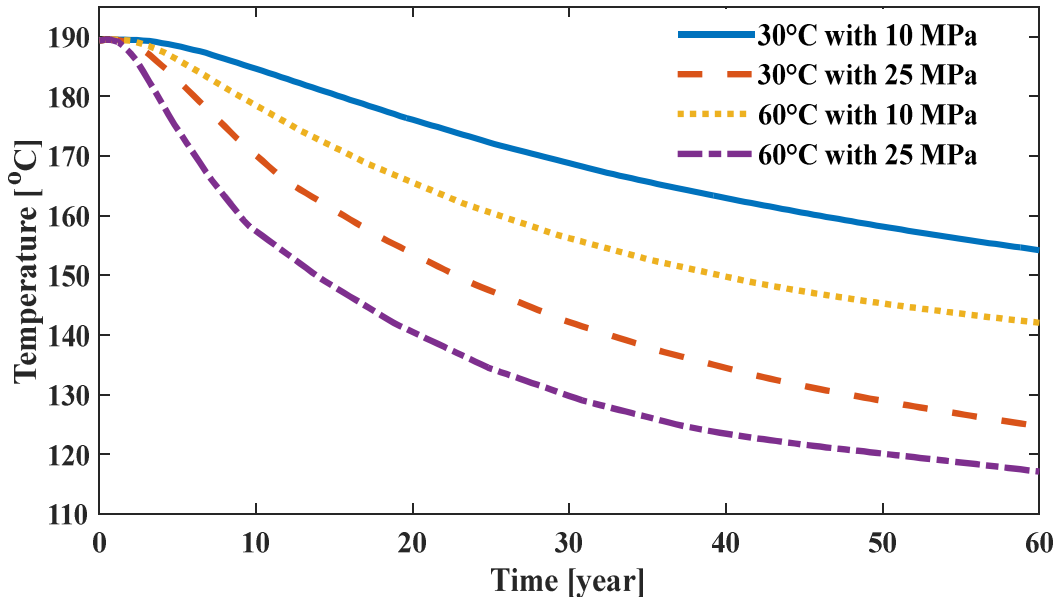


Figure 5.7: Production temperature at wellhead GPK2 with constant injection rate 10 l/s and 300 m lateral well spacing under the influence of various injection temperatures and pressures

Figure 5.8 presents the temperature profile at the production wellhead GPK2 for human-controlled parameters case two. In this case, the parameters that are kept constant are the lateral well spacing (600 m) and the injection rate (10 l/s) while the injection temperatures and pressures are varied throughout the simulations. The influence of parameter interaction is observed to be similar to the previous case, but the production temperature drawdown is more realistic in comparison to the previous case as shown in Figure 5.8. In the scenario, 30°C injection temperature with 10 MPa injection pressure, the production wellhead temperature decline is less than 1% as seen in Figure 5.8. On the other hand, when both the injection temperature and pressure are increased to 60°C and 25 MPa, respectively, a rapid decline is experienced. The decline starts just before the simulation reaches ten years, and from then onward, a constant decline rate is experienced up to the end of the simulation.

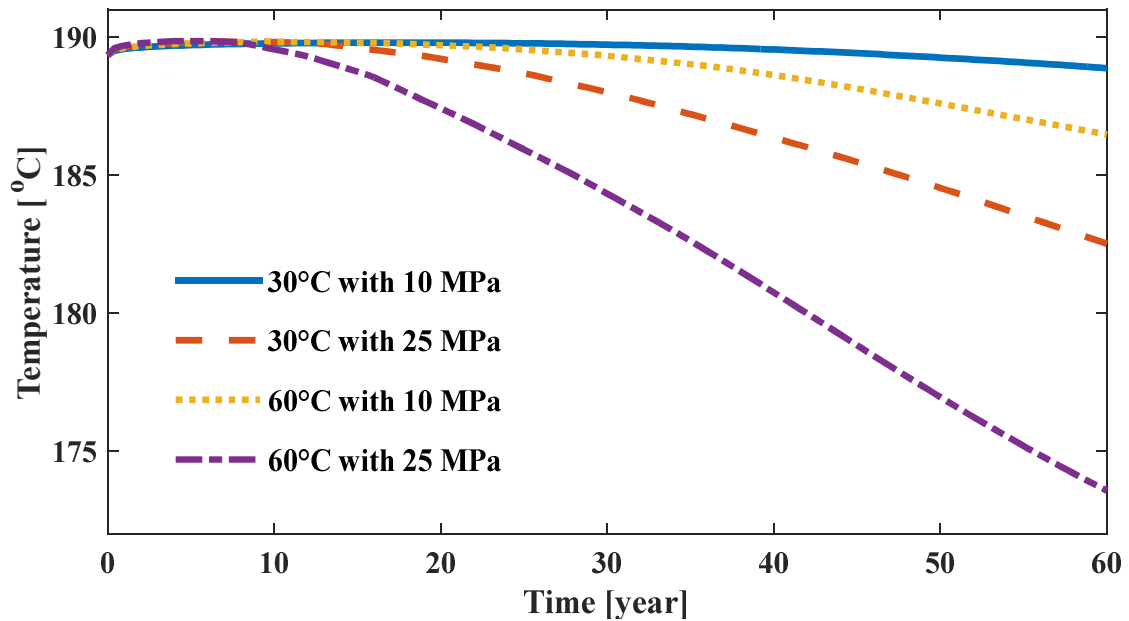


Figure 5.8: Production temperature at wellhead GPK2 with constant injection rate 10 l/s and 600 m lateral well spacing under the influence of various injection temperatures and pressures

Likewise, additional experimental simulations are conducted by changing the injection rate to 70 l/s while all other parameters remain the same, and the results were found to be exactly as in the previous case.

5.5.2 Parameter influence on reservoir cooling

In order to investigate which of the human-controlled parameters is the most influential in cooling the reservoir, different scenarios are run with varying injection pressure rates and fluid injection temperature rates under a constant lateral well distance of 600 m, as shown in Figures 5.9–5.12. As can be seen, the lower the pressure, the less the effect of cooling, whereas with higher injection pressure rates, the greater the cooling. The low-temperature fluid from the injection wellbore flows into the extraction wellbore via the fracture; the fluid temperature rises through convection and conduction from the high-temperature matrix, resulting in superheated fluid in the extraction wellbore. The significant temperature variation between the injected fluid temperature (low-temperature) and the matrix temperature (high-temperature) rapidly decreases the matrix temperature surrounding the injection wellbore. Thus, a relatively low-temperature area is formed during the initial

operation, as seen in Figures 5.9–5.12. The reservoir temperature gradually decreases as the exploitation continues, while the low-temperature area gradually expands.

It is observed in Figures 5.9–5.10 and 5.11–5.12 that higher injection pressure causes rapid cooling of the reservoir. This is because the increase of injection pressure transmits the injected fluid faster due to more openings in the reservoir and the injected fluid is at relatively low temperature. Thus, the temperature differences between the reservoir and the injected fluid will decrease with time due to cooling of the reservoir. The cold-water front will propagate in the reservoir, and it gradually penetrates the production wellbore and causes the decline in the production temperature with time. In the case of flow rate, the injection flow rate is inversely proportional to the injection pressure as proven experimentally at the Tianjin geothermal field in China (Kun, 2005). In general, as the injection pressure increases, the injection flow rate decreases and vice versa.

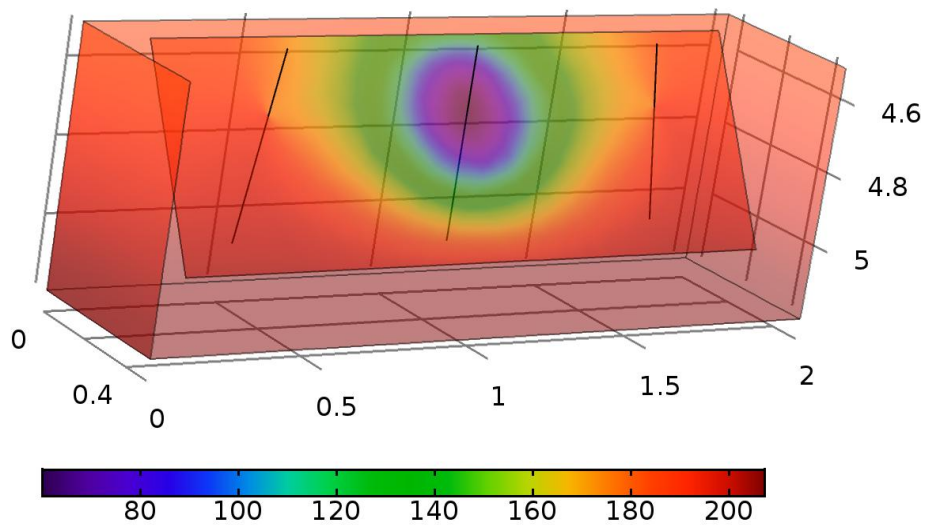


Figure 5.9: Reservoir cooling ($^{\circ}\text{C}$) under the effect of 60°C fluid injection temperature with 25 MPa injection pressure

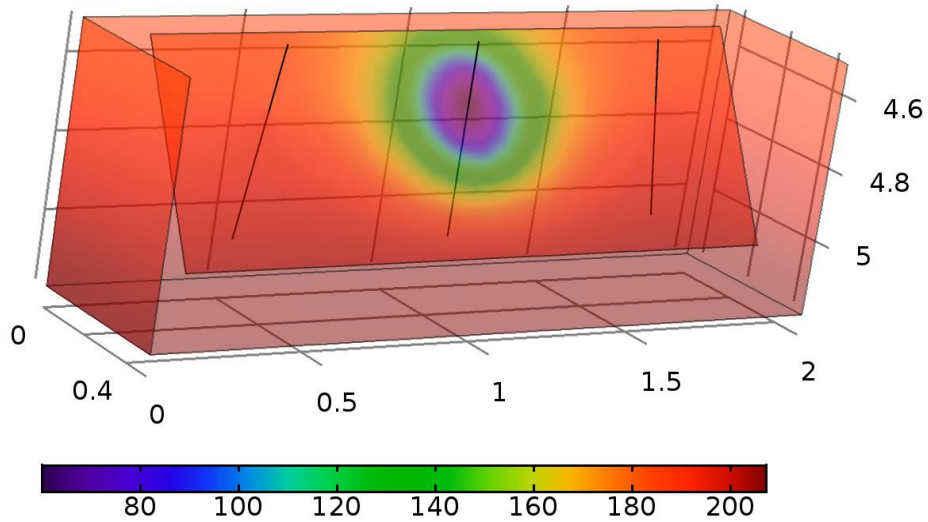


Figure 5.10: Reservoir cooling (°C) under the effect of 60°C fluid injection temperature with 10 MPa injection pressure

Therefore, it can be concluded that the most influencing parameter concerning the cooling of the reservoir is the injection pressure. To summarise the results of the above cases, the higher the temperature of the fluid at the injection wellbore when it interacts with any sufficient injection pressure of up to 10 MPa under a large wellbore spacing, the lesser the temperature decline at the production wellhead, and vice versa.

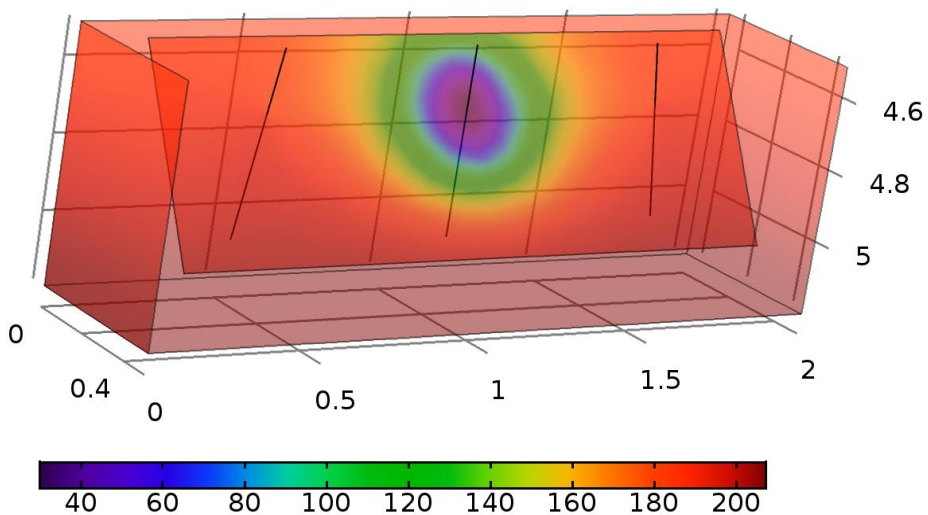


Figure 5.11: Reservoir cooling (°C) under the effect of 30°C fluid injection temperature with 25 MPa injection pressure

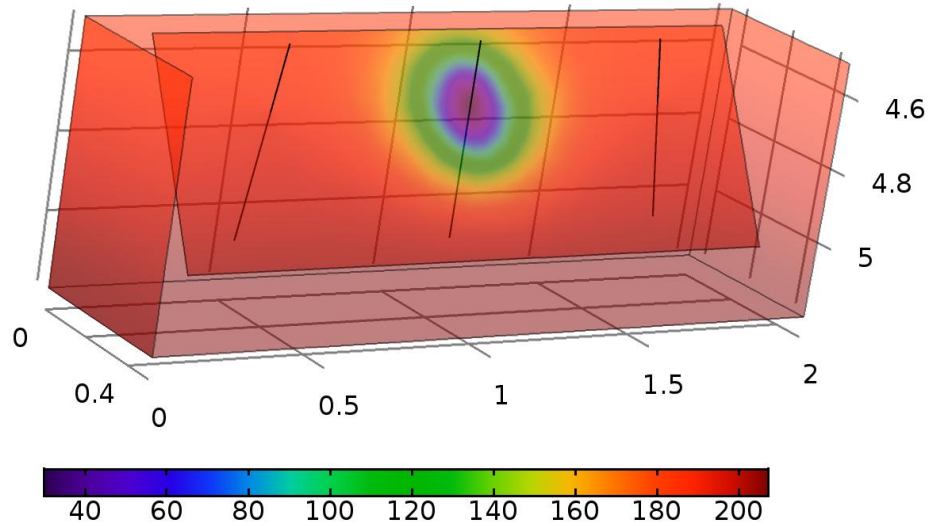


Figure 5.12: Reservoir cooling ($^{\circ}\text{C}$) under the effect of 30°C fluid injection temperature with 10 MPa injection pressure

5.5 Findings and limitations

The sensitivity analysis performed showed that reservoir parameters could be a significant asset to reservoir engineers/managers during planning, exploration, and exploitation stages. The parameters analysed were referred to as human-controlled parameters, which include fluid injection temperature, injection pressure rate, injection rate and lateral wellbore spacing.

Based on the results obtained in this investigation, the parameters that influence reservoir productivity in order of effect were: the injection pressure, the injection temperature, and lateral wellbore spacing. Therefore, injection pressure should not be too high nor too low, but instead should be moderate; whereas, in the case of injection temperature, is critical to be lower, which is very unlikely in a closed-loop operation. In the case of the lateral wellbore spacing, productivity is better if the spacing is more extensive, though sometimes it may result in leakages in the reservoir. Thus, efficient management of the human-controlled parameters could yield to optimum production rate.

Moreover, the study showed that there is a distinct trend in the variation of the production temperature with the change of each parameter. Based on the sensitivity analysis performed, two points are worth noting:

- (1) The proper knowledge of the geothermal gradient and reservoir permeability are crucial factors in geothermal energy mining.
- (2) The injection pressure has to be managed correctly because higher injection rates affect the reservoir productivity immensely.

Moreover, the interactions between the parameters investigated in this work should be considered in terms of their effect on the production temperature and not based on the financial viability or efficiency of the operation. For instance, the porosity does not affect reservoir productivity, but concerning drilling operations, the more porous the formation, the less the operational cost and vice versa.

5.6 Summary

Based on the geothermal energy plan of the Soultz (France) geothermal field, a 3-D numerical model has been developed for the lower reservoir (4500–5200 m) to examine the long-term performance of the reservoir using the finite element and factorial experimental design methods. With the factorial experimental design, various possible combinations of the reservoir parameters have been found, and their suitability is confirmed by comparing temperature histories at the production wellbores for all scenarios. The results obtained show that the human-controlled parameters have unstable temperature distribution at the production wellhead, and the parameter most affected regarding that is the fluid injection pressure. Hence, the results obtained reveal that the reservoir parameters, if properly managed, can help decision makers maximise reservoir productivity.

Chapter six – Numerical modelling of geothermal reservoir with interaction between the components

6.1 Introduction

In this chapter, a 3-D numerical model of deep and heterogeneous geothermal reservoir is developed with a discrete fracture using the Soultz enhanced geothermal system (EGS) scheme. The system proposed here considers the influence of the surrounding media, the reservoir and the fractures concurrently in predicting the long-term performance of a geothermal reservoir. In this case, the fluid is circulated through an inclined vertical well connected to the matrix (i.e., not a fracture) in a fully saturated porous medium, unlike the previously reported models in which the injection and the production wellbores communicate via a single planar fracture or multiple as shown in Figure 6.1.

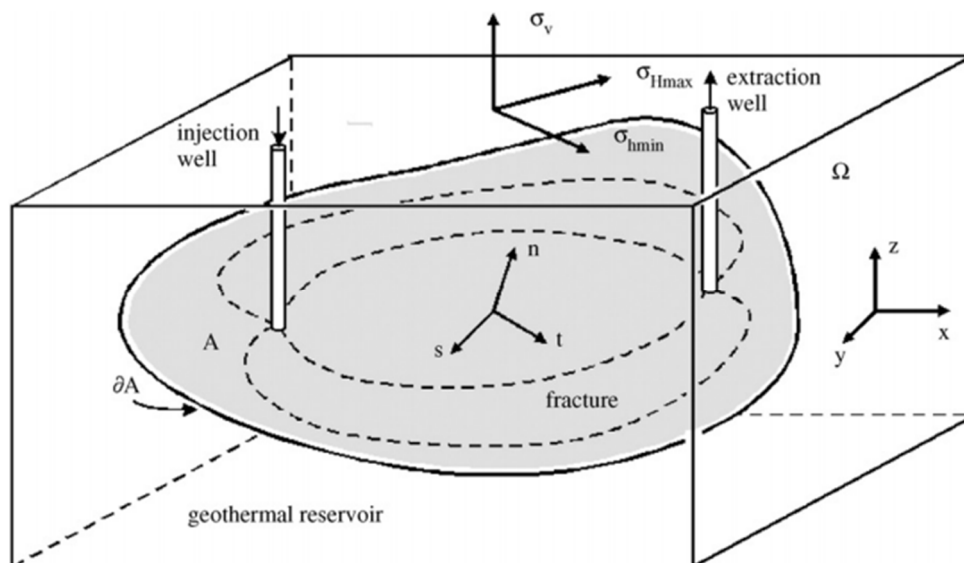


Figure 6.1: A typical geothermal reservoir with a single planar fracture

However, in the current model, a fracture is also included in the simulation which intersects the matrix at an angle but without a connection for the wellbores to communicate as shown in Figure 6.2. The reason for these assumptions in the current model is that sometimes the wellbores do not connect through fractures, as in the case of the Soultz triplet geothermal reservoir where a low connection between GPK3 (injection wellbore) and GPK4 (the second production wellbore) is encountered due to calcite deposition (Hebert and

Ledesert, 2012). Moreover, the geothermal reservoir is modelled as an open system that allows for additional sources or losses from the surrounding boundaries. As a result, water losses in the reservoir are accounted for in the model. The significance of this assumption can be supported by a real-life case of an existing geothermal reservoir. For instance, the five-month circulation test regarding hydraulics, conducted in the Soultz geothermal reservoir during 2005, showed that only 30% of fluid mass injected is recovered at the production wells, displaying the open nature of the reservoir (Hébert et al., 2010). The test result opposed the HDR concept that considered the reservoir to be a closed system with no naturally existing fluid present before its injection (Brown, 2009).

6.2 Research contribution

The contribution of the present work includes these three aspects. First, this study has proposed a mixed transport of fluid and heat in the reservoir from both the matrix block and the fracture, respectively. Second, the 3-D model takes into account the effect of fluid losses or gains concerning the nature of open systems in subsurface media, whose long-term influence on the extraction wellbore temperature cannot be underestimated for a 30-year extraction period. Third, in this investigation, each of the human-controlled parameters (injection flow rate, injection temperature, and lateral well spacing) are examined under different operational scenarios with other parameters. For example, injection flow rate in this study ranges from 20 l/s to 70 l/s. Therefore, when examining the effect of the injection flow rate on production, different cases of injection temperature and wellbore spacing are considered, because their impact can also affect reservoir productivity.

The model addresses the limitations of previous research, which ignored the influence of fracture connectivity, reservoir representation, open boundaries influence and the inclusion of different operational schemes. The study estimates the consequence of individual parameters on others and their corresponding influences on the productivity of a geothermal reservoir. Solving the structure of this heterogeneous system, which is nonlinear in parameters and has a coupled interaction in nature, requires the use of a powerful numerical solver.

6.3 Geothermal reservoir case study

Figure 6.2 shows a schematic representation of the reservoir geometry, which is based on the Soultz geothermal system (i.e. half of the reservoir), it depicts a deep geothermal system $800\text{ m} \times 800\text{ m} \times 5000\text{ m}$ deep. The reservoir is assumed to be 300 m in thickness and is located at about 4500 m below the ground surface, bounded at the top and bottom by impermeable layers of granite. The top and bottom layers in Figure 6.1 represent the overburden and underburden, and the middle layer in-between displays the reservoir. The wellbores constitute a doublet (single injector and producer) 6 m apart at the ground surface, and 600 m apart laterally at the reservoir level as given in the Soultz geothermal system. Also, the injection wellbore is positioned 100 m and 400 m in the horizontal and vertical distances, while the production wellbore is located at 700 m and 400 m in both the x and y coordinates as shown in Figure 6.1. Both the injector and producer are inclined to angles of 10° and -10° , respectively.

Moreover, a single fracture intersects the reservoir through the overburden down to the underburden layer as in Figure 6.2. The fracture dips at an angle of 60° , which is a normal faulting regime to be precise with an approximated aperture of 50 mm .

Table 6.1 presents the petro-physical properties and physical parameters used in the numerical model (Guillou-Frottier et al., 2013). The material properties are extracted from the Soultz geothermal system as in the literature (Dezayes et al., 2010; Genter et al., 2010b; Guillou-Frottier et al., 2013). For the fluid material properties, expressions presented in Chapter 3 are employed in the study, which includes density, viscosity, thermal conductivity and heat capacity. The system initial pressure is hydrostatic throughout the model, and the initial temperature (T_{init}) is given as $T_{init} = T_{surf} - 0.03[K/m] \times (-z)$, where T_{surf} is surface temperature and is assumed to be 10°C . The boundary condition applied for the temperature is 40°C (fluid injection temperature), and for the hydraulic process is 30 l/s (injection flow rate). Moreover, explicit details of the boundary conditions used in the geothermal reservoir model are provided in Table 6.2.

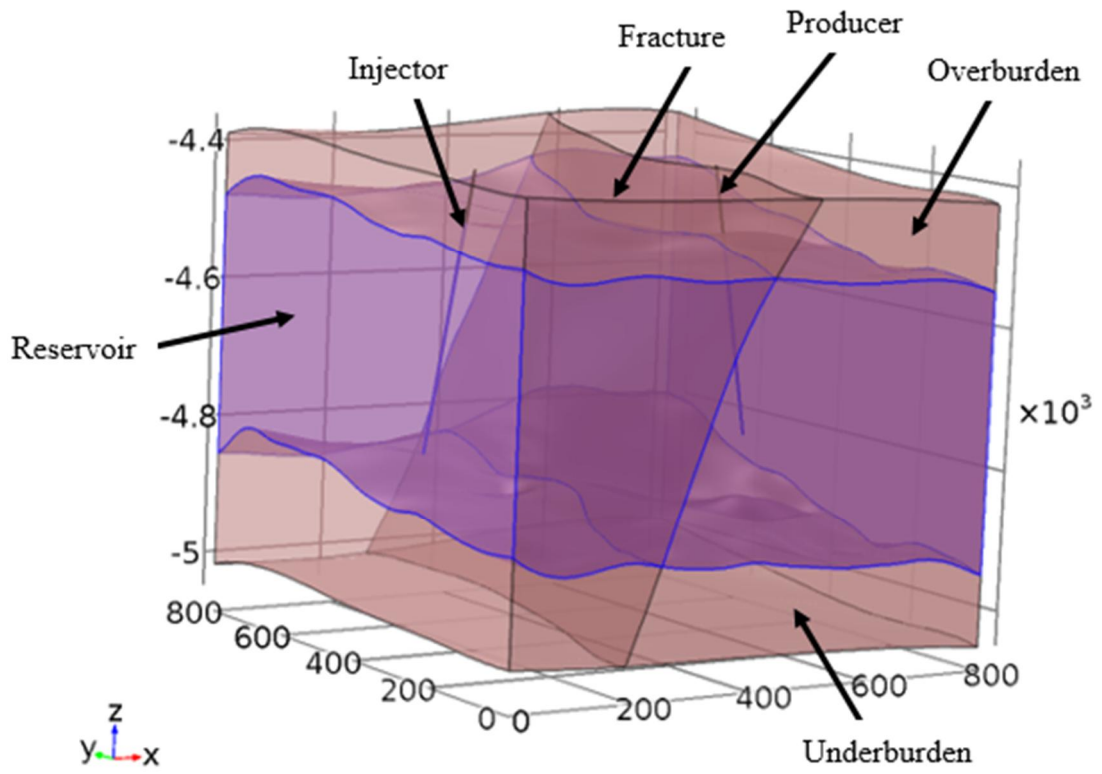


Figure 6.2: Geometry of the heterogeneous reservoir

Table 6.1: Geological properties of the system (Guillou-Frottier et al., 2013)

Parameter	Symbol	Value	Unit
Overburden Layer			
Thermal conductivity	λ_s	2	W/m/K
Density	ρ_s	2500	Kg/m ³
Heat capacity	$C_{\rho,S}$	900	J/kg/K
Porosity	ϕ	0.1	1
Permeability	κ	1 e-18	m ²
Reservoir			
Thermal conductivity	λ_s	3	W/m/K
Density	ρ_s	2650	Kg/m ³
Heat capacity	$C_{\rho,S}$	850	J/kg/K
Porosity	ϕ	0.3	1
Permeability	κ	1 e-16	m ²
Underburden Layer			
Thermal conductivity	λ_s	3.5	W/m/K
Density	ρ_s	2700	Kg/m ³
Heat capacity	$C_{\rho,S}$	850	J/kg/K
Porosity	ϕ	0.3	1
Permeability	κ	1 e-18	m ²
Fracture			
Thermal conductivity	$\lambda_{f,s}$	3.5	W/m/K
Density	$\rho_{f,s}$	1200	Kg/m ³
Heat capacity	$C_{\rho,S}$	800	J/kg/K
Porosity	ϕ_f	0.01	1
Permeability	κ_f	1 e-12	m ²

Table 6.2: The boundary conditions employed in the geothermal reservoir model

Physics	Boundary reference	Boundary condition
Hydraulic	Injection wellbore (i.e. injection flow rate)	$Q(t)_{injection} = 30 \text{ l/s}$ $0 \leq t \leq 30 \text{ years}$
	Production wellbore (i.e. production flow rate)	$Q(t)_{production} = ?$ $0 \leq t \leq 30 \text{ years}$
	Surfaces (top & bottom) except at the injection and production areas	$Q(t) = 0$ $0 \leq t \leq 30 \text{ years}$
	Surfaces (front, back, left and right)	$P(t) = \rho_L g (H_0 - D)$, <i>i.e.</i> , $-\partial H \times x$ $0 \leq t \leq 30 \text{ years}$
Thermal	Injection wellbore (i.e. injection temperature)	$T(t)_{injection} = 40^\circ\text{C}$ $0 \leq t \leq 30 \text{ years}$
	Production wellbore (i.e. unknown temperature to be calculated)	$T(t)_{production} = ?$ $0 \leq t \leq 30 \text{ years}$
	Surfaces (top & bottom) except at the injection and production areas. In this case, the boundaries are thermal insulated	$-n \cdot q(t) = 0$ $0 \leq t \leq 30 \text{ years}$
	Surfaces (front, back, left, and right)	$T(t) = T_{init}(t)$ if $n \cdot v < 0$, $-n \cdot q(t) = 0$, if $n \cdot v \geq 0$, $0 \leq t \leq 30 \text{ years}$

6.3.1 Mesh and solution convergence

In this model, the meshes are divided into three-dimensional (3-D) tetrahedral (for the matrix block), two-dimensional (2-D) triangular (for the fracture), and one-dimensional (1-D) line (for wellbores) elements, respectively. Figure 6.3 shows the mesh system that connects finer and fine grids in the calculation to reduce the impact of boundary effects. The implementation of the finer meshes on the wellbores is to increase the calculation accuracy;

and also reinforces the calculating intensity and workload. Therefore, the mesh division method not only increases calculation accuracy but also eradicates the deviation caused by density dependent boundary conditions, which have some significant effects on the long-term extracting vicinity and heat recovery after extraction.

The mesh convergence study of the proposed geothermal reservoir has been examined to explore the model computational efficiency in handling the cases of various structural variations mentioned as shown in Figure 6.4. Five mesh sizes are utilised: M1=20463, M2=39925, M3=68780, M4=189774 and M5=747838 starting from coarse to extra fine. Figure 6.3 shows the results representing temperature profiles along the production wellbore for all meshes. It is also evident that there is no significant difference in the results between the five meshes, though the results of the coarse and normal meshes, M1 and M2, are less accurate. However, it manifests no numerical oscillations. Notwithstanding, it can be deduced that the model converged at M3 mesh. The CPU time for 55-time steps are M1=108 s, M2=201 s, M3=363 s, M4 = 1083 s and M5=10177 s in an Intel(R) Core(TM) i5-5200U CPU @ 2.20 GHz, 2 cores.

To overcome numerical errors in the FEM solution, it is essential to check the convergence criterion for the solution. The convergence criterion presented in Chapter 3 was employed for the error estimation during solution iterations for the geothermal reservoir modelling. Figure 6.5 shows the number of iterations and the corresponding errors. The result indicates that an average of five iterations is sufficient to obtain an accurate solution.

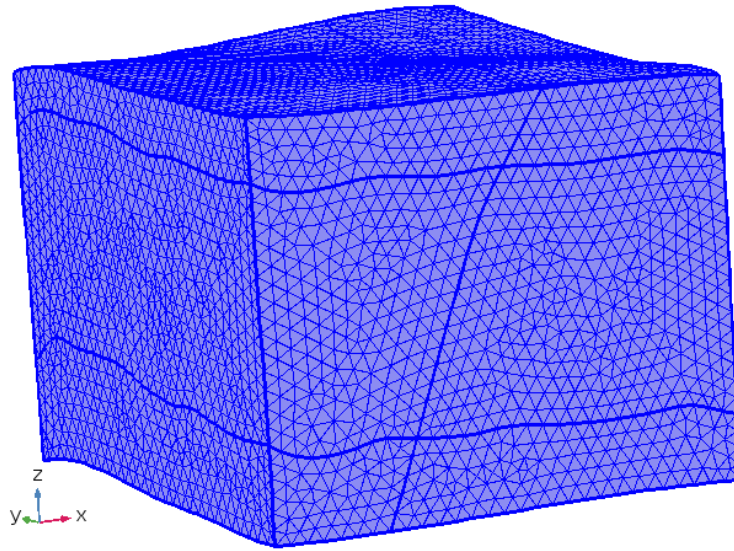


Figure 6.3: Reservoir mesh of the model

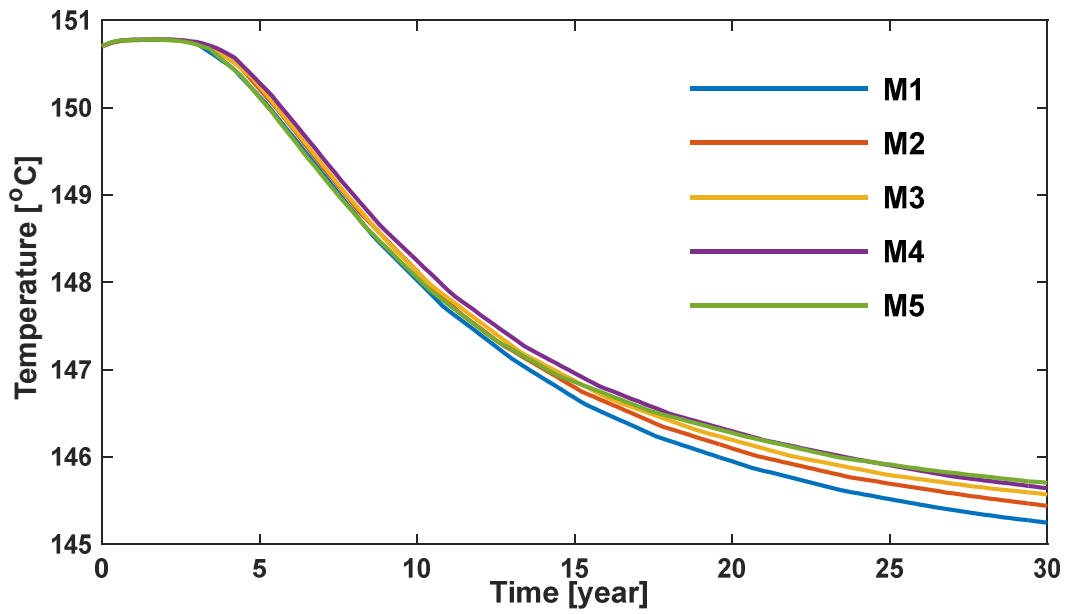


Figure 6.4: Mesh convergence study

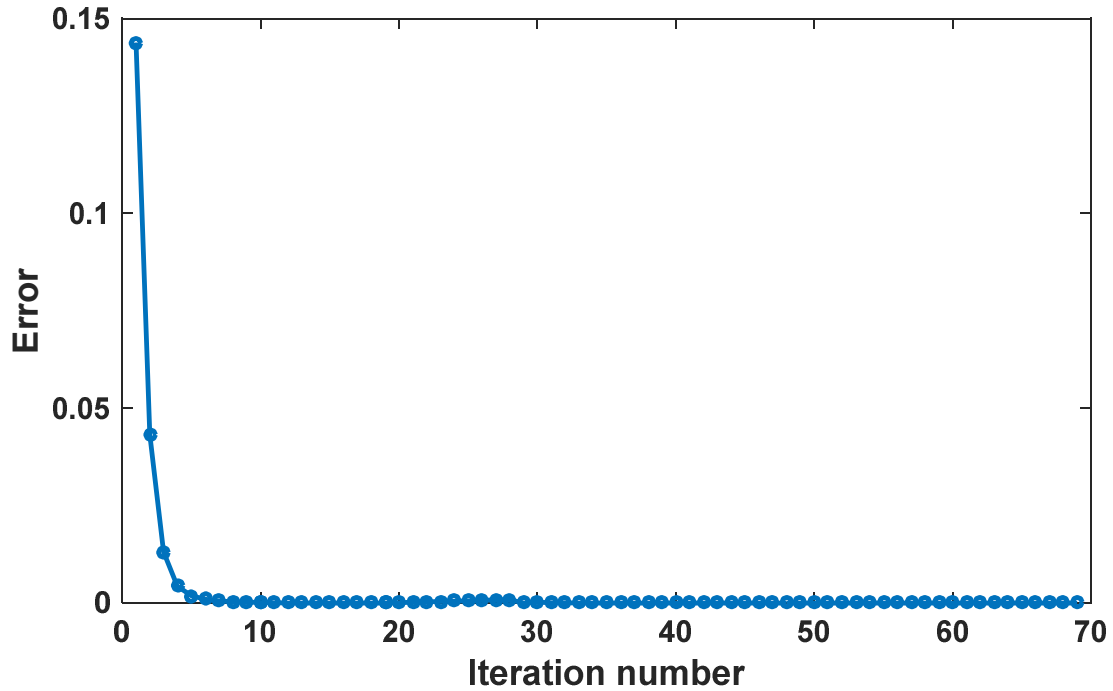


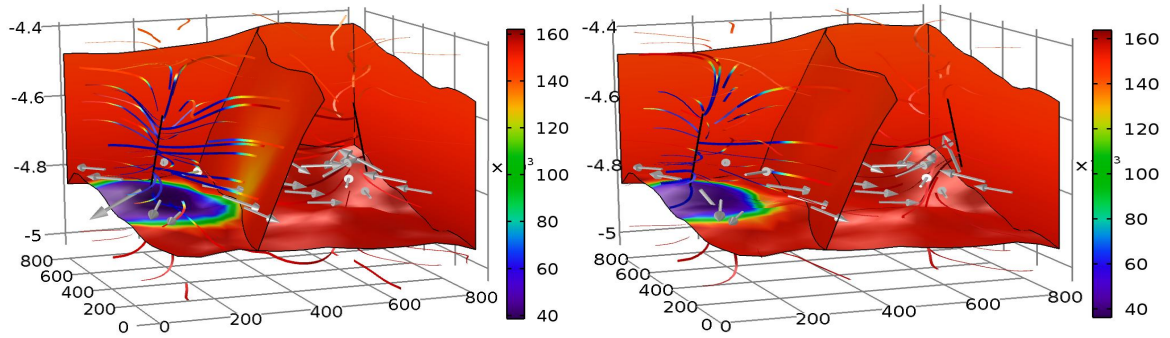
Figure 6.5: Error estimation

6.4 Results and discussions

6.4.1 Effect of cold-water front in the reservoir

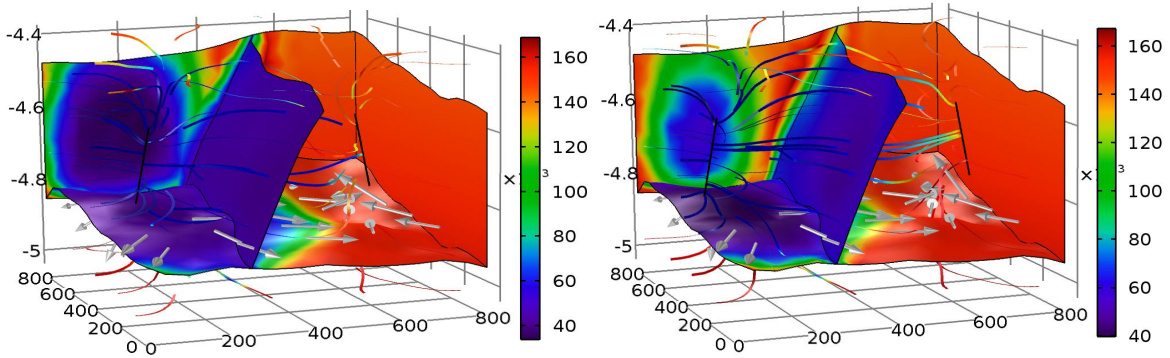
To investigate the effect of a cold-water front in the reservoir, the cold water, at a temperature of 40°C, is injected at a rate of 20 l/s through two different injection wellbore lateral spacing scenarios; one is situated 100 m and the other 50 m away from the left end. Hot water is extracted by the production wellbore with two different scenarios; the first is located at 700 m, and the second at 750 m from the left end, as shown in Figure 6.6(a–f). The effect of the cold-water front propagation is examined after 1, 15 and 30 years of simulation for 600 m and 700 m lateral wellbore spacing as shown in Figure 6.6(a–f). In all the cases analysed, it was observed that the injected fluid creates a cold front near the injection wellbore, which later evolves through the reservoir domain because the injected fluid was cooler than the geothermal reservoir.

Also, it can be noticed that the temperatures of the right boundaries were kept equal to the initial temperature of the reservoir until the cold-water front reaches the boundary, and after that the temperature of the boundary starts increasing as presented in Figure 6.6(c–f).



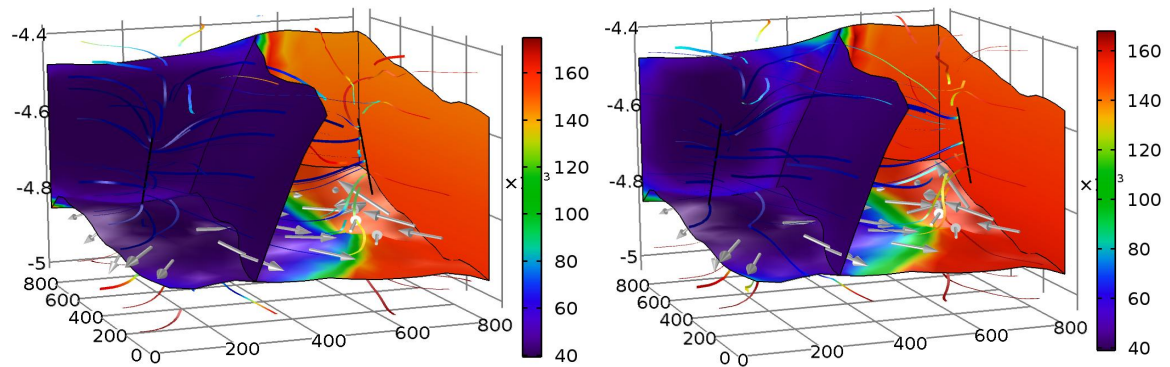
(a) 600 m wellbore spacing at 1 year

(b) 700 m wellbore spacing at 1 year



(c) 600 m wellbore spacing at 15 years

(d) 700 m wellbore spacing at 15 years



(e) 600 m wellbore spacing at 30 years

(f) 700 m wellbore spacing at 30 years

Figure 6.6: Cold-water front propagation within the reservoir ($^{\circ}\text{C}$) for different wellbore spacing at various simulation stages

6.4.2 Parametric studies

Developing a design model efficient in assessing the lifespan of a geothermal reservoir requires the understanding of some key controlled parameters during exploration and exploitation. In this study, three basic human-controlled parameters are analysed by varying one parameter at a time using the one factor at a time (OFAT) approach, while keeping the rest at a constant based on the Soultz geothermal case, as presented in section 6.3. The human-control parameters studied here are injection flow rate (discharge), injection fluid temperature and lateral wellbore spacing. Studying these three key parameters provides a preliminary evaluation of the effects of reservoir parameters on the commercial applicability of enhanced geothermal system utilisation. The effects of the parameters were assessed based on the productivity of the reservoir during the exploitation period of 30 years. The geothermal reservoir conditions specified were simulated to acquire the anticipated variations in temperature, pressure and thermal energy over 30 years. The parameters studied vary over the range of values that are acceptable for the geothermal exploitation of the Soultz site.

In a nutshell, the temperature of the reservoir was monitored using the parameters given above at the production wellhead with a simulation period of 30 years.

6.4.2.1 Effect of injection flow rate

The injection flow rate is one of the human-control parameters that have a direct effect on the reservoir lifespan. In order to quantify the effect, six cases were analysed. These cases range from 20 to 70 l/s with an incremental step of 10 l/s. Each of the cases was then studied under different scenarios of injection temperature and wellbore separation distances of 40°C and 50°C, and 600 and 700 m, respectively. All other parameters remain constant as explained earlier.

Figure 6.7 shows the temperature curves at the production wellbore for the different injection flow rates under a constant injection temperature of 40°C and lateral well spacing of 600 m. As seen, the temperature curves differ for the various cases; the higher rate declines earlier than the lower rate. For example, the 70 l/s injection flow rate starts to

decline just after 0.8 years of simulation, whereas the 20 l/s injection flow rate begins to decrease after approximately 2.6 years. As a result, the produced temperature is higher when the injection flow rate is lower, and vice versa. The reason for the variation is that the greater the injection flow rate, the faster the cooling of the reservoir occurs, and the lower the flow rate, the slower the cooling becomes. The same trend is observed when the injection fluid temperature is changed to 50°C in similar operational scenarios as in Figure 6.7, with slight shifts in the production temperature as shown in Figure 6.8. It is noted that the increase in the injection fluid temperature to 50°C has a lesser effect on the produced temperature in those cases.

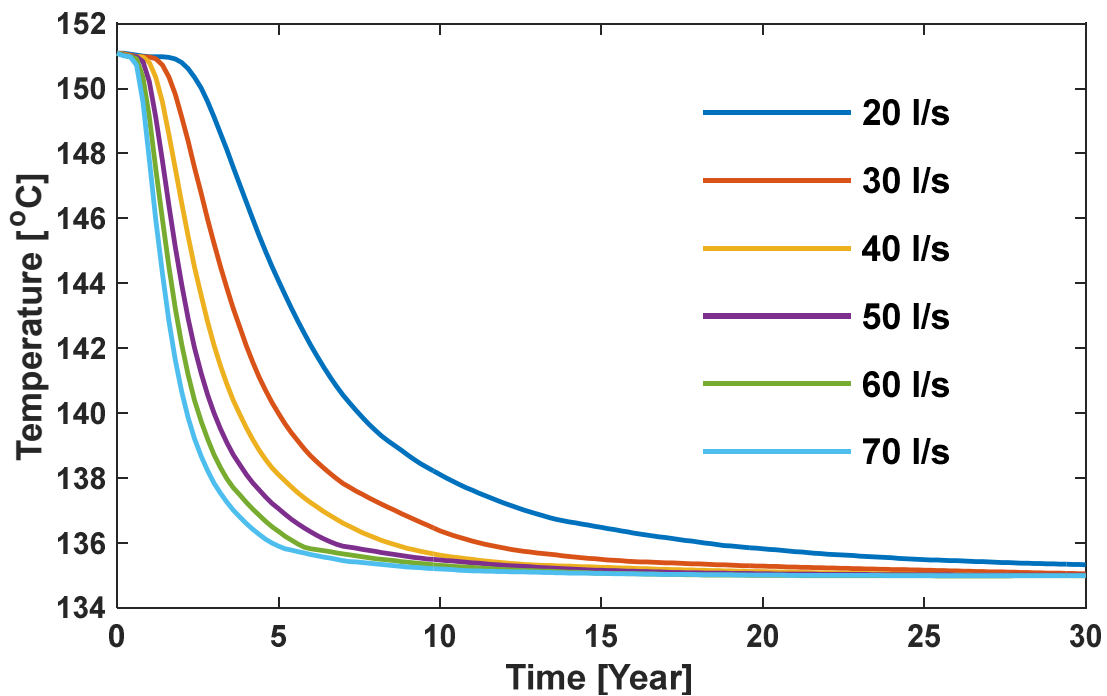


Figure 6.7: Production temperature history under 40°C with 600 m well spacing

Figure 6.9 presents the temperature breakthrough curves at the production wellbore for different injection flow rates under the influence of 40°C injection temperature and 700 m lateral well spacing. In these cases, the earliest decline starts after 1.6 years of simulation for the highest injection rate (i.e. 70 l/s) and 5.6 years in the case of lowest injection flow rate (20 l/s). Furthermore, the decrease in the production temperature at the extraction wellbore during the 30-year simulation is 8.31°C and 8.93°C for the lowest and highest injection flow rates, respectively. The low decline is recorded in these cases because the lateral well spacing between the injector and the producer is larger, so the production

wellbore is not affected much by the reservoir cooling after a 30-year simulation. Likewise, the same response is observed when the injection temperature was changed to 50°C with slight changes in the production temperature due to the increase in the injection fluid temperature.

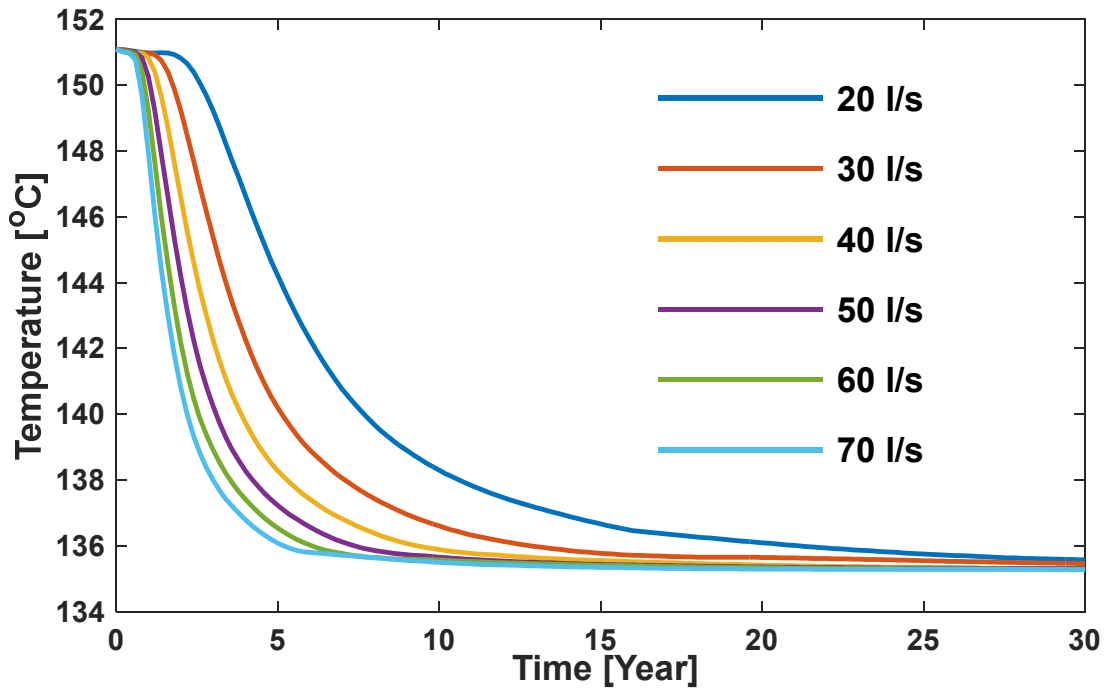


Figure 6.8: Fluid injection temperature 50°C with 600 m lateral well spacing

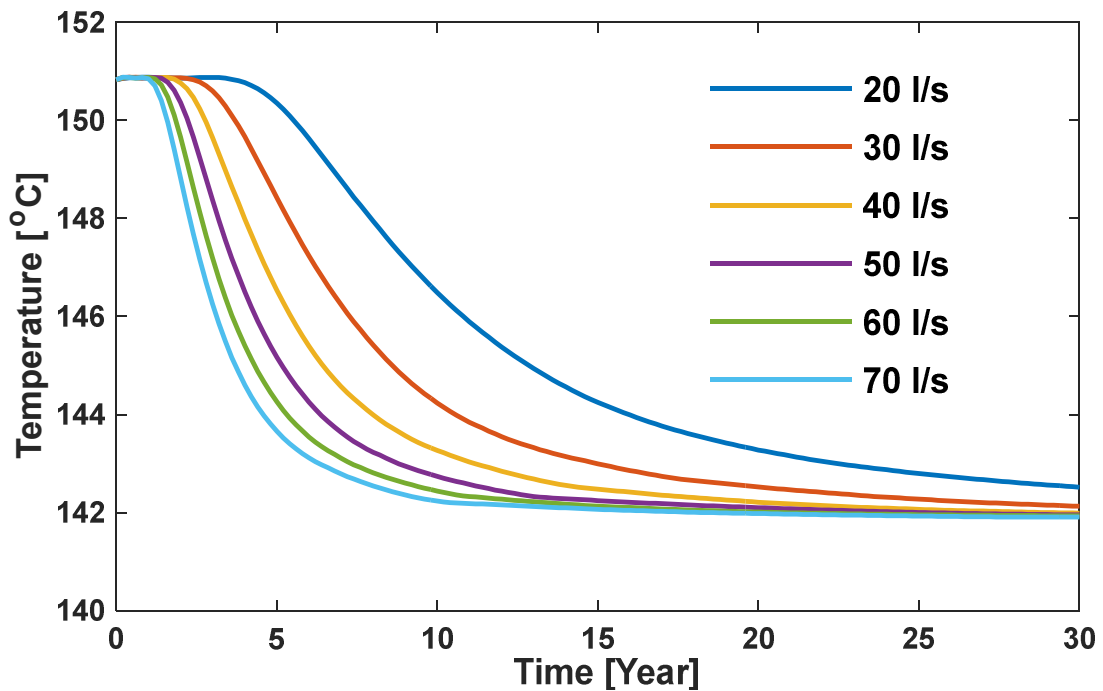


Figure 6.9: Production temperature history under 40°C with 700 m well spacing

In all the cases and scenarios, it is observed that as the injection rate increases, the reservoir temperature decreases rapidly. Moreover, the injection temperature and the well spacing also have some effects on the production rate. The maximum temperature is achieved when the injection flow rate is at its lowest and well spacing is at its largest, then combined with the lower injection rate as shown in the figures presented.

6.4.2.2 Effect of injection fluid temperature

The surrounding rock supplies some amount of the heat enthalpy conducted in the reservoir; however, the injected fluid temperature governs the major heat enthalpy added into the reservoir due to the convective heat transfer. In this study, six cases of fluid injection temperature are investigated. These cases range from 10°C to 60°C with an incremental step of 10°C, and each of the cases is additionally studied under varying scenarios of pumping rates of 20 l/s and 30 l/s, and well lateral spacing of 600 m and 700 m.

Figure 6.10 shows the breakthrough temperature curves at the production wellbore under the influence of 20 l/s and 600 m lateral wellbore spacing; the temperature curves begin to decline after approximately 1.8 years of simulation with a temperature of 150.93°C in almost all cases. After approximately 10–12 years of simulation, a little gap is observed between the different injection temperature scenarios, and it continues to widen up to the end of the 30-year simulation period. The reason for these similarities in the production temperature breakthrough curves is that the effect of reservoir cooling started in approximately the same period in all cases. Similarly, the production breakthrough curves for the different injection temperature scenarios when combined with 30 l/s injection flow rate and 600 m lateral wellbore spacing have a similar trend as Figure 6.10 with little difference. The idea behind the earlier variation between the different cases is the increase in the injection flow rate to 30 l/s, which causes the fast cooling of the reservoir.

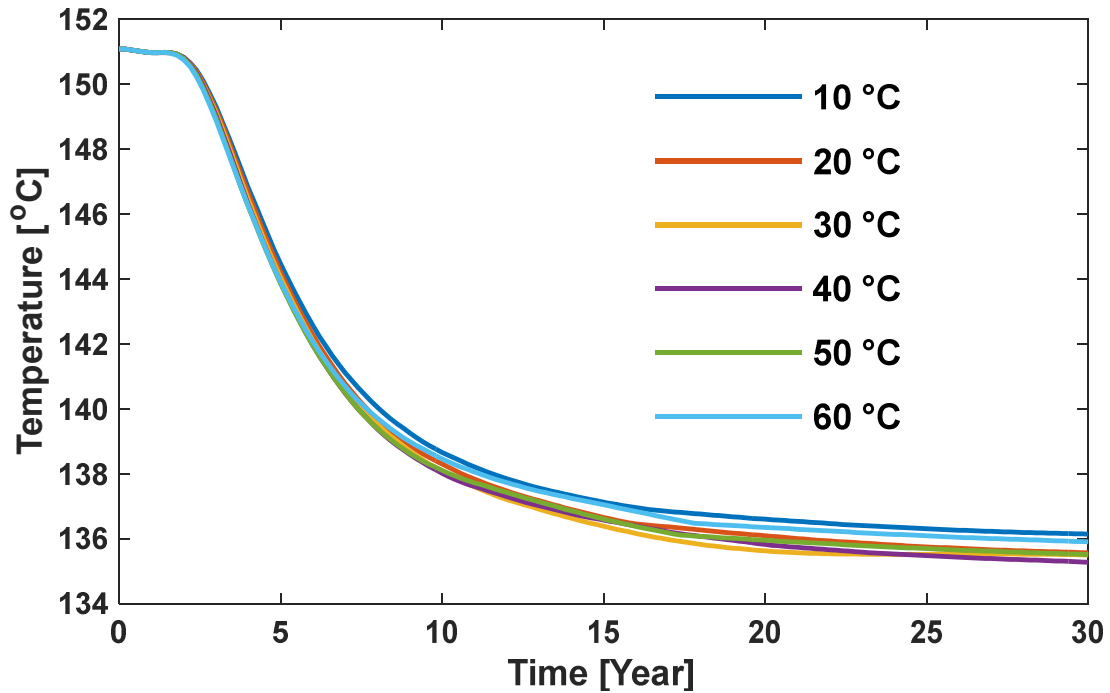


Figure 6.10: Production temperature history under 20 l/s with 600 m well spacing

Figure 6.11 shows the temperature curves at the production wellbore for different cases of the injection fluid temperature under the influences of 20 l/s injection flow rate and 700 m lateral well spacing. As seen, the temperature breakthrough curves have a similar trend except in the case of the 10°C injection fluid temperature rate. The production temperature began to decline after approximately 4.2 years of the simulation cases of 20°C to 60°C, while in the case of the 10°C injection scenario, it began at approximately 3 years of simulation. The temperatures at the decline stages are 150.73°C and 150.74°C, in both the former and the latter, respectively. As the simulation continues, the breakthrough curve for the 10°C injection case shows a sudden transition change from lower to higher between the 8.8 and 9.2 simulation period and maintains a regular pattern until the end of the simulation, whereas the other cases maintain the same decline pattern. The reason for the variation of the 10°C injection temperature case with the remaining scenarios is that after equilibrium is reached, the higher injection temperature transmits the fluid faster to the production wellbore than the lower rates. Likewise, in the case of 30 l/s under the same operating conditions, similar breakthrough curves as in Figure 6.11 occur with little difference in respect of the starting period of decline and the transition phases of the 10°C injection due to the increase in the injection flow rate. Apart from those points, all other trends remain the same.

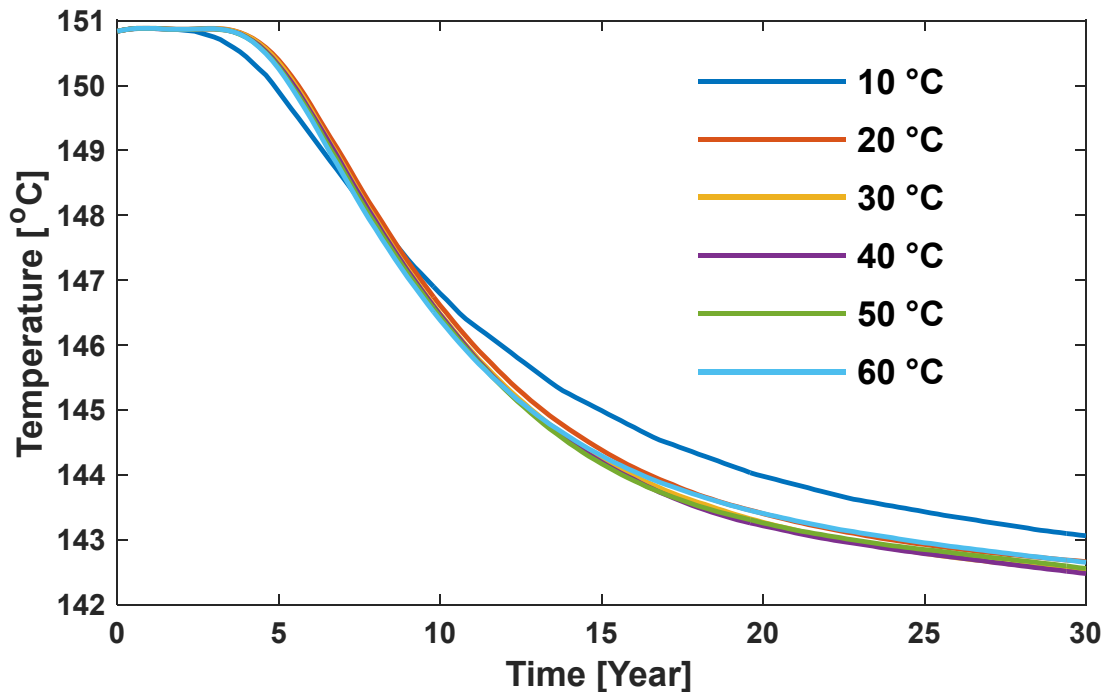


Figure 6.11: Production temperature history under 20 l/s with 700 m well spacing

In all the scenarios studied, it is observed that there were no significant changes in the produced temperature from the reservoir.

6.4.2.3 Effect of lateral well spacing

To overcome the cold-water effect and water losses that result from reduced productivity of reservoir wellbores, they must be placed at an optimum distance from each other. The choice of location will depend on the geological formation and production flow rates. Larger well spacing results in greater reservoir sizes and vice versa. However, with large spaces between wellbores, fluid losses are likely to be a significant problem, and with small spaces, the fluid losses are negligible. Therefore, the wellbore spacing must be optimised to achieve the maximum possible reservoir size and production flow rate. In this work, six scenarios of lateral wellbore spacing are examined. The spaces between the reservoir wellbores are chosen as 400, 500, 600, 650, 700 and 750 metres long, respectively. Also, in each of the scenarios, different injection rates, of 20 l/s and 30 l/s, and injection fluid temperatures, of 30°C and 40°C, are analysed.

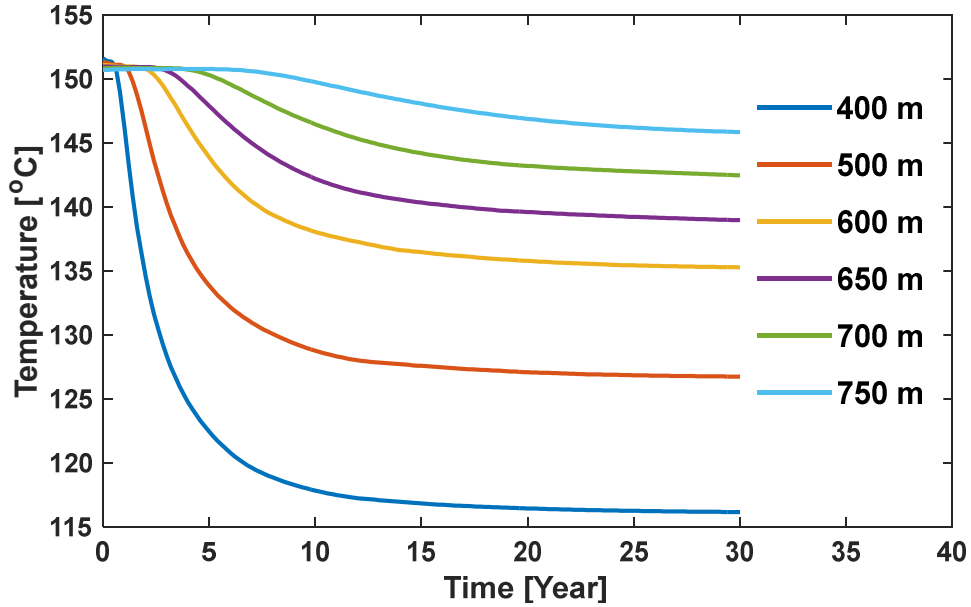


Figure 6.12: Production temperature history under 20 l/s with 30°C injection temperature

Figure 6.12 shows the temperature breakthrough curves at the extraction wellbore for the different scenarios of the lateral wellbore spacing when combined with an injection fluid temperature of 30°C and an injection flow rate of 20 l/s. As can be seen, the further the spacing, the higher the produced temperature, and vice versa. For instance, in the case of 400 m lateral wellbore spacing, the temperature begins to decrease just after 0.8 years of the simulation period. Concerning the 700 m lateral wellbore spacing, the decline starts after approximately 9.4 years. Moreover, after a simulation period of 30 years, the produced temperature for the closer wellbore spacing (i.e., 400 m) was approximately 116°C, and the largest spacing (750 m) was 145°C, which amounted to almost a 30°C temperature difference between the two cases. The reason for this significant deviation between the scenarios is the closer the spacing, the higher the impact of cold-water propagation on the production wellbore, and vice versa. Likewise, a similar trend was observed for the remaining cases, with slight deviation in the temperature breakthrough curves due to the different injection fluid temperatures and flow rates employed.

In all the scenarios, it is observed that as the lateral wellbore spacing increases, the production temperature rises.

6.4.3 Energy extraction rates

The model adopted in this investigation is the one proposed by Kruger (Kruger, 1995; Xia et al., 2017) for the calculations of the total energy extraction in all the scenarios and cases, expressed here as

$$\Delta E_i = Q_i C_{\rho,L} \Delta T_i \quad (6.1)$$

where ΔE_i is the annual energy produced in the i^{th} year, Q_i is the total production flow rate in the i^{th} year, $C_{\rho,L}$ is the specific heat capacity of the circulated fluid, and ΔT_i is the temperature difference between the extracted and injected fluid in the i^{th} year. The total energy produced from the system for 30 years of extraction can be written as

$$\Delta E = \sum_{i=1}^{30} \Delta E_i \quad (6.2)$$

Based on the limitations of the injection flow rate range and other parameter combinations studied in this work using the OFAT approach, the results show that as the injection flow rate increases, the energy extraction rate increases with a positive linear relationship as indicated in Figure 6.13, which shows that the injection rate increase affects the production output. Figure 6.13 also shows the influence of wellbore spacing and the effect of injection fluid temperature on the energy extraction rate when combined with injection scenarios. The results revealed that wider wellbore spacing coupled with lower fluid injection temperatures yields higher energy when compared to larger spacing with higher rates.

As for the effect of fluid injection temperature on the energy extraction rate, Figure 6.14 shows an inverse relationship between fluid injection temperature and the energy extraction rate. As the fluid injection temperature rises, the energy extracted from the reservoir declines significantly, because ΔT_i reduces with the rising fluid injection temperature. Hence, the reservoir lifespan is prolonged for the reproduction of hot water with the same temperature. Also, these cases are further investigated with different wellbore spacing and fluid injection rates, and the results showed that larger well spacing linked with a higher injection fluid rate generates greater extraction energy in comparison to other combinations.

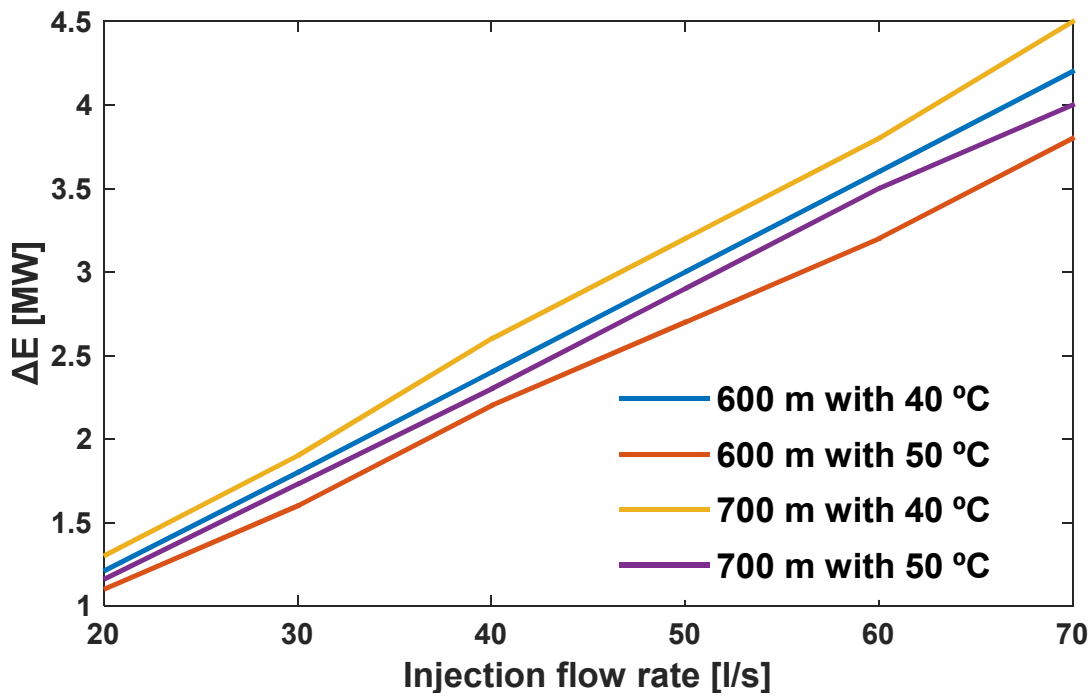


Figure 6.13: Production energy as function of fluid injection rate under different lateral well spacing and fluid injection temperatures

Figure 6.15 presents the effect of wellbore spacing on the extraction energy of the reservoir. In all the scenarios analysed, it is observed that, as the wellbore spacing increased, the energy extracted from the system increased rapidly due to the cold-water front propagation affecting the closer wellbores earlier than the further ones. The increase shown in Figure 6.15 occurs in a nonlinear manner with two different gradients; the gradient of the first two spacing is steeper than the remaining ones because the latter spacing have similar resistance to the cold-water front.

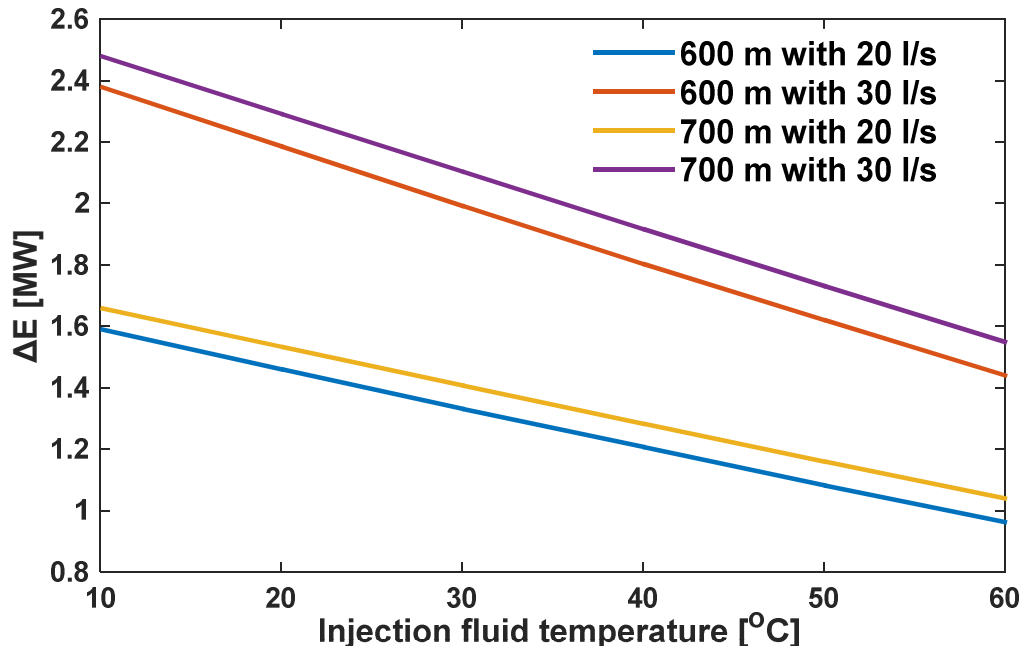


Figure 6.14: Production energy as function of fluid injection temperature under different lateral well spacing and fluid injection rates

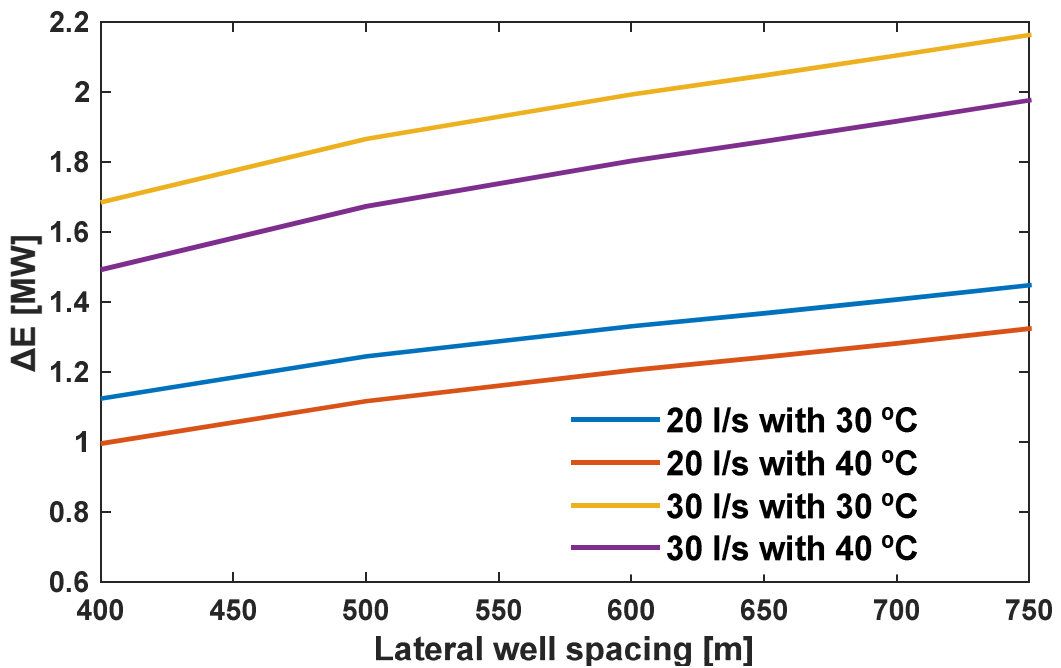


Figure 6.15: Production energy as function of lateral well spacing under different injection flow rates and fluid injection temperatures

6.5 Summary

In this chapter, a novel 3-D numerical model for coupled thermo-hydraulic processes in a heterogeneous fractured geothermal reservoir overlain and underlain by impermeable layers is proposed. The primary objectives of the study were targeted to three different goals. First, to investigate the mixed transport of fluid and heat in a reservoir from both the matrix block and the fracture, respectively. Second, to take into account the effect of fluid losses or gains concerning the nature of open systems in subsurface media, whose long-term influence on the extraction wellbore temperature cannot be underestimated for a 30-year extraction period. Third, to investigate the influence of injection flow rate, injection temperature, and lateral wellbore spacing on geothermal energy mining under different operational conditions. Based on the results obtained, the injection flow rate has a significant effect on energy production; as the rate increases, the energy extraction rate rises and the system lifetime decreases. Thus, higher injection flow rate is a positive factor in production and, at the same time, a negative factor on reservoir lifespan. In the case of fluid injection temperature, the effect is less significant to production because, as the injection temperature increases, the extraction energy declines rapidly and the reservoir lifespan increases. The lateral wellbore spacing also behaves similarly to the injection flow rate, but it is not as effective as the injection flow rate regarding energy extraction and provides a longer reservoir lifespan than the former. Thus, the model can also serve as a reference solution to other complex interactions encountered in reservoir simulations.

Chapter seven – Numerical modelling of geothermal reservoir with multiple pore media: A case of triple porosity-permeability model

7.1 Introduction

This chapter presents a numerical model to simulate energy mining in naturally fractured-faulted geothermal reservoirs using a triple porosity-permeability approach. The model fully coupled thermo-hydraulic (TH) processes in a unified geothermal reservoir simulator adopted. This approach enables the investigation of multiphysical phenomena in fractured-faulted formations characterised by multiple pore media. General studies on the effects of these media on coupled transient fluid and heat flow capture basic features related to energy mining in deep geological formations. Case studies demonstrate that the model can provide a long-term assessment of deep geothermal reservoirs in naturally fractured and faulted porous media. The work provides fundamental insight into the flow of heat and fluid through multiple pore media and the fracture-fault interface in deep geothermal reservoirs under various conditions and thus, provides a foundation for future research in the field of the enhanced energy recovery from geothermal reservoirs.

7.2 Background

In reservoir engineering, numerical models are valuable predictive tools for understanding subsurface resources (McDermott et al., 2006), being used to experiment or refine various conceptual models to estimate hydraulic, thermal, mechanical, and chemical parameters. Most importantly, the prediction of how a geothermal reservoir might respond to changes in the subsurface environment resulting from exploitation is required, as these will influence system performance during its service-life. In naturally fractured media, fractures and faults provide permeable pathways for fluid flow through aquifers containing hydrocarbons and geothermal resources (Barton et al., 1995). Fault systems are more permeable than fractures, and the structure of the former provides a more porous system than the latter. That said, field studies confirm that few fractures and faults in naturally fractured rock masses serve as the primary channels for fluid flow (Long et al., 1991).

In order to better articulate the heterogeneity of naturally fractured-faulted geothermal reservoirs, the concept of the triple porosity-permeability (TPP) model is adopted. A 3-D numerical model of a deep geothermal reservoir (based on the Soultz graben formation) is developed, in which the reservoir is conceptualised as a media with multiple interactions involving faults, fractures, and rock matrices. Thus, the model proposed here describes flow via naturally fractured and faulted reservoirs with different petro-physical properties, amongst which porosity and permeability are the principal interest. This media resides in a formation that is formed by three separate continua, as exemplified by the Soultz graben formation. In the Soultz geothermal system, fractures are interconnected to large faults, through which heat and fluid are transmitted.

Therefore, by understanding reservoir heterogeneity, lithology, and architecture of discontinuities, critical variables for improving reservoir modelling can be available to better predict heat transport, fluid flow, geomechanical deformation, and chemical precipitation and deposition. Furthermore, the knowledge gained from this approach can be used to refine models for similar geological formations to examine their potential for geothermal exploitation.

7.2.1 Motivation

In the design of a geothermal system, terrain geology and natural conditions are key considerations. Geothermal technological concepts can be adapted to different geological terrains based on field experiments, including Fenton Hill (US), Rosemanowes (UK), and Soultz (France). As mentioned in Chapter 2, the initial concept of deep geothermal systems was first examined and proposed by the Los Alamos Laboratory at the Fenton Hill site (US) in the mid-1970's (Kelkar et al., 2016). This system was considered to be impermeable HDR as reported in detail in Chapter 2. The HDR's reservoir concept was idealised as a penny-shaped fracture created in a rock mass as a result of high fluid pressure, linked to a new open fracture, which formed the heat exchange surface between the wellbores and the fracture, as shown in Figure 2.1 (i.e. Chapter 2) (Brown et al., 2012).

By the early 1980s, field experiments conducted at Rosemanowes (Cornwall, UK), confirmed that the dominant process in reservoir creation was the shearing of natural joints,

rather than the creation of new hydraulic fractures (MIT, 2006). The outcome of field experiment led to change in the fundamental understanding of HDR reservoir behaviour involving the uniqueness of a fractured rock mass subjected to a specific anisotropic stress regime (Baria et al., 1999). Figure 7.1 shows the schematic representation of the system (Tenzer, 2001).

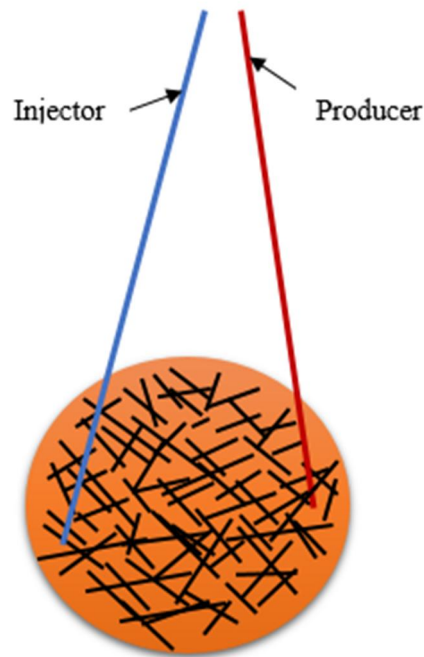


Figure 7.1: Network of micro-cracks, fissures and fractures (Rosemanowes Cornwall, UK
Adopted from: (Tenzer, 2001)

In the late 1980s, experimental studies on an abandoned oil field in Soultz (France) heralded a new chapter in the mining of geothermal energy, as it was realised that the reservoir had series of reactivated, interconnected, large-scale fractures and faults that were already partially open (Tenzer, 2001). The resulting reservoir model involved the hydraulic connection of discontinuities in the wellbores to the extensive fault-zone, as shown in Figure 7.2 (Clauser, 2006). Thus, it is not essential to directly connect two or more wellbores via an artificially created/stimulated fracture network; thereby making this a unique and challenging concept (Jain et al., 2015).

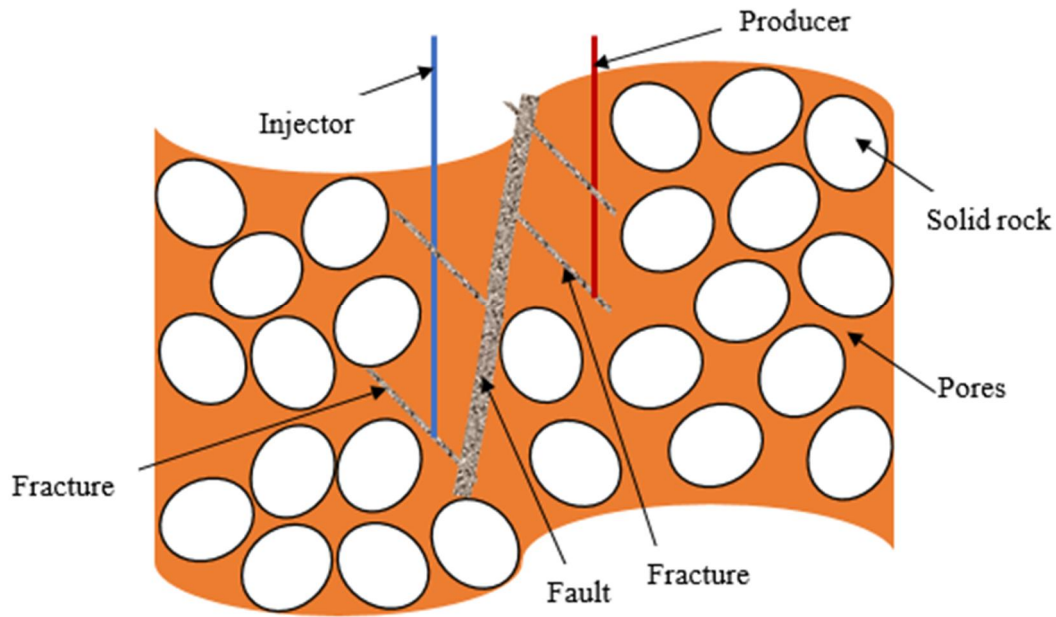


Figure 7.2: Interconnected large fractures and faults (Soultz, France) (Modified from: (Clauser, 2006))

7.3 Triple porosity-permeability model for the fractured porous reservoir

The TPP model accommodates transport in fractured porous media with different geological structures, e.g. the matrix, faults, fractures, and vugs. There are two distinct approaches to describing this system in the literature (Nelson, 2001). One assumes a two-matrix system with different physical properties and a third structure to represent the fracture system. In this case the matrix representation has one matrix represented as a porous block, while the other is a fault block. In the second approach, two fracture systems with different physical properties are considered to describe the fracture and fault system(s), and the third structure is the porous matrix block. In this study, the latter approach is chosen to describe a TPP transport model in a naturally fractured geothermal reservoir. Figure 7.3 presents a typical representation of the model, showing the different structures existing in the media. However, Figure 7.3 does not represent the real-life representation of this system; it just provides a simple demonstration of how to perceive the physical meaning of the model. It is also explicit from the model that both the fractures and fault systems are represented as plane surfaces.

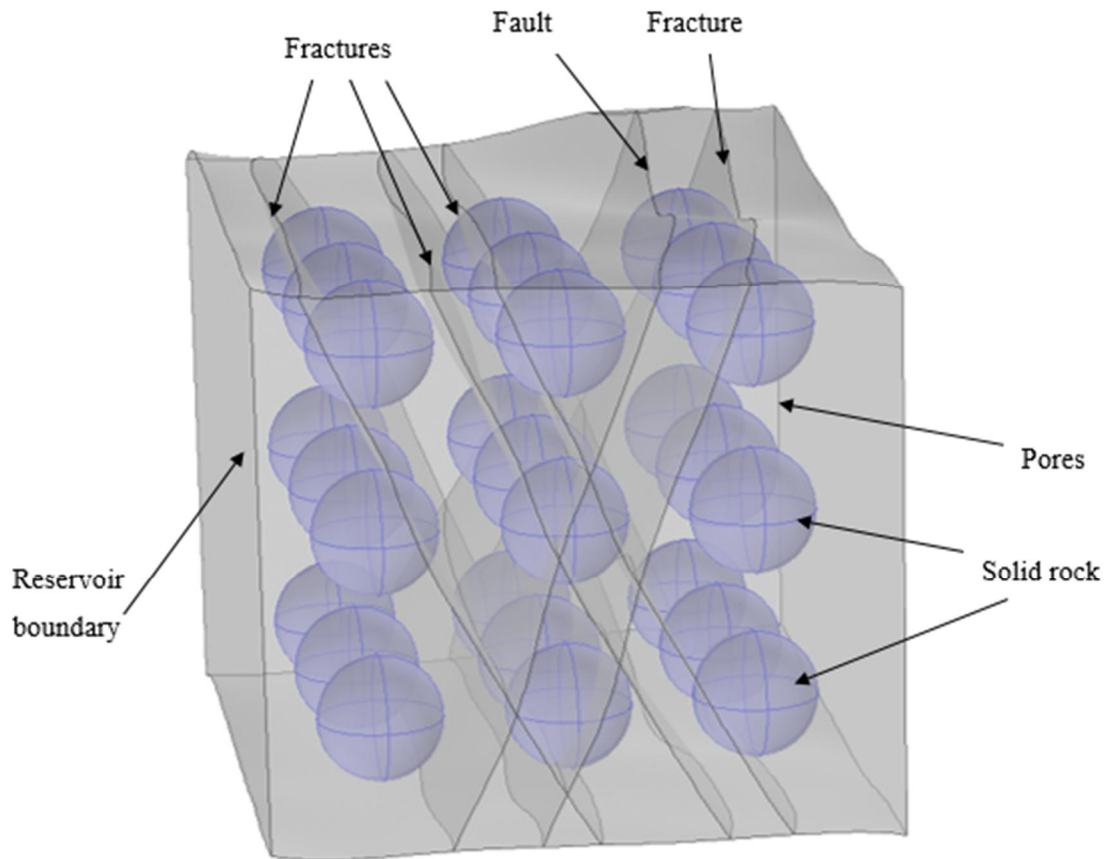


Figure 7.3: A typical representation of triple porosity-permeability (TPP) media

7.3.1 Theoretical assumptions for triple porosity-permeability media

The heat and fluid transport models are developed for the TPP with collective conservation equations for momentum and mass to define the field equations. The following assumptions are made for the equations:

- The geothermal reservoir is a naturally fractured porous media containing faults, fractures, and matrix; each medium is homogeneous.
- A single fluid phase is considered with temperature dependent density, dynamic viscosity, heat capacity, and thermal conductivity.

7.3.2 The transient flow of mass in triple porosity-permeability media

The TPP model adopted here for the fluid flow equations assumes that the porous media is fully saturated and consists of a single fluid phase. Thus, the governing equation employed is the combination of the mass conservation law and Darcy's equation. In this case, the three

different media share the same equation in general, with different flow patterns via the velocity term and the mass source term and the equations are presented in Appendix 4.

7.3.3 The transient flow of heat in triple porosity-permeability media

In this study, the heat exchange between the different media (i.e., the matrix, fracture or fault) and a moving medium (i.e., fluid) is calculated using the energy conservation law and Fourier's constitutive model. Thus, the general model adopted is that of a transient local thermal equilibrium, in which the rock mass temperature is considered to be in equilibrium with the fluid temperature. The assumption is that when rock and fluid at different temperatures come into contact, it takes very little time for the two media to come to a state of thermal balance. This assumption is not always true, but it does provide a basic understanding of heat transport in subsurface media and reduces the complexity of the problem at hand. The governing equations are coupled via the fluid velocity in Darcy's equation and by the boundary conditions at the interfaces of the various media. For this model the equations are given in Appendix 5.

7.4 Numerical case study one: Doublet geothermal reservoir

A 3-D numerical model is developed to represent a deep geothermal reservoir of $500 \times 500 \times 500 \text{ m}^3$ at the Soultz formation (Magenet et al., 2014a) using the proposed TPP model. The model consists of a fractured-faulted reservoir located at -4550 m below natural ground level, and a doublet representing an injection and production wellbores. Each of the wellbores intersects an active fracture, and both fractures are connected to a fault plane as shown in Figure 7.4. The wellbores are 460 m away from each other, and the penetration depths are -4750 and -4810 m for the injection and production wellbores, respectively.

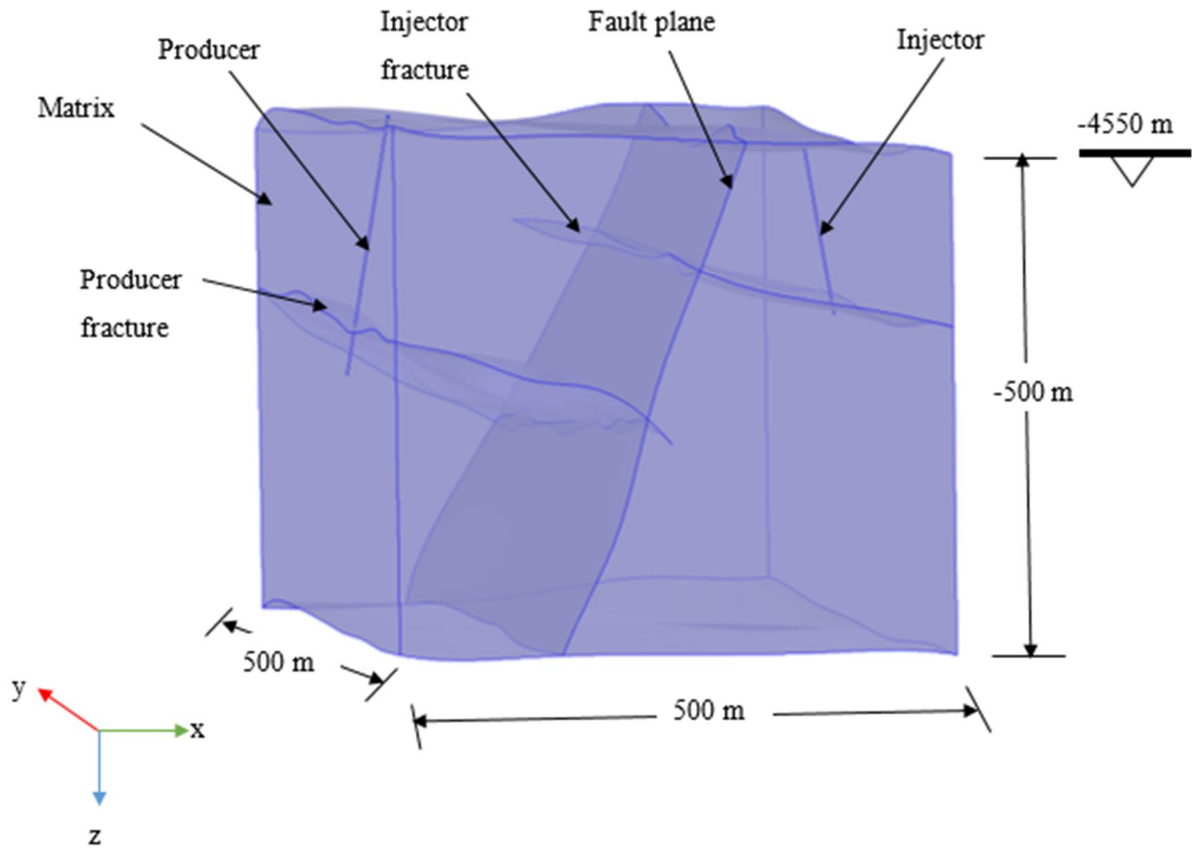


Figure 7.4: Doublet geometry of the triple porosity-permeability media

7.4.1 Material and petrophysical properties of the media

The objective of reservoir characterisation is to establish a 3-D image of material and petrophysical properties. The aim of this subsection is to define these properties based on the available field data for the proposed model. Thus, in the case where the required field data is absent, basic assumptions are made in the numerical model within the prescribed limit. Table 7.1 present the material and petrophysical properties of the reservoir as reported in the literature (Guillou-Frottier et al., 2013).

Table 7.1: Material properties employed for modelling the geothermal reservoir (Guillou-Frottier et al., 2013)

Parameter	Value	Symbol
Matrix		
Porosity (%)	1.0	ψ
Permeability (m ²)	0.001	κ
Thermal conductivity (W/m/K)	3.0	λ_s
Heat capacity (J/kg/K)	900	$C_{\rho,s}$
Density (kg/m ³)	2400	ρ_s
Faults		
Porosity (%)	15	ϕ_F
Permeability (m ²)	100	κ_F
Thermal conductivity (W/m/K)	2.5	λ_F
Heat capacity (J/kg/K)	750	$C_{\rho,F}$
Density (kg/m ³)	1200	ρ_F
Fractures		
Porosity (%)	0.1	ϕ_f
Permeability (m ²)	10	κ_f
Thermal conductivity (W/m/K)	3.0	λ_f
Heat capacity (J/kg/K)	800	$C_{\rho,f}$
Density (kg/m ³)	1300	ρ_f

7.4.2 Initial and boundary conditions

Initially, at $t = 0$, the temperature distribution is assumed as $T_0 = T_{surf} - \alpha_g \times (-z)$, in which T_0 is the initial temperature of the reservoir, α_g is the geothermal gradient, equal to 0.038 K/m in this case, T_{surf} is the surface temperature, which is assumed here as 12°C, and z is

the vertical depth in metres. For the hydraulic case the pore pressure distribution is hydrostatic at $t = 0$. In the case of boundary conditions, a constant temperature of 40° C is employed at the injection wellbore. Constant pressures of 10 MPa and -10 MPa are applied at the injection and production wellbores, respectively, and all other boundaries are thermally insulated.

7.4.3 Results

This subsection presents the results acquired from the triple porosity-permeability model of the doublet geothermal reservoir. The model is implemented using a fully coupled heat and fluid processes in the FE model developed.

Three sets of results are analysed here, starting from temperature distribution along the fault plane using contour plots. The second round of results investigated are the temperature changes along the injection fracture-fault interface. Finally, the last set of results concerns the pressure changes along the injection fracture-fault interface, to inspect the response of the interface relating to injection pressure.

7.4.3.1 Temperature contour plots along the fault plane

The transport of heat and fluid is implemented via a fault plane that connects the fractures and the two wellbores in the doublet geothermal reservoir system. Figures 7.5, 7.6, and 7.7 show the temperature distribution along the fault plane at several simulation stages using contour plots. Figure 7.5 presents the temperature contour plot after five years of simulation along the fault plane. As can be seen, the dark blue contour lines represent the low-temperature regions within the fault surface, while the lower part and some sections at the top on the edges of the plane have higher temperature distributions. In this case, the minimum temperature within the fault plane is approximately 80°C, while the highest observed is 198°C.

Figure 7.6 shows the contour plot of the temperature after 18 years of simulation. As seen, the dark blue contour line has expanded towards the lower section of the plane; making the cooler regions expand over time, while the hotter areas drop in temperature. In this

scenario, the highest temperature observed within the fault plane is approximately 196°C, which is 2°C less than in the case of the five-year simulation period. With respect to the lowest temperature after 18 years, it is approximately equal to 64°C, which is 16°C less than the previous scenario.

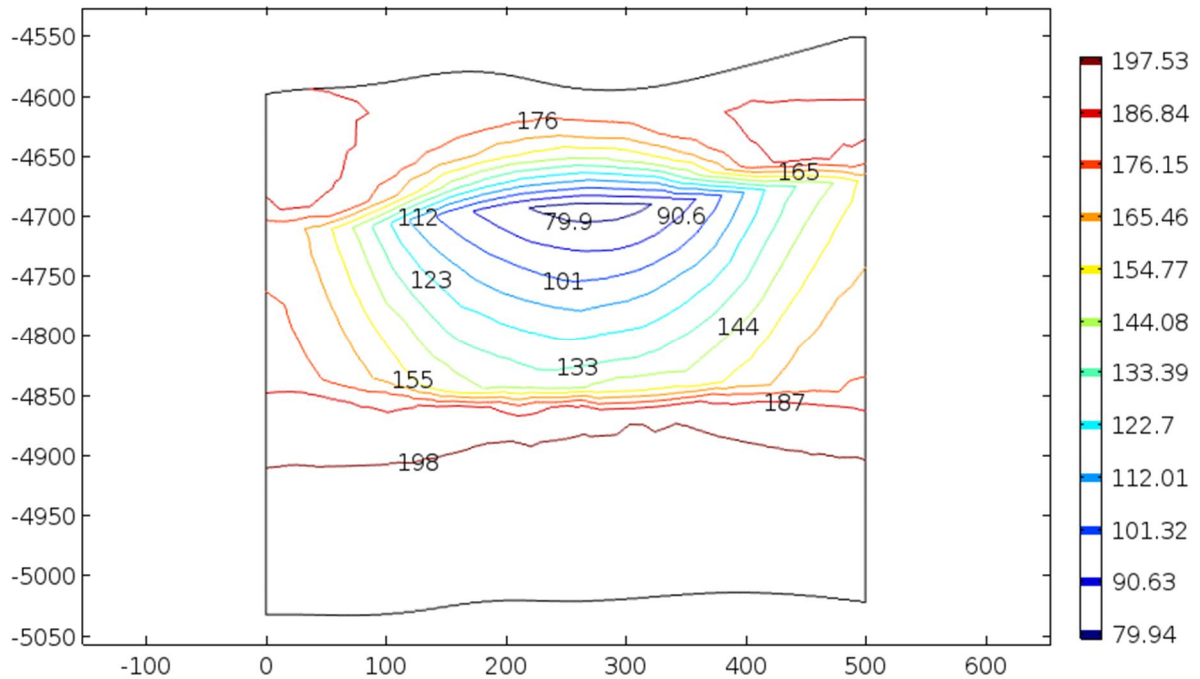


Figure 7.5: Temperature distribution (°C) within the fault plane (yz (m)) after 5 years of simulation

Figure 7.7 presents the temperature contour plot at exactly 30 years of simulation along the fault plane. The figure shows that the dark blue contour line continued to grow over time, and the hotter regions maintained their temperature, as in the case of the 18-year simulation period. In this instance, the lowest temperature is approximately 60°C, which is 20°C higher than the injection fluid temperature.

In all the figures (i.e. Figures 7.5, 7.6, and 7.7), the low-temperature fluid from the injection wellbore is transported into the production wellbore via the fault plane and the fractures. The fluid temperature rises through convection and conduction from the high-temperature rock matrix and also increases via convection-dominated transport from the fractures and fault. In both cases the effect results from superheated fluid in the extraction wellbore.

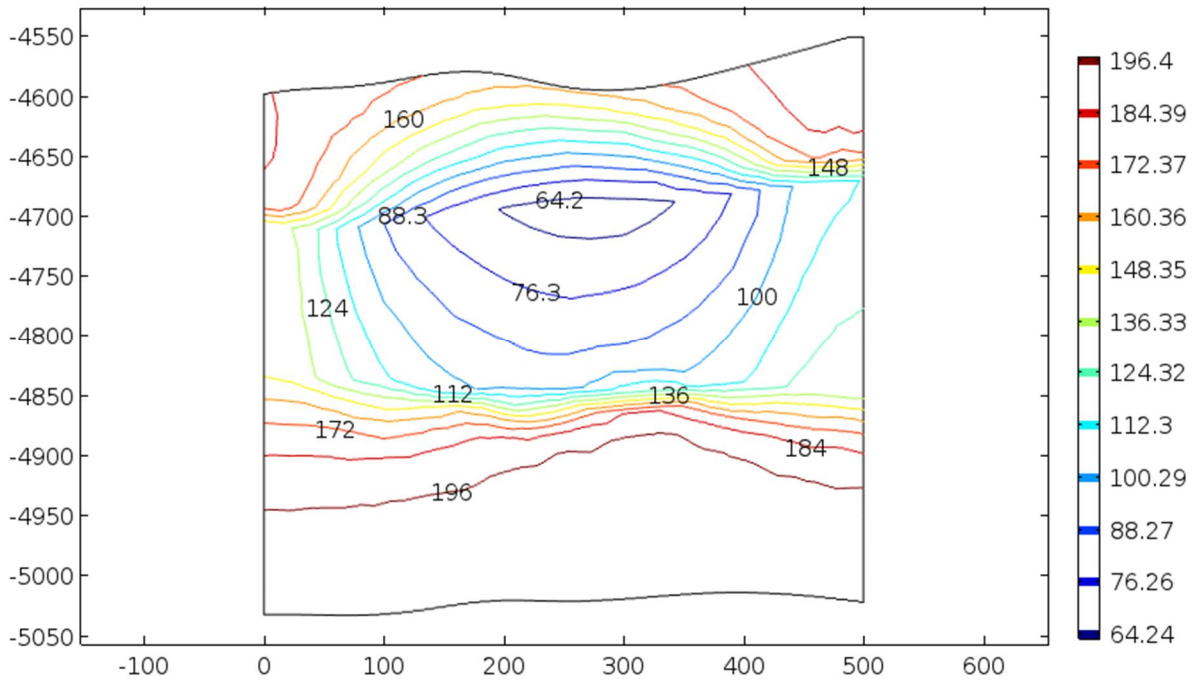


Figure 7.6: Temperature distribution ($^{\circ}\text{C}$) within the fault plane (yz (m)) after 18 years of simulation

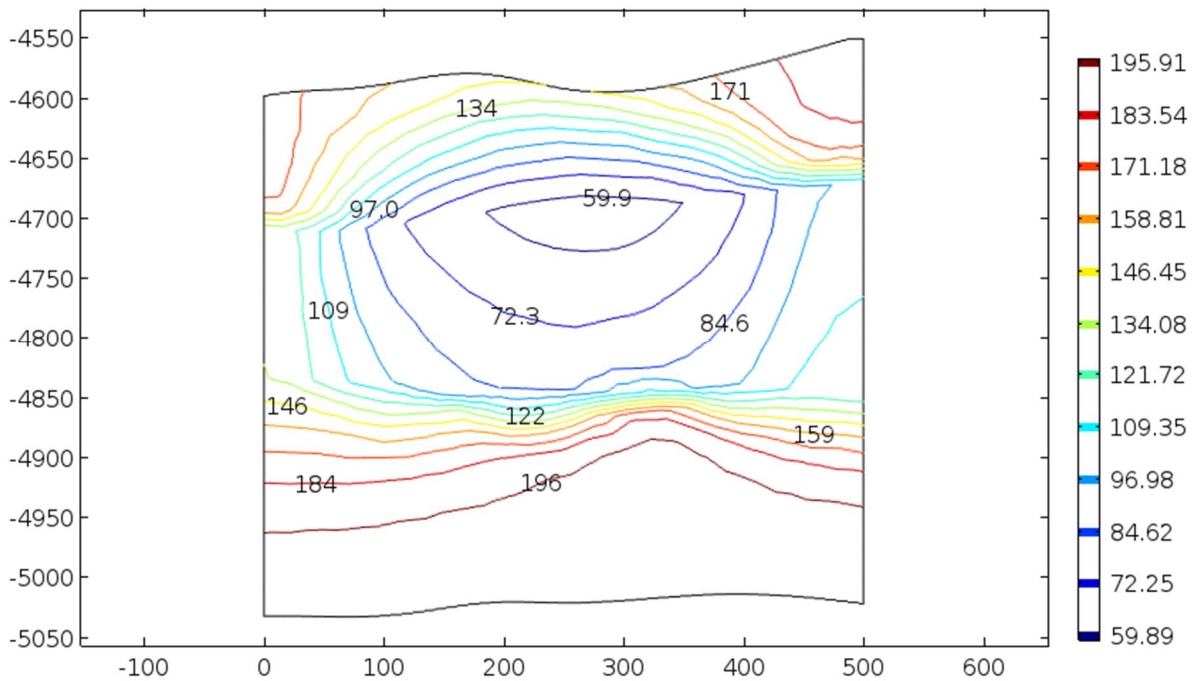


Figure 7.7: Temperature distribution ($^{\circ}\text{C}$) within the fault plane (yz (m)) after 30 years of simulation

In this subsection, the investigation is concerned with the temperature distribution along a fault plane that is connected to two fractures, in which each of the fractures is attached to either the injection or the production wellbore. The fault plane temperature begins to decline along the interface of the fracture-fault from the injection level as indicated by the dark blue contour line in Figure 7.5. It then continues to decrease faster as the injected cold fluid continues to propagate through convection with much influence from gravity because the production wellbore is at a much lower level than the injection, as shown in Figures 7.6 and 7.7. It is also clear from these figures that as the cold fluid injection continues, the temperature at the production fracture-fault interface declines fast (shown by the yellow contour line) at the bottom of the fracture, which is the exact position of the production wellbore. In general, these analyses show that it is possible to estimate heat mining via a geological structure that has multiple pore media in nature.

7.4.3.2 Temperature changes along the injection fracture-fault interface

The temperature change along the injection fracture-fault interface is analysed from the left edge of the y-axis to the right side as shown in Figure 7.8. For convenience, Figure 7.8 shows the temperature changes within the interface after 1, 10, 20, and 30 years of extraction. It can be observed that the left and right edges of the interface are not affected by the cold fluid injection after one year of production, and the temperature-distribution history reflects a heat transfer process that is dominated by convection. The cold fluid injection temperature-propagation speed depends on the fractures and fault petrophysical properties as well as the thermal conditions of the formation.

After 10, 20, and 30 years of extraction under the current simulation conditions, a significant drop in the temperature of the central part and the edges of the interface that forms a complete sag is observed, due specifically to the penetration effect of the cold fluid injection. The major contributing factor to this effect is that the fractures and fault have higher permeability than the formation matrix. Therefore, heat transfer is faster on the former media than the latter. It is evident from Figure 7.8 that the time required to transport heat within a system of multiple pore media depends on the petrophysical and thermal properties of the formation.

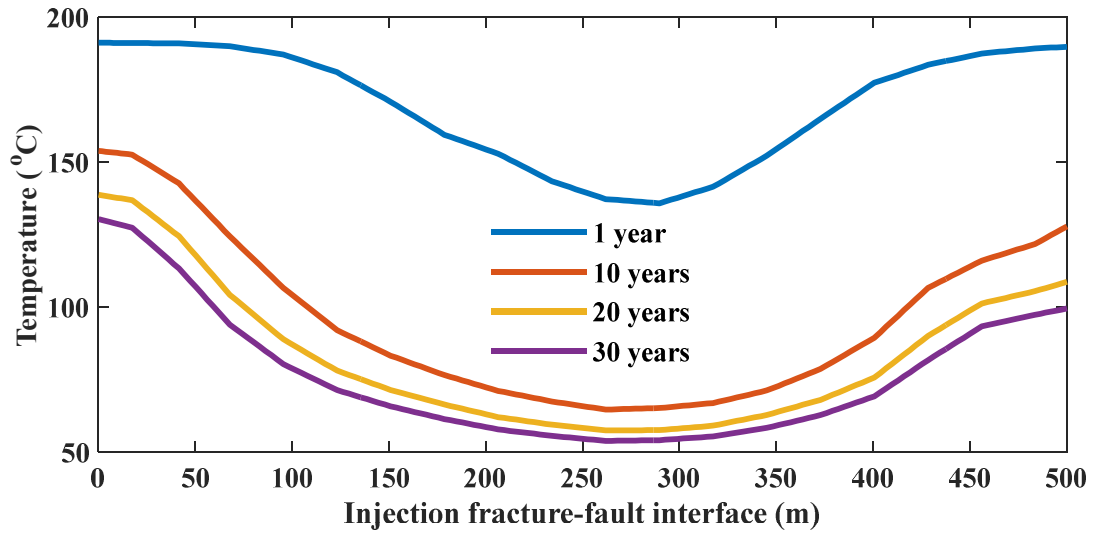


Figure 7.8: Temperature changes along the injection fracture-fault interface at various simulation stages

7.4.3.3 Pressure changes along the injection fracture-fault interface

Figure 7.9 presents the fluid pressure changes along the injection fracture-fault interface. The pressure at the injection wellbore is fixed, to obtain a smooth-running system, as described in the boundary conditions subsection, in which fluid pressures of 10 MPa and -10 MPa are applied at the injector and producer, respectively. The injected fluid temperature (i.e. quite low-temperature compared to the formation temperature) flows to the extraction wellbore along the fractures and fault under the influence of injected high pressure. The fluid pressure rapidly increases in the first year of operation along the central part of the interface that forms a hogging shape, while the edges maintain the formation pressure as shown in Figure 7.9. The reason for the increase along the central part of the interface after one year is because the pressure gradient is larger in the areas close to the injection wellbore, while the pressure gradient of the edge regions is smaller.

After 10, 20, and 30 years of production under the simulation conditions, it can be observed that the pressure regime around the interface has significantly increased from 37 MPa, initially obtained at a one-year simulation period, to a pressure of over 41 MPa after 30 years of simulation. However, the pressure increment is more significant in the initial simulation stages than succeeding periods, especially after ten years. After ten years, the

pressure seems to be stabilised with a minimum increment in the midrange because the pressure is very close to the reservoir pressure from that period onwards. Regarding the edges of the interface, after ten years, a rapid increase is observed; however, after that, the pressure pattern is maintained until the end of the simulation. Injection into a small initial fracture aperture changes the pressure along the fracture-fault interface.

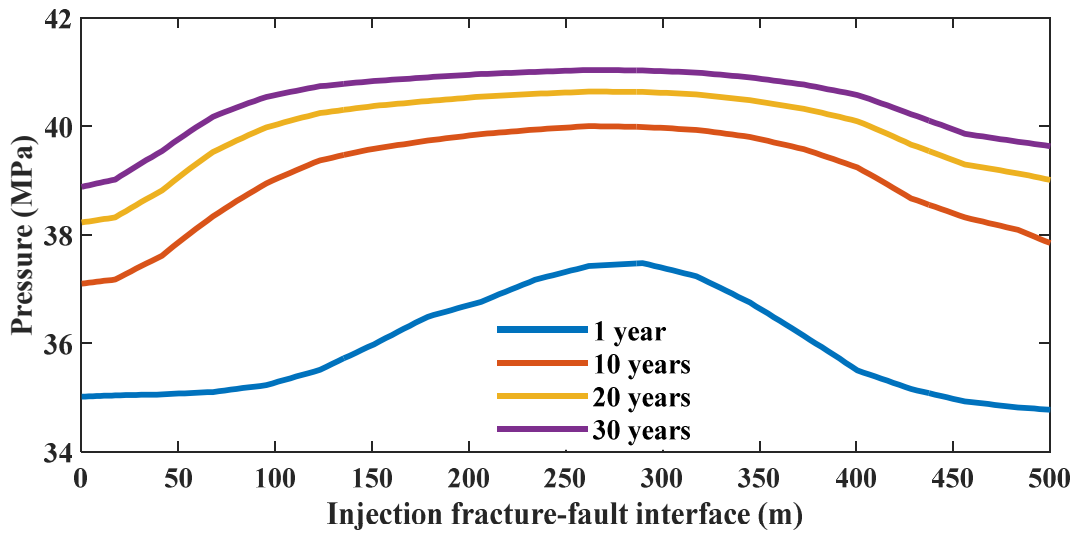


Figure 7.9: Pressure distribution along the injection fracture-fault interface at various simulation stages

7.5 Numerical case study two: Triplet geothermal reservoir

In this segment, a numerical model of a geothermal reservoir is developed using the TPP approach. Figure 7.10 presents the geometric system of the triplet reservoir, which is grouped into a matrix, fractures, faults, and wellbores (Gérard et al., 2006). The physical geometrical dimension of the triplet reservoir examined is $2 \times 0.5 \times 0.68 \text{ km}^3$, and consists of a multiplex system with fractures and faults and is located at 4.5 km under the ground level (Genter et al., 2010b). The reservoir comprises a triplet depicting an injection wellbore (GPK3) and two extraction wellbores (GPK2 and GPK4). The injection wellbore (GPK3) is located at x-y coordinates (1 km, 0.25 km), and the two extraction wellbores are positioned at 0.6 km and 1.6 km, respectively, with the same y-axis orientation as the injection wellbore (Genter et al., 2009).

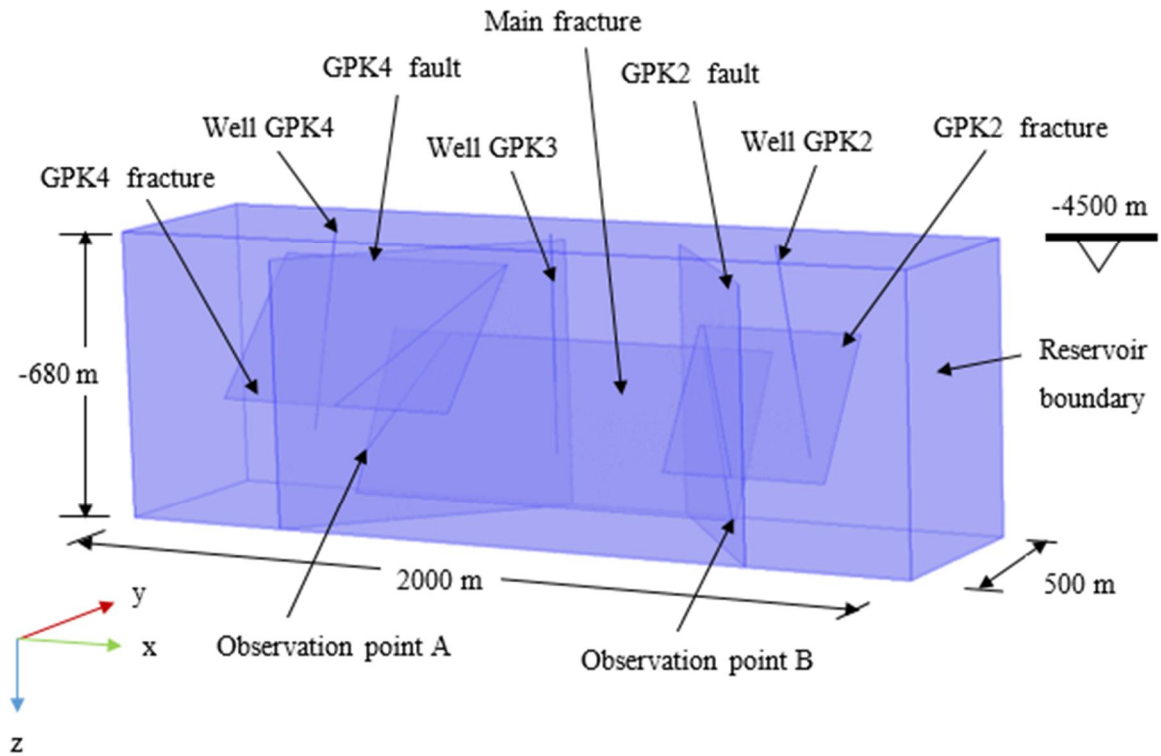


Figure 7.10: Geometry of the triplet reservoir with its various components

Figure 7.11 shows the finite element mesh quality of the triplet geothermal reservoir. The reservoir matrix block is discretised using 3-D tetrahedral elements, and the fractures and faults are meshed employing 2-D triangular elements. Furthermore, the wellbores are gridded using 1-D line elements. The generated grid comprises of 223,763 3-D four node elements, 10,202 2-D three node elements, 2,573 1-D two node elements, and 71 vertex elements. Due to the convolution of the system at hand, extra fine element sizes are applied for wellbores, whereas finer element sizes are employed for the matrix block, and intermediary element sizes are used on the fractures and faults with growth rates of 1.4 for the finer elements and 1.35 for the extra fine elements.

Figure 7.11 also represents the mesh quality of the model where 0 (i.e., zero) designate lower quality, and 1 (i.e., one) stands for the higher quality elements as shown by the legend. Thus, a better result is attained when the elements are not distorted or inverted as can be seen at the left and right edges of the reservoir. However, in the case where the elements are linked to other ones that have different shapes and orientation, for example, in the connection between wellbores and fractures or faults, then those elements will be

inverted to form other shapes with lower quality. The minimum element quality achieved from the numerical model is $3.056e-4$, with an average quality of 0.6222. The mesh volume of the model is 0.68 km^3 , with an element volume ratio of $1.336e-9$. In regard to growth rate, the maximum value obtained is 10.71, with an average rate of 2.084.

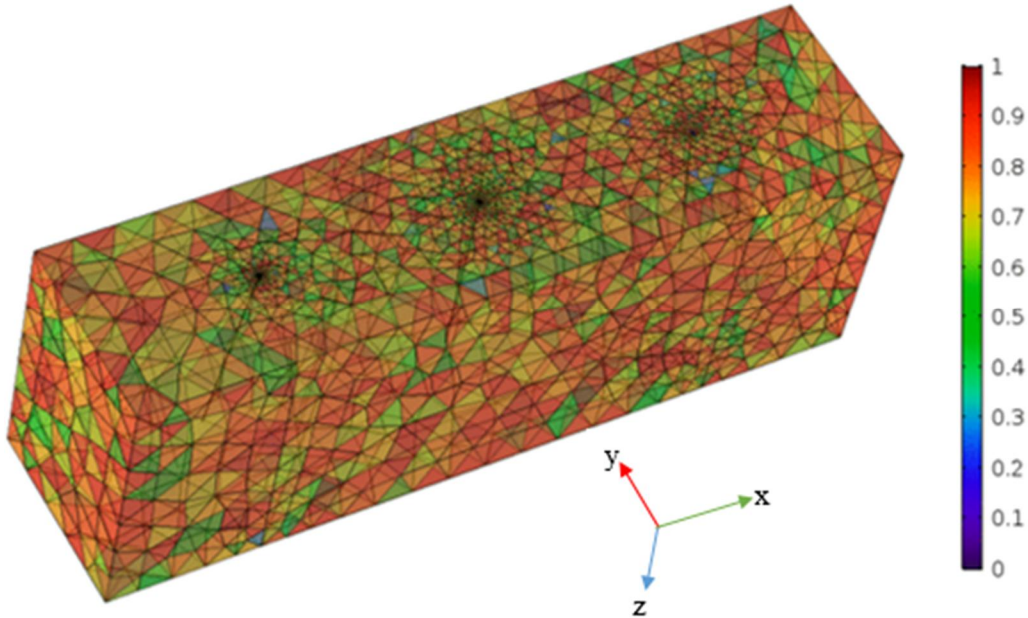


Figure 7.11: Mesh quality plot for the triplet reservoir

7.5.1 Reservoir initial and boundary conditions

In this work, the initial temperature is given as $T_0(z) = 12^\circ\text{C} - 38^\circ\text{C}/\text{km} \times (-z)$, where $T_0(z)$ is the initial reservoir temperature at time zero, 12°C is the assumed value of the surface temperature, $38^\circ\text{C}/\text{km}$ is the geothermal gradient, and z is the reservoir depth in kilometres. Also, the initial pressure is considered to be hydrostatic in the formation. As for the boundary conditions, a Dirichlet BC of 30°C is applied as the fluid injection temperature at injection wellbore GPK3, whereas for the hydraulic case, an injection pressure of 10 MPa is applied as the Dirichlet BC on the injection wellbore GPK3. Further, an underpressure Dirichlet BC of -10 MPa is employed on both the extraction wellbores GPK2 and GPK4, separately. All other boundaries are insulated during simulations. Table 7.1 above presents all the material and petrophysical properties employed for the analysis of both cases (i.e., doublet and triplet reservoirs), including geothermal reservoir conditions, fracture and fault conductivities, and matrix block thermal properties for a typical crystalline formation. The

material properties are similar to that of the doublet except this case where the injection fracture is shared by both production wellbores. A backwards difference formula is utilised in the solver to run the long-term simulation for 30 years. The method holds an advantage of reducing time steps because, in this study, it took only 51-time steps to simulate the 30-year numerical experimentation. The physical memory consumed is 5790 MB, and the virtual memory is 6170 MB.

7.5.2 Results

The following subsections present and discuss key results from the simulations of the triplet geothermal reservoir using the triple porosity-permeability model. The presented results are divided into three different sets. The first group of results presents the effect of conductive and convective heat fluxes during the long-term operation of 30 years. In the second set, the temperature contour plots are presented to examine the effect of temperature changes in the reservoir. The last round of results presents the pressure variation at some selected points along the fracture-fault interface.

7.5.2.1 Conductive and convective heat fluxes

In this segment, the heat flux directions were compared for both conduction and convection at various simulation stages using the arrow lines. The objective of this comparison is to show how each transfer mechanism contributes to the general solution of the problem and also to confirm the inclusion of the coupled effect processes in the entire simulation. Figure 7.12 shows the conductive heat flux direction after a one-year simulation time using the arrow lines. As can be observed, the arrow lines are pointing upwards in the reservoir volume, except at the injection point, and the upward direction indicates the heat flux direction. This shows that heat flow in the reservoir is from bottom to top because the lower region of the reservoir is hotter than the upper area. This effect is dominated within the rock matrix block and reservoir boundaries. However, in the case of the convective heat flux after a one-year simulation, the arrow lines are either pointing downwards or to left or right side, as shown in Figure 7.13. As can be seen, the arrows are pointing downwards to the reservoir boundaries while indicating left or right to the fractures and faults boundaries and their surrounding regions because heat flow within these areas is predominantly convective.

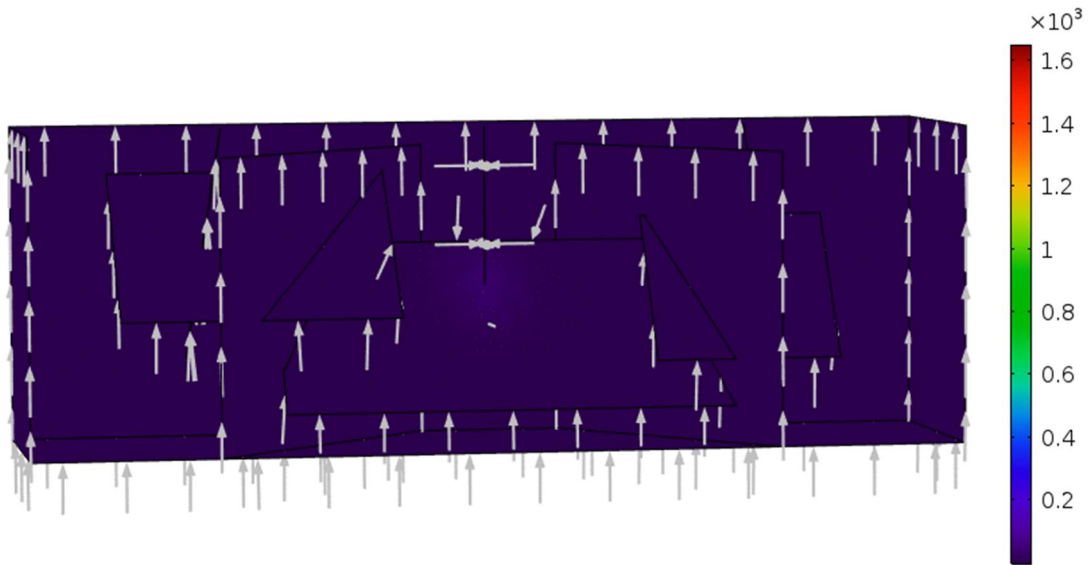


Figure 7.12: Conductive heat flux direction (W/m^2) after one-year of simulation

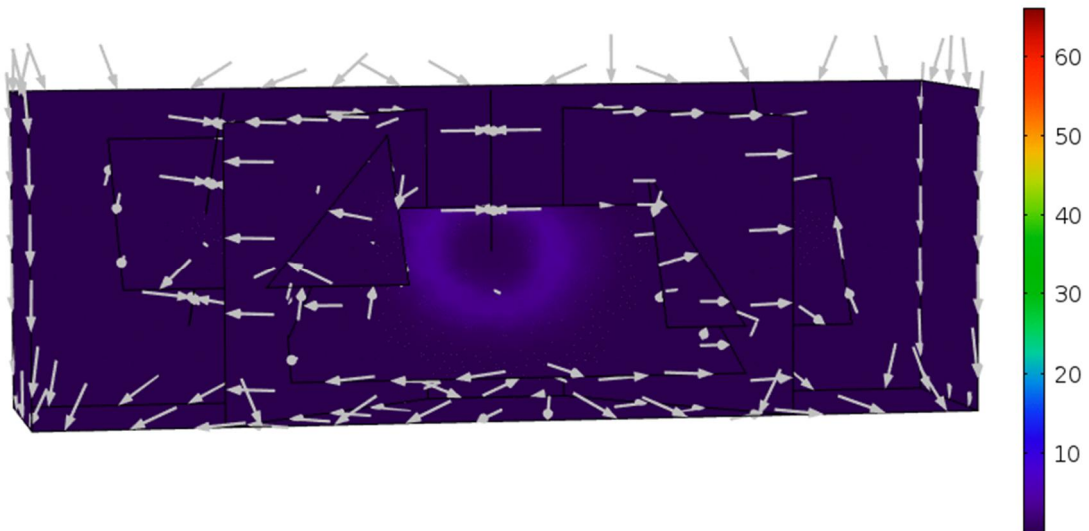


Figure 7.13: Convective heat flux direction (W/m^2) after one-year of simulation

Figure 7.14 presents the conductive heat flux after 30 years' operation using the arrow lines. In this case, some of the arrows that have previously pointed upwards in the one-year simulation time have realigned or changed direction at some particular regions. The regions in which the arrows shifted or changed orientation have experienced temperature losses. Cold water fluid injection under high pressure influences the temperature differences in those areas that cause the rock matrix to reduce its heat content through leakages at the edges of the fractures or faults.

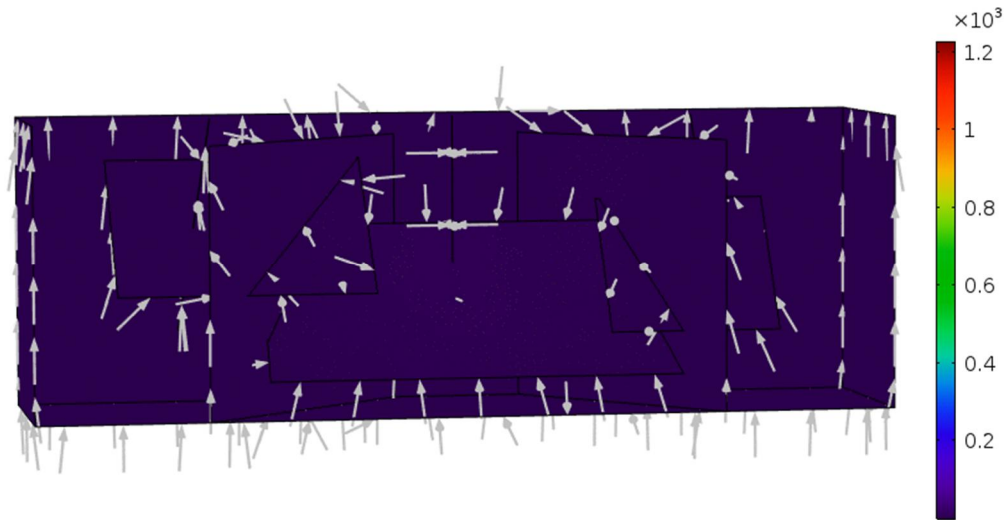


Figure 7.14: Conductive heat flux direction (W/m^2) after 30 years of simulation

Figure 7.15 shows the convective heat flux after 30 years' simulation employing the arrows as an indicator. As can be seen, the convective heat transport has dominated the fractures and faults as a result of forced circulation of fluid through these media from the injection wellbore to extraction wellbore in order to generate energy. As the simulation continues the rate of the convective heat transfer continues to decline with time because initially after the one-year operation the maximum heat flux is approximately equal to $65 \text{ W}/\text{m}^2$ and at the end of the 30-years simulation time convective heat flux drops to about $47 \text{ W}/\text{m}^2$. Besides, it is also evident from Figure 7.15 that the arrows are pointing towards the production wellbores that is either left or right in most cases, which makes it more different from the scenario of the conductive heat transfer.

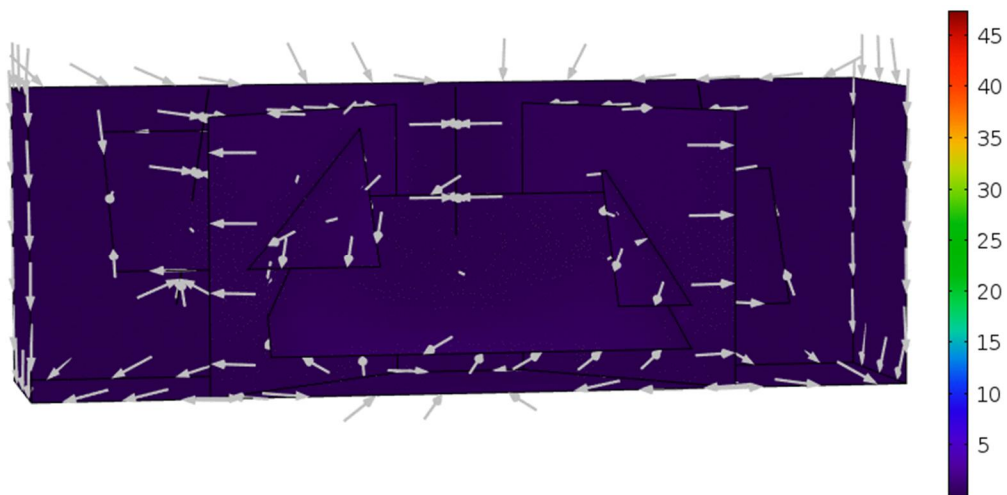


Figure 7.15: Convective heat flux direction (W/m^2) after 30 years of simulation

7.5.2.2 Coupled effect of temperature contour plots on the reservoir surfaces

Figure 7.16 shows the temperature contour plots after one year of operation within the reservoir under the coupled effect of both the conduction and convection heat transfer mechanisms. As can be observed from the temperature contour plot, there are some regions with a lower temperature while other areas have higher values such as the main fracture attached to the injection wellbore. The reason for this is that the fracture is of higher permeability than the matrix block, and therefore, fluid is transported via the fractured medium. Therefore, the cold fluid injection will have more of an effect on the fracture, as it is the main medium of communication between the injector and the producer. However, in this model, another medium is involved, which is the fault plane that serves as a mediator between the two. The lowest temperature observed at that region is approximately 61°C. Figure 7.17 presents the temperature contour plots after 30 years of simulation. As seen, after the operation continues, the cold-water region propagates and evolves on the fracture surface towards the adjacent fault planes due to their permeability properties. This medium is also linked to fracture, which is further connected to the producer. In this case, the lowest temperature observed is at the injection point, which is almost equal to the fluid injection temperature. Nevertheless, this does not show that the heat content of the reservoir cannot be further exploited; it is only a sign of decline within some sections of the reservoir that will be affected by the future exploitation.

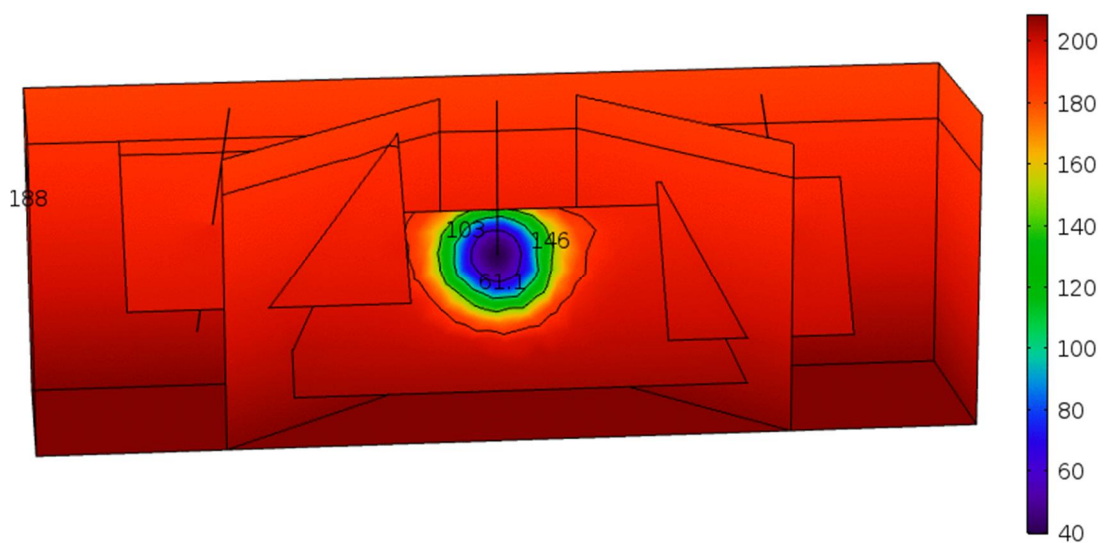


Figure 7.16: Temperature contour plot for the surfaces after one-year of simulation

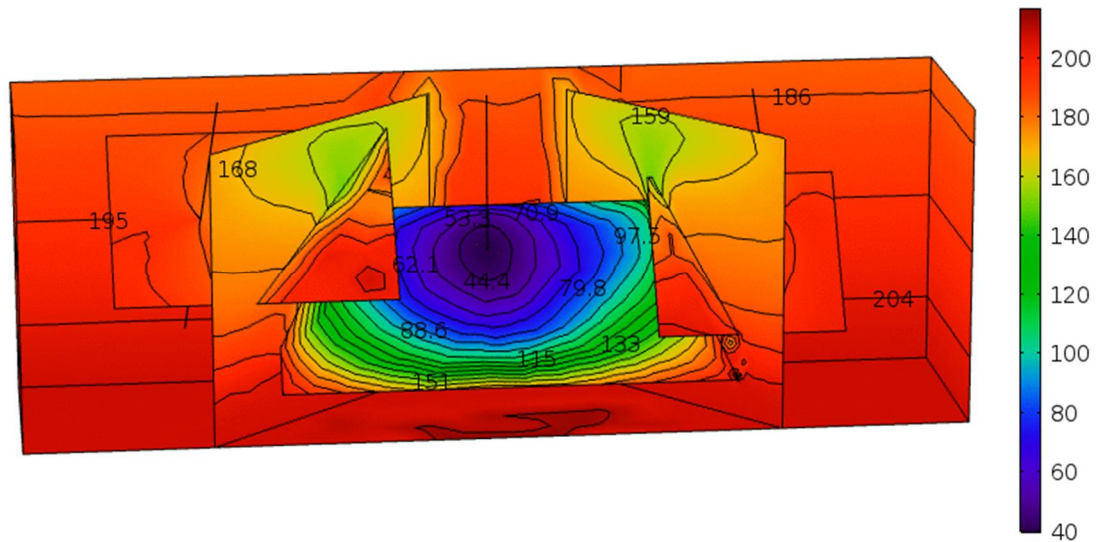


Figure 7.17: Temperature contour plot for the surfaces after 30-years of simulation

7.5.2.3 Fracture-fault fluid pressure at interface in the process of geothermal exploitation

Figure 7.18 shows the fluid pressure profile at observation points A and B (i.e., regarding Figure 7.10) during a long-term geothermal exploitation of 30 years. As can be seen, the fluid pressure rapidly increases throughout the operational stages. For instance, at point A, the initial pressure at time 0 is 48.1 MPa, and as the simulation continues, the fluid pressure increases to a maximum value of about 52.7 MPa at 30 years of operation. At point A, the change in pressure over time corresponds to a percentage increment in fluid pressure of 9.1%.

Figure 7.18 also presents the fluid pressure at point B using the same operation scenario as at point A. In this case, the initial fluid pressure at time 0 is 49.6 MPa, which is higher than in the previous case of point A because of the difference in the positioning of the points and the hydrostatic assumption of the pressure in the media. After 30 years of operation, the fluid pressure at point B increases to 53.3 MPa, but a maximum value of 53.4 MPa is achieved at 28.3 years. The reason for the variation of pressure towards the end of the profile could be due to gradient effect at the tip of the interface point. In this case, the percentage increase in fluid pressure with time is 7.5%, which is 1.6% less than the scenario at point A.

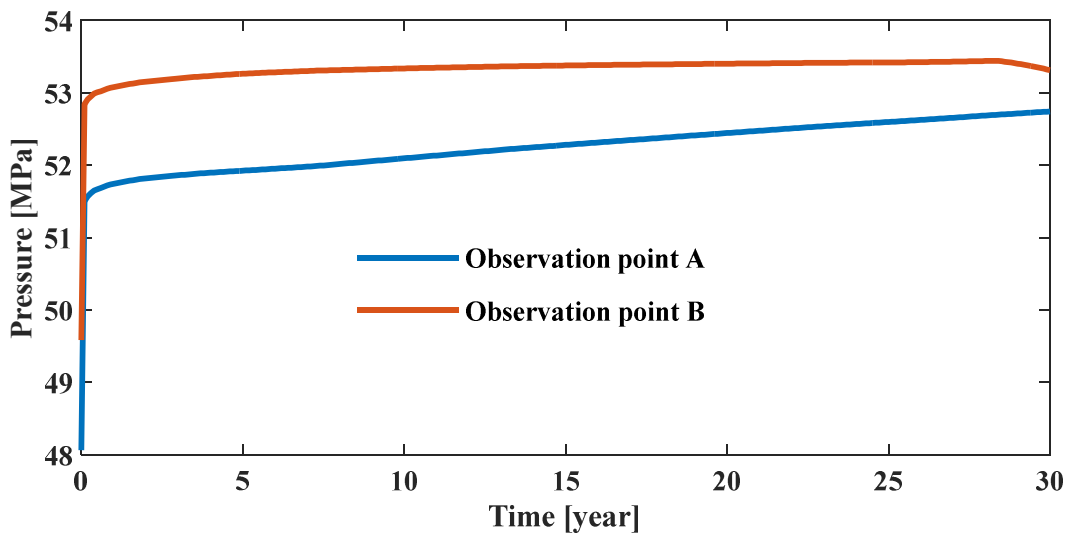


Figure 7.18: Pressure profile at observation points A and B

Furthermore, in both cases, at the early stages of the operation, the fluid pressure drastically fluctuates and then begins to increase up to the final exploitation period of 30 years where the ultimate maximum values are reached. Thus, the simulation results show that the fluid pressure of the fracture-fault pores increases with time, assuming that the fracture aperture remains constant throughout the operation.

7.6 Discussions

The successful implementation of the TPP model of deep geothermal reservoirs provides new insight on energy mining in complex geological formations. The approach facilitates integration of the different parts of multiple pore media. The contribution of each of the mediums in the naturally fractured-faulted system is implemented and addressed appropriately and accurately based on an existing geothermal field data of the Soultz (France). For instance, the fault plane serves as the fluid and heat pathway to both the injector and the producer by acceptance and delivery from the fractures connected to it. The proposed model can generate real-time exploitation using the long-term simulation forecasting of the system behaviour.

In the numerical case studies performed for both the doublet and triplet systems, it is evident that the reservoir pressure at the fracture-fault interface and observation points A

and B changes as the geothermal exploitation progresses. The pressure variations in the reservoir are a measure of the system performance regarding the productivity and injectivity indices. However, in real-life cases, the pressure is measured at the wellhead (i.e., at the surface) and is therefore affected by the transient characteristic of the fluid column in the wellbore. Thus, in the case where transients, such as temperature variations of the injected or produced fluid in the column, cannot be ignored, then the wellhead pressures must be corrected to compute reservoir pressures. Most importantly, the fluid density in the current model is a temperature dependent parameter; therefore, as the temperature changes in the reservoir due to the cold fluid injection under high pressure, it causes variations in the density of the fluid column and, as a result, leads to transient buoyancy effects.

The process of fluid and heat transport mechanism in a complex network of fractures and faults is a complicated phenomenon in which the final distribution of thermal energy depends on a series of factors, such as fault and fracture geometry, orientation, size, injection rate, and injection-fluid rheology. In reality, only a fraction of the fault and fracture network in the formation are active, and the effective activeness volume may play a dominant role in determining long-term productivity performance. Presenting a comprehensive evaluation from the economic point of view of the TPP method is out of the scope of this thesis. Nevertheless, the model can still assess the feasibility of energy mining in complex formations by examining the parameters needed for thermal exploitation and the corresponding extra-energy output.

The results presented in this study demonstrate that if the efficiency of the heat transfer process can be improved to open a significant amount of fluid pathways and enhance the overall flow capacity during the initial stage of the energy mining, then the ultimate recovery during the economic lifetime of the reservoir can be substantially enhanced. On the basis of the simulation results obtained from the previous sections, the net extra temperature produced within the fault plane through numerical modelling as shown in Figures 7.5, 7.6, and 7.7 can be used to estimate the amount of energy to be mined in the reservoir, which is because the fault plane transports the heat energy to the production wellbore via the fracture. From the results of case study two, where two producers are employed, it can be observed that the net recovery of extra pressure increases as the simulation continues, regardless of the matrix block permeability. In absolute terms, more

net extra temperature can be produced when permeability is higher, but in percentage terms (compared with the scenario where the triple porosity-permeability model is not applied), the TPP model seems efficient even when the permeability is lower. The results indicate much more extra temperature produced when heat transfer efficiency is improved, even within 30 years of thermal exploitation. It also shows that a longer operation time leads to more net recovery of extra heat in absolute terms but results in less extraction of additional temperature by percentage due to a cooling effect as shown in Figure 7.17.

From the results and analyses, it can be concluded that the TPP model has great potential to significantly improve geothermal reservoir ultimate recovery prediction by allowing the inclusion of other pore media effects to increase the overall flow capacity of the formation. However, the effectiveness of the TPP model on ultimate recovery largely depends on how much time it takes to create a communication between the injector and the producer. Because the creation of the connection has compound effects on the coupled underlying physics, the effects are cumulative. The sooner the link between the wellbores, the better the temperature at the outlet, and the longer the lifetime of the reservoir. As a result, the effectiveness of the energy mining can be enhanced significantly.

7.7 Summary

This chapter proposed a modelling-based approach of a triple porosity-permeability technique for a deep geothermal reservoir with multiple pore media. Two numerical models of geothermal reservoirs (i.e., doublet and triplet) are developed using a computationally efficient finite element method for coupled transient fluid and heat transport in a fully saturated porous media. The fluid and heat interaction among the fractures, faults, matrix, and wellbore components are explicitly incorporated in the numerical model, enabling the conversion of the spatial discretisation from 3-D to 1-D and making the model flexible to adopt the different scales.

Several results are obtained and analysed in-depth, such as the behaviour of the fracture-fault interface, the fault surface, and many others under the long-term operation of 30 years. The outcomes are to be interesting and promising because the model can set a foundation for future research efforts in modelling complex geological formations.

As a result of the computational capability and precision, the proposed numerical model provides the means for more insight into modelling naturally fractured-faulted reservoirs with multiple pore media that might assist in improving the approaches used for capturing realistic reservoir behaviour in the long-term.

Chapter eight – Conclusions and recommendations for future work

8.1 Introduction

This chapter presents the conclusions of the completed research conducted in this thesis based on the research questions presented in Chapter 1. It also discusses the achievements made on the current research and outline directions for the future work.

8.2 Conclusions

This section provides a comprehensive set of conclusions for the thesis based on the individual contributions of each of the chapters presented.

8.2.1 Review of existing models

An extensive literature review (Chapter 2) was conducted on HDR geothermal energy, which provided the required background knowledge for this thesis in respect of the fundamental understanding of theories, conceptual models, modelling approaches and the coupled processes. The contributions of the review to this thesis include the compilation of literature about the origin of HDR geothermal energy, detailed analyses of different modelling approaches and techniques resulting from the previous and current literature, highlights on coupled processes needed in subsurface modelling, and a brief introduction to porosity and permeability models. As part of the review, modelling was chosen as the sole focus of concern, as it provides more significant means of improving geothermal utilisation across the globe. The critical factors required in modelling HDR geothermal energy were identified, and their limitations mentioned.

8.2.2 FE formulation and solutions

In this thesis, equations were derived based on the conservation laws of mass, energy and momentum. Then, by that, the framework of the FEM for coupled thermo-hydraulic processes in naturally fractured geothermal reservoirs was developed and implemented (Chapter 3). The developed FEM model takes into account fully saturated porous media

connected to a fault system or discrete fractures, which operate concurrently together. The main contribution, in this case, was the development of the FE model that supports intersected and multiple fractures in 2-D space, which allows interaction with its surrounding media (matrix block, faults or reservoir boundaries). The fluid and heat transport processes behave like interacted multiple domain systems between the porous media and the fractures or faults domain. The field variables such as pressure and temperature were assumed to be continuous over the domains of all the structures (i.e. matrix block, fractures and faults) present in the model. The superposition of equations for the systems enables the model to solve them as a single algebraic system.

8.2.3 FE model verification and validation

The FE model developed was extensively verified and validated against well-established analytical solutions and field experimental measurements. The results obtained confirmed the reliability and robustness of the model in modelling deep HDR geothermal reservoirs and other related subsurface technologies. Therefore, the developed model has achieved its intended purpose since it can be applied to solve complex problems in deep subsurface media that are relevant to coupled TH processes.

8.2.4 Numerical modelling of a field case study

The successful execution of the verification and validation studies on the model has qualified the modelling of a field case study for testing of the model efficiency and prediction capability. The field case study chosen in this thesis is the Soultz geothermal system due to the wide availability of literature and its practicability. A 3-D numerical model of the Soultz lower reservoir was developed and simulated to test its long-term performance behaviour during 60 years of exploitation. Before conducting the simulation, issues associated with meshing were first encountered due to its practical implication in achieving a reliable FE solution. The major problem faced by many geothermal simulators is the inability to run the mesh conformity between the different scales encountered in the media. For example, regarding the dimensional scale difference between the wellbore and the reservoir matrix block, the former dimension scale is in millimetres while the latter is in kilometres. Thus, this work had succeeded in solving this problem efficiently as discussed in Chapters 5, 6 and

7, which is a significant contribution in modelling deep subsurface media. After implementing the mesh, a long-term simulation over 60 years was performed to forecast the performance behaviour of the reservoir during exploitation by employing factor experimentation design for the sensitivity analyses. The outcomes achieved from the field case study will contribute significantly to parameter control during real-life operations.

8.2.5 Numerical modelling of geothermal reservoirs with feedback interaction

The contribution of this thesis is the development of a new approach that allows the fluid transport to take place through a matrix before flowing through the fractures or vice versa, which is a new approach that is flexible in handling different scenarios encountered in subsurface media. The reason for this development is that the previous models relied on the principles that the fluid pathway must come from the fracture before moving into the matrix block, but some field experiments had contradicted this hypothesis; for example, the Soultz geothermal plant, as explained in Chapter 6. As a result of that, in this research, a 3-D numerical model of a deep heterogeneous geothermal reservoir was developed to study the effect of such events over the long-term performance of 30 years using parametric studies. Critical parameters that can be controlled were analysed under different operational scenarios to check the productivity of the system and its performance during the intended reservoir lifespan. The results obtained provided in-depth information on heat and fluid transport in deep HDR geothermal systems and energy mining in particular. It is of significant interest to the geothermal community, especially stakeholders and reservoir engineers, in further enhancing the growth of the field.

8.2.6 Numerical modelling of geothermal systems with multiple pore media

The application of multiple pore media in modelling deep geothermal systems is one of the outstanding issues from the advent of geothermal technology; however, in this research, the multiple pore media model was implemented using the triple porosity-permeability approach. The implementation of the model in the FE solver in 3-D space has made it one of the unique contribution in the field based on the author's knowledge. As a result of the successful implementation, several problems were modelled and analysed in-depth. The interaction of the fault system with fractures was part of the particular problems that require

broad investigation to understand its impact on energy mining. The numerical models developed in this case were grouped into two: the first set dealt with a doublet geothermal system while the second category studied a triplet system. In both cases, detailed analyses were conducted, and the influence of the different pore media upon energy mining, particularly the temperature variation during exploitation, was examined. In the end, the outcomes achieved in the development of a new technique in modelling deep geothermal systems will possibly open a new chapter in the field of computational modelling of subsurface technology.

8.2.7 Concluding statement

In this thesis, a new model is developed for the analyses of HDR geothermal energy in complex geological formations. The model is capable of modelling transient coupled thermo-hydraulic processes of geothermal systems and other related technologies. After conducting an extensive verification and validation studies on the FE model, the results confirm its accuracy and reliability in modelling HDR systems. Then, an existing field case study of HDR geothermal energy was implemented, and the long-term performance of the system over 60 years of exploitation was simulated. Also, sensitivity analyses were performed to determine which of the parameters affect energy productivity during exploitation. Furthermore, a new model of a heterogeneous geothermal reservoir that transmits fluid directly to the matrix block (i.e. instead of fractures) was developed, and the effect of human-controlled parameters on energy mining was analysed. In the end, a new HDR geothermal reservoir model with multiple pore media (i.e. matrix block, fractures and faults) was implemented using the triple porosity-permeability approach to determine the contribution of multiple pore media, in particular, the fracture-fault interface to overall reservoir performance. The outcomes obtained were promising and may well open a new chapter in the field of HDR geothermal energy.

8.3 Recommendations for future work

This thesis has addressed the application of a coupled modelling approach in predicting the long-term performance of an HDR geothermal system. Based on the results and findings

accomplished, there are some suggestions needed to be addressed in future research due to the model limitations. The recommendations are presented in the following subsections.

8.3.1 Development of mini-scale experiment to further validate the model

The development of mini-scale experiment is necessary to confirm the validity of the developed model further, although experimental validations were already performed, this will further help to improve the results obtained in the current model. The reason for this suggestion is the application of a full-scale experiment is costly and the limitation of the current technology in capturing the significant data needed during exploration/exploitation. Therefore, the mini-scale experiment will provide some fundamental insight on how this complex system works and contributes to further improvements of the model.

8.3.2 Implementation of mechanical and chemical processes

The implementation of a fully coupled model that incorporates the mechanical and chemical processes, in addition to the thermal and hydraulic processes already developed in this thesis, is critical for the deeper understanding of the effects of the other physics on the long-term performance of HDR systems. The mechanical process provides information on changes in the course of fluid injection and the heat transport during reservoir exploration/exploitation that results in the deformation and contraction of the porous medium and the fractures encountered in the subsurface. On the other hand, the chemical process shows the effect of the operations on the existing chemical found in the media including calcite and amorphous silicate, which precipitate and deposit as a result of the injection, temperature changes and the stress variation in the media. The resulting effect will be a complete blockage of the wellbores and the fluid pathways, especially the fractures. Thus, a more robust model that will capture the complete interaction processes in a multiphysics context is necessary for further understanding of HDR renewable energy in the broader perspective.

8.3.3 Implementation of fracture propagation models

In geothermal exploitation, fractures play a vital role in providing pathways for fluid flow and heat exchange. The fractures in subsurface media propagate at the direction of the minor

principal stress based on the Anderson Fault classification. The propagation occurs when the pressure applied (injection pressure) is higher than the less principal stress. The implementation of this process in a geothermal simulator is crucial in understanding the extent of the propagation during operation to further enhance energy mining. The fractures open when subjected to higher pressure with little thermal stresses; on the other hand, the fractures close whenever the pressure is reduced or other fractures open that are more extensive than the initial ones with higher thermal stresses. The opening and closing processes of the fractures affect the propagation rate and reservoir productivity. Furthermore, experimental works are also essential when developing a fracture propagation model to provide an accurate representation of the conceptual and mathematical assumption of the model proper.

8.3.4 Incorporation of non-Darcian flow

The application of non-Darcian flow, especially to the fracture surfaces, is a critical research area that requires further investigation for more in-depth insight on flow pattern in subsurface technology, in particular, the HDR systems. The roughness of the fracture surface will yield a turbulent flow within its vicinity, and that may likely affect the outcome of the computational results in either overestimating or underestimating the flow intensity. Therefore, it is necessary to extend the available mathematical or empirical models to take into account the effect of the fracture flow to overall HDR system performance.

8.3.5 Development of multi-phase flow models

The development of a partially saturated media model that allows a two-phase flow in HDR systems is significant in estimating the rates of steam and water produced by a geothermal facility. The injection of cold fluid into the reservoir under higher pressure forms a contact that allows the fluid to flow back through the wellbore; as the injection process continues, the cold fluid in the wellbore rises when it starts to lose pressure. Then, the fluid will eventually begin to boil, and this leads to a steam-water two-phase flow. Mathematical formulations of the problem are required to understand how this process evolves under a long-term exploitation of the HDR systems.

8.3.6 Development of realistic 3-D model of reservoirs

Realistic HDR models are needed for further justification of the available computational models of geothermal systems. In this regard, the primary concern is the number of degrees of freedom (DOF) that will be dealt with, which may sometimes result in 100-million DOFS, and the computational power to solve such a problem will be too expensive. Therefore, more robust modelling techniques are required to address this shortcoming with the help of parallel computing. A numerical model developed using the realistic approach gives a real-life representation of the HDR systems. The understanding of interface connectivity between the fractures is a very critical research area that will provide a further breakthrough in computational methods; this is because the fractures will overlap and each of the elements has to be treated separately before obtaining a reliable solution. As a result of that, the development of more dynamic meshing techniques is necessary for improving the solution efficiency of realistic HDR models.

References

- Aguilar, R.G., Dennis, B.R., Dreesen, D.S., Fehler, M.C., Hendron, R.H., House, L.S., Ito, H., Kelkar, S.M., Malzahn, M.V., 1989. ICFT: An initial closed-loop flow test of the Fenton Hill Phase II HDR reservoir. Los Alamos, NM.
- Arola, T., Eskola, L., Hellen, J., Korkka-Niemi, K., 2014. Mapping the low enthalpy geothermal potential of shallow Quaternary aquifers in Finland. *Geotherm. Energy* vol. 2, pp. 1-20.
- Axelsson, G., 1989. Simulation of Pressure Response Data from Geothermal Reservoirs by Lumped Parameter Models. In: *Proceedings of Fourteenth Workshop on Geothermal Reservoir Engineering* Stanford University, Stanford, California, January 24-26, 1989 SCP-TR-122, pp. 257–263.
- Axelsson, G., 2003. Essence of geothermal resource management. In: *IGC2003 Short Course*. Reykjavík, Iceland, pp. 129–151.
- Axelsson, G., 2013. Dynamic modelling of geothermal systems. *Short Course V Concept. Model. Geotherm. Syst*, pp 1-21.
- Bahrami, D., Danko, G., Fu, P., Guo, B., Podgorney, R., White, M., Xia, Y., 2015. Poroelastic and Self-Propped Single Fracture THM Models for EGS Studies. In: *Proceedings of Fortieth Workshop on Geothermal Reservoir* Stanford University, Stanford, California, , January 26-28, 2015, SGP-TR-204, pp. 1–20.
- Barbier, E., 2002. Geothermal energy technology and current status: an overview. *Renew. Sustain. Energy Rev.* vol. 6, pp. 3–65.
- Baria, R., Baumgärtner, J., Rummel, F., Pine, R.J., Sato, Y., 1999. HDR/HWR reservoirs: Concepts, understanding and creation. *Geothermics* vol. 28, pp. 533–552.
- Barth, T.J., Griebel, M., Keyes, D.E., Nieminen, R.M., Roose, D., Schlick, T., 2010. *Lecture Notes in Computational Science and Engineering*, Springer.
- Barton, C.A., Zoback, M.D., Moos, D., 1995. Fluid flow along potentially active faults in crystalline rock. *Geology* vol. 23, pp. 683–686.

- Batchelor, A., 1986. Reservoir behaviour in a stimulated hot dry rock system. In: Proceedings of Eleventh Workshop on Geothermal Reservoir Engineering Stanford University, Stanford, California, January 21-23, 1986, SCP-TR-93. pp. 35–41.
- Bayer, P., Rybach, L., Blum, P., Brauchler, R., 2013. Review on life cycle environmental effects of geothermal power generation. *Renew. Sustain. Energy Rev.* vol. 26, pp. 446–463.
- Bear, J., 1993. *Flow and Contaminant Transport in Fractured Rock*. Academic Press, Inc, London.
- Bertani, R., 2015. Geothermal Power Generation in the World 2010 – 2014 Update Report. In: Proceedings World Geothermal Congress, 19-25 April 2015, Melbourne, Australia. pp. 1–19.
- Bertani, R., 2016. Geothermal power generation in the world 2010-2014 update report. *Geothermics* vol. 60, pp. 31–43.
- Blázquez, C.S., Martín, A.F., García, P.C., Sánchez Pérez, L.S., del Caso, S.J., 2016. Analysis of the process of design of a geothermal installation. *Renew. Energy* vol. 89, pp. 188–199.
- Blöcher, M.G., Zimmermann, G., Moeck, I., Brandt, W., Hassanzadegan, A., Magri, F., 2010. 3D numerical modeling of hydrothermal processes during the lifetime of a deep geothermal reservoir. *Geofluids* vol. 10, pp. 406–421.
- Bowen, R., 1989. *Geothermal Resources*, Edition, S. ed. Springer Netherlands, Dordrecht.
- Bower, K.M., Zyvoloski, G., 1997. A numerical model for thermo-hydro-mechanical coupling in fractured rock. *Int. J. Rock Mech. Min. Sci.* vol. 34, pp. 1201–1211.
- Boyd, L., 2013. Geothermal Energy: A Glance Back and a Leap Forward [WWW Document]. *Off. Energy Effic. Renew. Energy*. URL <http://energy.gov/eere/articles/geothermal-energy-glance-back-and-leap-forward> (accessed 16.10.17).

Brown, D.W., 1997. Review of Fenton Hill HDR Test Results. In: Conference: New Energy and Industrial Technology Development Organization (NEDO) Geothermal and HRD Conference, Sendai (Japan), 10-17 Mar 1997; Other Information: PBD: 1997. Washington, pp. 1–8.

Brown, D.W., 2009. Hot dry rock geothermal energy: important lessons from Fenton Hill. In: Proceedings of Thirty-Fourth Workshop on Geothermal Reservoir Engineering, Stanford University, Stanford, California, February 1-3, 2010, SGP-TR-188, pp. 3–6.

Brown, D.W., Duchane, D. V., Heiken, G., Hriscu, V.T., 2012. Mining the Earth's Heat: Hot Dry Rock Geothermal Energy, First Edit. ed. Springer Berlin Heidelberg, Berlin, Heidelberg.

Brown, D.W., Duchane, D. V., 1999. Scientific progress on the Fenton Hill HDR project since 1983. *Geothermics* vol. 28, pp. 591–601.

Brunner, M., Gorhan, H.L., Rybach, L., 2015. Geothermal Energy: Plentiful and Environmentally Friendly. Germany.

Burnell, J., Sullivan, M.O., Sullivan, J.O., Kissling, W., Croucher, A., Pogacnik, J., Caldwell, G., Ellis, S., Zarrouk, S., Climo, M., 2015. Geothermal Supermodels : the Next Generation of Integrated Geophysical , Chemical and Flow Simulation Modelling Tools. In: Proceedings of World Geothermal Congress, April 2015, Melbourne, Australia, pp. 19-25.

Charl ty, J., Cuenot, N., Dorbath, L., Dorbath, C., Haessler, H., Frogneux, M., 2007. Large earthquakes during hydraulic stimulations at the geothermal site of Soultz-sous-For ts. *Int. J. Rock Mech. Min. Sci.* vol. 44, pp. 1091–1105.

Chen, T., Clauser, C., Marquart, G., Willbrand, K., B sing, H., 2016. Modeling anisotropic flow and heat transport by using mimetic finite differences. *Adv. Water Resour.* vol. 94, pp. 441–456.

Cheng, A. H.-D., Ghassemi, A., Detournay, E., 2001. Integral equation solution of heat extraction from a fracture in hot dry rock. *Int. J. Numer. Anal. Methods Geomech.* vol. 25, pp. 1327–1338.

- Cheng, P., Lau, K.H., 1973. Numerical modelling of Hawaiian geothermal resources. *Geothermics* vol. 2, pp. 90–93.
- Cheng, W.-L., Li, T.-T., Nian, Y.-L., Wang, C.-L., 2013. Studies on geothermal power generation using abandoned oil wells. *Energy* vol. 59, pp. 248–254.
- Cheng, W.L., Liu, J., Nian, Y. Le, Wang, C.L., 2016a. Enhancing geothermal power generation from abandoned oil wells with thermal reservoirs. *Energy* vol. 109, 537–545.
- Cheng, W.L., Wang, C.L., Nian, Y. Le, Han, B.B., Liu, J., 2016b. Analysis of influencing factors of heat extraction from enhanced geothermal systems considering water losses. *Energy* vol. 115, 274–288.
- Choi, E.S., Cheema, T., Islam, M.R., 1997. A new dual-porosity/dual-permeability model with non-Darcian flow through fractures. *J. Pet. Sci. Eng.* vol. 17, 331–344.
- Clauser, C., 2006. Geothermal Energy. In: *Advanced Materials and Technologies*. Springer-Verlag, Heidelberg-Berlin, pp. 493–604.
- Collins, L.M., Dziak, J.J., Kugler, K.C., Trail, J.B., 2014. Factorial Experiments. *Am. J. Prev. Med.* vol. 47, pp 498–504.
- Cowles, B., Backman, D., Dutton, R., 2012. Verification and validation of ICME methods and models for aerospace applications. *Integr. Mater. Manuf. Innov.* vol. 1, pp. 2.
- Cremer, G.M., Duffield, R.B., Smith, M.C., Wilson, M.G., 1980. Hot Dry Rock Geothermal Energy Development Program. Annual report, fiscal year 1979, Annual Report. Los Alamos, NM, pp 1-256.
- Dash, Z.V., Murphy, H.D., Aamodt, R.L., Aguilar, R.G., Brown, D.W., Counce, D.A., Fisher, H.N., Grigsby, C.O., Keppler, H., Laughlin, A.W., Potter, R.M., Tester, J.W., Trujillo, P.E., Zyvoloski, G., 1983. Hot dry rock geothermal reservoir testing: 1978 to 1980. *J. Volcanol. Geotherm. Res.* vol. 15, 59–99.
- Dayan, G.M., Ambunya, M., 2015. Geothermal Energy-Making It Renewable and Sustainable. In: *Proceedings of Fortieth Workshop on Geothermal Reservoir Stanford University, Stanford, California, January 26-28, 2015, SGP-TR-204*, pp. 1–8.

- Dempsey, D., Kelkar, S., Devatzes, N., Hickman, S., Moos, D., Zemach, E., 2014. Evaluating the Roles of Thermoelastic and Poroelastic Stress Changes in the Desert Peak EGS Stimulation. In: Proceedings of Thirty-Ninth Workshop on Geothermal Reservoir Stanford University, Stanford, California, February 24-26, 2014, SGP-TR-202, pp. 1–14.
- Dempsey, D., Kelkar, S., Lewis, K., 2013. Modeling Shear Stimulation of the Desert Peak EGS Well 27-15 Using a Coupled Thermal-Hydrological-Mechanical Simulator. In: 47th US Rock Mechanics/Geomechanics Symposium. San Francisco, CA, pp. 1–15.
- Dezayes, C., Chèvremont, P., Tourlière, B., Homeier, G., Genter, A., 2005. Geological study of the GPK4 HFR borehole and correlation with the GPK3 borehole (Soulz-sous-Forêts, France), BRGM/RP-53697-FR, pp. 1-51.
- Dezayes, C., Genter, A., Chevremont, P., Glen Homeier, Gerridina Hooijkaas, B.T., Stein, G., Degouy, M., 2004. Deep Seated Geology of the Soultz Basement Based on Geological Data of GPK3 and GPK4 Wells. In: BRGM. pp. 1–12.
- Dezayes, C., Genter, A., Valley, B., 2010. Structure of the low permeable naturally fractured geothermal reservoir at Soultz. *Comptes Rendus Geosci.* vol. 342, pp. 517–530.
- Dezayes, C., Gentier, S., Genter, A., 2005. Deep Geothermal Energy in Western Europe: The Soultz Project. France.
- Duchane, D., Brown, D., 1994. Hot Dry Rock Geothermal Energy Development in the USA, Cint.Lanl.Gov. Norwood.
- Duchane, D., Brown, D., 2002. Hot Dry Rock (HDR) Geothermal Energy Research and Development at Fenton Hill, New Mexico. Norwood.
- Duchane, D. V., 1995. Heat Mining to Extract Hot Dry Rock (HDR) Geothermal Energy: Technical & Scientific Progress. Los Alamos National Laboratory, Geothermal Energy R&D Program, New Mexico.
- DuTeaux, R., Swenson, D., Hardeman, B., 1996. Insight from modelling discrete fractures using GEOCRACK. In: Proceedings of Twenty-First Workshop on Geothermal Reservoir Engineering. Stanford. California. January 27-29, 1997, SGP-TR- 155, pp. 287–293.

Elsworth, D., 1986. A hybrid boundary element-finite element analysis procedure for fluid flow simulation in fractured rock masses. *Int. J. Numer. Anal. Methods Geomech.* vol. 10, pp. 569–584.

Elsworth, D., 1989a. Theory of thermal recovery from a spherically stimulated hot dry rock reservoir. *J. Geophys. Res.* vol. 94, pp. 1927-1934.

Elsworth, D., 1989b. Thermal recovery from a multiple stimulated HDR reservoir. *Geothermics* vol. 18, pp. 761–774.

Elsworth, D., 1990. A comparative evaluation of the parallel flow and spherical reservoir models of HDR geothermal systems. *J. Volcanol. Geotherm. Res.* vol. 44, pp. 283–293.

Elsworth, D., Gan, Q., Hao, Y., 2016. Benchmark Problems of the Geothermal Technologies Office Code Comparison Study. Alexandria, VA.

Fagan, M.J., 1992. *Finite Element Analysis: Theory and Practice*, Illustrate. ed. Longman Scientific & Technical, Essex, England.

Fairs, T.H., Younger, P.L., Parkin, G., 2015. Parsimonious numerical modelling of deep geothermal reservoirs. In: *Proceedings of the Institution of Civil Engineers, Energy*. pp. 1–11.

Farghally, H.M., Atia, D.M., El-madany, H.T., Fahmy, F.H., 2014. Control methodologies based on geothermal recirculating aquaculture system. *Energy* vol. 78, pp. 826–833.

Farmahini-farahani, M., Ghassemi, A., 2015. Analysis of Fracture Network Response to Fluid Injection. In: *Proceedings of Fourtieth Workshop on Geothermal Reservoir Engineering Stanford University, Stanford, California, January 26-28, 2015*, pp. 1–10.

Faust, C.R., Mercer, J.W., 1979a. Geothermal reservoir simulation: 2. Numerical solution techniques for liquid- and vapor-dominated hydrothermal systems. *Water Resour. Res.* vol. 15, pp. 31–46.

Faust, C.R., Mercer, J.W., 1979b. Geothermal reservoir simulation: 1. Mathematical models for liquid- and vapor-dominated hydrothermal systems. *Water Resour. Res.* vol. 15, pp. 23–30.

- Fischer, T., Naumov, D., Sattler, S., Kolditz, O., Walther, M., 2015. GO2OGS 1.0: A versatile workflow to integrate complex geological information with fault data into numerical simulation models. *Geosci. Model Dev.* vol. 8, pp. 3681–3694.
- Genter, A., Baumgärtner, J., Cuenot, N., Graff, J.J., T. Kölbel, Sanjuan, B., 2010a. The EGS case study : lessons learnt after two decades of geothermal researches . In: *Second European Geothermal Review- Geothermal Energy for Power Production*, June 21-23, 2010, Mainz, Germany. pp. 4–7.
- Genter, A., Castaing, C., Dezayes, C., Tenzer, H., Traineau, H., Villemin, T., 1997. Comparative analysis of direct (core) and indirect (borehole imaging tools) collection of fracture data in the Hot Dry Rock Soultz reservoir (France). *J. Geophys. Res.* 102, 15,419–15,431.
- Genter, A., Evans, K., Cuenot, N., Baticci, F., Dorbath, L., Graff, J., Sanjuan, B., 2009. The EGS Soultz project (France): From reservoir development to electricity production. *Trans. - Geotherm. Resour. Counc.* vol. 33, pp. 346–351.
- Genter, A., Evans, K., Cuenot, N., Fritsch, D., Sanjuan, B., 2010b. Contribution of the exploration of deep crystalline fractured reservoir of Soultz to the knowledge of enhanced geothermal systems (EGS). *Comptes Rendus Geosci.* vol. 342, pp. 502–516.
- Genter, A., Evans, K., Cuenot, N., Fritsch, D., Sanjuan, B., 2010c. Contribution of the exploration of deep crystalline fractured reservoir of Soultz to the knowledge of enhanced geothermal systems (EGS). *Comptes Rendus Geosci.* vol. 342, pp. 502–516.
- Genter, A., Goerke, X., Graff, J., Cuenot, N., Krall, G., Schindler, M., Ravier, G., 2010d. Current Status of the EGS Soultz Geothermal Project (France). In: *World Geothermal Congress*, 2010, France, pp. 25–29.
- Gérard, A., Genter, A., Kohl, T., Lutz, P., Rose, P., Rummel, F., 2006. The deep EGS (Enhanced Geothermal System) project at Soultz-sous-Forêts (Alsace, France). *Geothermics* vol. 35, pp. 473–483.
- Ghasemi, H., Sheu, E., Tizzanini, A., Paci, M., Mitsos, A., 2014. Hybrid solar–geothermal power generation: Optimal retrofitting. *Appl. Energy* vol. 131, pp. 158–170.

Ghassemi, A., 2007. Stress and Pore Pressure Distribution Around a Pressurized , Cooled Crack in Low Permeability Rock. In: Proceedings of Thirty-Second Workshop on Geothermal Reservoir Engineering Stanford University, Stanford, California, January 22-24, 2007, pp. 1–7.

Ghassemi, A., Cheng, A.H.-D., Diek, A., Roegiers, J.-C., 2001. A complete plane strain fictitious stress boundary element method for poroelastic media. *Eng. Anal. Bound. Elem.* vol. 25, pp. 41–48.

Ghassemi, A., Kelkar, S., McClure, M., 2015. Influence of Fracture Shearing on Fluid Flow and Thermal Behavior of an EGS Reservoir - Geothermal Code Comparison Study. In: Proceedings of Fourtieth Workshop on Geothermal Reservoir Engineering Stanford University, Stanford, California, January 26-28, 2015, pp. 1–14.

Ghassemi, A., Nygren, A., Cheng, A., 2008. Effects of heat extraction on fracture aperture: A poro–thermoelastic analysis. *Geothermics* vol. 37, pp. 525–539.

Ghassemi, A., Tarasovs, S., 2006. Fracture Slip and Opening in Response to Fluid Injection into a Geothermal Reservoir. In: Thirty-First Workshop on Geothermal Reservoir Engineering Stanford University, Stanford, California, January 30-February 1, 2006, pp. 1–8.

Ghassemi, A., Tarasovs, S., Cheng, A.H.D., 2007. A 3-D study of the effects of thermomechanical loads on fracture slip in enhanced geothermal reservoirs. *Int. J. Rock Mech. Min. Sci.* vol. 44, pp. 1132–1148.

Ghassemi, A., Zhang, Q., 2004. Poro-Thermoelastic Mechanisms in Wellbore Stability and Reservoir Stimulation. In: Twenty-Ninth Workshop on Geothermal Reservoir Engineering Stanford University, Stanford, California, January 26-28, 2004 SGP-TR-173. California, pp. 1–7.

Ghassemi, A., Zhang, Q., 2004. A transient fictitious stress boundary element method for porothermoelastic media. *Eng. Anal. Bound. Elem.* vol. 28, pp. 1363–1373.

Ghassemi, A., Zhang, Q., 2006. Poro thermoelastic Analysis of the Response of a Stationary Crack Using the Displacement Discontinuity Method. *J. Eng. Mech.* vol. 132, pp. 26–33.

Ghassemi, A., Zhou, X.X., Rawal, C., 2013. A three-dimensional poroelastic analysis of rock failure around a hydraulic fracture. *J. Pet. Sci. Eng.* vol. 108, pp. 118–127.

Guillou-Frottier, L., Carré, C., Bourguine, B., Bouchot, V., Genter, A., 2013. Structure of hydrothermal convection in the Upper Rhine Graben as inferred from corrected temperature data and basin-scale numerical models. *J. Volcanol. Geotherm. Res.* vol. 256, pp. 29–49.

Hamza, V.M., Cardoso, R.R., Ponte Neto, C.F., 2008. Spherical harmonic analysis of earth's conductive heat flow. *Int. J. Earth Sci.* vol. 97, pp. 205–226.

Hardeman, B., Swenson, D., 1998. A Geometric Modeling Framework for the Numerical Analysis of Geothermal Reservoirs. In: *Proceedings of Twenty-Third Workshop on Geothermal Reservoir Engineering* Stanford University, Stanford, California, January 26–28, 1998, pp. 147–151.

Hebert, R., Ledesert, B., 2012. Calcimetry at soultz-sous-forêts enhanced geothermal system: relationships with fracture zones, flow pathways and reservoir chemical stimulation results. In: Yang, J. (Ed.), In “*Geothermal Energy, Technology and Geology*”, Edited by Jianwen Yang, Nova Science Publishers Inc., NY, Chapter 3. Nova Science Publishers, Inc., pp. 93–113.

Hébert, R.L., Ledésert, B., Bartier, D., Dezayes, C., Genter, A., Grall, C., 2010. The Enhanced Geothermal System of Soultz-sous-Forêts: A study of the relationships between fracture zones and calcite content. *J. Volcanol. Geotherm. Res.* vol. 196, pp. 126–133.

Held, S., Genter, A., Kohl, T., Kölbl, T., Sausse, J., Schoenball, M., 2014. Economic evaluation of geothermal reservoir performance through modeling the complexity of the operating EGS in Soultz-sous-Forêts. *Geothermics* vol. 51, pp. 270–280.

Hicks, T.W., Pine, R.J., Willis-Richards, J., Xu, S., Jupe, A.J., Rodrigues, N.E.V., 1996. A hydro-thermo-mechanical numerical model for HDR geothermal reservoir evaluation. *Int. J. Rock Mech. Min. Sci. Geomech.* vol. 33, pp. 499–511.

Holtz, M., 2012. *Thermo-Hydro-Mechanical-Chemical Processes in Porous Media*, Science, Lecture Notes in Computational Science and Engineering. Springer Berlin Heidelberg, Berlin, Heidelberg.

Holzbecher E.O., 1998. Modeling density-driven flow in porous media. Berlin, Heidelberg: Springer Berlin Heidelberg.

Huang, K., Ghassemi, A., 2012a. Modeling 3D Thermal Fracturing Using Virtual Multidimensional Internal Bonds. GRC Trans. vol. 36, pp. 469–474.

Huang, K., Ghassemi, A., 2012b. Modeling 3D Hydraulic Fracture Propagation and Thermal Fracturing Using Virtual Multidimensional Internal Bonds. In: Proceedings of Thirty-Sixth Workshop on Geothermal Reservoir Engineering Stanford University, Stanford, California, January 30 - February 2, 2012, pp. 1–11.

Huang, Y., Ren, S., Zhang, D., 2015. Current Status and Developing Trend of Direct Use in Global Geothermal Resource. In: Proceedings of Fortieth Workshop on Geothermal Reservoir Engineering Stanford University, Stanford, California, January 26-28, 2015 SGP-TR-204, pp. 1–8.

Hughes, T.J.R., 1987. The Finite Element Method: Linear Static and Dynamic Finite Element Analysis, 1st ed, Prentice-Hall, Inc. Prentice-Hall, Inc., Englewood Cliffs, N.J.

Huttrer, G.W., 1996. The status of world geothermal power production 1990–1994. Geothermics vol. 25, pp. 165–187.

Huttrer, G.W., 2001. The status of world geothermal power generation 1995–2000. Geothermics vol. 30, pp. 1–27.

International Energy Agency, 2013. IEA Geothermal Implementing Agreement Annual Report 2013. USA.

IPGT, 2012. International Partnership for Geothermal Technology Geothermal Reservoir Modeling Recommendations for Research and Development. Iceland.

Jaime Jemuel C. Austria, J., Sullivan, M.J.O., 2015. Dual Porosity Models of a Two-phase Geothermal Reservoir. In: Proceedings of World Geothermal Congress 2015 Melbourne, Australia, 19-25 April 2015, pp. 1–2.

Jain, C., Vogt, C., Clauser, C., 2015. Maximum potential for geothermal power in Germany based on engineered geothermal systems. Geotherm. Energy vol. 3, pp. 1-20.

Jeremić, B., Cheng, Z., Taiebat, M., Dafalias, Y., 2008. Numerical simulation of fully saturated porous materials. *Int. J. Numer. Anal. Methods Geomech.* vol. 32, pp. 1635–1660.

Jupe, A., Bruel, D., Hicks, T., Hopkirk, R., Kappelmeyer, O., Kohl, T., Kolditz, O., Rodrigues, N., Wallroth, T., Willis-Richards, J., Xu, S., 1995. Numerical Modelling of HDR Reservoirs. In: *Proceedings of World Geothermal Congress, Florence, Italy, 18-31 May 1995*, pp. 2571–2574.

Jupe, A.J., Bruel, D., Hicks, T., Hopkirk, R., Kappelmeyer, O., Kohl, T., Kolditz, O., Rodrigues, N., Smolka, K., Willis-Richards, J., Wallroth, T., Xu, S., 1995. Modelling of a european prototype hdr reservoir. *Geothermics* vol. 24, pp. 403–419.

Karvounis, D.C., Wiemer, S., 2015. Decision making software for forecasting induced seismicity and thermal energy revenues in enhanced geothermal systems. In: *Proceedings of World Geothermal Congress 2015. Melbourne, Australia*, pp. 1–10.

Kelkar, S., WoldeGabriel, G., Rehfeldt, K., 2016. Lessons learned from the pioneering hot dry rock project at Fenton Hill, USA. In: *Geothermics. CNR-Istituto di Geoscienze e Georisorse*, pp. 5–14.

Kohl, T., Bächler, D., Rybach, L., 2000. Steps towards a comprehensive thermo-hydraulic analysis of the HDR test site Soultz-sous-Forêts. In: *Proceedings of World Geothermal Congress 2000 Kyushu - Tohoku, Japan, May 28 - June 10, 2000*, pp. 3459–3464.

Kohl, T., Evans, K.F., Hopkirk, R.J., Jung, R., Rybach, L., 1997. Observation and simulation of non-Darcian flow transients in fractured rock. *Water Resour. Res.* vol. 33, pp. 407–418.

Kohl, T., Evans, K.F., Hopkirk, R.J., Rybach, L., 1995. Coupled hydraulic, thermal and mechanical considerations for the simulation of hot dry rock reservoirs. *Geothermics* vol. 24, pp. 345–359.

Kohl, T., Hopkirk, R.J., 1995. “FRACure” — A simulation code for forced fluid flow and transport in fractured, porous rock. *Geothermics* vol. 24, pp. 333–343.

Kohl, T., Rybach, L., 1996. Thermal and hydraulic aspects of the KTB drill site. *Geophys. J. Int.* vol. 124, pp. 756–776.

Kolditz, O., Bauer, S., Bilke, L., Böttcher, N., Delfs, J.O., Fischer, T., Görke, U.J., Kalbacher, T., Kosakowski, G., McDermott, C.I., Park, C.H., Radu, F., Rink, K., Shao, H., Shao, H.B., Sun, F., Sun, Y.Y., Singh, A.K., Taron, J., Walther, M., Wang, W., Watanabe, N., Wu, Y., Xie, M., Xu, W., Zehner, B., 2012a. OpenGeoSys: an open-source initiative for numerical simulation of thermo-hydro-mechanical/chemical (THM/C) processes in porous media. *Environ. Earth Sci.* vol. 67, pp. 589–599.

Kolditz, O., Clauser, C., 1998. Numerical simulation of flow and heat transfer in fractured crystalline rocks: Application to the Hot Dry Rock site in Rosemanowes (U.K.). *Geothermics* vol. 27, pp. 1–23.

Kolditz, O., Görke, U.-J., Shao, H., Wang, W., Bauer, S., 2015. Thermo-Hydro-Mechanical-Chemical Processes in Fractured Porous Media: Modelling and Benchmarking, *Terrestrial Environmental Sciences*. Springer International Publishing, Cham.

Kolditz, O., Görke, U.-J., Shao, H., Wang, W., Bauer, S., 2016. Thermo-Hydro-Mechanical-Chemical Processes in Fractured Porous Media: Modelling and Benchmarking, *Terrestrial Environmental Sciences*. Springer International Publishing, Cham.

Kolditz, O., Jakobs, L. a, Huenges, E., Kohl, T., 2013. Geothermal Energy: a glimpse at the state of the field and an introduction to the journal. *Geotherm. Energy* vol. 1, pp. 1-2.

Kruger, P., 1995a. Heat Extraction from HDR Geothermal Reservoirs. In: *Proceedings of World Geothermal Congress, Florence, Italy, 18-31 May 1995*, pp. 2517–2520.

Kruger, P., Aragon, A., Maciel, R., Lucio, C., Villa, J., 1988. Preproduction simulation of thermal decline at LA PRIMA VERA first 5-MW wellhead units. *Geotherm. Resour. Counc. Trans.* vol. 12, pp. 475–480.

Kruger, P., Hicks, T., Willis-Richards, J., 1992. The Potential for Thermal Energy Extraction from Cornish Granite. *Geotherm. Resour. Counc. Trans.* vol. 16, pp. 465–472.

Kruger, P., Quijano, L., 1995. Thermal Extraction Analysis of Five Los Azufres Production Wells. In: *Proceedings of Twentieth Workshop on Geothermal Reservoir Engineering Stanford University, Stanford, California, January 24-26 1995*, pp. 17–22.

Kruger, P., Sato, Y., Shinohara, N., 1996. Analysis of Energy Extraction in the 1995 Hijiori 25-Day Circulation Test. *Geotherm. Resour. Counc. Trans.* vol. 20, pp. 457–463.

Kun, W., 2005. Studies of the Reinjection Tests in Basement Geothermal Reservoir , Tianjin , China. In: *Proceedings World Geothermal Congress 2005 Antalya, Turkey, 24-29 April 2005*, pp. 1–6.

Lanyon, G.W., Batchelor, A.S., Ledingham, P., 1993. Results from a Discrete Fracture Network Model of a Hot Dry Rock System. In: *Proceedings of Eighteenth Workshop on Geothermal Reservoir Engineering Stanford University, Stanford, California, January 26-28, 1993*, SGP-TR-145, pp. 101–109.

Lee, S., Ghassemi, A., 2011. Three-dimensional thermo-poro-mechanical modeling of reservoir stimulation and induced microseismicity in geothermal reservoir. In: *Proceedings of Thirty-Sixth Workshop on Geothermal Reservoir Engineering Stanford University, Stanford, California, January 31 - February 3, 2011* SGP-TR-191, pp. 1-12.

Lee, S.H., Ghassemi, A., 2010. Thermo-Poroelastic Analysis of Injection-Induced Rock Deformation and Damage Evolution. In: *Proceedings of Thirty-Fifth Workshop on Geothermal Reservoir Engineering Stanford University, Stanford, California, February 1-3, 2010* SGP-TR-188, pp. 1–9.

Lewis, R.W., Nithiarasu, P., Seetharamu, K.N., 2005. *Fundamentals of the Finite Element Method for Heat and Fluid Flow*, Wiley. John Wiley & Sons, Ltd, Chichester, UK.

Li, K., 2013. Comparison of Geothermal With Solar and Wind Power Generation. In: *Proceedings of Thirty-Eighth Workshop on Geothermal Reservoir Engineering Stanford University, Stanford, California, February 11-13, 2013*, SGP-TR-198, pp. 1–10.

Li, K., Bian, H., Liu, C., Zhang, D., Yang, Y., 2015. Comparison of geothermal with solar and wind power generation systems. *Renew. Sustain. Energy Rev.* vol. 42, pp. 1464–1474.

Lim, K.T., Aziz, K., 1995. Matrix-fracture transfer shape factors for dual-porosity simulators. *J. Pet. Sci. Eng.* vol. 13, pp. 169–178.

Long, J.C.S., Karasaki, K., Davey, A., Peterson, J., Landsfeld, M., Kemeny, J., Martel, S., 1991. An inverse approach to the construction of fracture hydrology models conditioned by geophysical data. An example from the validation exercises at the Stripa Mine. *Int. J. Rock Mech. Min. Sci.* vol. 28, pp. 121–142.

Lund, J.W., 2007. Characteristics, development and utilization of geothermal resources, *Geo-Heat Center Quarterly Bulletin*.

Magnenet, V., Fond, C., Genter, A., Schmittbuhl, J., 2014a. Two-dimensional THM modelling of the large scale natural hydrothermal circulation at Soultz-sous-Forêts. *Geotherm. Energy* vol. 2, pp. 1-21.

McDermott, C., Haszeldine, R., Edlmann, K., Edwards, M., Robbins, B., De la Rosa Illescas, A., 2012. Report on the effect of Thermal, Hydraulic, Mechanical and Chemical Coupled Processes on Caprock Integrity from Analogue Analysis, Edinburgh Research Explorer. EU FP7 Project.

McDermott, C.I., Randriamanjatoa, A.R.L., Tenzer, H., Kolditz, O., 2006. Simulation of heat extraction from crystalline rocks: The influence of coupled processes on differential reservoir cooling. *Geothermics* vol. 35, pp. 321–344.

Mercer, J.W., Pinder, G.F., 1973. Galerkin finite-element simulation of a geothermal reservoir. *Geothermics* vol. 2, pp. 81–89.

Min, K.S., Huang, K., Ghassemi, A., 2011. A Study of Numerical Simulations of Mixed-Mode Fracture Propagation in Rock. In: *Proceedings of Thirty-Sixth Workshop on Geothermal Reservoir Engineering Stanford University, Stanford, California, January 31 - February 2, 2011*, pp. 1–12.

Minkoff, S.E., Stone, C.M., Bryant, S., Peszynska, M., Wheeler, M.F., 2003. Coupled fluid flow and geomechanical deformation modeling. *J. Pet. Sci. Eng.* vol. 38, pp. 37–56.

MIT, 2006. *The Future of Geothermal Energy: Impact of Enhanced Geothermal Systems (EGS) on the United States in the 21st Century*. Idaho Falls, ID.

Murphy, H.D., 1979. Heat Production On From A Geothermal Reservoir Formed By Hydraulic Fracturing - Comparison Of Field And Theoretical Results. In: SPE Annual Technical Conference and Exhibition. Society of Petroleum Engineers, p. 1-7.

Murphy, H.D., Tester, J.W., Grigsby, C.O., Potter, R.M., 1981. Energy extraction from fractured geothermal reservoirs in low-permeability crystalline rock. *J. Geophys. Res.* vol. 86, pp. 7145 -7158.

Nelson, R.A., 2001. *Geologic Analysis of Naturally Fractured Reservoirs*, Second. ed. Butterworth–Heinemann, United States.

Nie, R.-S., Meng, Y.-F., Jia, Y.-L., Zhang, F.-X., Yang, X.-T., Niu, X.-N., 2012. Dual Porosity and Dual Permeability Modeling of Horizontal Well in Naturally Fractured Reservoir. *Transp. Porous Media* vol. 92, pp. 213–235.

Nield, D. a, Bejan, A., 2006. *Convection in Porous Media Third Edition*, Springer.

Norbeck, J., Horne, R., 2015. Injection-Triggered Seismicity: An Investigation of Prothermoelastic Effects Using a Rate-and- State Earthquake Model. In: *Proceedings of Fourtieth Workshop on Geothermal Reservoir Engineering Stanford University, Stanford, California, January 26-28, 2015*, pp. 1–14.

O.C.Zienkiewicz, R.L.Taylor, Morgan, K., Hassan, O., Weatherill, N.P., 2000. *The Finite Element Method*, 1st ed, Butterworth–Heinemann. Butterworth–Heinemann, Oxford.

O’sullivan, M.J., 1985. Geothermal reservoir simulation. *Int. J. Energy Res.* vol. 9, pp. 319–332.

O’Sullivan, M.J., Pruess, K., Lippmann, M.J., 2000. *Geothermal Reservoir Simulation : the State-of-Practice and Emerging Trends*. In: *Proceedings of World Geothermal Congress, Kyushu - Tohoku, Japan, May 28 - June 10, 2000*, pp. 4065–4070.

O’Sullivan, M.J., Pruess, K., Lippmann, M.J., 2001. State of the art of geothermal reservoir simulation. *Geothermics* vol. 30, pp. 395–429.

O’Sullivan, M.J., Yeh, A., Mannington, W.I., 2009. A history of numerical modelling of the Wairakei geothermal field. *Geothermics* vol. 38, pp. 155–168.

Oberkampf, W.L., Trucano, T.G., 2002. Verification and validation in computational fluid dynamics. *Prog. Aerosp. Sci.* vol. 38, pp. 209–272.

Oberkampf, W.L., Trucano, T.G., Hirsch, C., 2004. Verification, validation, and predictive capability in computational engineering and physics. *Appl. Mech. Rev.* vol. 57, pp. 345-419.

Ogata, A., Banks, R.B., 1961. A solution of the differential equation of longitudinal dispersion in porous media. *Geol. Surv. (U.S.); Prof. Pap.* pp. A1–A7.

Okabe, T., Kirihara, K., Hayashi, K., Karasawa, K., Swenson, D., Schroeder, R., 2000. Analysis in Preparation for Hijiori Long Term Circulation Test. In: *Proceedings of World Geothermal Congress 2000 Kyushu - Tohoku, Japan, May 28 - June 10, 2000*, pp. 3823–3828.

Podgorney, R., Ketilsson, J., Driesner, T., Regenauer-Lieb, K., 2011. The Next Generation of Geothermal Reservoir Simulators: A Draft-Summary of the Recommendations from the International Partnership for Geothermal Technology Reservoir Modeling Working Group. *Geotherm. Resour. Counc. Trans.* vol. 35, pp. 1519–1527.

Poulsen, S.E., Balling, N., Nielsen, S.B., 2015. A parametric study of the thermal recharge of low enthalpy geothermal reservoirs. *Geothermics* vol. 53, pp. 464–478.

Pruess, K., 1988. Modeling of Geothermal Reservoirs: Fundamental Processes, Computer Simulation, and Field Applications. In: *Proc. 10th New Zealand Geothermal Workshop*. New Zealand, pp. 15–21.

Ranjbar, E., Hassanzadeh, H., 2011. Matrix–fracture transfer shape factor for modeling flow of a compressible fluid in dual-porosity media. *Adv. Water Resour.* vol. 34, pp. 627–639.

Robinson, B.A., Kruger, P., 1988. A Comparison of Two Heat Transfer Models for Estimating Thermal Drawdown in Hot Dry Rock Reservoirs. In: *Thirteen Stanford Geothermal Workshop*. Stanford, US, pp. 113–120.

Rutqvist, J., Tsang, C., 2012. Multiphysics processes in partially saturated fractured rock: Experiments and models from Yucca Mountain. *Rev. Geophys.* vol. 50, pp. 1–30.

Safari, M.R., Ghassemi, A., 2011. 3D Analysis of Huff and Puff and Injection Tests in Geothermal Reservoirs. In: Proceedings of Thirty-Sixth Workshop on Geothermal Reservoir Engineering Stanford University, Stanford, California, January 31 - February 2, 2011, pp. 1–10.

Safari, R., Ghassemi, A., 2015. 3D thermo-poroelastic analysis of fracture network deformation and induced micro-seismicity in enhanced geothermal systems. *Geothermics* vol. 58, pp. 1–14.

Sanjuan, B., Millot, R., Dezayes, C., Brach, M., 2010. Main characteristics of the deep geothermal brine (5km) at Soultz-sous-Forêts (France) determined using geochemical and tracer test data. *Comptes Rendus Geosci.* vol. 342, pp. 546–559.

Sanyal, S.K., Butler, S.J., Swenson, D., Hardeman, B., 2000. Review of the State-of-the-Art of numerical simulation of enhanced geothermal systems. Proceedings of World Geothermal Congress 2000 Kyushu - Tohoku, Japan, May 28 - June 10, 2000, pp. 3853–3858.

Sargent, R.G., 1999. Validation and Verification of Simulation Models. In: Proceedings of the 2004 Winter Simulation Conference, 2004. IEEE, pp. 13–24.

Sausse, J., Dezayes, C., Dorbath, L., Genter, A., Place, J., 2010. 3D model of fracture zones at Soultz-sous-Forêts based on geological data, image logs, induced microseismicity and vertical seismic profiles. *Comptes Rendus Geosci.* vol. 342, pp. 531–545.

Schroeder, R., Swenson, D., Shinohara, N., Okabe, T., 1999. Fracture dispersion effects in tracer analysis. In: Proceedings of Twenty-Fourth Workshop on Geothermal Reservoir Engineering Stanford University, Stanford, California, January 25-27, 1999 SGP-TR-162, pp. 3–9.

Schroeder, R., Swenson, D., Shinohara, N., Okabe, T., Takasugi, S., Hayashi, K., 1998. Strategies for the Hijiori Long Term Flow Test. In: Proceedings of Twenty-Third Workshop on Geothermal Reservoir Engineering Stanford University, Stanford, California, January 26-28. 1998 SGP-TR-I 58, pp. 351–358.

Shibuya, Y., Sekine, H., Takahashi, Y., Abé, H., 1985. Multiple Artificial Geothermal Cracks in a Hot Dry Rock Mass for Extraction of Heat. *J. Energy Resour. Technol.* vol. 107, pp. 274-279.

Smith, M.C., Nunz, G.J., Wilson, M.G., 1985. Hot Dry Rock Geothermal Energy Development Program. Annual report, fiscal year 1983. Los Alamos, NM.

Society for Computer Simulation, 1979. Terminology for model credibility. *Simulation* vol. 32, pp. 103–104.

Spichak, V., Geiermann, J., Zakharova, O., Calcagno, P., Genter, A., Schill, E., 2015. Estimating deep temperatures in the Soultz-sous-Forêts geothermal area (France) from magnetotelluric data. *Near Surf. Geophys.* vol. 13, pp. 397–408.

Strack, O.D.L., 1982. Assessment of effectiveness of geologic isolation systems. Analytic modeling of flow in a permeable fissured medium. Washington, USA.

Suirez-Arriaga, M.-Cc., 2002. Tetra-Porosity Models of Geothermal Reservoirs With Faults. *Geotherm. Resour. Counc. Trans.* vol. 26, pp. 847–852.

Swenson, D., 1997. Modeling, design, and life performance prediction for energy production from geothermal reservoirs. First quarter progress report. Idaho Falls, ID.

Swenson, D., 1998a. Modeling, design, and life performance prediction for energy production from geothermal reservoirs. Quarterly report, January--March 1998. Idaho Falls, ID.

Swenson, D., 1998b. Modeling, design, and life performance prediction for energy production from geothermal reservoirs. Final report. Idaho Falls, ID.

Swenson, D., Chopra, P., Wyborn, D., 2000. Initial Calculations of Performance for an Australian Hot Dry Rock Reservoir. In: *Proceedings of World Geothermal Congress 2000 Kyushu - Tohoku, Japan, May 28 - June 10, 2000*, pp. 3907–3912.

Swenson, D., Duteau, R., Sprecker, T., 1995. Modeling flow in a jointed geothermal reservoir. In: *Proceedings of World Geothermal Congress. New Mexico*, pp. 2553–2558.

Swenson, D., Hardeman, B., 1997. Using Thermal Drawdown and Recovery Signatures to Identify. In: *Proceedings of Twenty-First Workshop on Geothermal Reservoir Engineering Itanford University, Stanford, California, January 27-29, 1997 IGP-TR-I 55*, pp. 117–183.

Swenson, D., Schroeder, R., Shinohara, N., Okabe, T., 1999. Analyses of the Hijiori Long Term Circulation Test. In: Proceedings of Twenty-Fourth Workshop on Geothermal Reservoir Engineering Stanford University, Stanford, California, January 25-27, 1999 SGP-TR-162, pp. 1-7.

Tao, Q., Ghassemi, A., 2010. Poro-thermoelastic borehole stress analysis for determination of the in situ stress and rock strength. *Geothermics* vol. 39, pp. 250–259.

Taron, J., Elsworth, D., 2010. Coupled mechanical and chemical processes in engineered geothermal reservoirs with dynamic permeability. *Int. J. Rock Mech. Min. Sci.* vol. 47, pp. 1339–1348.

Tenzer, H., 2001. Development of Hot Dry Rock Technology. *Int. Work. hot dry rock Techno.* pp. 1-14.

Tester, J.W., 1979. Hot dry rock energy extraction field test: 75 days of operation of a prototype reservoir at Fenton Hill, Segment 2 of Phase I, Internal Report. Los Alamos, NM.

Thacker, B., Doebling, S., Hemez, F., Anderson, M., Pepin, J., Edward, A., 2004. Concepts of Model Verification and Validation. Natl. Nucl. Secur. Agency (NNSA), Los Alamos Natl. Laboratory LA-14167-M.

Thacker, B.H., Anderson, M.C., Senseny, P.E., Rodriguez, E.A., 2006. The role of nondeterminism in model verification and validation. *Int. J. Mater. Prod. Techno.* vol. 25, pp. 144-163.

Tsang, C.-F., 1985. Mass Transport in Low Permeability Rocks Under The Influence of Coupled Thermomechanical and Hydrochemical Effects--An Overview. In: International Congress on Hydrology of Rocks of Low Permeability, Tucson, AZ, USA, 7 Jan 1985, pp. 1–17.

Tsang, C.-F., 1986. Coupled Processes in Single Fractures, Double Fractures and Fractured Porous Media. In: Workshop on Numerical Modeling for Radioactive Waste Repositories, Madrid, Spain, December 10-12, 1986, pp. 1–21.

Tsang, C.-F., 1991. Coupled hydromechanical-thermochemical processes in rock fractures. *Rev. Geophys.* 29, 537–551.

Tsang, C.-F., 1999. Linking Thermal, Hydrological, and Mechanical Processes in Fractured Rocks. *Annu. Rev. Earth Planet. Sci.* vol. 27, pp. 359–384.

U.S. Department of Energy, 1999. Assessment of the State-of-the-Art of Numerical Simulation of Enhanced Geothermal Systems. United States.

U.S. Department of Energy, 2006. A History of Geothermal Energy Research and Development in the United States: Reservoir Engineering (1976-2006).

Verde, A., Ghassemi, A., 2013. Fracture Network Response to Injection Using an Efficient Displacement Discontinuity Method. *GRC Trans.* vol. 37, pp. 863–870.

Vidal, J., Genter, A., Durringer, P., Schmittbuhl, J., Strasbourg, U. De, Descartes, R., Cedex, F.-S., 2015. Natural Permeability in Fractured Triassic Sediments of the Upper Rhine Graben from Deep Geothermal Boreholes. In: Proceedings of World Geothermal Congress, Melbourne, Australia, 19-25 April 2015, pp. 1–13.

Wall, E., 2010. United States Geothermal Support and the International Partnership for Geothermal Technology. In: Proceedings of World Geothermal Congress, Bali, Indonesia, 25-29 April 2010, pp. 1–4.

Wang, X., Ghassemi, A., 2012. A Three-Dimensional Poroelastic Model for Naturally Fractured Geothermal Reservoir Stimulation. *Geotherm. Resour. Counc. Trans.* vol. 36, pp. 575–582.

White, D.E., Williams, D.L., 1975. Assessment of Geothermal Resources of the United States--1975, Geological Survey Circular.

White, M.D., Phillips, B.R., 2015. Code Comparison Study Fosters Confidence in the Numerical Simulation of Enhanced Geothermal Systems. In: Proceedings of Fortieth Workshop on Geothermal Reservoir Engineering Stanford University, Stanford, California, January 26-28, 2015, SGP-TR-204, pp. 1–12.

White, S.K., Purohit, S., Boyd, L., 2015. Using GTO-Velo to Facilitate Communication and Sharing of Simulation Results in Support of the Geothermal Technologies Office Code Comparison Study. In: Proceedings of Fourtieth Workshop on Geothermal Reservoir Engineering Stanford University, Stanford, California, January 26-28, 2015, SGP-TR-204, pp. 1–10.

Willis-Richards, J., Wallroth, T., 1995. Approaches to the modelling of HDR reservoirs: A review. *Geothermics* vol. 24, pp. 307–332.

Wong, Z.Y., Horne, R., Voskov, D., 2016. Comparison of Nonlinear Formulations for Geothermal Reservoir Simulations. In: 41st Workshop on Geothermal Reservoir Engineering, Stanford. Stanford, US, pp. 1–16.

World Energy Council, 2013. *World Energy Resources: Geothermal, Worldwide Report*.

Xia, Y., Plummer, M., Mattson, E., Podgorney, R., Ghassemi, A., 2017. Design, modeling, and evaluation of a doublet heat extraction model in enhanced geothermal systems. *Renew. Energy* vol. 105, pp. 232–247.

Xia, Y., Plummer, M., Podgorney, R., Ghassemi, A., 2016. An Assessment of Some Design Constraints on Heat Production of a 3D Conceptual EGS Model Using an Open-Source Geothermal Reservoir Simulation Code. In: Forty-First Workshop on Geothermal Reservoir Engineering Stanford University, Stanford, California, February 22-24, 2016 SGP-TR-209, pp. 1–24.

Xia, Y., Podgorney, R., Huang, H., 2017. Assessment of a Hybrid Continuous/Discontinuous Galerkin Finite Element Code for Geothermal Reservoir Simulations. *Rock Mech. Rock Eng.* vol. 50, pp. 719–732.

Xing, H., Liu, Y., Gao, J., Chen, S., 2015. Recent development in numerical simulation of enhanced geothermal reservoirs. *J. Earth Sci.* vol. 26, pp. 28–36.

Zeng, Y., Zhan, J., Wu, N., Luo, Y., Cai, W., 2016. Numerical simulation of electricity generation potential from fractured granite reservoir through vertical wells at Yangbajing geothermal field. *Energy* vol. 103, pp. 290–304.

Zhang, L., Li, X., Zhang, Y., Cui, G., Tan, C., Ren, S., 2017. CO₂ injection for geothermal development associated with EGR and geological storage in depleted high-temperature gas reservoirs. *Energy* vol. 123, pp. 139–148.

Zheng, B., Xu, J., Ni, T., Li, M., 2015. Geothermal energy utilization trends from a technological paradigm perspective. *Renew. Energy* vol. 77, pp. 430–441.

Zhou, X., Ghassemi, A., 2008. A three-dimensional poroelastic model for water injection into a geothermal reservoir. In: *Proceedings of Thirty-Third Workshop on Geothermal Reservoir Engineering* Stanford University, Stanford, California, January 28-30, 2008, pp. 1–7.

Zhou, X., Ghassemi, A., 2011. Three-dimensional poroelastic analysis of a pressurized natural fracture. *Int. J. Rock Mech. Min. Sci.* vol. 48, pp. 527–534.

Zhu, J., Hu, K., Zhang, W., Lu, X., 2017. A study on generating a map for selection of optimum power generation cycles used for Enhanced Geothermal Systems. *Energy* vol. 133, pp. 502–512.

Zienkiewicz, O.C., Taylor, R.L., 2000. *The Finite Element Method Volume 1 : The Basis*, 1st ed, Butterworth–Heinemann. Butterworth–Heinemann, Oxford.

Zienkiewicz, O.C., Taylor, R.L., Zhu, J.Z., 2005. *The Finite Element Method: Its Basis and Fundamentals*, Sixth edition, Sixth. ed, Butterworth–Heinemann. Butterworth–Heinemann, Oxford.

Zimmerman, R.W., 2000. Coupling in poroelasticity and thermoelasticity. *Int. J. Rock Mech. Min. Sci.* vol. 37, pp. 79–87.

Zimmerman, R.W., Chen, G., Hadgu, T., Bodvarsson, G.S., 1993. A numerical dual-porosity model with semianalytical treatment of fracture/matrix flow. *Water Resour. Res.* vol. 29, pp. 2127–2137.

Zyvoloski, G.A., Robinson, B.A., Dash, Z. V., Trease, L.L., 1999. *Models and Methods Summary for the FEHM Application*, FEHM Manual. New Mexico.

Appendices

Appendix one: Numerical implementation of the FE model

1.A.1 Implementation of the FE model

The FE model developed is nonlinear in space and time. Therefore, the system of the coupled equations is solved through LiveLink simulation. The procedure employed is shown in Figure 1.A.1 and summarised as follows:

1. After creating the model geometry, the model is discretised into a set of representative elementary volume (REV)s using Gmsh.
2. From the meshed file generated an algorithm is then developed in MATLAB that generates the element connectivity.
3. The initial and boundary conditions for the thermal and hydraulic properties are then applied.
4. The FE model performs a fully coupled simulation via LiveLink in COMSOL, and the pressure and temperature fields for each of the REV)s are obtained.
5. The mesh convergence is checked based on the outcomes of the field variables (i.e. pressure and temperature), and if the results converge, then, the next time step is added. On the other hand, if it does not converge the mesh will be refined until convergence is reached.
6. If the convergence criterion in equation (3.81) is satisfied, then the solution returns to step 4, alternatively steps 1-5 are repeated.

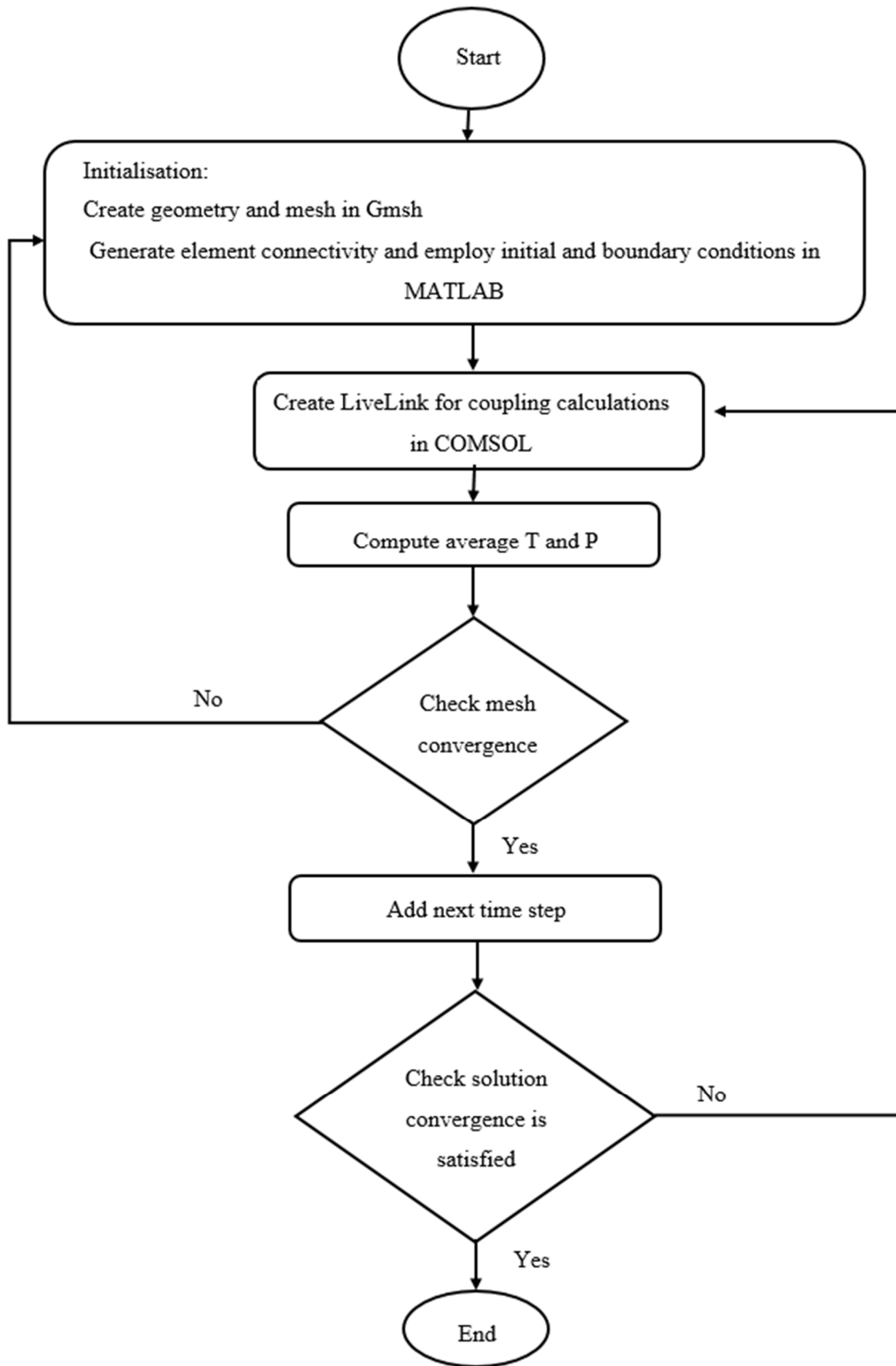


Figure 1.A.1: Procedure for the numerical implementation of the FE model

Appendix two: Analytical solution for heat transfer in porous medium

2.A.1 Heat transport in porous medium

The mass conservation equation of fluid flow in porous medium (Kolditz et al., 2016) can be reduced to a Laplacian equation of flow as

$$\tau \nabla^2 P + Q = 0 \quad (2.A.1)$$

where P is the pressure and Q is the injection flow rate, which gives a uniform velocity v_x along the x -axis. Hence, to couple the fluid flow equation with a heat transport, Faust and Mercer (1979a) describe a linear flow of hot incompressible fluid through a porous medium by the following equation:

$$\lambda \frac{\partial^2 \bar{T}}{\partial x^2} - v_x \rho_L C_{P,L} \frac{\partial \bar{T}}{\partial x} + \frac{2}{H} \lambda_S \frac{\partial \bar{T}}{\partial z} = \rho C_P \frac{\partial \bar{T}}{\partial t}, z = 0, x > 0, t > 0. \quad (2.A.2)$$

in which \bar{T} is the normalised temperature, and is equivalent to $(T - T_0)/(T_{inj} - T_0)$, where T_{inj} and T_0 are the injection and initial temperature, respectively. The parameter H is the formation thickness, and λ is the effective thermal conductivity, which is given as $\lambda = \phi_S \lambda_S + (1 - \phi_S) \lambda_L$. The properties ρC_P is the effective density and heat capacity, and is given as: $\rho C_P = \phi_S (\rho_L C_{P,L}) + (1 - \phi_S) \rho_S C_{P,S}$.

Equation (2.A.2) above is subject to the following conditions:

$$\begin{aligned} \bar{T}(x, 0) &= 0, x > 0; \\ \bar{T}(0, t) &= 1, z = 0, t \geq 0; \\ \text{Limit } \bar{T} &= 0; \\ x^2 + z^2 &\rightarrow \infty \end{aligned} \quad (2.A.3)$$

The generalised analytical solution of the above equations is given by Avdonin (1964) (Faust and Mercer, 1979a) as:

$$\bar{T}(\chi, \tau) = \frac{\chi}{\sqrt{\pi \tau}} \int_0^1 \left\{ \exp \left[- \left(s \gamma \sqrt{\tau} - \frac{\chi}{2s\sqrt{\tau}} \right)^2 \right] \operatorname{erfc} \left(\frac{\alpha s^2 \sqrt{\tau}}{2\sqrt{1-s^2}} \right) \right\} \frac{ds}{s^2} \quad (2.A.4)$$

where the unknown parameters are defined below as

$$\chi = \frac{2x}{H}; \quad \tau = \frac{4\lambda t}{\rho C_p H^2}; \quad \gamma = \frac{Q \rho_L C_{p,L}}{4\lambda}; \quad \text{and} \quad \alpha = \sqrt{\frac{\lambda_s \rho_s C_{p,S}}{\lambda \rho C_p}} \quad (2.A.5)$$

Appendix three: Analytical solutions for the heat transport in fractures

3.A.1 Heat transfer in a fracture

Ogata and Banks (1961) developed an analytical solution capable of modelling 1-D transport processes driven by advection and diffusion, which is expressed as

$$T(x, t) = \frac{T_{inj}}{2} \left\{ \operatorname{erfc} \left(\frac{x - v_x t}{2\sqrt{\alpha t}} \right) + \exp \left(\frac{v_x x}{\alpha} \right) \operatorname{erfc} \left(\frac{x + v_x t}{2\sqrt{\alpha t}} \right) \right\} \quad (3.A.1)$$

where T is the temperature at the location x at time t , T_{inj} is the injection temperature, α and is the diffusivity coefficient which is expressed as

$$\alpha = \frac{\lambda}{\rho C_p} \quad (3.4.2)$$

Equation (3.A.1) above can also be written in terms of dimensionless parameters as

$$T(x, t) = \frac{T_{inj}}{2} \left[\operatorname{erfc} \left(\frac{1 - \xi}{2\sqrt{\xi \eta}} \right) + \exp \left(\frac{1}{\eta} \right) \operatorname{erfc} \left(\frac{1 + \xi}{2\sqrt{\xi \eta}} \right) \right] \quad (3.A.3)$$

where

$$\xi = \frac{v_x t}{x}, \text{ and } \eta = \frac{\alpha}{v_x x} \quad (3.A.4)$$

Appendix four: Fluid transport in triple porosity-permeability media

4.A.1 The transient flow of mass in triple porosity-permeability media

In this case, the three different media share the same equation in general, with different flow patterns via the velocity term and the mass source term (Bear, 1993), and the equation is given as:

$$\rho_L S_j \frac{\partial P_j}{\partial t} + \nabla \cdot \rho_L v_j = Qm_j \quad (4.A.1)$$

$$\forall j = m, f, F \quad (4.A.2)$$

$$v_j = -\frac{\kappa_j}{\mu} \nabla P_j \quad (4.A.3)$$

The sub index j represents transport in the matrix (m), in the fracture (f) and in the fault (F), respectively. The variables ρ_L is the fluid density, S_j is the linearised storage, P_j is the fluid pressure, v_j is Darcy's velocity, Qm_j is the source/sink term, and κ_j is the permeability. Also, the fracture/fault permeability can be expressed as

$$v_{f,F} = \frac{b_{f,F}^2}{12\mu} \nabla P_{f,F}, \text{ or } = \frac{b_{f,F}^3}{12w\mu} \nabla P_{f,F} \quad (4.A.4)$$

However, the fracture and fault's mass source term are calculated by adding the mass flow rate per unit surface from the side walls of the fracture and fault, which can be expressed as

$$Q_{f,F} = Q_{left}^{f,F} + Q_{right}^{f,F} \quad (4.A.5)$$

$$Q_{left}^{f,F} = -\rho_L \frac{\kappa_j}{\mu_j} \frac{\partial P_{left}}{\partial n_{left}} \quad (4.A.6)$$

$$Q_{right}^{f,F} = -\rho_L \frac{\kappa_j}{\mu_j} \frac{\partial P_{right}}{\partial n_{right}} \quad (4.A.7)$$

Appendix five: Heat transport in triple porosity-permeability media

5.A.1 The transient flow of heat in triple porosity-permeability media

The governing equations are coupled via the fluid velocity in Darcy's equation and by the boundary conditions at the interfaces of the various media. For this model the equations are given as

$$(\rho C_p)_j \frac{\partial T_j}{\partial t} + \rho_L C_{p,L} v_j \cdot \nabla T + \nabla \cdot q_j = Q_j \quad (5.A.1)$$

$$(\rho C_p)_j = \phi_S (\rho_L C_{p,L}) + (1 - \phi_S) \rho_S C_{p,S} \quad (5.A.2)$$

$$q_j = -\lambda_j \nabla T \quad (5.A.3)$$

$$\lambda_j = \phi_S \lambda_S + (1 - \phi_S) \lambda_L \quad (5.A.4)$$

The variables ρ and C_p (i.e. ρC_p) are the effective densities and specific heat capacities, respectively, T_j is the temperature, q_j is the heat flux density, and t is time. Parameters $C_{p,S}$ and $C_{p,L}$ corresponds specific heat capacity of solid and fluid, ρ_S is the solid density, Q_j is the heat source/sink term, λ_j is the effective thermal conductivities, ϕ_S is the solid porosity, and λ_S and λ_L are solid and fluid thermal conductivities, respectively.

Publications from the PhD research

1. **Aliyu M. D.** and H. Chen, (2017), Optimum control parameters and long-term productivity of geothermal reservoirs using coupled thermo-hydraulic process modelling, *Renew. Energy*, vol. 112, pp. 151–165, Nov. 2017 (Impact Factor=4.52).
2. **Aliyu M. D.** and H. Chen, (2017), Sensitivity analysis of deep geothermal reservoir: Effect of reservoir parameters on production temperature, *Energy*, vol. 129, pp. 101–113, Jun. 2017 (Impact Factor=4.357).
3. **Aliyu M. D.**, H. Chen, and C. D. Hills (2017), Enhanced geothermal system modelling with multiple pore media: thermo-hydraulic (TH) coupled processes,” *Applied Energy*, under review, submitted in November 2017 (Impact Factor=7.182).
4. **Aliyu, M.D.**, Chen, H., HILLS, C.D., Harireche, O., (2017), A Fully-coupled model of heat and fluid flow in discretely fractured geothermal reservoir. In: 15th UK HEAT TRANSFER CONFERENCE, UKHTC2017, Brunel University London, 4-5 September 2017. University of Brunel, London, pp. 1–2.
5. **Aliyu M. D.** and H. Chen, (2017), Numerical modelling of geothermal reservoirs using the triple porosity-permeability approach, in *Proceedings of the 25th UKACM Conference on Computational Mechanics 12 –13 April 2017, University of Birmingham, Birmingham, United Kingdom*, 2017, no. April, pp. 10–13.
6. **Aliyu M. D.**, H. Chen, O. Harireche, C. D. Hills, (2017), Numerical modelling of geothermal reservoirs with multiple pore media, in *Proceedings, 42nd Workshop on Geothermal Reservoir Engineering Stanford University, Stanford, California, February 13-15, 2017 SGP-TR-212*, 2017, pp. 1–12.
7. **Aliyu M. D.**, and H. Chen, (2016), Numerical modelling of coupled hydro-thermal processes of the soultz heterogeneous geothermal system, in *Proceedings of the VII European Congress on Computational Methods in Applied Sciences and Engineering (ECCOMAS Congress 2016)*, 2016, no. June, pp. 1659–1671.

8. **Aliyu M. D.**, H. Chen, and O. Harireche, (2016), Finite element modelling for productivity of geothermal reservoirs via extraction well, in *Proceedings of the 24th UK Conference of the Association for Computational Mechanics in Engineering 31 March– 01 April 2016, Cardiff University, Cardiff*, 2016, no. April, pp. 331–334.

9. Chen, H., **Aliyu, M.D.**, (2017), Numerical modelling of coupled thermo-hydraulic problems for long-term geothermal reservoir. In: VII International Conference on Computational Methods for Coupled Problems in Science and Engineering, Coupled Problems 2017, M. Papadrakakis, E. Oñate and B. Schrefler (Eds), pp. 234-243.